



Dipl.-Ing. Lukas Schafzahl, BSc

# **Parasitic and Interphase Chemistries in Li-ion Batteries and Beyond**

## **DISSERTATION**

zur Erlangung des akademischen Grades

Doktor der technischen Wissenschaften

eingereicht an der

**Technischen Universität Graz**

Betreuer

Univ.-Prof. Dr.rer.nat. Martin Wilkening

Institut für Chemische Technologie von Materialien

Dipl.-Ing. Dr.sc.ETH Stefan A. Freunberger

Graz, Februar 2018



## **EIDESSTATTLICHE ERKLÄRUNG**

Ich erkläre an Eides statt, dass ich die vorliegende Arbeit selbstständig verfasst, andere als die angegebenen Quellen/Hilfsmittel nicht benutzt, und die den benutzten Quellen wörtlich und inhaltlich entnommenen Stellen als solche kenntlich gemacht habe. Das in TUGRAZonline hochgeladene Textdokument ist mit der vorliegenden Dissertation identisch.

---

Datum

---

Unterschrift





*Not all those who wander are lost.*





## Danksagung

Mein Dank gilt meinem Betreuer Stefan Freunberger, der trotz vieler anderer Pflichten stets für mich erreichbar war und mich mit seiner Unterstützung und seinen Ideen durch diese drei Jahre begleitet hat. In dieser Zeit durfte ich die Welt der Batterieforschung kennenlernen und auch selbst ein winziges Stück zum wissenschaftlichen Fortschritt beitragen. Außerdem möchte ich Martin Wilkening danken, der in entscheidenden Situationen ein offenes Ohr für mich hatte und mir mit seinem Rat zur Seite stand.

Weiterhin gilt mein Dank all jenen, ohne die diese Arbeit nicht möglich gewesen wäre: Johann Schlegl fertigte unzählige Messaufbauten und Kleinteile an, Manfred Kriechbaum steuerte wichtige SAXS-Diffraktogramme bei, Petra Kaschnitz unterstützte mich bei NMR-Messungen, Gernot Strohmeier beantwortete meine vielen Fragen zur HPLC und Sergey Borisov ermöglichte die Fluoreszenzmessungen. Weitere wichtige Messungen wurden von Heike Ehmman, Franz-Andreas Mautner, Brigitte Bitschnau und Jürgen Sattelkow durchgeführt. Auch Sandra Grumm hat mit ihrer Masterarbeit und ihrem Projektlabor zum Gelingen dieser Arbeit beigetragen, wie auch Christian Slugove mit vielen produktiven Diskussionen. Nicht zuletzt möchte ich jenen danken, die den Laden hier am Laufen halten: Birgit Ehmman, Christina Albering, Mathilde Frießnegg, Liane Hochgatterer, Renate Trebizan und den Damen.

Besonders danken möchte ich auch den Mitgliedern meiner Arbeitsgruppe, Bettina, Nika, Christian, Aleksej, Anita, Mani, Eléonore, Yann und Christian, die für ein angenehmes Arbeitsklima gesorgt und Licht in dunkle Kellerstunden gebracht haben. Unsere Ausflüge zu holprigen Kegelbahnen und gefräßigen Murmeltieren werden mir stets im Gedächtnis bleiben. Auch Yu und Petra haben meine Zeit hier immer wieder bereichert, genau wie meine Schreibraunkollegen Klaus, Sarah, Martin und Matthias.

Doch die letzten drei Jahre haben nicht nur aus Wissenschaft bestanden und mein tiefer Dank gilt meinen Freunden. Danke Bernhard, Hari und Berni für die gemeinsamen Abenteuer; danke an David, Sandi, Yassi und Yu für die gemeinsam beschrittenen Pfade; danke an Basti, Rahel und alle anderen für die schönen Spieleabende und Kletternachmittage.

Auch meiner Familie möchte ich danken. Gisi und Hans, eure bedingungslose Unterstützung habe ich niemals als selbstverständlich gesehen und nur dank euch bin ich überhaupt so weit gekommen. Vielen, vielen Dank! Christine und Max, ihr habt mich in eure Familie aufgenommen und dafür bin ich sehr dankbar. Mein letzter und wichtigster Dank gilt aber meiner Frau Bettina. Du warst für mich notwendige Unterstützung, willkommen Ablenkung und perfekte Ergänzung. Ich könnte mir keine bessere Begleiterin vorstellen als dich.



## Kurzfassung

In den letzten Jahrzehnten sind Batterien im täglichen Leben allgegenwärtig geworden. Li-Ionen-Batterien betreiben Unterhaltungselektronik, Elektrowerkzeuge, Hybridfahrzeuge und Elektroautos und werden auch neue Anwendungen wie Speicherkraftwerke erobern. Diese neuen Anwendungen erfordern weitere Verbesserungen der Energiedichte, Sicherheit, Nachhaltigkeit und Lebenszeit. Das entfacht enormes Interesse an weiterentwickelten Li-Ionen-Batterien, aber auch an weiterführenden Batterietechnologien, die Li-Ionen-Batterien ergänzen oder ersetzen könnten. Na-Ionen-Batterien versprechen eine nachhaltigere und wirtschaftlichere Technologie zu sein, während Li-O<sub>2</sub>- und Na-O<sub>2</sub>-Batterien weit höhere Energiedichten erreichen könnten. All diese weiterführenden Technologien leiden jedoch an niedrigen Lebensdauern, die hauptsächlich durch Nebenreaktionen verursacht werden. Dieses Phänomen ist selbst in Li-Ionen-Batterien noch nicht völlig erforscht, und in weiterführenden Technologien noch viel weniger. Diese Dissertation widmet sich daher den Nebenreaktionen, ihren Ursachen und Auswirkungen auf Li-Ionen-Batterien und weiterführende Batteriesysteme.

In Li- und Na-Ionen-Batterien treten Nebenreaktionen auf, wenn der flüssige Elektrolyt mit hochreaktiven Elektrodenoberflächen in Berührung kommt. Eine „Solid Electrolyte Interphase“ (SEI) bildet sich, die Ionentransport erlaubt, aber weitere Zersetzung verhindert. Zentrale SEI-Bestandteile sind Li- und Na-Alkylcarbonate (LAC und SAC); von ihnen wurde eine homologe Serie hergestellt und bezüglich Struktur, Ionenleitfähigkeit und Steifigkeit charakterisiert. Abgesehen von Lithiummethylcarbonat formen diese Verbindungen Schichtstrukturen. Bei LAC sinken die ionischen Leitfähigkeiten mit zunehmender Kettenlänge, die Steifigkeit liegt konstant bei 1 GPa. Bei NAC ist es genau umgekehrt.

Na-Ionen-Halbzellen verdeutlichen die Folgen einer dysfunktionalen SEI, wie sie von Carbonatelektrolyten auf metallischem Na und Na-Interkalationsanoden gebildet wird: Ständige Nebenreaktionen verfälschen die Messdaten. Verlässlichere Ergebnisse können mit einem hochkonzentrierten Elektrolyten erzielt werden, der aus Natriumbis(fluorosulfonyl)imid (NaFSI) in Dimethoxyethan (DME) besteht und Na effektiv stabilisiert. Das erlaubte die Abscheidung von Na mit 98 % Coulombeffizienz für über 300 Zyklen ohne Dendritenbildung. Weiter wurde gezeigt, dass der NaFSI/DME-Elektrolyt mit Anoden aus amorphem Kohlenstoff und Na<sub>3</sub>V<sub>2</sub>(PO<sub>4</sub>)<sub>3</sub>-Kathoden kompatibel ist.

Die SEI ist lebenswichtig für Li-Ionen- und Na-Ionen-Batterien, aber Passivierungsschichten bilden sich auch in Li-O<sub>2</sub>- und Na-O<sub>2</sub>-Systemen, in denen der Elektrolyt Nebenreaktionen mit Alkalimetallperoxiden oder -superoxiden eingeht. Obwohl Nebenprodukte also allgegenwärtig sind, fehlt eine Methode um ihre Gesamtmenge zu bestimmen. Wir präsentieren eine verbesserte Methode, die den Kohlenstoff aus organischen und anorganischen Nebenprodukten separat quantifiziert. Gleichzeitig kann die Menge an Alkalimetallperoxiden oder -superoxiden bestimmt werden, wodurch sich die Methode besonders zur Quantifizierung der SEI, wie auch zur Analyse von Nebenreaktionen in Metall-Sauerstoff Batterien eignet. Mit Hilfe dieser Methode und anderer *in situ* und *ex situ* Analysen konnten wir feststellen, dass sich in Na-O<sub>2</sub>-Batterien Singulett-Sauerstoff bildet. Er entsteht während der Entladung, Ladung und Lagerung und ist eine Hauptursache für Nebenreaktionen, welche die Lebenszeit der Batterie verkürzen. Ein genaueres Verständnis von Nebenreaktionen ist daher unumgänglich, um die vielversprechenden, weiterführenden Batteriesysteme zu realisieren.



## Abstract

Over the last decades, batteries have become ubiquitous in everyday life. Li-ion batteries power consumer electronics, power tools, hybrid vehicles and electric cars and are expected to expand in new applications such as large-scale energy storage. These new applications demand further improvements with respect to energy density, safety, sustainability and lifetime. This has spurred immense interest in advanced Li-ion batteries, as well as novel “beyond Li-ion” technologies to complement or replace them. Na-ion batteries promise to be a more sustainable and economical technology, while Li-O<sub>2</sub> and Na-O<sub>2</sub> batteries could far surpass the energy density of Li-ion batteries. All beyond Li-ion technologies are, however, severely limited by low lifetimes resulting predominantly from parasitic reactions. This phenomenon is still not fully understood in Li-ion batteries and even less so in beyond Li-ion technologies. Thus, this thesis aims to elucidate the origin and impact of parasitic reactions in Li-ion batteries and beyond.

In Li-ion and Na-ion batteries, parasitic reactions occur when the liquid organic electrolyte is in contact with highly reactive electrode surfaces. The reaction products form a solid electrolyte interface (SEI), which allows ion transport, but prevents further decomposition. Li and Na alkyl carbonates (LACs and SACs) were selected as key SEI components; a homologous series of them was synthesized and characterized with respect to structure, ionic conductivity and stiffness. The compounds assume layered structures except for lithium methyl carbonate. For LACs conductivities decrease with chain length, while stiffnesses remain constant around 1 GPa. For SACs the exact opposite is the case.

Na-ion half cells demonstrate the consequences of poor SEI formation; state-of-the-art carbonate electrolytes fail to passivate metallic Na and Na intercalation anodes and continuous parasitic reactions compromise the obtained data. More reliable results can be ensured by employing a highly concentrated sodium bis(fluorosulfonyl)imide (NaFSI) in dimethoxyethane (DME) electrolyte, which efficiently stabilizes Na. This permitted nondendritic Na cycling with 98 % coulombic efficiency for up to 300 cycles. The NaFSI/DME electrolyte was also shown to be compatible with hard carbon anodes and Na<sub>3</sub>V<sub>2</sub>(PO<sub>4</sub>)<sub>3</sub> cathodes.

The SEI is vital for Li-ion and Na-ion batteries, but passivation layers are also formed in Li-O<sub>2</sub> and Na-O<sub>2</sub> systems, where the electrolyte undergoes parasitic reactions with alkaline peroxide or superoxide. Despite the fact that side products are ubiquitous, an accurate and integral quantification method remains elusive. Herein, we present a refined method that sensitively quantifies carbonaceous side products, separating them into organic and inorganic ones. At the same time the method additionally quantifies alkaline peroxides or superoxides, rendering it an ideal tool to study parasitic reactions in metal-oxygen batteries. This tool was combined with other *in-situ* and *ex-situ* techniques to investigate parasitic reactions in Na-O<sub>2</sub> batteries. It was found that singlet oxygen forms at all stages of cycling and during rest and is a major source of parasitic reactions, which reduce the battery’s lifetime. A more thorough understanding of parasitic reactions is thus required to enable highly promising beyond Li-ion technologies.

# Contents

<b>1</b>	<b>Li-ion batteries and beyond</b>	<b>1</b>
1.1	Li-ion batteries . . . . .	1
1.1.1	Past developments . . . . .	1
1.1.2	State of the art . . . . .	2
1.1.3	Future developments . . . . .	3
1.2	Beyond Li-ion batteries . . . . .	3
1.2.1	Na-ion batteries . . . . .	4
1.2.2	Li-O <sub>2</sub> batteries . . . . .	4
1.2.3	Na-O <sub>2</sub> batteries . . . . .	5
1.3	Parasitic reactions and interphases . . . . .	6
<b>2</b>	<b>Alkyl carbonates as SEI components</b>	<b>9</b>
2.1	Carbonates as electrolyte solvents . . . . .	10
2.2	The solid electrolyte interphase . . . . .	10
2.2.1	SEI composition . . . . .	11
2.2.2	SEI properties . . . . .	13
2.3	Contribution . . . . .	14
2.4	Long-chained carbonate solvents as SEI modifiers . . . . .	23
2.4.1	Ionic conductivity . . . . .	24
2.4.2	Electrochemical stability and passivation efficiency . . . . .	25
2.4.3	DOC as electrolyte additive . . . . .	27
<b>3</b>	<b>Reversible cycling of sodium metal and Na intercalation compounds</b>	<b>31</b>
3.1	Stabilizing Na-ion half cells . . . . .	32
3.1.1	Are half cells reliable? . . . . .	32
3.1.2	Passivating sodium metal . . . . .	33
3.2	Contribution . . . . .	35
3.3	Optimizing concentration and cycling conditions . . . . .	43
3.3.1	Solvent to salt ratio . . . . .	43
3.3.2	Cycling conditions . . . . .	44
<b>4</b>	<b>Quantifying superoxide, peroxide and carbonaceous compounds</b>	<b>45</b>
4.1	Side product and interphase analysis . . . . .	46
4.1.1	X-ray photoelectron spectroscopy . . . . .	46
4.1.2	Fourier transform infrared spectroscopy . . . . .	46
4.1.3	Determining total amounts of SEI components . . . . .	47
4.2	Contribution . . . . .	48



<b>5</b>	<b>Singlet oxygen in the Na-O<sub>2</sub> battery</b>	<b>55</b>
5.1	Singlet oxygen and its reactivity . . . . .	56
5.2	Contribution . . . . .	58
5.3	Contribution (german) . . . . .	63
5.4	An attempt to mitigate <sup>1</sup> O <sub>2</sub> induced parasitic reactions . . . . .	68
<b>6</b>	<b>Conclusion and outlook</b>	<b>71</b>
<b>A</b>	<b>Appendix</b>	<b>73</b>
A.1	Supplementary Material . . . . .	73
A.1.1	Long Chain Alkyl Carbonates as Solid Electrolyte Interface Components: Structure, Ion Transport and Mechanical Properties . . .	74
A.1.2	An Electrolyte for Reversible Cycling of Sodium Metal and Intercalation Compounds . . . . .	78
A.1.3	Quantifying Total Superoxide, Peroxide and Carbonaceous Compounds in Metal-O <sub>2</sub> Batteries and the Solid Electrolyte Interface .	83
A.1.4	Singlet Oxygen during Cycling of the Aprotic Sodium-O <sub>2</sub> Battery	92
A.2	Abbreviations . . . . .	102
<b>B</b>	<b>Bibliography</b>	<b>105</b>



# 1. Li-ion batteries and beyond

Modern life would be hard to imagine without batteries. Starting from small handheld consumer electronics, batteries have penetrated almost all areas of everyday life. In the next years, batteries are expected to conquer new fields of application like individual transport and large-scale energy storage. These applications demand further developments both within and beyond the Li-ion technology, some of which are briefly summarized in this chapter.

## 1.1 Li-ion batteries

### 1.1.1 Past developments

It was a series of breakthroughs that led to the realization of Li-ion batteries: In 1980, the group of Goodenough discovered that  $\text{Li}^+$  could be reversibly intercalated into a  $\text{LiCoO}_2$  (LCO) host.<sup>1</sup> Other materials of the  $\text{LiMO}_2$  type shared this feature, as does spinel  $\text{Li}_2\text{Mn}_2\text{O}_4$  (LMO).<sup>2</sup> These materials were the first functional intercalation cathodes\* and maintain a large market share even today.<sup>3</sup>

The route towards a suitable anode proved more problematic.<sup>4</sup> At the early stages of development, researchers were drawn to metallic Li as anode material because of its superb capacity of  $3860 \text{ mAh g}^{-1}$ . Moreover, Li is very light and the most electronegative element with a potential of  $-3.05 \text{ V}$  *versus* the standard hydrogen electrode. These combined features give rise to fantastic energy densities, but Li also entails serious safety issues.<sup>5,6</sup> Its surface undergoes parasitic reactions with the electrolyte, which will be eventually depleted if no passivation layer is formed. Moreover,  $\text{Li}^+$  deposition leads to needle-like structures, called dendrites, which are prone to deteriorate capacity or even short the cell with disastrous outcome.<sup>7,8</sup>

As these issues could not be fully overcome, researchers instead turned to carbonaceous materials that could reversibly intercalate  $\text{Li}^+$ . Seminal cells employed petroleum coke as  $\text{Li}^+$ -host, which was later substituted for hard carbon and finally graphite.<sup>9</sup> Until then, graphite had been considered unstable because the commonly used electrolyte solvent propylene carbonate (PC) would co-intercalate and subsequently destroy the graphite layers.<sup>10,11</sup> PC was then replaced by ethylene carbonate (EC), which decomposes in parasitic reactions and forms a stable interphase to protect the graphite (see Section 2.2 for a detailed discussion).<sup>12</sup> The stable graphite anode constitutes the second milestone in the development of Li-ion batteries.

---

\*This work follows the convention in the battery community, where the terms cathode and anode designate the positive and negative electrode of the cell, respectively, even though this is per definition untrue on charge.

### 1.1.2 State of the art

Li-ion batteries are assembled in the discharged state, thus battery operation begins with charge:  $\text{Li}^+$  is removed from the LCO cathode material and enters the electrolyte. In the cathode material,  $\text{Co}^{3+}$  is simultaneously oxidized to  $\text{Co}^{4+}$  to preserve electroneutrality. Electrons are liberated and travel through the outer circuit to the anode, where they reduce graphite while  $\text{Li}^+$  is inserted. Upon discharge, the whole process is reversed and  $\text{Li}^+$  is shuttled back to the cathode completing the cycle. Importantly, Li remains in oxidation state +1 throughout cycling and is merely shuttled back and forth; this coined the terms “rocking chair battery”, “shuttlecock battery” and also “Li-ion battery”, which ultimately prevailed.

Since their commercialization in 1991, Li-ion batteries have not seen a revolution, but experienced a steady evolution and diversification. At the anode side, graphite is still used in an overwhelming share of Li-ion batteries;<sup>3</sup> sometimes small amounts of Si are now added to improve its capacity.<sup>4</sup> At the cathode, several new materials compete with  $\text{LiCoO}_2$ , see Table 1.1. While layered LCO still dominates the market due to its high cycle life and energy density, the structurally similar  $\text{LiNi}_{0.33}\text{Mn}_{0.33}\text{Co}_{0.33}\text{O}_2$  (NMC) shows a promising combination of energy density, power capability and safety.<sup>13–15</sup>  $\text{LiNi}_{0.80}\text{Co}_{0.15}\text{Al}_{0.05}\text{O}_2$  (NCA) is another layered material that suffers from moisture sensitivity, but offers high power and energy density.<sup>16</sup> Energy density is, however, only one property to be considered, as exemplified by the success of LMO.<sup>3</sup> This material compensates low energy density with lower prices and high safety.  $\text{LiFePO}_4$  (LFP) is another material that offers excellent cyclic and thermal stability at the expense of energy density.<sup>17,18</sup> Overall, cathode materials are diverse and are chosen depending on the application.

**Table 1.1:** Characteristics of common Li-ion cathode materials. LCO is  $\text{LiCoO}_2$ , LMO is  $\text{LiMn}_2\text{O}_4$ , NCA is  $\text{LiNi}_{0.80}\text{Co}_{0.15}\text{Al}_{0.05}\text{O}_2$ , NMC is  $\text{LiNi}_{0.33}\text{Mn}_{0.33}\text{Co}_{0.33}\text{O}_2$ , LFP is  $\text{LiFePO}_4$ . Data from Ref 4.

Material	Av. voltage <i>vs</i> $\text{Li}/\text{Li}^+/\text{V}$	Spec. capacity / $\text{mAh g}^{-1}$	Advantages	Disadvantages
LCO	3.9	155	good cycle life, good energy density	low thermal stability in charged state, sensitive to overcharge
LMO	4.0	100 - 120	good thermal stability, inexpensive, very good power capability	moderate cycle life, low energy density
NCA	3.7	180	good energy density, good power capability, good cycle life	moderate thermal sta- bility in charged state, moisture sensitive
NMC	3.8	160	good energy density good power capability, good cycle life, good thermal stability	patent issues
LFP	3.4	160	very good cycle life, good thermal stability, good power capability	lower energy, special preparation conditions

### 1.1.3 Future developments

As customers demand more powerful portable devices and higher range electric vehicles, the need for higher energy density drives many new developments. The energy is given by

$$E = Q \times \Delta V \quad (1.1)$$

where  $Q$  is the specific capacity of the cell and  $\Delta V$  is the average potential difference between cathode and anode; increasing one of these values will result in a higher energy. The capacity can be increased by storing multiple electrons in a material with minimal dead weight. A Si anode comes close to this ideal; a single Si atom can form an alloy with up to 3.75 Li atoms, resulting in a theoretical specific capacity of 3579 mAh g<sup>-1</sup>.<sup>19</sup> Unfortunately, even this huge step in theoretical capacity translates only in a modest increase of 15 - 20 % energy density of the cell.<sup>19</sup> This is because Si greatly expands upon alloying and this extra space must be taken into consideration when designing the cell. The volume expansion also threatens the structural integrity of the material resulting in limited cycle life. Intense efforts were devoted to resolve this issue with clever nanoengineering,<sup>20-22</sup> which enabled first commercial Li-ion batteries based on Si.<sup>3</sup> Thus, the realization of Si nicely illustrates both challenges and opportunities of new developments.

Higher cell voltages are the second pathway to superior energy density and directly translate to cell energy density. The anode potential cannot be lowered since it is already close to the potential where metallic Li is formed; moving below that potential would introduce severe safety risks, Section 1.1.1. As a consequence, most efforts have focused on high-voltage cathodes that significantly surpass the roughly 3.8 V of current cathode materials. LiNi<sub>0.5</sub>Mn<sub>1.5</sub>O<sub>2</sub>, for example, operates at 4.7 V resulting in a 12 % gain in energy density compared to LiCoO<sub>2</sub>.<sup>23,24</sup> This increased potential, however, induces aggressive reactions between electrode and electrolyte and a short lifetime, which will have to be addressed.<sup>25,26</sup>

In the next years, we will see further developments in terms of energy density, safety and lifetime of batteries. The presented examples, however, also demonstrate that the improvements will be gradual and that a huge leap in energy density is unlikely due to inherent limitations of the Li-ion battery. Thus, researchers are looking to beyond Li-ion systems as candidates for future energy storage.

## 1.2 Beyond Li-ion batteries

Beyond Li-ion systems encompass a wide field that relies on oxygen or sulfur redox chemistry, alternative cations like Na<sup>+</sup> or K<sup>+</sup> or multivalent ions such as Mg<sup>2+</sup> or Al<sup>3+</sup>. Essentially, these systems have little in common save that they are *not* Li-ion; this chapter will therefore focus on Na-ion, Li-O<sub>2</sub> and Na-O<sub>2</sub> systems, which are particularly relevant for this work. Li-S and multivalent ion chemistries are covered in dedicated reviews by Manthiram *et al.*<sup>27</sup> and Muldoon *et al.*,<sup>28</sup> respectively, and will be omitted here.

Often new developments are fueled by the demand for higher energy densities, but a second major motivation is the quest for cheaper and/or more sustainable battery systems. The production of a Li-ion battery that stores 1 kWh consumes more than 400 kWh,<sup>29</sup> most of it for the production of the materials. Moreover, these materials often contain elements that are scarce and expensive, such as Co and Cu (for the current collector), raising concerns over the sustainability of Li-ion systems in large-scale applications. Some

alarmists already regard the relatively abundant Li as the “gold of the next century.”<sup>29</sup> This has sparked interest in potentially more sustainable batteries with Na-ion batteries being the most prominent candidate.

### 1.2.1 Na-ion batteries

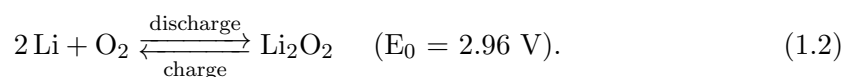
Na-ion batteries are often considered more sustainable, because Na is more abundant and more evenly distributed in the earth’s crust<sup>30</sup> and its presence in sea-water renders Na an almost unlimited resource that could support large-scale energy storage. Large-scale applications also demand low cost and this is where Na excels: Currently,  $\text{Na}_2\text{CO}_3$  as important precursor for battery salts is 50 times cheaper than  $\text{Li}_2\text{CO}_3$  and the gap is expected to widen further.<sup>29</sup> An even larger advantage, however, arises from the current collector. Li-ion batteries use Cu current collectors at the anode, because Li would alloy with an Al current collector. Na does not, thus Na-ion batteries could substitute Cu for Al, which is not only three times cheaper,<sup>31</sup> but also avoids the high environmental impact of Cu production. In fact, Cu causes more than 90 % of the natural capital cost\* of Li-ion batteries.<sup>31</sup> Thus, replacing Cu with Al is economically and ecologically sensible.

The extensive knowledge on Li-ion batteries greatly accelerated the development of Na-ion batteries. Materials and methods could be adapted, because the operating mechanisms are virtually identical apart from the ion that is shuttled between the electrodes. As a consequence, the scientific community has come up with promising electrolytes<sup>33</sup>, anodes<sup>34</sup> and cathodes<sup>35</sup> in less than a decade. However, these materials still need to be optimized to minimize the losses of  $\text{Na}^+$  in the first cycle and improve lifetime.<sup>36</sup>

Another downside of Na-ion batteries originates from a more fundamental level. Na-ion batteries operate similar to Li-ion batteries, which entails similar limitations concerning their energy density. At present, it seems that Na-ion batteries will fall short of Li-ion energy density due to the greater weight and size of  $\text{Na}^+$ . This requires larger host structures for intercalation and thus more dead weight that decreases capacity. Here, the cathode is particularly inefficient, because transition metals have high formula weight but store only one electron. This has led to increased interest in cathode chemistries that do not rely on intercalation and therefore promise higher energy densities and, by avoiding transition metals, environmental benefits.

### 1.2.2 Li-O<sub>2</sub> batteries

The room-temperature non-aqueous Li-O<sub>2</sub> battery was discovered by accident when an untight apparatus yielded  $\text{Li}_2\text{O}_2$  instead of the desired Li-intercalation.<sup>37</sup> The underlying reaction was



Here,  $\text{O}_2$  is reduced at a porous cathode and combines with  $\text{Li}^+$  from the electrolyte to form  $\text{Li}_2\text{O}_2$ , which fills the pores. As lightweight  $\text{Li}_2\text{O}_2$  stores two electrons and the cathode adds little dead weight, fantastic energy densities can be obtained. If we could practically achieve only one seventh of the theoretical energy density, this would more than double the energy density of a Li-ion battery.<sup>38</sup> The simple overall reaction equation,

\*The natural capital cost sums up what people are willing to pay to revert detrimental impacts on human health, ecosystem production capacity, biodiversity, abiotic resources and recreational and cultural values.<sup>32</sup>

however, masks the fact that the cell chemistry in Li-O<sub>2</sub> batteries is highly complex and strongly depends on the electrolyte.

Li<sub>2</sub>O<sub>2</sub> formation during discharge exemplifies this complexity. First, O<sub>2</sub> is reduced to O<sub>2</sub><sup>-</sup> at the cathode and forms LiO<sub>2</sub>. While this step does not depend on the electrolyte, the following one does:<sup>39,40</sup> When an electrolyte with a low donor number is used, LiO<sub>2</sub> will remain on the cathode and will be further reduced to Li<sub>2</sub>O<sub>2</sub> covering the electrode in a thin layer. Due to its poor electrical conductivity, Li<sub>2</sub>O<sub>2</sub> inhibits subsequent reactions leading to low capacities and early cell death.<sup>40,41</sup> An electrolyte with a high donor number will instead dissolve the LiO<sub>2</sub> that later dissociates to Li<sub>2</sub>O<sub>2</sub>, forming large particles in the process, Figure 1.1b.<sup>39</sup> To complicate things further, the donor number is not the only factor that guides Li<sub>2</sub>O<sub>2</sub> formation; current density, lithium salt and water content must be considered too.<sup>38,42-44</sup>

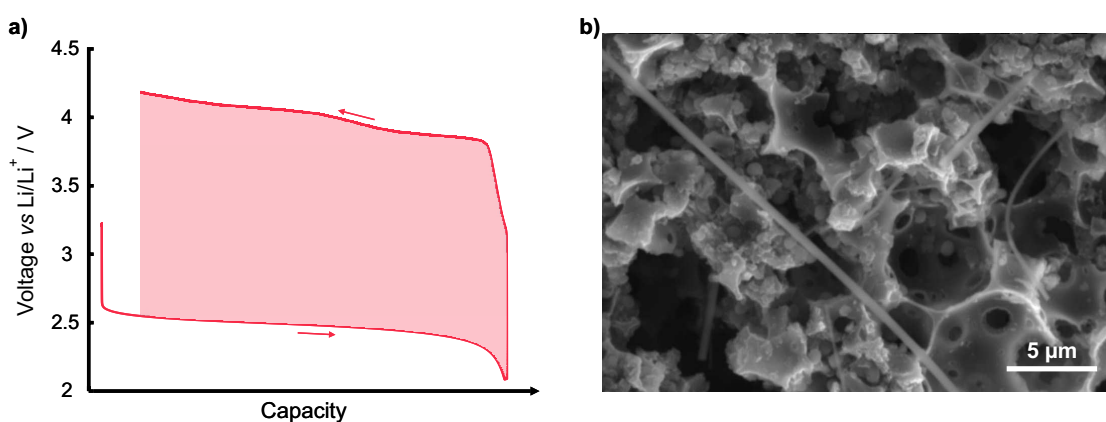


**Figure 1.1:** A schematic cycling curve of a Li-O<sub>2</sub> battery showing large overpotentials (a) and Li<sub>2</sub>O<sub>2</sub> particles in a porous cathode (b).

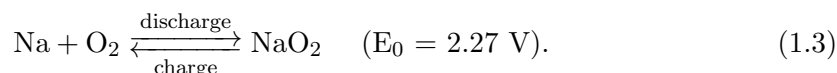
During charge, Li<sub>2</sub>O<sub>2</sub> decomposition is accompanied with high overpotentials resulting in charge potentials beyond 4 V, Figure 1.1a.<sup>45,46</sup> The overpotentials were attributed to the low conductivity of Li<sub>2</sub>O<sub>2</sub>,<sup>47,48</sup> which obstructs electron transfer from the electrode to the particle/electrolyte interface and parasitic reactions, which form components that are even harder to decompose than Li<sub>2</sub>O<sub>2</sub>. An alternative means for electron transfer could be provided by soluble mediators, which oxidize Li<sub>2</sub>O<sub>2</sub> and are subsequently re-oxidized at the cathode.<sup>49-53</sup>

Generally, today's Li-O<sub>2</sub> batteries suffer from poor cycle life due to severe parasitic reactions.<sup>54,55</sup> Until recently, these parasitic reactions were thought to originate from the reactive oxygen species O<sub>2</sub><sup>-</sup> and O<sub>2</sub><sup>2-</sup>,<sup>56,57</sup> but newer reports suggest that <sup>1</sup>O<sub>2</sub> drives these reactions instead.<sup>58,59</sup> Further parasitic reactions could be induced by the Li anode. Metallic Li is a well-known safety concern, see Section 1.1.1, which is further exacerbated by the high reactivity of some Li-O<sub>2</sub> electrolytes with Li.<sup>60,61</sup> An alloying anode could alleviate this problem, but would severely penalize energy density at the same time. Overall, more fundamental research is required to understand and eventually overcome the parasitic reactions that plague Li-O<sub>2</sub> batteries.

### 1.2.3 Na-O<sub>2</sub> batteries

In some ways, Li-O<sub>2</sub> and Na-O<sub>2</sub> batteries reiterate the story of their ion analogues. Again, the younger Na chemistry addresses shortcomings of their Li counterparts at the price of energy density, while profiting from research on the Li system. The cell reaction, however,

differs.<sup>62</sup> While  $\text{Na}_2\text{O}_2$ <sup>63–65</sup> or its hydrate<sup>66,67</sup> have sometimes been detected as discharge product, some of these reports have presented ambiguous or even incorrect data.<sup>68</sup> In contrast, more reliable data has identified  $\text{NaO}_2$  as the main discharge product,<sup>62,69–74</sup> which results in an overall reaction of



Upon discharge, large cubic  $\text{NaO}_2$  crystals are typically observed, Figure 1.2. Although  $\text{NaO}_2$ , like  $\text{Li}_2\text{O}_2$ , is considered an electrical insulator, the overpotentials upon charge are very low in  $\text{Na-O}_2$  batteries ( $<200 \text{ mV}$ ).<sup>62,70</sup> This deviates from  $\text{Li-O}_2$  cells that show high overpotentials on charge, see previous Section. The striking contradiction was resolved when protons from water impurities were shown to act as phase transfer catalysts, transporting  $\text{O}_2^-$  from the electrode to the surface of the growing crystal and *vice versa*.<sup>70</sup> Only with these protons, the  $\text{Na-O}_2$  battery can maintain its low overpotentials that differentiate it from the  $\text{Li-O}_2$  cell. Moreover, the  $\text{Na-O}_2$  cell harnesses the benefits of using Na, namely the use of more abundant resources and Al current collectors, rendering it a promising and arguably more feasible beyond Li-ion technology.<sup>75</sup>

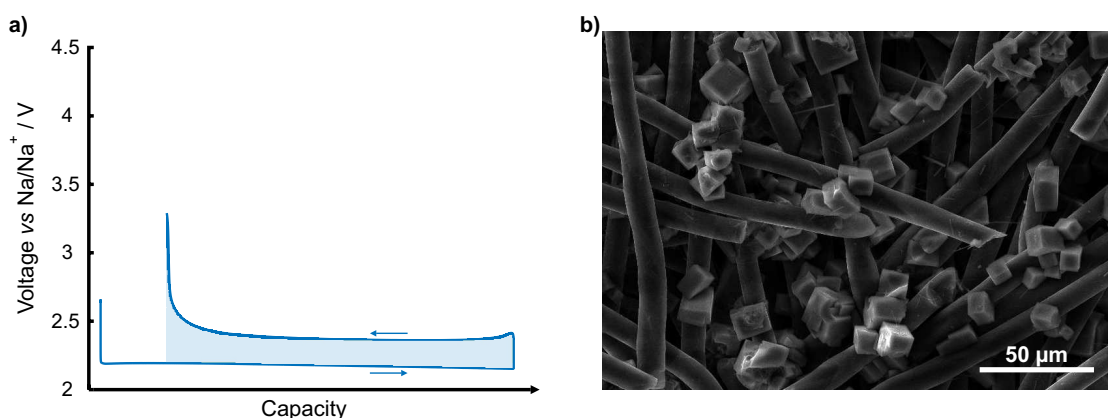


**Figure 1.2:** A schematic cycling curve of a  $\text{Na-O}_2$  battery showing low overpotentials (a) and  $\text{NaO}_2$  cubes in a carbon paper electrode (b).

However, low lifetimes remain the main obstacle that prevents the realization of  $\text{Na-O}_2$  batteries.<sup>70,76</sup>  $\text{Na-O}_2$  cells, too, employ an alkali metal anode inducing parasitic reactions with the electrolyte and dendrite formation.<sup>72,73</sup> Further parasitic reactions occur as  $\text{NaO}_2$  decomposes and leave behind a hollow shell instead of the original cube.<sup>77</sup> The side products then accumulate during cycling and eventually poison the cell.

### 1.3 Parasitic reactions and interphases

Throughout the last sections, side reactions have played a deeply ambiguous role. In Li-ion and Na-ion batteries, they build a stable and protective interphase on the anode, which is vital for cell operation. Conversely, uncontrolled and sustained parasitic reactions result in poor cyclic stability and low lifetimes that prevent the realization of beyond Li-ion batteries.

It is therefore essential to understand the origins and the impact of parasitic reactions in battery chemistries; and although very different battery chemistries are investigated in this thesis, parasitic reactions and interphases are always in the focus of the research.



---

The results of this thesis are presented in the next four chapters, each of them built around a peer-reviewed contribution (and one submitted paper). A chapter starts with a short summary and an introduction providing the necessary context. Then the contribution follows and is sometimes complemented with additional unpublished material.



## 2. Alkyl carbonates as SEI components

The SEI is highly diverse and its composition depends not only on electrolyte composition, but also on the electrode surface and cycling history. This, together with its thinness and sensitivity towards oxygen and moisture, renders it an elusive component of Li- and Na-ion batteries that is still not entirely understood, but nonetheless of central importance. Therefore, this part of the work is dedicated to shed some light on how the composition of the SEI determines its properties and how it could be influenced to improve them.

I selected a central class of SEI components, Li and Na alkyl carbonates (LAC and SAC), synthesized them and characterized them with respect to structure, ionic transport, and mechanical properties. Short-chained SACs and LACs were complemented with medium- and long-chained ones to investigate how these properties change with chain length and if they could be improved thereby. This will add to our knowledge of this class of compounds that is so far limited to spectroscopic properties of short-chained LACs,<sup>78-80</sup> while for SACs not even that was known.

The additional unpublished material describes my efforts to apply these new insights. Electrolytes were synthesized that yield medium- to long chained LACs upon breakdown and could thus modify the SEI. Unfortunately, these long chain LACs were shown to ultimately deteriorate the passivation behavior of the electrolyte.

### **Long Chain Alkyl Carbonates as Solid Electrolyte Interface Components: Structure, Ion Transport and Mechanical Properties**

Lukas Schafzahl, Heike M. A. Ehmman, Manfred Kriechbaum, Jürgen Sattelkow, Thomas Ganner, Harald Plank, Martin Wilkening, Stefan A. Freunberger

*submitted to Chemistry of Materials, 2018*

## 2.1 Carbonates as electrolyte solvents

Since the commercialization of Li-ion batteries, carbonates have been almost ubiquitously employed as electrolyte solvents. While other cell components have evolved or eventually been replaced, see Section 1.1.2, carbonates still form the backbone of today's electrolytes. Moreover, when interest in Na-ion batteries reawakened, carbonates soon played a similarly dominant role there.<sup>31,81</sup> To understand their huge success in both Li-ion and Na-ion batteries, one has to consider the stringent criteria for electrolyte solvents:<sup>82</sup>

1. The solvent should have a wide electrochemical stability window that accommodates both anode and cathode to avoid electrochemical parasitic reactions. In case they cannot be prevented, they should passivate the electrode surface to preclude continuous decomposition and allow for reversible cycling.
2. The solvent should support an electrolyte with high conductivity. This requires a contradictory combination of a high relative permittivity ( $\epsilon$ ) and a low viscosity ( $\eta$ ); the former enable high salt concentrations, while the latter facilitates ion transport.
3. The solvent should be liquid in a wide temperature range, safe, environmentally friendly and economical.

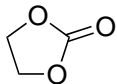
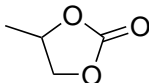
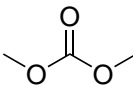
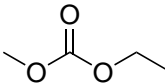
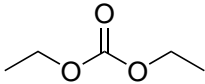
The first criterion already severely limits the choice of electrolytes as it eliminates all protic solvents. Despite their excellent solvating abilities, both protic groups and respective anions decompose within 2.0-4.0 V vs Li/Li<sup>+</sup><sup>83</sup> and therefore lack the necessary stability. In contrast, a mixture of linear and cyclic carbonates manages to fulfill these criteria due to their synergistic properties: They withstand the voltages of common cathodes and passivate anodes that would be outside their electrochemical stability window, such as Li and graphite. Cyclic carbonates possess very high relative permittivity that allow for high salt concentrations,<sup>84</sup> while their high viscosities are compensated by the high fluidities of linear carbonates like dimethyl carbonate (DMC), diethyl carbonate (DEC) and methyl ethyl carbonate (EMC), Table 2.1.<sup>85</sup> These combined features result in high conductivities. Moreover, binary or ternary mixtures also allow Li-ion batteries to operate at temperatures as low as  $-30$  °C despite the high melting point of EC (36 °C).<sup>86,87</sup> Overall, excellent synergies between linear and cyclic carbonates warrant their huge success as electrolyte solvents.

## 2.2 The solid electrolyte interphase

While carbonate electrolytes are inert towards typical 4-V-cathodes, the anode lies beyond its electrochemical stability window and will inevitably induce parasitic reactions. Fortunately, these side reactions yield products that form a protective layer on the anode surface, the solid electrolyte interphase (SEI). The SEI prevents further diffusion of solvent molecules to the anode surface and thus stops sustained parasitic reactions. It is only thanks to the SEI that Li- and Na-ion batteries operate; but despite immense research we are still far from fully understanding it.<sup>88-91</sup>

The next sections nevertheless aim to summarize our current understanding of the SEI. It should be noted that these sections overwhelmingly draw upon reports on Li-ion batteries, but that their findings also apply to Na-ion batteries; important exceptions are pointed out in the respective sections.

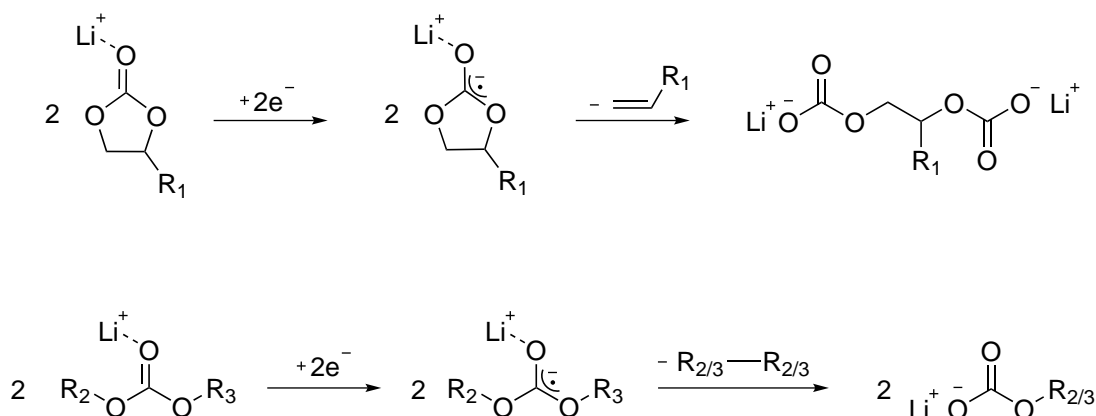
**Table 2.1:** Relevant properties of carbonate solvents. Data from Ref 82.

Name	Structure	$\epsilon_{25} \text{ } ^\circ\text{C}$	$\eta_{25} \text{ } ^\circ\text{C} / \text{cP}$	$T_m / \text{ } ^\circ\text{C}$	$T_b / \text{ } ^\circ\text{C}$
EC		89.8*	1.9*	36.4	248
PC		64.9	2.5	-48.8	242
DMC		3.1	0.59 <sup>†</sup>	4.6	91
EMC		3.0	0.65	-53	110
DEC		2.8	0.75	-74.3	126

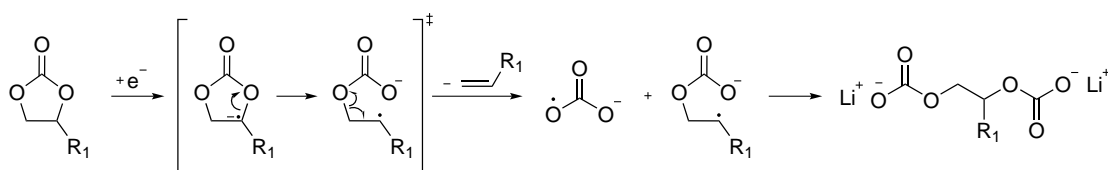
\*at 40  $^\circ\text{C}$ ; <sup>†</sup>at 20  $^\circ\text{C}$ 

### 2.2.1 SEI composition

Without doubt, semicarbonates are amongst the most universal SEI components.<sup>78,92-97</sup> They were first reported by Doron Aurbach,<sup>98</sup> who argued that they are formed in a one electron reduction from carbonate electrolytes, Scheme 2.1. The electron transforms the carbonate to the corresponding radical anion that subsequently dimerizes while releasing a gaseous hydrocarbon. When the substrate is a cyclic carbonate, this reduction yields an lithium alkyl dicarbonate (LADC), while linear carbonates form LACs.

**Scheme 2.1:** One-electron reduction of carbonate electrolytes.

While the presence of semicarbonates is without doubt, alternative formation mechanisms have been suggested.<sup>99</sup> A ring opening mechanism was proposed after paramagnetic resonance spectra failed to detect any cyclic radicals, Scheme 2.2. Moreover, that mechanism does not require two very short-lived cyclic radicals to recombine, as the reaction proceeds via a carbonate radical cation instead. The mechanism be therefore kinetically more favorable and would yield the same gaseous products.



**Scheme 2.2:** Alternative mechanism for the one-electron reduction of EC.

Another debate erupted over the question whether LADCs or LACs are more abundant in the SEI. Or, from a different perspective, whether cyclic carbonates or linear carbonates are reduced preferentially. Some findings show that LADC predominate,<sup>93,100,101</sup> which was rationalized by the fact that  $\text{Li}^+$  is primarily solvated by cyclic carbonates. Cyclic carbonates could thus come in more intimate contact with the anode surface. Other reports, however, suggest the exact opposite.<sup>79,102</sup> In a rather conclusive study by Leifer *et al.*, the carbonate solvents were labelled with  $^{13}\text{C}$ .<sup>103</sup> When the SEI was then investigated by solid state NMR, no clear preference for either LADCs or LACs was found. It seems that the abundance of LADCs and LACs depends not only on electrolyte composition, but also on other factors such as cell aging, cycling conditions and electrode surface.

The reduction of carbonates electrolyte yields a variety of additional organics. Oxalates, succinates and alkoxides,<sup>104</sup> as well as orthocarbonates, acetals and orthoesters<sup>103</sup> were found in the solid electrolyte interphase. More importantly, many reports demonstrate that crosslinked polymeric species exist in the SEI.<sup>92,105,106</sup> These polymers consist of ether- and carbonate based building blocks that are crosslinked in three dimensions and are sometimes attributed a vital protective role in the SEI.<sup>107</sup>

The SEI also comprises inorganic components. Inorganics can be derived from various sources, such as oxygen impurities leading to  $\text{Li}_2\text{O}$ .<sup>108,109</sup>  $\text{Li}_2\text{CO}_3$  was believed to originate from the carbonate solvent, but more recent findings suggest that it likely forms when  $\text{Li}_2\text{O}$  or  $\text{Li}_2\text{O}_2$  reacts with  $\text{CO}_2$ .<sup>110</sup> Another controversial SEI constituent is  $\text{LiF}$ . Originally, the fluoride was thought to be an impurity of the  $\text{LiPF}_6$  salt commonly used in Li-ion batteries.<sup>82</sup> The sheer abundance of  $\text{LiF}$  under certain conditions, however, suggest that it is instead formed by reduction of  $\text{PF}_6^-$  anion.<sup>93,94</sup> However, not only the origin, but also the effects of  $\text{LiF}$  remain unclear. Some reports claim a beneficial impact,<sup>93,94</sup> while in other studies  $\text{LiF}$  seems to be detrimental.<sup>111–113</sup> Both positions can be reconciled considering that the abundance of  $\text{LiF}$  might not be the only factor in play; its distribution and interaction with other SEI components could be just as important.

To further complicate matters, all these components are not distributed uniformly within the SEI. Most studies conclude that the SEI is highly heterogeneous; its composition varies both laterally and with depth.<sup>108,109,114</sup> This led to a two-layered SEI model where a brittle, inorganic inner layer is covered by a softer, organic outer layer.<sup>114–117</sup> While there are exceptions,<sup>94</sup> this model appears to be appropriate in most cases.

This overall picture, which resulted from extensive research on Li-ion batteries, generally also holds true for Na-ion batteries.<sup>31,118</sup> This can be rationalized considering that the most important factors are electrolyte composition and electrode potential, both of which are similar in Li- and Na-ion batteries. In contrast, differences like the cation of the electrolyte salt and the electrode surface are of subordinate importance. Still, two differences are worth pointing out: First, the SEI in Na-ion batteries comprises more inorganic components.<sup>118</sup> Second, its distribution is more homogenous rendering the two-layered model invalid.<sup>119</sup>

### 2.2.2 SEI properties

For reversible cell operation, the SEI must block diffusion of electrolyte molecules while allowing ion transport. Consequently, the SEI requires sufficient ion mobility. For Li-ion batteries, a series of computational studies have investigated  $\text{Li}^+$  mobility in SEI components. In  $\text{Li}_2\text{CO}_3$ ,  $\text{Li}^+$  could move via a displacement mechanism resulting in low energy barriers of 0.35 eV.<sup>120,121</sup> Lithium ethyl dicarbonate ( $\text{C}_2\text{Li}_2$ ), the decomposition product of EC, was calculated to show  $\text{Li}^+$ -conductivities of  $10^{-8}$  to  $10^{-10}$   $\text{S cm}^{-1}$ .<sup>122</sup> These values agreed with an experimental conductivity of  $10^{-9}$   $\text{S cm}^{-1}$ . Another simulation on  $\text{C}_2\text{Li}_2$  revealed that an ordered arrangement would have higher conductivities than a disordered one.<sup>123</sup> The energy barrier amounted to 0.6 eV. It has, however, been argued that  $\text{Li}^+$  transport through the SEI might not be the limiting factor in overall  $\text{Li}^+$  mobility, because for the  $\text{Li}^+$  to enter the SEI, it must first be stripped of its solvation sheath. This process has shown activation energies of roughly 0.52 eV which is comparable to those arising from  $\text{Li}^+$  transport within the SEI.<sup>122</sup> For Na-ion batteries, no studies on ion mobility in the SEI exist so far. In general, however, the SEI in Na-ion batteries seems to be more resistive as evidenced by higher polarization overpotentials.<sup>124</sup>

Another vital requirement for the SEI is mechanical flexibility. Graphite expands by roughly 10% upon intercalation, while conversion and alloying materials, such as Si, undergo huge volume changes; the charged materials expand by up to 310%.<sup>125</sup> The SEI needs to withstand this enormous stress. If it is too brittle, it will continuously break and reform leading to low coulombic efficiency (CE) and early cell death. Some researchers have investigated the mechanical properties of the SEI in Li-ion<sup>114,126–129</sup> and Na-ion<sup>130</sup> batteries by atomic force microscopy (AFM). Typically, these reports yield Young's moduli that spread over 2-3 orders of magnitude which is ascribed to the heterogenous nature of the SEI. Interestingly, however, the SEI in Na-ion batteries was found to be more ductile which seems to be at odds with its more inorganic nature (see previous Section).

Overall, diffusion and mechanical flexibility are two central properties of the solid electrolyte interface and will be investigated in the following contribution. Due to the heterogenous and diverse nature of the SEI, our contribution focuses on one universal class of SEI components, the semicarbonates.

# Long Chain Li and Na Alkyl Carbonates as Solid Electrolyte Interface Components: Structure, Ion Transport and Mechanical Properties

Lukas Schafzahl<sup>1</sup>, Heike M. A. Ehmman<sup>1</sup>, Manfred Kriechbaum<sup>2</sup>, Jürgen Sattelkow<sup>3,4</sup>, Thomas Ganner<sup>3</sup>, Harald Plank<sup>3,4</sup>, Martin Wilkening<sup>1,5</sup>, Stefan A. Freunberger<sup>1\*</sup>

<sup>1</sup>Institute for Chemistry and Technology of Materials, Graz University of Technology, Stremayrgasse 9, 8010 Graz, Austria

<sup>2</sup>Institute of Inorganic Chemistry, Graz University of Technology, Stremayrgasse 9, 8010 Graz, Austria

<sup>3</sup>Institute of Electron Microscopy and Nanoanalysis (FELMI), Graz University of Technology, Steyrergasse 17, 8010 Graz, Austria

<sup>4</sup>Graz Centre for Electron Microscopy (ZFE), Steyrergasse 17, 8010 Graz, Austria

<sup>5</sup>Christian Doppler Laboratory for Lithium Batteries, and Institute for Chemistry and Technology of Materials, Graz University of Technology, Stremayrgasse 9, 8010 Graz, Austria

**KEYWORDS** *lithium ion battery, sodium ion battery, solid electrolyte interface, structure, ion transport, mechanical properties*

---

**ABSTRACT:** The solid electrolyte interphase (SEI) in Li and Na ion batteries forms when highly reducing or oxidizing electrode materials get in contact with liquid organic electrolyte. Its ability to form a mechanically robust, ion conducting and electron insulating layer critically determines performance, cycle life and safety. Li or Na alkyl carbonates (LAC and SAC), respectively, are lead SEI components in state-of-the-art carbonate based electrolytes and their fundamental understanding regarding charge transport and mechanical properties may hold key to designing electrolytes forming an improved SEI. We synthesized a homologous series of LACs and SACs from methyl to octyl analogs and characterized them with respect to structure, ionic conductivity and stiffness. The compounds assume layered structures except for the lithium methyl carbonate. Room temperature conductivities were found to be  $\sim 10^{-9}$  S $\cdot$ cm $^{-1}$  for lithium methyl carbonate and  $< 10^{-12}$  S $\cdot$ cm $^{-1}$  for the other LACs and  $< 10^{-12}$  S $\cdot$ cm $^{-1}$  for the SACs with ion transport mostly attributed to grain boundaries. While LACs show stiffnesses around 1 GPa, SACs become significantly softer with increasing chain lengths. These findings will help to more precisely interpret the complex results from charge transport and mechanical characterization of real SEIs and can give a rationale to influence the SEI's mechanical properties via the electrolyte.

---

## INTRODUCTION

Cycle life, safety, irreversible capacity, and interfacial resistance of alkaline metal and alkaline ion batteries critically depend on the solid electrolyte interface (SEI). It forms when the electrolyte decomposes in contact with anode materials like Li or Na metal, graphite, silicon or hard carbon, or transition metal cathode materials.<sup>1-10</sup> The SEI then must prevent further decomposition by forming a mechanically robust passivation layer that impedes electron transfer and provides at the same time sufficient ionic conductivity.

Much recent work was focusing on understanding the SEI's role in cell impedance in Li batteries.<sup>1-6, 11-18</sup> It is yet under debate whether impedance is dominated by cation desolvation or ion transport through the SEI layer.<sup>11, 12</sup> While the former is mostly determined by the electrolyte, the latter is known to add substantially to cell impedance due to sluggish Li<sup>+</sup> transport in the SEI.<sup>13-18</sup> Ion transport is directly linked to texture and chemical composition. In-

organic compounds such as Li<sub>2</sub>CO<sub>3</sub> and Li oxides dominate the inner layer whereas the outer layer mostly comprises alkaline mono or dicarbonates (ROCO<sub>2</sub>M, R(OCO<sub>2</sub>M)<sub>2</sub>).<sup>1-8, 17-22</sup> To unravel individual contributions to ion transport in the complicated multi-component texture, there has been an upsurge of experimental and theoretical research to understand ion dynamics on a fundamental level by investigating pure components such as Li<sub>2</sub>CO<sub>3</sub>, LiF, oxides, and lithium ethylene dicarbonate (LEDC).<sup>13-18, 23, 24</sup>

Given the significant volume changes upon ion insertion/deinsertion in carbon and even more so in alloying and metal anodes, the mechanical properties of the SEI are of prime importance for robust separation of the electrolyte from the electrode. There has therefore been a growing number of works focusing on the mechanical properties of the SEI.<sup>25-33</sup> They typically report a broad distribution of Young's moduli, which was somewhat tentatively attributed to inorganic and organic constituents for hard and soft components, respectively.



Much effort has recently been devoted to developing Na metal and Na ion batteries and researchers can leverage much of the decades of research on the Li counterpart.<sup>34-38</sup> However, knowledge of the SEI is by far less advanced as compared to Li batteries and research so far agrees on similar components but significantly differing fractions, texture, and stability.<sup>39-42</sup> Moreover, Na<sup>+</sup> dynamics and mechanical properties remain nearly uncharted areas. Taken together, molecular level understanding of ion dynamics and mechanical properties of pure SEI components is key to understand their contribution to the complex SEI and may help designing electrolytes and additives to form much-needed interphases for Li and Na batteries with enhanced properties.

Here we take one step to elucidate the structure-property relation and particularly to tune the mechanical properties of the SEI. We selected Li and Na alkyl carbonates (LAC and SAC) as key SEI components, synthesized a homologous series and analyzed them with respect to structure, ion dynamics, and mechanical properties. The series contains short-chained alkyl carbonates that form in common electrolyte solvents like dimethyl carbonate (DMC) or diethyl carbonate (DEC). We expand the series with longer-chained alkyl carbonates that could be introduced to the SEI by using longer-chained dialkyl carbonate solvents. While the former provide reference values to more precisely interpret complex results from SEIs in commonly used solvents, the latter help to rationalize how SEI properties could be tuned by varying the electrolyte. In particular, the long chain SAC can yield a softer SEI without compromising Na transport.

## EXPERIMENTAL

**Synthesis.** Dry dichloromethane (DCM) was obtained by distillation over P<sub>2</sub>O<sub>5</sub>. Alcohols were refluxed and distilled over lithium metal (Sigma-Aldrich) under an inert atmosphere. Subsequently, DCM and the alcohols were stored at least one day over molecular sieves that had been activated at 200 °C in high vacuum before being used. The water content determined by Karl-Fischer-titration was in the range of 20 ppm. All preparation and purification steps involving moisture sensitive alkyl carbonates were performed in an Ar-filled glove box containing <1 ppm H<sub>2</sub>O.

Synthesis followed a literature method involving nucleophilic attack of the metal alcoholate on CO<sub>2</sub>.<sup>43</sup> The alkali metal (1.0 eq) was dissolved in dry alcohol (10-25 eq) and subsequently diluted with 10 mL DCM. CO<sub>2</sub> was dried by flowing through a cooling trap (-40 °C) and a CaCl<sub>2</sub> filled tube and then flushed through the vigorously stirred suspension. A colorless precipitate started to form almost immediately. After 45 minutes the solvent was removed and the product washed by suspending it in 10 mL DCM, centrifugation and decanting (2x), yielding 30-88 % colorless powder.

**Characterization.** FTIR spectra were collected on a Nicolet 6700 spectrometer (Thermo Fisher Scientific). SAXS measurements were recorded on a high-flux SAXS-Sess camera linked to a Debyeflex 3003 X-ray generator with CuK $\alpha$  radiation at 40 kV. The Goebel-mirror focused and a Kratky-slit collimated beam was line-shaped with 17 mm horizontal dimension at the sample. Scattered radiation was measured in transmission mode within an angular range from 0.1° to 10° (2 $\Theta$ ) with an exposure time of 100 s. PXRD patterns were collected with an Empyrean reflectometer (Panalytical) with CuK $\alpha$  radiation (1.54 Å) at 40 kV and a PIXcel<sup>3D</sup> detector. All samples for SAXS and PXRD measurements were placed in flame-sealed glass capillaries.

Impedance spectra were recorded on a Concept 80 broadband dielectric spectrometer (Novocontrol) equipped with an Alpha-A analyzer. A Quattro cryosystem (Novocontrol) regulated the temperature within a ZGS active sample cell. Samples were cold-pressed with an uniaxial pressure of 10 kN to cylindrical pellets (7 mm diameter, roughly 0.5 mm thickness). The pellets were gold-sputtered in a MB EVAP high vacuum coating unit (Braun) and embodied in air-tight aluminum laminated pouch cells. Spectra were recorded at temperatures ranging from 273 to 473 K.

AFM investigations were performed with a FastScan Bio instrument (Bruker Nano) operated by a Nanoscope V controller. All measurements were done in PeakForce based Quantitative Nanomechanical Measurement mode (PF QNM) using RTESPA-150 (Bruker Nano) with reflective aluminum backside coating with nominal spring constant  $k$  of 5 N·m<sup>-1</sup> according to the expected modulus values. The initial setup comprised deflection sensitivity determination on a flat ruby calibration sample followed by cantilever spring constant determination using thermal tune and was finalized by tip end radius estimation using TiO<sub>2</sub> calibration samples (as included in the Bruker calibration kit PFQNM-SMPKIT-12M). After calibration, the sample was transferred from the sealed glass vial under the already calibrated AFM scanner and sealed with an in-house modified micro volume cell. Instead of liquid, the micro volume cell was constantly flushed by nitrogen 5.0 gas to realize a widely H<sub>2</sub>O free atmosphere during AFM measurements. Flow rates have been previously optimized to prevent any interference with AFM performance. To minimize external vibrational noise, an acoustic hood with damping table isolates the microscope from surroundings (standard Bruker accessory). At least 3 different spots were measured on each sample with a scan rate of 1 Hz. Peak forces and parameters were optimized until stable imaging conditions have been established. NanoScope Analysis 1.5 (Bruker Nano Surface Offices, Santa Barbara, CA) was used for data analysis using DMT (Derjagin, Muller, Toropov)<sup>44</sup> based modulus calculations. Areas in the AFM modulus image were excluded in the analysis that did not meet the criteria of the DMT model.<sup>44</sup>

## RESULTS AND DISCUSSION

**Synthesis.** We synthesized a homologous series of lithium alkyl carbonates (LAC) and sodium alkyl carbonates (SAC) with chain lengths from methyl to octyl. The synthesis was based on nucleophilic attack of alkoxides onto  $\text{CO}_2$ , see Experimental for details. The samples will be referred to as  $\text{C}_x\text{M}$  with  $x$  being the number of carbon atoms in the alkyl chain and  $\text{M}$  the respective alkaline metal, e.g.  $\text{C}_1\text{Li}$  for lithium methyl carbonate. Synthesis, purification and analysis were performed under rigorous exclusion of moisture, because alkyl carbonates react with water to form the corresponding alcohol,  $\text{CO}_2$  and  $\text{M}_2\text{CO}_3$ .

To confirm identity and purity, the alkyl carbonates were assessed by FTIR, Figure 1. The characteristic bands of the  $\text{M}_2\text{CO}_3$  at 1504, 1460, and 862  $\text{cm}^{-1}$  ( $\text{M} = \text{Li}$ ) and 1400 and 862  $\text{cm}^{-1}$  ( $\text{M} = \text{Na}$ ) are absent in all spectra, as are alcohol signals in the range from 3200–3700  $\text{cm}^{-1}$ , confirming that the alkyl carbonates were not exposed to moisture. The observed signals match expectations for this class of compounds. Characteristic O-C=O vibrations appear at 1600–1660  $\text{cm}^{-1}$ , and the intensities of the C-H stretching modes at 2800–3000  $\text{cm}^{-1}$  clearly increase with chain length. A further assignment in accord with literature on short-chained LAC is presented in Table 1.<sup>45</sup> Overall, the FTIR spectra clearly show that pure alkyl carbonates were obtained.

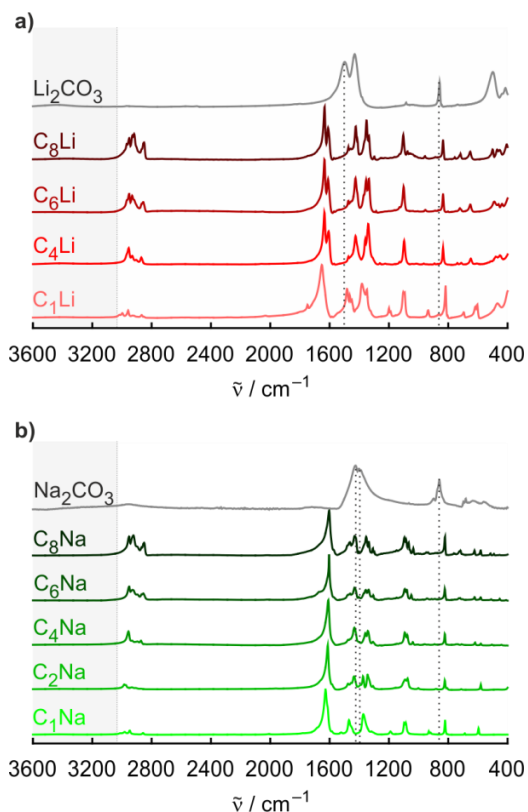


**Figure 1.** FTIR spectra of lithium alkyl carbonates (LACs) (a) and sodium alkyl carbonates (SACs) (b) and reference  $\text{M}_2\text{CO}_3$ .  $\text{C}_n\text{Li}$  and  $\text{C}_n\text{Na}$  refer to LACs and SACs with  $n$  C-atoms in the alkyl chain. Main  $\text{M}_2\text{CO}_3$  signals and O-H vibrations above 3000  $\text{cm}^{-1}$  (shaded gray) are missing, ruling out contamination with moisture.

**Table 1.** FTIR vibration assignment for LAC and SAC.

Vibration	LAC / $\text{cm}^{-1}$	SAC / $\text{cm}^{-1}$
C-H stretch.	3000–2860	3000–2800
O-C=O asymm. stretch.	1660–1610	1650–1600
	1450–1410	1460–1400
	1380–1330	1390–1310
C-O-C asymm. stretch.	1130–1080	1110–1050
$\text{CO}_3$ bend.	850–810	850–810

**Structure.** With the purity of the alkyl carbonates confirmed, we investigated their structure by small angle X-ray scattering (SAXS) and X-ray diffraction (XRD), Figure 2. The most striking feature of these patterns are the equidistantly spaced reflections at low angles, which indicate a lamellar structure.<sup>46, 47</sup> Lamellar structures are thus observed for  $\text{C}_8\text{Li}$  and  $\text{C}_6\text{Li}$ , which both show three recurring peaks.  $\text{C}_4\text{Li}$  with a medium chain displays a single reflection at a  $\sim 6^\circ$ , which precisely matches the expected spacing as inferred from  $\text{C}_8\text{Li}$  and  $\text{C}_6\text{Li}$ . But as further equidistantly spaced reflections are missing, we cannot unequivocally assign a lamellar structure. The short-chained  $\text{C}_1\text{Li}$ , too, does not adopt a lamellar structure as is expected from its short alkyl chain. Overall, LACs adopt a lamellar structure once a chain length of four carbon atoms is reached. In contrast, all SACs are lamellar, although the corresponding reflections are far less pronounced for  $\text{C}_1\text{Na}$ .

The diffraction patterns also allow us to derive the interlayer  $d$ -spacing of the lamellae, as shown in Figure 3. The spacing linearly increases with chain length for both SACs and LACs except for  $\text{C}_1\text{Li}$  and thus reflects the common structure. The measured  $d$ , however, is always smaller than the length of two fully extended molecules (for a detailed calculation see the Supporting Information), especially for LACs. This means that the alkyl carbonate structure deviates from an idealized model of highly ordered bilayers sheets consisting of two fully extended molecules. The deviation may be due to one or more of three reasons: First, the molecules could not be fully extended in all-*trans* conformation, but instead contain a significant amount of *gauche* defects that reduce their effective length. However, a large part of all-*trans* conformation can be deduced from the asymmetric and symmetric  $\nu_{\text{as}}$  and  $\nu_{\text{s}}$   $\text{CH}_2$  stretch vibrations that appear around 2900  $\text{cm}^{-1}$ , Figure S1.<sup>48</sup> Second, instead of extending perpendicularly from the metal layer, the molecules could be slightly tilted. The angle can be determined from the slope of the linear relationship in Figure 3; a right angle would result in a slope of 2.54 Å per C-atom.<sup>49</sup> In our case, the slope is 2.45 for SAC and 2.13 for LAC, which corresponds to angles of  $74^\circ$  and  $57^\circ$ , respectively, with respect to the metal plane. The former compares well with previous works reporting angles of  $77\text{--}75^\circ$  for silver

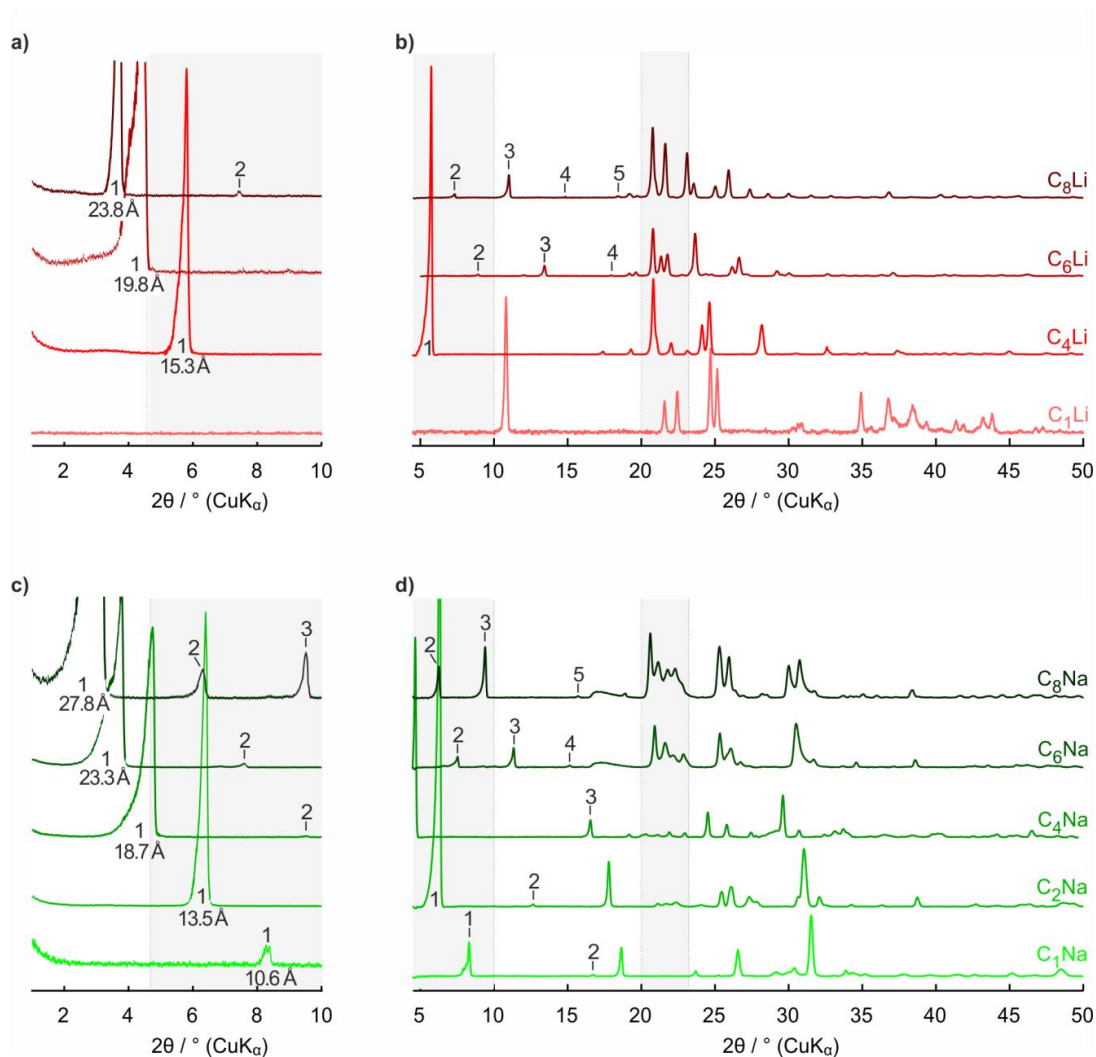


**Figure 2.** SAXS (a, c) and XRD (b, d) diffractograms of LACs (a, b) and SACs (c, d); the overlapping areas of both diffractograms are shaded in gray. The SAXS diffractograms are scaled for reflections in the overlapping area to have roughly equal intensities. Equidistantly spaced reflections at 2–15° indicate a lamellar structure and are denoted with numbers and the corresponding  $d$ -spacing is given at the first reflection. At 20–23°, overlapping reflections signify lateral Van-der-Waals forces for long-chained SAC, but not for LAC (see text).

carboxylates.<sup>48, 49</sup> Thus, a slight tilt of the alkyl chains could explain the lower  $d$ -spacing of SACs, but is unlikely to cause the large deviations we observed for LACs. The most likely reason for the lower  $d$  in LACs is the third, partially interdigitating chains.

Partially interdigitating chains, however, would necessarily interfere with chain packing, resulting in a less ordered structure with cavities between the alkyl chains. These cavities, in turn, decrease the interactions of adjacent alkyl chains; and in fact, evidence for decreased interactions is found both in the XRD patterns and in the FTIR spectra. The XRD patterns of SAC feature overlapping reflections at above 20° that are attributed to Van-der-Waals interactions between the alkyl chains.<sup>50, 51</sup> This assignment is consistent with the fact that the overlapping reflections decrease with decreasing chain length and do not appear at all in SMCs. In contrast, no addi-

tional reflections appear in long-chained LACs, which points to weak Van-der-Waals interactions in LACs. In the FTIR spectra, two bands are of particular interest. The first at 720  $\text{cm}^{-1}$  stems from methylene rocking and splits because of interchain vibrational interaction.<sup>52, 53</sup> Two maxima appear for long-chained SACs while the band remains a singlet for long-chained LACs, again indicating reduced interchain interaction, Figure S2. The second band at 2956  $\text{cm}^{-1}$  originates from the asymmetric methyl stretching and serves as a telltale for the environment at the chain end. A highly symmetric environment results in a single band,<sup>54, 55</sup> as is observed for SACs. In contrast, the band splits for LACs due to a more disordered environment, Figure S1. We therefore conclude that LAC chains partially interdigitate, but SAC do not. Instead, SACs are slightly tilted with respect to the metal plane.

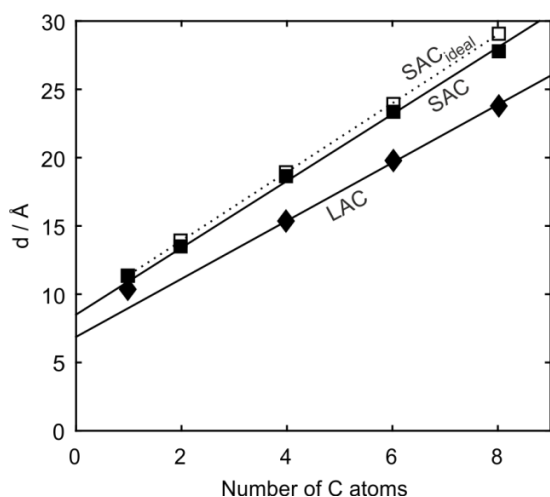


**Figure 3.** The interlayer spacing  $d$  as a function of the number of C atoms in the alkyl chain. All homologues, except  $C_1Li$ , show a linear increase in  $d$ , reflecting a common lamellar structure. The solid lines are linear fits of the SACs and LACs (except  $C_1Li$ ), respectively. The  $d$  is lower than the theoretical value for two extended SACs (hollow squares); the theoretical  $d$  for the LACs is almost the same and omitted for clarity.

While it may be tempting to think that alkyl carbonates, and especially SACs, assume a nearly ideal layered structure, there are more indicators of disorder within these systems. First, the equidistantly spaced reflections are less prominent compared to highly ordered carboxylate or thiolate bilayers.<sup>48-51, 54, 55</sup> They are, however, much more pronounced compared to poorly ordered branched carboxylates.<sup>51</sup> Second, methylene stretching vibrations are shifted to higher wavenumbers. They appear at 2847 and 2916  $cm^{-1}$  in ordered crystalline alkanes and at 2856 and 2928  $cm^{-1}$  in disordered liquid alkanes, Figure S1.<sup>49</sup> Both  $C_8Na$  and  $C_8Li$  display bands at 2850 and 2922  $cm^{-1}$  and therefore range between those extremes. Third, the intensity ratio between the methylene stretching vibrations  $I_{2850}/I_{2922}$  is proportional to conformational order.<sup>56</sup> Highly ordered alkyl chains reach values close to unity, whereas long-chained SACs and LACs only attain values around 0.65. These values compare well with the value of 0.75 that was obtained for a  $C_{12}$  europium carboxylate in a previous report when accounting for the shorter chain length.<sup>55</sup> Overall, FTIR and X-ray scattering in combination indicate that SACs and LACs assume a lamellar structure with a certain degree of disorder.

**Ionic transport.** Ionic transport was investigated using electrochemical impedance spectroscopy in a wide temperature range from  $-100$  to  $+100$  °C. The resulting conductivity spectra for the LACs at 20 and 100 °C are shown in Figure 4a. At 20 °C, the long-chained LACs show almost identical behavior while  $C_1Li$  stands out with a significantly higher conductivity. At 100 °C, his general trend still applies, but the picture becomes more varied. dc plateaus appear in the low frequency response of  $C_1Li$  and  $C_4Li$  and, less pronounced, also for  $C_6Li$  and  $C_8Li$ ; the corresponding dc conductivities are  $6 \times 10^{-10} S \cdot cm^{-1}$  for  $C_1Li$

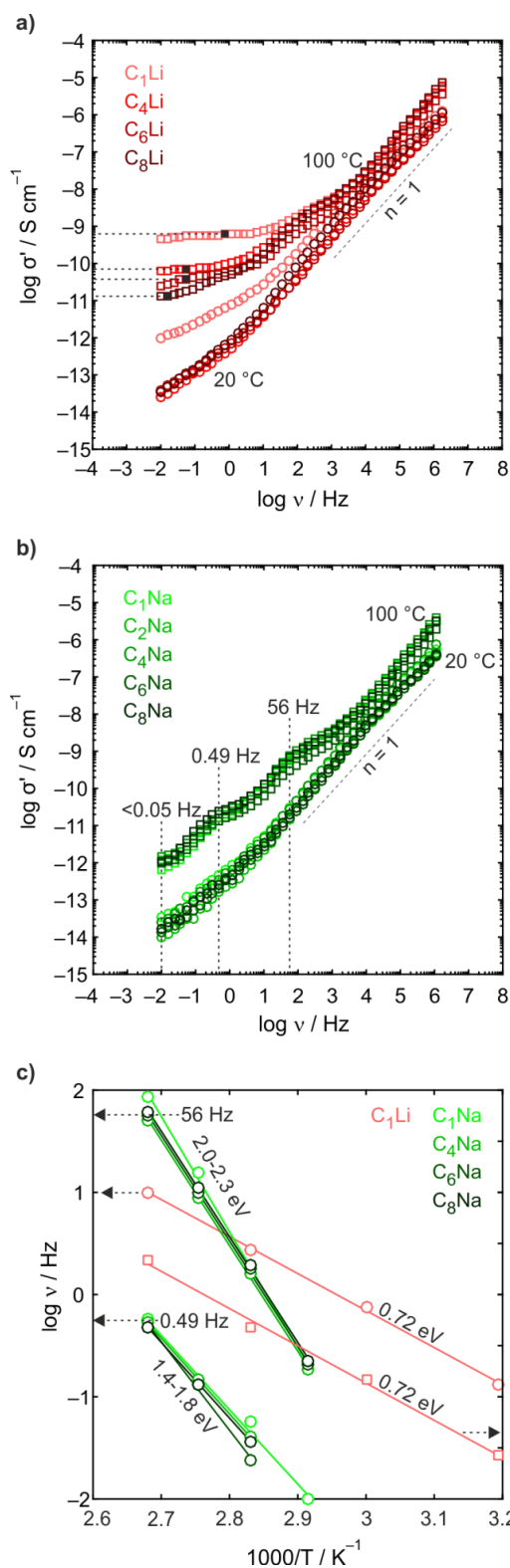


**Figure 4.** Conductivity spectra of LACs at 20 and 100 °C, displaying dc plateaus at 100 °C (a) and of SACs at 20 and 100 °C, revealing three less well defined plateaus (b, see also Figure S5). (c) Temperature dependence of the maximum of the electric modulus  $M''$  for the SACs (see Fig. S4). For  $C_1Li$ , data extracted from conductivity spectra are plotted versus the right axis for comparison.



and in the range of  $10^{-11}$  S $\cdot$ cm $^{-1}$  for the longer-chained analogues. These conductivities agree with the ones derived from fitting the spectra with equivalent circuits, Figure S3 and Table S1. The absence of pronounced electrode polarization in both plots is explained by slow ion transport through the samples. Interestingly, the conductivity decreases by one order of magnitude by moving from crystalline C<sub>1</sub>Li to lamellar C<sub>4</sub>Li. Once the samples assume a lamellar structure, however, a longer chain decreases conductivity only marginally.

The capacitances of the observed response are in the range of 150 to 300 pF (Table S1), indicating ionic movements along the grain boundaries. The activation energy of this process can be obtained from an Arrhenius diagram. Unfortunately, C<sub>1</sub>Li was the only LAC to display plateaus over a sufficiently wide temperature range to allow reliable analysis. Its activation energy was determined to be 0.72 eV, Figure 4c and S4. This agrees well with the activation energies of 0.66–0.87 eV that Borodin et. al obtained for the structurally similar dilithium ethylene dicarbonate (LEDC) by molecular dynamics simulations.<sup>15</sup> LEDC's room-temperature conductivity, however, was found to be  $1 \times 10^{-9}$  and therefore several orders of magnitude higher than the  $< 1 \times 10^{-12}$  of C<sub>1</sub>Li. In lithium ion batteries, LEDC is formed when ethylene carbonate is reduced at the anode, whereas C<sub>1</sub>Li originates from the linear dimethyl carbonate.<sup>1</sup> While LEDC is traditionally credited with forming a more stable SEI,<sup>2, 4, 57</sup> these results suggest it also has a higher conductivity compared to linear alkyl carbonates.

Conductivity spectra for SAC are shown in Figure 4b. Strikingly, the responses for all SAC are identical regardless of chain length, both at 20 °C and 100 °C. While the conductivities decline in an almost featureless slope at 20 °C, at 100 °C a series of pseudo-plateaus appears at medium to low frequencies. Two of these plateaus can be identified more clearly by plotting the electric modulus  $M''$  against the frequency, Figure S4; their frequencies are 56 Hz and 0.49 Hz for all SACs. The onset of a third plateau at very low frequencies  $< 0.05$  Hz is revealed in the complex plane plot, Figure S5b. The capacities around 200 pF (Table S2) suggest that the responses at 0.49 Hz and  $< 0.05$  Hz stem from grain boundaries. For the second plateau at 0.49 Hz, activation energies could be obtained, Figure 4c. They range between 1.45 eV for C<sub>1</sub>Na and 1.71 eV for C<sub>8</sub>Na, which is a strong increase from the 0.72 eV that were observed for C<sub>1</sub>Li. Activation energies for the second plateau at 56 Hz are even higher. These very high activation energies indicate that long-range ionic movements are not responsible for this process, whose origin currently remains unknown. Overall, SACs are extremely poor Na<sup>+</sup> conductors. This could explain, at least in part, why Na-metal electrodes show higher polarization than Li-metal when cycled in carbonate-based electrolytes.<sup>40, 58</sup> The lamellar structure that is assumed by long-chained LACs and all SACs only weakly decreases conductivity with growing chain length.

**Mechanical properties.** The mechanical properties of the SEI are crucial to ensure lasting passivation and long cycle life. A brittle SEI is likely to crack during cycling, especially if the electrode material undergoes volume changes. The crack then exposes the electrode to fresh electrolyte, which continuous SEI formation. A resilient and elastic SEI, characterized by a low Young's modulus, would thus be better suited to accommodate volume changes.

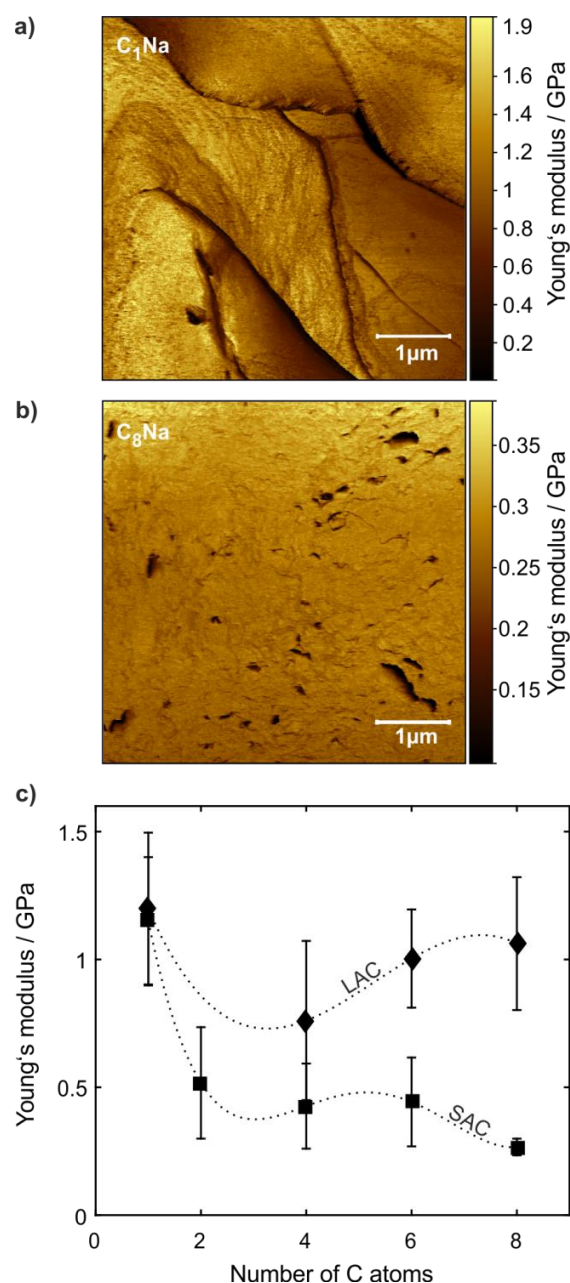


**Figure 5.** AFM nanomechanical measurements to determine material stiffness. (a, b) Exemplary AFM scans with the color code representing Young's modulus for C<sub>1</sub>Na (a) and C<sub>8</sub>Na (b). (c) Young's modulus of LACs (diamonds) and SACs (squares) as a function of alkyl chain length; the dotted lines are guides to the eye.

Figure 5 shows AFM nanomechanical measurements to determine material stiffnesses of the LACs and SACs. The samples were pressed onto a glass substrate and then subjected to AFM measurements as detailed in the Experimental. Fig. 5a and b show exemplary areal distributions of Young's modulus across scan areas for C<sub>1</sub>Na and C<sub>8</sub>Na. The surface morphology already suggests C<sub>1</sub>Na to be quite rigid, while C<sub>8</sub>Na appears to be much more adaptable to the pressing die surface. Figure 5c presents a statistical data summary of Young's modulus of all analyzed LACs and SACs. The LACs show moduli in a range between 1.2 GPa for C<sub>1</sub>Li to 1 GPa for C<sub>8</sub>Li with a minimum of 0.8 GPa for C<sub>4</sub>Li. In contrast, SAC show a clearly decreasing trend with increasing chain length. The short-chained crystalline C<sub>1</sub>Na has the by far highest modulus of 1.2 GPa. Upon moving to longer chains, the values drop to 0.5 GPa for C<sub>2</sub>Na and decrease then gradually to 0.3 GPa for C<sub>8</sub>Li. Compared to other SEI components, alkyl carbonates show intermediate to low modulus; LACs are slightly stiffer and long chain SACs are softer than polymeric components like polyethylene oxide (0.4 GPa, Ref. <sup>39</sup>); all are significantly softer than inorganic components such as LiF and Li<sub>2</sub>CO<sub>3</sub> (>35 GPa, Ref. <sup>25</sup>).

Our results are in good agreement with AFM measurements of the SEI in Li- and Na-ion batteries.<sup>25-33</sup> These measurements typically yield Young's moduli distributed over two to three orders of magnitude, which is ascribed to the inhomogeneous surface of the SEI. However, when probing a predominantly organic area, the Moduli converge to 1.0±0.2 GPa.<sup>25</sup> The electrolyte used in this study contained DMC and thus decomposes to C<sub>1</sub>Li for which we obtained a Modulus of 1.2±0.3 GPa. These values are identical within the margin of error. Furthermore, a study on the SEI in Na-ion batteries reported comparably low Moduli in the range of 0.1-0.6 GPa.<sup>38</sup> This can be rationalized considering that the electrolyte contained DEC that yields C<sub>2</sub>Na upon decomposition, which is the softest short chain SAC (0.5±0.2 GPa). The latter example also shows that our work has direct implications for the choice of electrolyte. In Na-ion batteries, for example, employing DEC instead of DMC could increase the elasticity of the SEI without sacrificing ionic transport. In contrast, long chained carbonates in Li-ion batteries are likely to decrease SEI conductivity while their mechanical properties remain largely unchanged.

## CONCLUSION

We synthesized a homologous series of Li and Na alkylcarbonates and characterized them with respect to structure, ion transport and mechanical properties. Aside from short chain Li alkyl carbonate, alkyl carbonates assume a lamellar structure but retain a certain degree of disorder. These structures are accompanied by conductivities lower than that of other typical SEI components and that are largely independent of chain length. Longer chain lengths make, however, Na alkyl carbonates significantly softer whereas Li alkyl carbonates show only weak de-

pendence of stiffness on chain length. The findings will allow a more precise interpretation of the complex results that are typically obtained from mechanical measurements on real SEI layers and give a guideline for influencing SEI mechanical properties via the choice of solvents.

## ASSOCIATED CONTENT

**Supporting Information.** Magnified versions of the FTIR spectra, complex plane plots, Arrhenius diagrams and detailed fitting results. This material is available free of charge via the Internet at <http://pubs.acs.org>.

## AUTHOR INFORMATION

### Corresponding Author

\*E-mail: [freunberger@tugraz.at](mailto:freunberger@tugraz.at)

### Notes

The authors declare no competing financial interest.

## ACKNOWLEDGMENT

The authors are indebted the Austrian Federal Ministry of Economy, Family and Youth, and the Austrian National Foundation for Research, Technology and Development, under the research program Research Studios Austria (Project number 844759).

## REFERENCES

- (1) Xu, K., Electrolytes and Interphases in Li-Ion Batteries and Beyond. *Chem. Rev.* **2014**, *114*, 11503-11618.
- (2) Gauthier, M.; Carney, T. J.; Grimaud, A.; Giordano, L.; Pour, N.; Chang, H.-H.; Fenning, D. P.; Lux, S. F.; Paschos, O.; Bauer, C.; Maglia, F.; Lupart, S.; Lamp, P.; Shao-Horn, Y., Electrode-Electrolyte Interface in Li-Ion Batteries: Current Understanding and New Insights. *J. Phys. Chem. Lett.* **2015**, *6*, 4653-4672.
- (3) Verma, P.; Maire, P.; Novák, P., A review of the features and analyses of the solid electrolyte interphase in Li-ion batteries. *Electrochim. Acta* **2010**, *55*, 6332-6341.
- (4) Aurbach, D., Review of selected electrode-solution interactions which determine the performance of Li and Li ion batteries. *J. Power Sources* **2000**, *89*, 206-218.
- (5) Edström, K.; Gustafsson, T.; Thomas, J. O., The cathode-electrolyte interface in the Li-ion battery. *Electrochim. Acta* **2004**, *50*, 397-403.
- (6) Philippe, B.; Hahlin, M.; Edström, K.; Gustafsson, T.; Siegbahn, H.; Rensmo, H., Photoelectron Spectroscopy for Lithium Battery Interface Studies. *J. Electrochem. Soc.* **2016**, *163*, A178-A191.
- (7) Edström, K.; Herstedt, M.; Abraham, D. P., A new look at the solid electrolyte interphase on graphite anodes in Li-ion batteries. *J. Power Sources* **2006**, *153*, 380-384.
- (8) Younesi, R.; Christiansen, A. S.; Scipioni, R.; Ngo, D.-T.; Simonsen, S. B.; Edström, K.; Hjelm, J.; Norby, P., Analysis of the Interphase on Carbon Black Formed in High Voltage Batteries. *J. Electrochem. Soc.* **2015**, *162*, A1289-A1296.
- (9) Aurbach, D.; Levi, M. D.; Levi, E.; Teller, H.; Markovsky, B.; Salitra, G.; Heider, U.; Heider, L., Common Electroanalytical Behavior of Li Intercalation Processes into Graphite and Transition Metal Oxides. *J. Electrochem. Soc.* **1998**, *145*, 3024-3034.
- (10) Yabuuchi, N.; Yoshii, K.; Myung, S.-T.; Nakai, I.; Komaba, S., Detailed Studies of a High-Capacity Electrode Material for Rechargeable Batteries.

- $\text{Li}_2\text{MnO}_3$ - $\text{LiCo}_{1/3}\text{Ni}_{1/3}\text{Mn}_{1/3}\text{O}_2$ . *J. Am. Chem. Soc.* **2011**, *133*, 4404-4419.
- (11) Xu, K.; von Wald Cresce, A., Li<sup>+</sup>-solvation/desolvation dictates interphasial processes on graphitic anode in Li ion cells. *J. Mater. Res.* **2012**, *27*, 2327-2341.
- (12) Xu, K.; von Cresce, A.; Lee, U., Differentiating Contributions to "Ion Transfer" Barrier from Interphasial Resistance and Li<sup>+</sup> Desolvation at Electrolyte/Graphite Interface. *Langmuir* **2010**, *26*, 11538-11543.
- (13) Bedrov, D.; Borodin, O.; Hooper, J. B., Li<sup>+</sup> Transport and Mechanical Properties of Model Solid Electrolyte Interphases (SEI): Insight from Atomistic Molecular Dynamics Simulations. *J. Phys. Chem. C* **2017**, *121*, 16098-16109.
- (14) Borodin, O.; Bedrov, D., Interfacial Structure and Dynamics of the Lithium Alkyl Dicarboxylate SEI Components in Contact with the Lithium Battery Electrolyte. *J. Phys. Chem. C* **2014**, *118*, 18362-18371.
- (15) Borodin, O.; Zhuang, G. V.; Ross, P. N.; Xu, K., Molecular Dynamics Simulations and Experimental Study of Lithium Ion Transport in Dilithium Ethylene Dicarboxylate. *J. Phys. Chem. C* **2013**, *117*, 7433-7444.
- (16) Dunstan, M. T.; Griffin, J. M.; Blanc, F.; Leskes, M.; Grey, C. P., Ion Dynamics in  $\text{Li}_2\text{CO}_3$  Studied by Solid-State NMR and First-Principles Calculations. *J. Phys. Chem. C* **2015**, *119*, 24255-24264.
- (17) Yamada, Y.; Sagane, F.; Iriyama, Y.; Abe, T.; Ogumi, Z., Kinetics of Lithium-Ion Transfer at the Interface between  $\text{Li}_{0.35}\text{La}_{0.55}\text{TiO}_3$  and Binary Electrolytes. *J. Phys. Chem. C* **2009**, *113*, 14528-14532.
- (18) Shi, S.; Lu, P.; Liu, Z.; Qi, Y.; Hector, L. G.; Li, H.; Harris, S. J., Direct Calculation of Li-Ion Transport in the Solid Electrolyte Interphase. *J. Am. Chem. Soc.* **2012**, *134*, 15476-15487.
- (19) Gachot, G.; Grugeon, S.; Armand, M.; Pilard, S.; Guenot, P.; Tarascon, J.-M.; Laruelle, S., Deciphering the multi-step degradation mechanisms of carbonate-based electrolyte in Li batteries. *J. Power Sources* **2008**, *178*, 409-421.
- (20) Gireaud, L.; Grugeon, S.; Laruelle, S.; Pilard, S.; Tarascon, J.-M., Identification of Li Battery Electrolyte Degradation Products Through Direct Synthesis and Characterization of Alkyl Carbonate Salts. *J. Electrochem. Soc.* **2005**, *152*, A850-A857.
- (21) Eshetu, G. G.; Grugeon, S.; Kim, H.; Jeong, S.; Wu, L.; Gachot, G.; Laruelle, S.; Armand, M.; Passerini, S., Comprehensive Insights into the Reactivity of Electrolytes Based on Sodium Ions. *ChemSusChem* **2016**, *4*, 462-471.
- (22) Sasaki, T.; Abe, T.; Iriyama, Y.; Inaba, M.; Ogumi, Z., Formation mechanism of alkyl dicarbonates in Li-ion cells. *J. Power Sources* **2005**, *150*, 208-215.
- (23) Dunst, A.; Epp, V.; Hanzu, I.; Freunberger, S. A.; Wilkening, M., Short-range Li diffusion vs long-range ionic conduction in nanocrystalline lithium peroxide  $\text{Li}_2\text{O}_2$  — the discharge product in lithium-air batteries. *Energy Environ. Sci.* **2014**, *7*, 2739-2752.
- (24) Benitez, L.; Seminario, J. M., Ion Diffusivity through the Solid Electrolyte Interphase in Lithium-Ion Batteries. *J. Electrochem. Soc.* **2017**, *164*, E3159-E3170.
- (25) Shin, H.; Park, J.; Han, S.; Sastry, A. M.; Lu, W., Component-/structure-dependent elasticity of solid electrolyte interphase layer in Li-ion batteries: Experimental and computational studies. *J. Power Sources* **2015**, *277*, 169-179.
- (26) Danis, L.; Gateman, S. M.; Kuss, C.; Schougaard, S. B.; Mauzeroll, J., Nanoscale Measurements of Lithium-Ion-Battery Materials using Scanning Probe Techniques. *ChemElectroChem* **2017**, *4*, 6-19.
- (27) Zhang, J.; Wang, R.; Yang, X.; Lu, W.; Wu, X.; Wang, X.; Li, H.; Chen, L., Direct Observation of Inhomogeneous Solid Electrolyte Interphase on MnO Anode with Atomic Force Microscopy and Spectroscopy. *Nano Letters* **2012**, *12*, 2153-2157.
- (28) Xu, W.; Vegunta, S. S. S.; Flake, J. C., Surface-modified silicon nanowire anodes for lithium-ion batteries. *J. Power Sources* **2011**, *196*, 8583-8589.
- (29) Li, G.; Gao, Y.; He, X.; Huang, Q.; Chen, S.; Kim, S. H.; Wang, D., Organosulfide-plasticized solid-electrolyte interphase layer enables stable lithium metal anodes for long-cycle lithium-sulfur batteries. *Nat. Commun.* **2017**, *8*, 850.
- (30) Tikekar, M. D.; Choudhury, S.; Tu, Z.; Archer, L. A., Design principles for electrolytes and interfaces for stable lithium-metal batteries. *Nat. Energy* **2016**, *1*, 16114.
- (31) He, Y.; Hu, H.; Zhang, K.; Li, S.; Chen, J., Mechanical insights into the stability of heterogeneous solid electrolyte interphase on an electrode particle. *J. Mater. Sci.* **2017**, *52*, 2836-2848.
- (32) Zheng, J.; Zheng, H.; Wang, R.; Ben, L.; Lu, W.; Chen, L.; Chen, L.; Li, H., 3D visualization of inhomogeneous multi-layered structure and Young's modulus of the solid electrolyte interphase (SEI) on silicon anodes for lithium ion batteries. *Phys. Chem. Chem. Phys.* **2014**, *16*, 13229-13238.
- (33) Kuznetsov, V.; Zinn, A.-H.; Zampardi, G.; Borhani-Haghighi, S.; La Mantia, F.; Ludwig, A.; Schuhmann, W.; Ventosa, E., Wet Nanoindentation of the Solid Electrolyte Interphase on Thin Film Si Electrodes. *ACS Appl. Mater. Interf.* **2015**, *7*, 23554-23563.
- (34) Ellis, B. L.; Nazar, L. F., Sodium and sodium-ion energy storage batteries. *Curr. Opin. Solid State Mater. Sci.* **2012**, *16*, 168-177.
- (35) Senguttuvan, P.; Rousse, G.; Arroyo y de Dompablo, M. E.; Vezin, H.; Tarascon, J. M.; Palacin, M. R., Low-Potential Sodium Insertion in a NASICON-Type Structure through the Ti(III)/Ti(II) Redox Couple. *J. Am. Chem. Soc.* **2013**, *135*, 3897-3903.
- (36) Yabuuchi, N.; Matsuura, Y.; Ishikawa, T.; Kuze, S.; Son, J.-Y.; Cui, Y.-T.; Oji, H.; Komaba, S., Phosphorus Electrodes in Sodium Cells: Small Volume Expansion by Sodiation and the Surface-Stabilization Mechanism in Aprotic Solvent. *ChemElectroChem* **2014**, *1*, 580-589.
- (37) Clément, R. J.; Bruce, P. G.; Grey, C. P., Review—Manganese-Based P2-Type Transition Metal Oxides as Sodium-Ion Battery Cathode Materials. *J. Electrochem. Soc.* **2015**, *162*, A2589-A2604.
- (38) Weadock, N.; Varongchayakul, N.; Wan, J.; Lee, S.; Seog, J.; Hu, L., Determination of mechanical properties of the SEI in sodium ion batteries via colloidal probe microscopy. *Nano Energy* **2013**, *2*, 713-719.
- (39) Ponrouch, A.; Monti, D.; Boschini, A.; Steen, B.; Johansson, P.; Palacin, M. R., Non-aqueous electrolytes for sodium-ion batteries. *J. Mat. Chem. A* **2015**, *3*, 22-42.
- (40) Dugas, R.; Ponrouch, A.; Gachot, G.; David, R.; Palacin, M. R.; Tarascon, J. M., Na Reactivity toward Carbonate-Based Electrolytes: The Effect of FEC as Additive. *J. Electrochem. Soc.* **2016**, *163*, A2333-A2339.
- (41) Bommier, C.; Leonard, D.; Jian, Z.; Stickle, W. F.; Greaney, P. A.; Ji, X., New Paradigms on the Nature of Solid Electrolyte Interphase Formation and Capacity Fading of Hard Carbon Anodes in Na-Ion Batteries. *Adv. Mater. Interf.* **2016**, *3*, 1600449.
- (42) Kumar, H.; Detsi, E.; Abraham, D. P.; Shenoy, V. B., Fundamental Mechanisms of Solvent Decomposition Involved in Solid-Electrolyte Interphase Formation in Sodium Ion Batteries. *Chem. Mat.* **2016**, *28*, 8930-8941.
- (43) Behrendt, W.; Gattow, G.; Draeger, M., On Chalcogenolates. I. Studies on Hemiesters of Carbonic Acid. 1. Preparation and Properties of Monomethyl and Monoethyl Carbonates. *Z. anorg. allg. Chem.* **1973**, *397*, 237-246.

- (44) Derjaguin, B. V.; Muller, V. M.; Toporov, Y. P., Effect of contact deformations on the adhesion of particles. *J. Colloid Interface Sci.* **1975**, *53*, 314-326.
- (45) Xu, K.; Zhuang, G. V.; Allen, J. L.; Lee, U.; Zhang, S. S.; Ross, P. N.; Jow, T. R., Syntheses and Characterization of Lithium Alkyl Mono- and Dicarbonates as Components of Surface Films in Li-Ion Batteries. *J. Phys. Chem. B* **2006**, *110*, 7708-7719.
- (46) Biswas, M.; Dule, M.; Samanta, P. N.; Ghosh, S.; Mandal, T. K., Imidazolium-based ionic liquids with different fatty acid anions: phase behavior, electronic structure and ionic conductivity investigation. *Phys. Chem. Chem. Phys.* **2014**, *16*, 16255-16263.
- (47) Glatter, O.; Kratky, O., *Small Angle X-ray Scattering*. Academic Press: London, 1982.
- (48) Nelson, P. N.; Ellis, H. A.; Taylor, R. A., Odd-even alternation in a homologous series of Zn (II) n-alkanoates. *J. Mol. Struct.* **2011**, *986*, 10-15.
- (49) Bensebaa, F.; Ellis, T. H.; Kruus, E.; Voicu, R.; Zhou, Y., Characterization of Self-Assembled Bilayers: Silver-Alkanethiolates. *Langmuir* **1998**, *14*, 6579-6587.
- (50) Nelson, P. N.; Taylor, R. A., Powder X-ray diffraction, infrared and <sup>13</sup>C NMR spectroscopic studies of the homologous series of some solid-state zinc(II) and sodium(I) n-alkanoates. *Spectrochim. Acta A* **2015**, *138*, 800-806.
- (51) Corkery, R. W., A variation on Luzzati's soap phases. Room temperature thermotropic liquid crystals. *Phys. Chem. Chem. Phys.* **2004**, *6*, 1534-1546.
- (52) Chapman, D., The 720 cm<sup>-1</sup> band in the infrared spectra of crystalline long-chain compounds. *J. Chem. Soc.* **1957**, 4489-4491.
- (53) Li, H.-W.; Strauss, H. L.; Snyder, R. G., Differences in the IR Methylene Rocking Bands between the Crystalline Fatty Acids and n-Alkanes: Frequencies, Intensities, and Correlation Splitting. *J. Phys. Chem. A* **2004**, *108*, 6629-6642.
- (54) Sandhyarani, N.; Pradeep, T., An investigation of the structure and properties of layered copper thiolates. *J. Mat. Chem.* **2001**, *11*, 1294-1299.
- (55) Li, H.; Bu, W.; Qi, W.; Wu, L., Self-Assembled Multibilayers of Europium Alkanoates: Structure, Photophysics, and Mesomorphic Behavior. *J. Phys. Chem. B* **2005**, *109*, 21669-21676.
- (56) Snyder, R. G.; Strauss, H. L.; Elliger, C. A., Carbon-hydrogen stretching modes and the structure of n-alkyl chains. 1. Long, disordered chains. *J. Phys. Chem.* **1982**, *86*, 5145-5150.
- (57) Aurbach, D.; Markovsky, B.; Shechter, A.; Ein-Eli, Y.; Cohen, H., A Comparative Study of Synthetic Graphite and Li Electrodes in Electrolyte Solutions Based on Ethylene Carbonate-Dimethyl Carbonate Mixtures. *J. Electrochem. Soc.* **1996**, *143*, 3809-3820.
- (58) Iermakova, D. I.; Dugas, R.; Palacín, M. R.; Ponrouch, A., On the Comparative Stability of Li and Na Metal Anode Interfaces in Conventional Alkyl Carbonate Electrolytes. *J. Electrochem. Soc.* **2015**, *162*, A7060-A7066.
- (59) Ferretti, A.; Carreau, P. J.; Gerard, P., Rheological and mechanical properties of PEO/block copolymer blends. *Polym. Eng. Sci.* **2005**, *45*, 1385-1394.

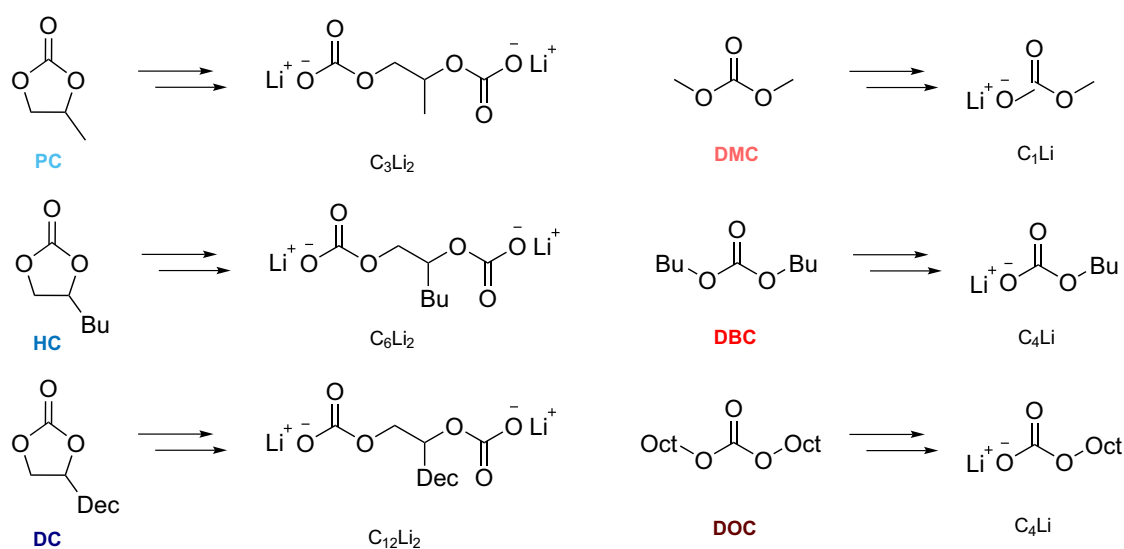


## 2.4 Long-chained carbonate solvents as SEI modifiers

In order to apply our findings on alkyl carbonate SEI components in real battery environments, I required electrolytes that would yield these components upon breakdown. Fortunately, the breakdown reactions leading to alkyl carbonates have been thoroughly scrutinized, especially on the negative electrode,<sup>80,102</sup> Scheme 2.1.

In both cases the reaction proceeds at the polar head group, but retains the alkyl chain. Consequently, a linear carbonate electrolyte would result in the corresponding alkyl carbonate while a cyclic carbonate forms the respective alkyl dicarbonate. (Alkyl dicarbonates were not investigated in this work, but have been analyzed in my Master's Thesis.<sup>131</sup>) Carbonate electrolytes could therefore be used to form LACs and SACs *in-situ* and probe their effect on the SEI. As medium to long chain alkyl carbonate electrolytes are not commercially available, they had to be synthesized. Cyclic carbonates were prepared from the corresponding epoxides and CO<sub>2</sub> using triphenylphosphine hydroiodide as a catalyst. Linear carbonates were synthesized by transesterification of DMC with the respective alcohol with a dibutyl tin oxide catalyst. Further synthetic details can be found elsewhere.<sup>131–133</sup>

An overview of the prepared electrolytes and their respective breakdown products can be found in Scheme 2.3. The custom-made electrolytes were completed with commercial short chained ones, such as the cyclic PC and the linear DMC, to give a more comprehensive picture of how chain length influences electrolyte and SEI properties. Clearly, one of the most relevant electrolyte properties is ionic conductivity as it is vital for battery performance, especially at high rates. In this case, however, ionic conductivity is not merely a performance metric; instead it decides how the carbonate can be incorporated in the battery. A highly conductive carbonate could be used as bulk electrolyte, whereas a poorly conductive carbonate can only be employed as additive.



**Scheme 2.3:** An overview of the solvents that were used for further experiments, as well as the breakdown products that are predominantly formed upon their reduction. The nomenclature of breakdown products follows the one introduced in the previous sections.

### 2.4.1 Ionic conductivity

Ionic conductivity was measured by impedance spectroscopy over a temperature range from  $-20$  to  $70$  °C, Figure 2.1. For reference, a standard electrolyte mixture was included in the measurement. It originally consisted of EC/DMC 1/1 (m/m), but DMC has a boiling point of only  $90$  °C<sup>87</sup> and would slowly evaporate and form gas bubbles, which interfere with the measurement. In the experiments presented here, DMC was therefore replaced by the less volatile PC. All solvents were blended with  $0.2$  M  $\text{LiPF}_6$  except for DC where the concentration was lowered to  $0.1$  M  $\text{LiPF}_6$  due to limited solubility.

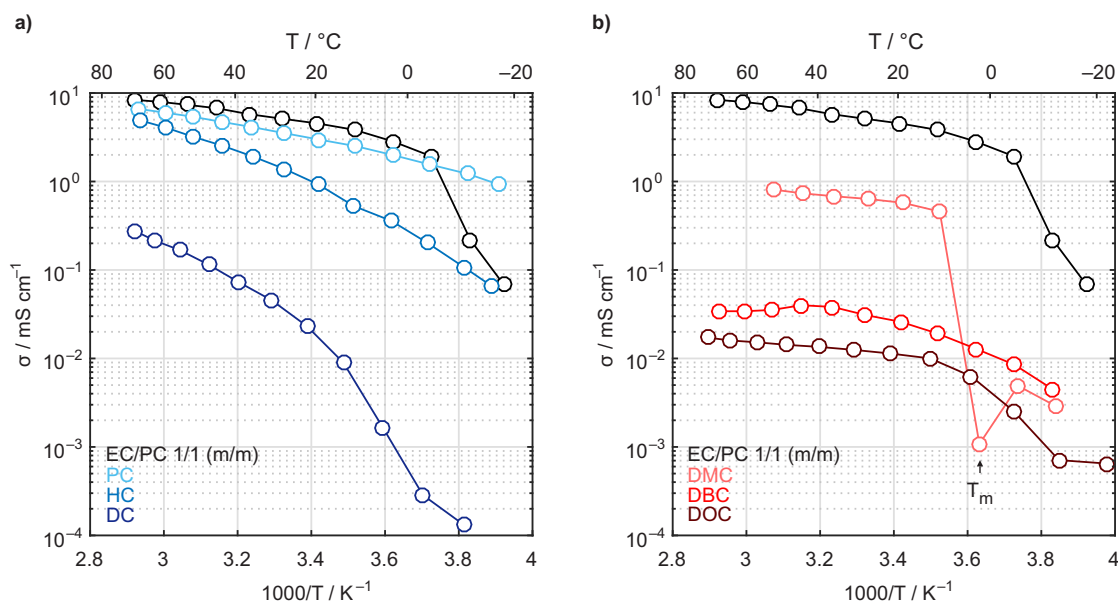


**Figure 2.1:** Specific ionic conductivities of cyclic (a) and linear (b) carbonate solvents in a temperature range from  $-20$  to  $70$  °C. All solvents were blended with  $0.2$  M  $\text{LiPF}_6$  prior to measurement, except DC which contained only  $0.1$  M  $\text{LiPF}_6$ . An EC/PC mixture was included as reference.

Figure 2.1a shows that cyclic carbonates mirror the trend that was observed for solid LACs: Ionic conductivity decreases with polarity and increasing chain length. The conductivity of short-chained PC only slightly undercuts the conductivities of the reference electrolyte – which comes as no surprise as the reference consists of 50 % PC and 50 % of the structurally very similar EC. Pure PC even outperforms the reference at temperatures below  $-5$  °C, most likely because the reference mixture is well below the melting point of its EC component ( $36$  °C) and eventually solidifies.<sup>87</sup> The medium-chained HC shows inferior albeit still acceptable conductivities of roughly  $1$  mS  $\text{cm}^{-1}$  at room temperature. However, the gap between PC and HC widens at low temperatures, which could indicate that viscosity starts to play a role. Viscosity is even more apparent for DC. At room temperature, the DC blend already forms a highly viscous, honey-like fluid that shows very low conductivities. This trend further exacerbates at lower temperatures.

In Figure 2.1b, the linear carbonates display a markedly different behavior. All linear carbonates show comparably low conductivities reflecting the fact that their lower viscosity cannot compensate for their inferior relative permittivity. This in turn leads to ion pair formation.<sup>84</sup> DMC additionally suffers from a comparably narrow liquid window that ranges from  $90$  to  $4$  °C.<sup>87</sup> Below that temperature, the conductivity plummets by two orders of magnitude. Yet, even the conductivity of solid DMC can compete with the ones from liquid DBC and DOC, which are similar to DC at room temperature.

Overall, medium- and long-chained carbonate electrolytes should be employed as

additives, rather than bulk electrolytes, with the possible exception of HC. While this would limit their negative impact on performance, it also results in another prerequisite: lower electrochemical stability. As additives typically constitute a few percent of the electrolyte mixture, they have to decompose prior to bulk components to ensure their presence in the SEI.

### 2.4.2 Electrochemical stability and passivation efficiency

The electrochemical stability was assessed by cyclic voltammetry in a setup that closely resembled a real battery. Conductive carbon (SuperP) composite working electrodes were combined with Li metal or partially delithiated LFP counter electrodes for testing the reductive and oxidative stability in a Swagelok<sup>®</sup> cell. The working electrode was then polarized at a constant rate of  $1 \text{ mV s}^{-1}$ ; once the voltage exceeds the stability window of the electrolyte, decomposition occurs. The electrolyte undergoes electrochemical reduction or oxidation and the resulting current density is detected. Consequently, the onset of a significant current density marks the limit of electrolyte stability.

Upon repeating the polarization steps, decomposition products accumulate at the electrode surface and a SEI forms. The SEI reduces diffusion of electrolyte molecules to the electrode surface and inhibits further decomposition. This process manifests in decreasing current densities that provide essential information: How efficient is the electrolyte in passivating the electrode surface? The more efficient the passivation, the faster and the more will current densities decrease.

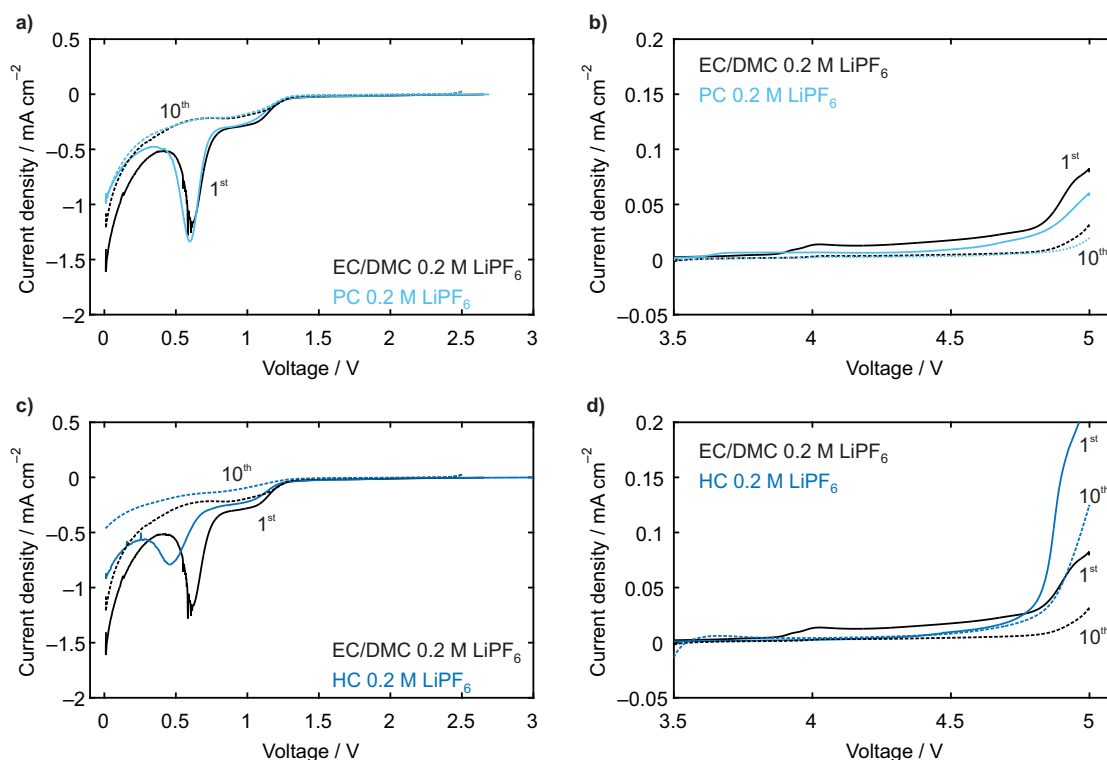


**Figure 2.2:** Cyclic voltammograms of cyclic carbonate solvents PC (a,b) and DOC (c,d) with  $0.2 \text{ M LiPF}_6$  at  $1 \text{ mV s}^{-1}$  on a conductive carbon composite electrode. Solid lines denote the first cycle, dashed lines the tenth cycle. A commonly used solvent mixture, EC/DMC 1/1 (w/w), is shown for comparison. The small increase in current at approximately 4 V seems to originate from an impurity in EC.

Cyclic voltammograms for the cyclic carbonate electrolytes are presented in Figure 2.2. Electrochemical stability and passivation efficiency of the short-chained PC does not differ significantly from the reference electrolyte EC/DMC with 0.2 M  $\text{LiPF}_6$ . The decomposition onsets for both EC/DMC and PC are at 1.3 and  $>4.5$  V, respectively. Additionally, both electrolytes show a pronounced increase in current densities at 0.6 V that disappears in subsequent cycles. The medium-chained HC adheres to this general pattern while deviating in details. The current peak is shifted to 0.45 V indicating a higher stability towards reduction. In contrast, HC fails to provide efficient protection from oxidation as the current densities remain high after ten cycles. The long-chained DC could not be investigated as its extremely high viscosity prevented thorough wetting of the separator leading to irreproducible results and premature cell death.

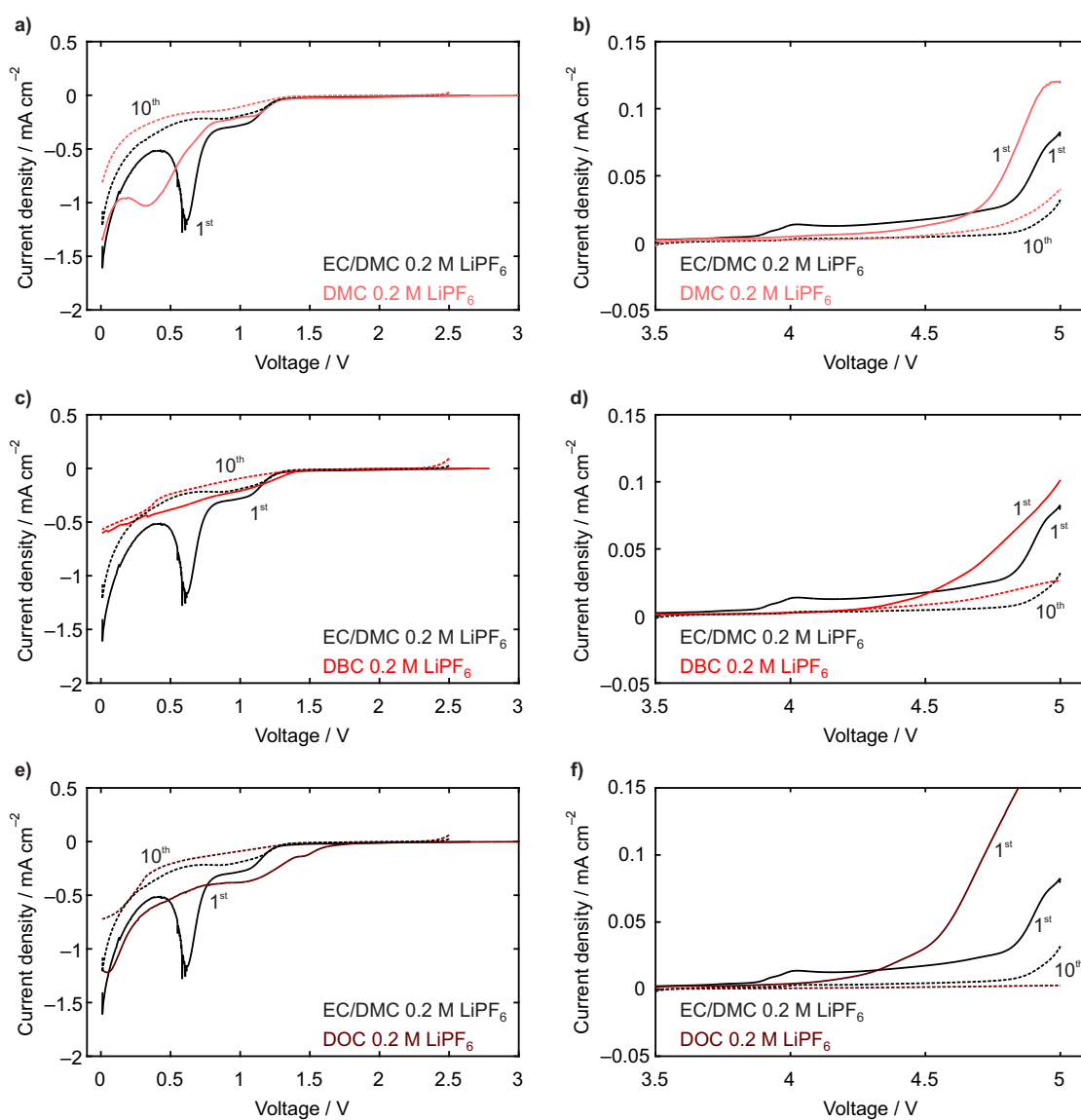


**Figure 2.3:** Cyclic voltammograms of linear carbonate solvents DMC (a,b), DBC (c,d) and DOC (e,f) with 0.2 M  $\text{LiPF}_6$  at  $1 \text{ mV s}^{-1}$  on a conductive carbon composite electrode. Solid lines denote the first cycle, dashed lines the tenth cycle. A commonly used solvent mixture, EC/DMC 1/1 (w/w), is shown for comparison. The small increase in current at approximately 4 V seems to originate from an impurity in EC.

Cyclic voltammograms from linear carbonate electrolytes are shown in Figure 2.3. While the current responses vary in many details, a few general trends can be stated. First, the reductive stability decreases upon increasing chain length; DBC is reduced slightly above 1.3 V, DOC already at about 1.5 V. Second, oxidative stability decreases as well, both in terms of onset potential and current density. DOC, however, efficiently passivates the electrode surface at high voltages; after ten cycles only a negligible current density remains. DOC thus combines low electrochemical stability with efficient passivation of the cathode up to 5 V.

Further evidence that DOC passivates the cathode surface comes from electrochemical impedance spectroscopy (EIS). Impedance data was collected from the pristine cell and after 10 cycles, Figure 2.4. DOC shows considerably higher resistances in the pristine cells that reflect its lower conductivity. This difference, however, pales in comparison to the cycled cell where the resistance has increased by roughly two orders of magnitude. In contrast, the impedance response of the EC/DMC electrolyte changed only slightly, while the resistance in DMC increased fivefold. Overall, the impedance data clearly shows that DOC participates in forming a protective layer, but this layer is highly resistive. Both of these properties, however, may change when DOC is employed as an additive instead of a bulk electrolyte.

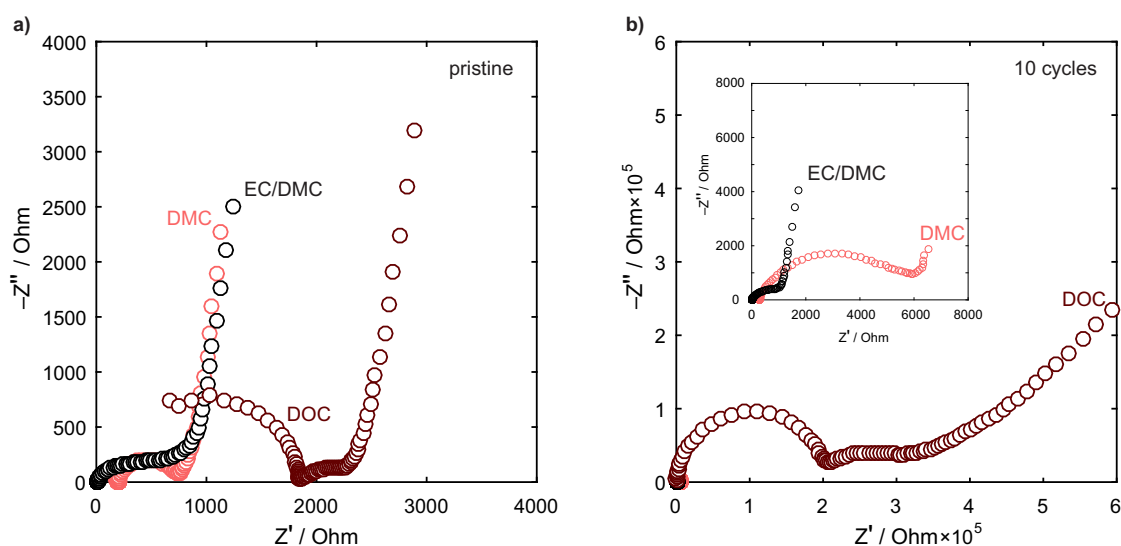


**Figure 2.4:** Complex plane plot of a pristine cell (a) and after 10 cycles at  $1 \text{ mV s}^{-1}$  from OCV to 5 V (b). The cell consisted of a conductive carbon working electrode, a Li-metal counter electrode and either DOC, DMC or EC/DMC 1/1 (w/w) with 0.2 M  $\text{LiPF}_6$ . The inset shows a magnified image of b).

### 2.4.3 DOC as electrolyte additive

For the next series of tests, DOC should be blended with EC/DMC/1 M  $\text{LiPF}_6$ , a standard electrolyte for many high voltage applications.<sup>134</sup> However, the first test already revealed a sobering result: The miscibility of DOC with EC/DMC/1 M  $\text{LiPF}_6$  is rather limited. At 10 vol% additive concentration, a phase separation occurred with a layer of DOC at the top. In order to obtain fully dissolved mixtures, I had to further explore the mixing behavior of DOC with bulk electrolytes.

Interestingly, the solvents itself are miscible in any ratio and the phase separation occurs only upon addition of the electrolyte salt. Most likely, the salt is then solvated by the smaller, more polar solvent molecules, further increasing their polarity and, as

a consequence, causing phase separation. This phenomenon is corroborated by the fact that upon decreasing the salt concentration from 1 to 0.2 M, the solubility increases from 4.0 to 5.8 vol%, see Table 2.2. Solubility was increased further by replacing the “hard”  $\text{PF}_6^-$  anion with the “softer” bis(trifluoromethane)sulfonimide ( $\text{TFSI}^-$ ) anion, which distributes charge more evenly.<sup>85</sup> A 0.2 M solution of  $\text{LiTFSI}$  in EC/DMC could accommodate 8.3 vol% of DOC. Changing the electrolyte could permit an even higher solubility; exchanging EC/DMC for dimethoxyethane (DME), for example, yielded a solubility of more than 25 vol%. Due to other unwanted properties of DME as electrolyte solvent, such as its high volatility and poor passivation behavior, this remains only a theoretical option. Fortunately, a solubility of 4 %vol suffices for a typical additive in a Li-ion battery.<sup>135–137</sup>

**Table 2.2:** Miscibility of DOC with various electrolytes.

Electrolyte	Solubility / vol%
EC/DMC with 1 M $\text{LiPF}_6$	4.0
EC/DMC with 0.2 M $\text{LiPF}_6$	5.8
EC/DMC with 0.2 M $\text{LiTFSI}$	8.3
DME with 0.2 M $\text{LiTFSI}$	>25

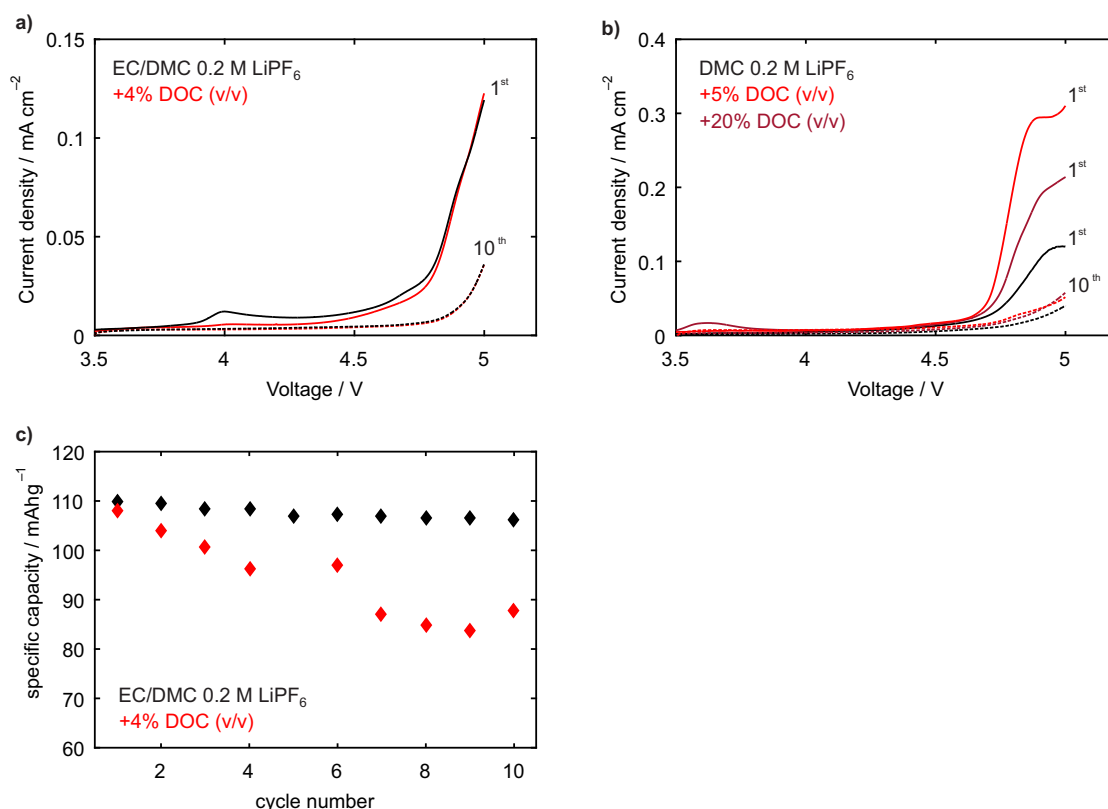


**Figure 2.5:** Cyclic voltammetry of EC/DMC (a) and DMC (b) with 0.2 M  $\text{LiPF}_6$  and varying amounts of DOC at  $1 \text{ mVs}^{-1}$  on a conductive carbon composite electrode. Galvanostatic cycling (c) of  $\text{LiNi}_{0.5}\text{Mn}_{1.5}\text{O}_4$  at C/10 rate in EC/DMC with 0.2 M  $\text{LiPF}_6$  and with or without 4 vol% DOC.

In the next experiment, EC/DMC/0.2 M  $\text{LiPF}_6$  was mixed with 4 vol% DOC, Figure 2.5. Surprisingly, current responses with and without DOC are virtually identical,

both in the first and the tenth cycle. It seems that despite its lower thermodynamic stability, kinetic factors prevent DOC from decomposing on the cathode surface. Yu *et al.* have shown that cyclic carbonates adsorb preferentially at cathode surfaces.<sup>138</sup> Possibly, the linear and unpolar DOC never reaches the active surface and does not decompose as a consequence.

To test this hypothesis, DOC was mixed with only the linear carbonate DMC, Figure 2.5b. While, surprisingly, 5 vol% of DOC resulted in a higher current density than 20 vol% of DMC, maybe due to the higher conductivity of the former electrolyte mixture, DOC in any case increased the current response in the first cycle. After 10 cycles, however, the current responses strongly resemble each other. In conclusion, DOC participates in the decomposition reactions, but does not stabilize the cathode surface further and is eventually consumed. This behavior could be explained by underlying solubility issues of the decomposition products. Generally, the decomposition products are ionic and thus more polar than their parent electrolytes. As DOC itself is rather unpolar, they precipitate at the cathode surface and form a protective layer. In contrast, DMC could be polar enough to continuously dissolve the decomposition products of DOC and prevent a protective layer from forming.

If this were to be correct, a fundamental problem would preclude DOC's application as an electrolyte additive. Still one last experiment was performed in a cell consisting of a  $\text{LiNi}_{0.5}\text{Mn}_{1.5}\text{O}_4$  working electrode, a Li counter electrode and an EC/DMC/0.2 M  $\text{LiPF}_6$  electrolyte with and without 4 vol% DOC, Figure 2.5c. DOC increases capacity fade and self-discharge; when the charged cell was left at OCV for 100 h, the cell discharged almost completely from 5 V to 4.25 V, compared to 4.7 V for the base electrolyte.

In conclusion, DOC shows a remarkable passivation behavior when employed in bulk, but fails when mixed with a state-of-the-art carbonate electrolyte, likely due to better solubility of its decomposition products. In combination with a high voltage cathode material, DOC is detrimental to cell performance.





### 3. Reversible cycling of sodium metal and Na intercalation compounds

Na half cells are unreliable, because state-of-the-art carbonate electrolytes fail to passivate the Na counter electrode. Here, Na and Na intercalation electrodes were stabilized by using a highly concentrated electrolyte based on Na bis(fluoro)sulfonylimide (NaFSI) and dimethoxyethane (DME). This mixture was particularly promising, given that a similar electrolyte was shown to efficiently passivate Li<sup>139</sup> and that FSI<sup>-</sup> is known form functional interphases.<sup>140</sup>

This enabled reliable cycling of Na half cells with hard carbon and Na<sub>3</sub>V<sub>2</sub>(PO<sub>4</sub>)<sub>3</sub> (NVP). Shortly after, very similar electrolyte systems were published independently by the groups of Choi<sup>141</sup> and Yamada<sup>142</sup>.

The unpublished material complements the contribution, presenting how the conditions were optimized to ensure reliable cycling of Na. The varied parameters include salt concentration, as well as current density and capacity during the plating experiment.

#### **An Electrolyte for Reversible Cycling of Sodium Metal and Intercalation Compounds**

Lukas Schafzahl, Ilie Hanzu, Martin Wilkening, Stefan A. Freunberger

*ChemSusChem* 2017, 10, 401-408. Reprinted with permission.

## 3.1 Stabilizing Na-ion half cells

After a long sleep, the interest in Na-ion batteries has been soaring since 2010.<sup>143</sup> The progress was accelerated by the extensive knowledge about Li-ion batteries that could be adapted for the similar Na-ion technology. Thus, carbonates (see Table 2.1) almost instantaneously became the preferred electrolyte solvents. As in Li-ion batteries, many researchers first focused on PC.<sup>31</sup> However, PC was shown to cause capacity fade of hard carbon anodes<sup>81</sup> and further effort was devoted to mixtures of various carbonates. Here, the binary mixture of EC/DEC proved more favorable than EC/EMC or EC/DMC in combination with both anode and cathode electrodes.<sup>144,145</sup> A systematic study investigated mixtures of PC, EC, DMC, DEC, DME and tetrahydrofuran with NaClO<sub>4</sub> and NaPF<sub>6</sub> in terms of conductivity, electrochemical and thermal stability.<sup>81</sup> While the salts performed similarly, EC/PC emerged as the solvent mixture of choice. The rate performance of this mixture could be further increased by adding 10 vol% of DMC.<sup>33</sup> With this electrolyte, a Na-ion full cell was constructed that showed excellent capacity retention and similar energy densities to that of Li-ion batteries.

full cells resemble commercial batteries in terms of cathode and anode materials. Yet, full cells are seldomly employed in research because of practical reasons. First, a full cell's capacity is limited by the electrode with the lower capacity. Thus, the mass ratio of cathode and anode has to be balanced correctly for the cell to work. Second, the potentials of both electrodes vary during cycling which has to be considered when setting the cutoff potentials. Third, the amount of total Na<sup>+</sup> in the cell is limited. Materials under research sometimes have low CE and will continuously consume Na<sup>+</sup> leading to rapid cell failure. For these reasons, so-called half cells are employed more often by researchers. In a half cell, the working electrode consists of the material to be investigated, while Na metal serves as the counter electrode. The Na counter electrode has a relatively stable potential and can supply a near-unlimited amount of Na<sup>+</sup>. Consequently, half cells are a more practical tool for assessing new electrolytes and electrode materials.

### 3.1.1 Are half cells reliable?

All this is built on the premise, however, that the half cell performance reflects the performance of the working electrode only; the counter electrode must not influence the performance and should be stable. After decades of experience, Li counter electrodes are unanimously considered to be stable, but Na half cells give a somewhat different picture. When NVP was cycled in a half cell, an electrolyte containing PC/NaClO<sub>4</sub> showed poor CE of around 94% while the CE increased to roughly 98% in PC/NaFSI or EC/DEC/NaFSI.<sup>146</sup> The latter electrolytes also showed smaller capacity fading. This is stunning, because the operating potential of NVP is 3.35 V and side-reactions are not to be expected at the working electrode. Thus the choice of electrolyte should not influence the CE and even less the capacity fading – unless the Na counter electrode compromises the results.

Since then further reports have corroborated the detrimental impact of the Na counter electrode in half cells. Hatchard and Obrovac demonstrated severe capacity fading and low CE of their NaCrO<sub>2</sub> cathodes due to side-reactions of the electrolyte with the Na counter electrode.<sup>147</sup> Again the effects were more pronounced in PC than in EC/DEC that seems to better passivate Na. This passivation, however, is not without fault; Rudola *et al.* found that EC/PC mixtures introduce an unexpected voltage step that originates, again, from the Na counter electrode.<sup>148</sup> Lastly, Bommier *et al.* proved SEI formation on Na to

be the main source of poor performance in Na half cells. Moreover, they could rejuvenate a badly aged cell by replacing the Na counter-electrode.<sup>149</sup> Overall, these reports clearly indicate that the Na counter-electrode deteriorates cell performance because carbonate-based electrolytes fail to passivate it sufficiently. Moreover, this failure could also apply to Na intercalation electrodes that operate at similar potentials, such as the widely used hard carbon.

The reason for this discrepancy between Li and Na half cells remains unclear. Possibly, the higher solubility of Na-SEI components is responsible.<sup>124</sup> What is clear, however, are the consequences: researchers can either resort to more cumbersome full cells, or develop an electrolyte that efficiently and reliably passivates Na to eliminate the influence of the counter electrode. The latter option was pursued in this work.

### 3.1.2 Passivating sodium metal

To develop a suitable electrolyte, most conveniently an additive would be blended with an existing carbonate electrolyte. Several common additives in Li-ion batteries have been tested in Na-ion cells, including vinylene carbonate (VC) and fluoroethylene carbonate (FEC).<sup>150</sup> While the former is frequently used in Li-ion batteries, only the latter proved beneficial in Na-ion environments. Still, mixed results were reported about its efficiency.<sup>81,151</sup> While FEC could mitigate reactions with Na,<sup>152</sup> it also causes adverse side effects such as strongly increased cell impedance, continuous gas evolution and voltage anomalies.<sup>153</sup> Thus, currently available additives cannot resolve the problem of Na stabilization and we instead turned to alternative electrolyte formulations and, more precisely, highly concentrated electrolytes.

Highly concentrated electrolytes present one exciting development in the field of Li-electrolytes. The peculiar effect of high concentrations became first apparent when it was found that PC could suddenly support reversible  $\text{Li}^+$  intercalation and deintercalation into graphite. This was hitherto considered impossible, because PC would cointercalate with  $\text{Li}^+$  disrupting the layered structure of graphite and eventually destroying the material.<sup>154</sup> Later reports demonstrated that this was not limited to PC, but could also be achieved with a surprising variety of solvents including dimethyl sulfoxide (DMSO), DME, acetonitrile (ACN), sulfoxides and sulfones, as long as the salt concentration was  $>3$  M.<sup>155-157</sup> A mixture of DME with 3.6 M LiFSI even outperformed conventional carbonate electrolytes in terms of rate capability.<sup>158</sup> The benefits of highly-concentrated electrolytes are, however, by no means limited to the cycling of graphite:<sup>155,159,160</sup>

1. High salt concentrations increase resilience towards reduction. This was attributed to a shifted lowest unoccupied molecular orbital (LUMO) of the electrolyte salt, which is below the solvent LUMO. The salt is therefore reduced preferentially and passivates the anode surface, if it has a suitable anion like LiFSI or LiTFSI.
2. High concentrations can enhance the stability towards oxidation. When the salt/solvent molar ratio approaches 1, almost all solvent molecules will engage in complexation reactions. Lone pairs of the solvent are donated to the  $\text{Li}^+$ . This decreases the solvents HOMO and yields increased stability towards oxidation.
3. Surprising rate capabilities have been achieved with highly concentrated electrolytes despite their high viscosities. With strongly Lewis basic anions, such as  $\text{NO}_3^-$ ,  $\text{Li}^+$  forms ion pairs, Figure 3.1b. Weakly Lewis basic anions, however, such as TFSI<sup>-</sup> and FSI<sup>-</sup>, form solvent- $\text{Li}^+$  complexes, Figure 3.1c. This results in comparably well

dissociated mixtures with a high density of charge carriers and surprisingly large transport numbers for  $\text{Li}^+$  (around 0.5).

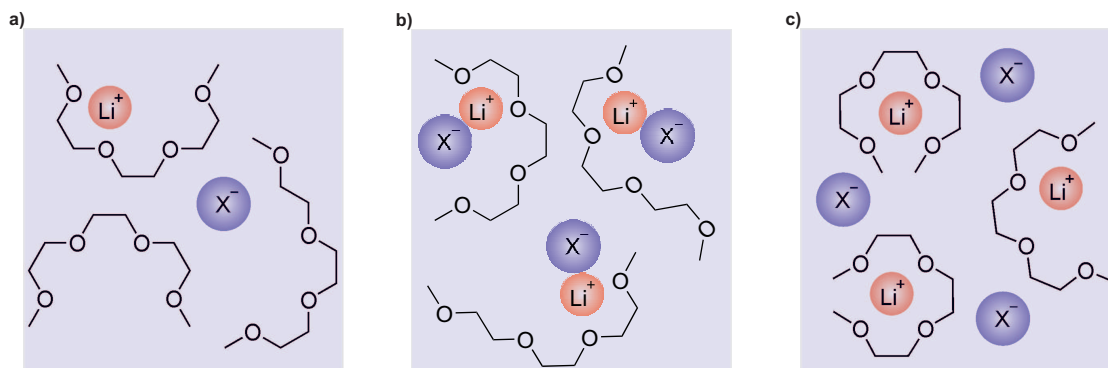


**Figure 3.1:** Schematic comparison of solvent structures in an electrolyte containing triglyme with  $\text{LiX}$  in (a) a low concentration, (b) a high concentration with a strong Lewis basic anion leading to ion pair formation and (c) a high concentration with a weak Lewis basic anion leading to solvent- $\text{Li}^+$  complexes (“pseudo-ionic liquid”).

Highly concentrated electrolytes share additional advantages with ionic liquids, such as high thermal stability, low volatility and low flammability. Thus, they are sometimes referred to as “pseudo-ionic liquids” or “solvate ionic liquids”. Moreover, some drawbacks of ionic liquids do not apply fully to highly concentrated electrolytes: They are cheaper, show higher  $\text{Li}^+$  conductivity and are conveniently obtained in high purities. This unique features have enabled 4-V-Li-ion batteries based entirely on ethyl acetate,<sup>161</sup> more stable Li-S batteries<sup>162</sup> and, perhaps most impressively, an aqueous Li-ion battery with a stability window of 3 V.<sup>163</sup> When this work was in the making, however, only one report on Na-ion batteries was published; it focused on the physiochemical properties of an glyme/TFSI electrolyte.<sup>164</sup>

An electrolyte based on LiFSI and DME was reported to allow cycling of Li at unprecedented rates for thousands of cycles;<sup>139</sup> we therefore reasoned that an analogous electrolyte might better stabilize Na, too, and open new avenues for more reliable Na-ion half cells.

# An Electrolyte for Reversible Cycling of Sodium Metal and Intercalation Compounds

Lukas Schafzahl, Ilie Hanzu, Martin Wilkening, and Stefan A. Freunberger\*<sup>[a]</sup>

Na battery chemistries show poor passivation behavior of low voltage Na storage compounds and Na metal with organic carbonate-based electrolytes adopted from Li-ion batteries. Therefore, a suitable electrolyte remains a major challenge for establishing Na batteries. Here we report highly concentrated sodium bis(fluorosulfonyl)imide (NaFSI) in dimethoxyethane (DME) electrolytes and investigate them for Na metal and hard carbon anodes and intercalation cathodes. For a DME/NaFSI ratio of 2, a stable passivation of anode materials was found

owing to the formation of a stable solid electrolyte interface, which was characterized spectroscopically. This permitted non-dendritic Na metal cycling with approximately 98% coulombic efficiency as shown for up to 300 cycles. The NaFSI/DME electrolyte may enable Na-metal anodes and allows for more reliable assessment of electrode materials in Na-ion half-cells, as is demonstrated by comparing half-cell cycling of hard carbon anodes and Na<sub>3</sub>V<sub>2</sub>(PO<sub>4</sub>)<sub>3</sub> cathodes with a widely used carbonate and the NaFSI/DME electrolyte.

## Introduction

Batteries based on Na rather than Li could be potentially cheaper and more sustainable, and have therefore led to increasing research activities.<sup>[1]</sup> Whereas economically exploitable Li reserves are scarce and over 90% of the reserves are owned by only four countries, Na constitutes more than 2% of Earth's mass and is ubiquitous, resulting in significantly lower alkali metal cost.<sup>[2]</sup> Moreover, the negative current collector in Na-ion batteries can consist of inexpensive and more abundant Al instead of Cu. Together, this renders Na-ion batteries a promising technology to rival Li-ion batteries.<sup>[3]</sup>

Competitive Na-ion batteries necessitate suitable electrolytes and electrode materials. Electrolytes for Na-ion batteries generally consist of organic carbonates,<sup>[1,4]</sup> but ionic liquids have been explored as an alternative.<sup>[1,5]</sup> Materials for negative intercalation electrodes have been described, including hard carbon (HC), metal alloys, and oxides.<sup>[1,6]</sup> Most activities, however, have focused on positive intercalation materials or non-intercalation chemistries, such as Na–O<sub>2</sub> and Na–S.<sup>[1,6,7]</sup> Non-intercalation batteries draw their superb theoretical specific energies in part from the Na metal anode with a specific capacity of 1165 mAh g<sup>-1</sup>.

Na anodes, however, are highly reactive towards organic electrolytes and need to be stabilized by a strongly passivating solid electrolyte interface (SEI) to allow reversible Na cycling. Unfortunately, carbonate electrolytes form a rather unstable SEI on Na, as evidenced by high overpotentials and low metal plating/stripping efficiency.<sup>[8]</sup> Only recently, it was demonstrat-

ed that carbonate electrolyte decomposition at the Na counter electrode is the primary source of fading in HC half-cells.<sup>[9]</sup> Thus, an electrolyte that fails to form a stable SEI on Na does not only prevent Na anodes, but could also compromise all results obtained in Na-ion half-cells.

To improve SEI stability, several additives for Li-ion batteries were assessed for Na-ion chemistries; fluoroethylene carbonate (FEC) was found to be the most effective.<sup>[10]</sup> FEC enhanced the capacity retention on anodes that experience large volume expansion,<sup>[11]</sup> whereas reports on HC remain controversial.<sup>[10,12]</sup> FEC also mitigates irreversible reactions with Na anodes, allowing cycling efficiencies of 70–90%<sup>[10,13]</sup> at the price of strongly increased cell impedance, voltage anomalies, and continuous gas evolution.<sup>[14]</sup> This calls for further research to stabilize the Na counter electrode and to allow for more reliable Na-ion half cells.

Here we report a sodium bis(fluorosulfonyl)imide (NaFSI)/dimethoxyethane (DME) electrolyte that combines the unusual stability of highly concentrated electrolytes<sup>[15]</sup> and the unique film-forming properties of the FSI anion<sup>[16]</sup> to stabilize the SEI on Na. This electrolyte enables non-dendritic Na cycling at average efficiencies of 97.7% for up to 300 cycles at 0.2 mA cm<sup>-2</sup>. Spectroscopic characterization shows that the SEI is composed of organic ethers and salt decomposition products. The NaFSI/DME electrolyte may enable Na metal anodes and allows for more reliable assessment of electrode materials in Na-ion half-cells to spur further advances in Na-ion batteries. The latter is demonstrated by comparing half-cell cycling of HC anodes and Na<sub>3</sub>V<sub>2</sub>(PO<sub>4</sub>)<sub>3</sub> (NVP) cathodes with a widely used carbonate and the NaFSI/DME electrolyte.

[a] L. Schafzahl, Dr. I. Hanzu, Prof. M. Wilkening, Dr. S. A. Freunberger  
Institute of Chemistry and Technology of Materials  
Graz University of Technology, Graz (Austria)  
E-mail: freunberger@tugraz.at

Supporting Information and the ORCID identification number(s) for the author(s) of this article can be found under <http://dx.doi.org/10.1002/cssc.201601222>.

## Results and Discussion

### Sodium plating and stripping

Cells with a Cu working electrode and Na-metal counter electrode were constructed as described in the Experimental Section. They were subjected to galvanostatic cycling with  $0.2 \text{ mA cm}^{-2}$ ; Na was deposited for 2.5 h, and stripped to an upper voltage cut-off of 0.5 V vs. Na/Na<sup>+</sup>. Electrolytes chosen were 1 M NaClO<sub>4</sub> in ethylene carbonate (EC)/propylene carbon-

ate (PC) (1:1 *m/m*) and DME electrolytes with a NaFSI/DME molar ratio of 0.1, 0.4, 0.5, and 0.6. The latter corresponds to an ether-oxygen to Na<sup>+</sup> ratio of 20, 5, 4, and 3 1/3, respectively. The results for the 1<sup>st</sup>, 2<sup>nd</sup>, and 10<sup>th</sup> cycle are shown in Figure 1a. The coulombic efficiency is obtained by comparing the stripping capacity to the preceding deposition capacity. It is a key indicator for interface stability, as it is deteriorated by side reactions owing to incomplete passivation or dendrite growth leading to isolated particles. Accordingly, high efficiency signifies efficient passivation and uniform film growth.

The NaFSI/DME=0.5 electrolyte delivers excellent efficiencies. In the 1<sup>st</sup> cycle, it reaches 85% compared to 59% for the carbonate electrolyte (Figure 1a). The other DME electrolytes lie in between. In the following cycles, the diluted DME electrolytes deteriorate quickly; the ratio of NaFSI/DME=0.1 fails in the 1<sup>st</sup> cycle (not shown here), NaFSI/DME=0.4 in the 3<sup>rd</sup> cycle. The more concentrated DME electrolytes can sustain prolonged cycling and their efficiency increases after the first cycles, where the SEI seems to be formed. The NaFSI/DME=0.5 electrolyte reached the highest efficiencies and was further investigated in more detail. Figure 1b compares the cycling efficiencies of NaFSI/DME=0.5 and the carbonate electrolyte. The efficiency of the carbonate electrolyte dropped from the initial 59% in the first cycle to below 50%, leading to early cell failure. In contrast, the efficiency of NaFSI/DME=0.5 averages 97.7% over more than 250 cycles.

To understand the possible influences of electrolyte conductivity, it was measured using impedance spectroscopy over a temperature range from  $-20$  to  $60^\circ\text{C}$ , Figure 2. Higher temperatures were omitted as the volatile DME evaporated and formed bubbles that erroneously decreased the measured conductivities. We expected the conductivity to decline with increasing salt concentrations owing to higher viscosity and ion pair formation. This trend is reflected in the results. The carbonate electrolyte displays a conductivity of approximately

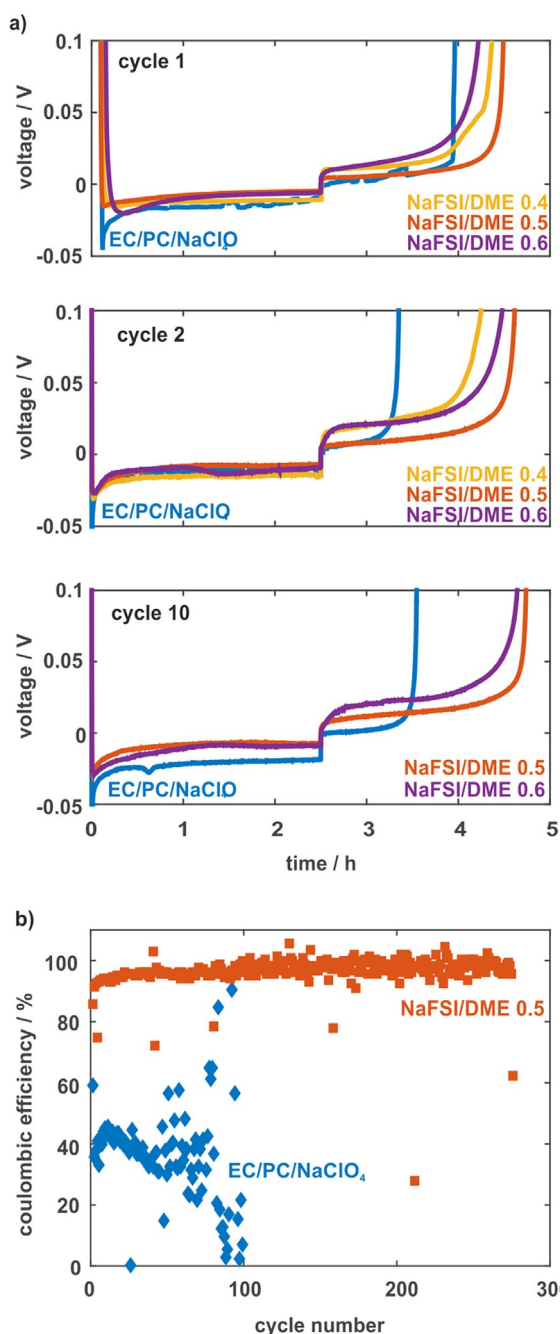


**Figure 1.** Galvanostatic plating and stripping of Na at  $0.2 \text{ mA cm}^{-2}$ . (a) Potential profiles of the 1<sup>st</sup>, 2<sup>nd</sup>, and 10<sup>th</sup> cycle in 1 M NaClO<sub>4</sub> in EC/PC (1:1 *m/m*) and NaFSI/DME electrolytes. (b) Coulombic efficiencies of carbonate and NaFSI/DME=0.5 electrolytes.

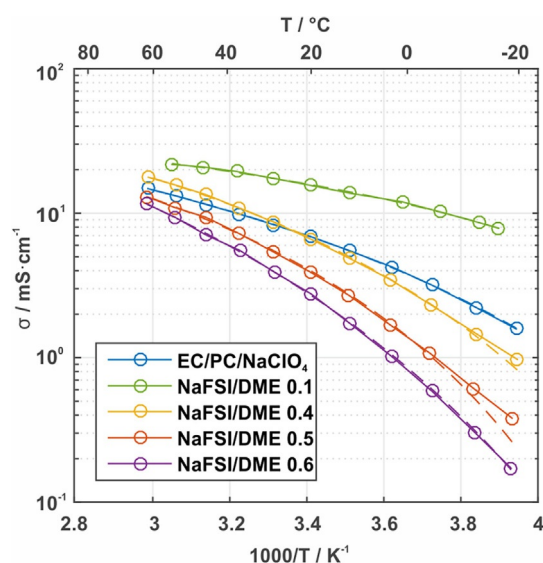


**Figure 2.** Specific ionic conductivity versus inverse temperature for 1 M NaClO<sub>4</sub> in EC/PC (1:1 *m/m*) and NaFSI/DME electrolytes, including the corresponding VTF fits (dashed lines).



**Table 1.** Specific ionic conductivities and parameters of the VTF fits to the impedance data shown in Figure 2.

Electrolyte	$\sigma_{20}^{[a]}$ [mS cm <sup>-1</sup> ]	$\sigma_{60}^{[a]}$ [mS cm <sup>-1</sup> ]	$\sigma_{inf}$ [mS cm <sup>-1</sup> ]	$E_a$ [eV]	$T_0$ [K]
carbonate	6.9	14	141 ± 7	0.032 ± 0.001	171 ± 2
NaFSI/DME = 0.1	16	22	66 ± 9	0.014 ± 0.003	180 ± 10
NaFSI/DME = 0.4	6.6	17	220 ± 30	0.032 ± 0.003	187 ± 6
NaFSI/DME = 0.5	4.0	13	190 ± 40	0.031 ± 0.005	199 ± 8
NaFSI/DME = 0.6	2.8	11	600 ± 200	0.054 ± 0.007	179 ± 8

[a]  $\sigma_{20}$  and  $\sigma_{60}$  are the specific conductivities at 20 and 60 °C, respectively.

7 mS cm<sup>-1</sup> at 20 °C, which is in good agreement with literature values (Table 1).<sup>[4b]</sup> Diluted DME electrolytes, such as NaFSI/DME = 0.1, far surpass the carbonate electrolyte; upon increasing ratios, however, the balance turns. NaFSI/DME = 0.4 is comparable to the carbonate electrolyte showing superior conductivities above room temperature, but inferior ones at lower temperatures. Finally, the highest concentrations of NaFSI/DME = 0.5 and 0.6 are less conductive than the carbonate electrolyte over the entire temperature range.

The activation energies for ion transport paint a similar picture. Activation energies were determined using the Vogel–Tamann–Fulcher (VTF) equation [Eq. (1)]:

$$\sigma(T) = \sigma_{inf} \left( -\frac{E_a}{k_b(T - T_0)} \right) \quad (1)$$

Herein,  $\sigma_{inf}$  (S cm<sup>-1</sup>) is the ionic conductivity at infinite temperature,  $E_a$  (eV) is the activation energy for ion transport,  $k_b$  ( $8.62 \times 10^{-5}$  eV K<sup>-1</sup>) is the Boltzmann constant,  $T$  (K) is the absolute temperature and  $T_0$  (K) is a parameter describing the deviation from Arrhenius behavior. Fits according to Equation (1) are included in Figure 2; the corresponding values for  $\sigma_{inf}$ ,  $E_a$ , and  $T_0$  are presented in Table 1. The  $E_a$  values generally follow the conductivity trend, excluding the stark increase when moving from NaFSI/DME = 0.5 to 0.6. Interestingly, this increase coincides with the fact that above NaFSI/DME = 0.5, less than four oxygen atoms are available for solvating each Na-ion. In conclusion, we chose the NaFSI/DME = 0.5 electrolyte for further experiments because it represents the best compromise between low activation energy, high conductivity, and high plating efficiency.

Clearly, the superior plating behavior of the NaFSI/DME = 0.5 electrolyte cannot be attributed to higher conductivity or lower activation energies; instead we ascribe it to the SEI development. Scanning electron micrographs of the SEI at the Cu electrode are shown in Figure 3. Some differences are visible to the bare eye; the NaFSI/DME = 0.5 electrolyte results in a smooth surface, whereas the carbonate electrolyte forms a millimeter-thick, rough, and cracked layer. The scanning electron microscopy (SEM) images of this layer reveal dendrites up to 100  $\mu$ m in diameter protruding from a highly uneven surface. Individual particles cannot be discerned as they are covered by a thick sheet of decomposition products. In NaFSI/DME = 0.5, Na is deposited more evenly and uniformly with

a surface roughness in the micrometer range. This agrees with the plating and stripping polarizations in Figure 1a. The average polarization attains a stable value of 10 and 20 mV for NaFSI/DME = 0.5. For the carbonate electrolyte, polarization fluctuates and increases during plating, reflecting the instable SEI on Na. Increasing polarization and impedance for the carbonate electrolyte were also observed in Na/Na symmetric cells, Figure S2. In contrast, symmetric cells with NaFSI/DME = 0.5 shows stable impedance and slightly decreasing polarization.

These results are consistent with previous findings questioning the stability of the SEI on Na electrodes

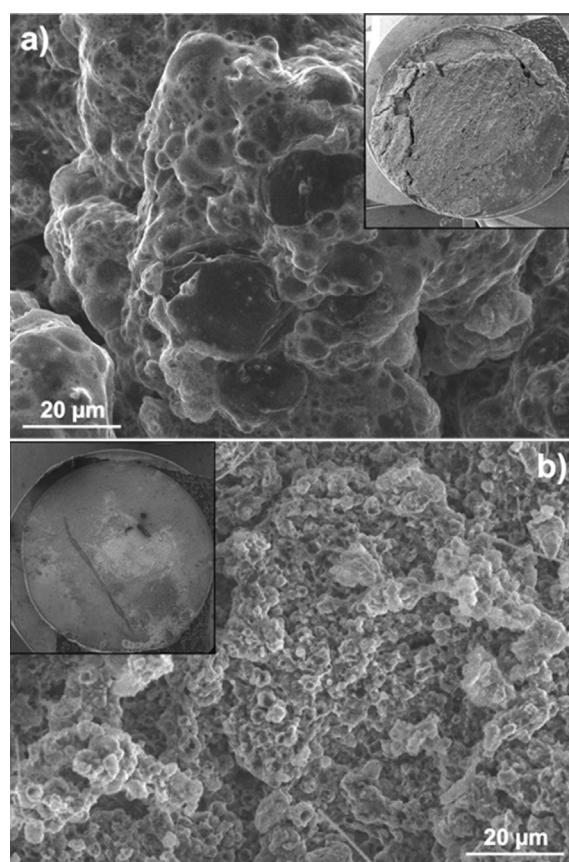


**Figure 3.** SEM images of Cu electrodes after one week of plating/stripping at 0.2 mA cm<sup>-2</sup> in (a) carbonate and (b) etheral electrolyte. Electrodes were harvested at the end of plating. Insets: Low magnification images of the respective electrodes.

in carbonate electrolytes, leading to poor electrochemical performance and high and growing impedance.<sup>[8]</sup> Importantly, the poor stability of Na in the carbonate electrolyte could compromise results obtained from half-cell configurations, especially with respect to coulombic efficiency and cyclability. In contrast, the highly concentrated etheral electrolyte efficiently passivates Na electrodes. The NaFSI/DME = 0.5 electrolyte could, therefore, enable more reliable Na-ion half-cells, provided it is compatible with intercalation electrode materials.

### Electrolyte compatibility with hard carbon and sodium vanadium phosphate

The NaFSI/DME=0.5 electrolyte is compatible with Na intercalation electrodes and allows to reliably evaluate them in half-cells (Figure 4).

As the anode material, we have chosen a high surface area HC (around  $600 \text{ m}^2 \text{ g}^{-1}$ ) that puts the passivation behavior at low potentials to a tough test. Results are presented in Figure 4a–c. The first cycles in the carbonate electrolyte show a nearly featureless curved reduction trace (Figures S3 and 4a,c). In comparison, NaFSI/DME=0.5 displays a series of

pseudo-plateaus and slightly higher initial efficiencies. This is consistent with smaller cathodic currents at glassy carbon electrodes in this potential range (Figure S4). In the following cycles, the voltage profiles for both electrolytes become quite featureless and flatten towards the lower cut-off voltage, but a true low voltage plateau is not observed. It should be noted that this particular voltage profile is not caused by the electrolyte but by the HC material, as both electrolytes do show the typical low voltage plateau and higher capacities with low surface area HC (Figure S5).

Let us now turn back to the high surface area HC. In NaFSI/DME=0.5, the capacity fades slightly more until a stable ca-

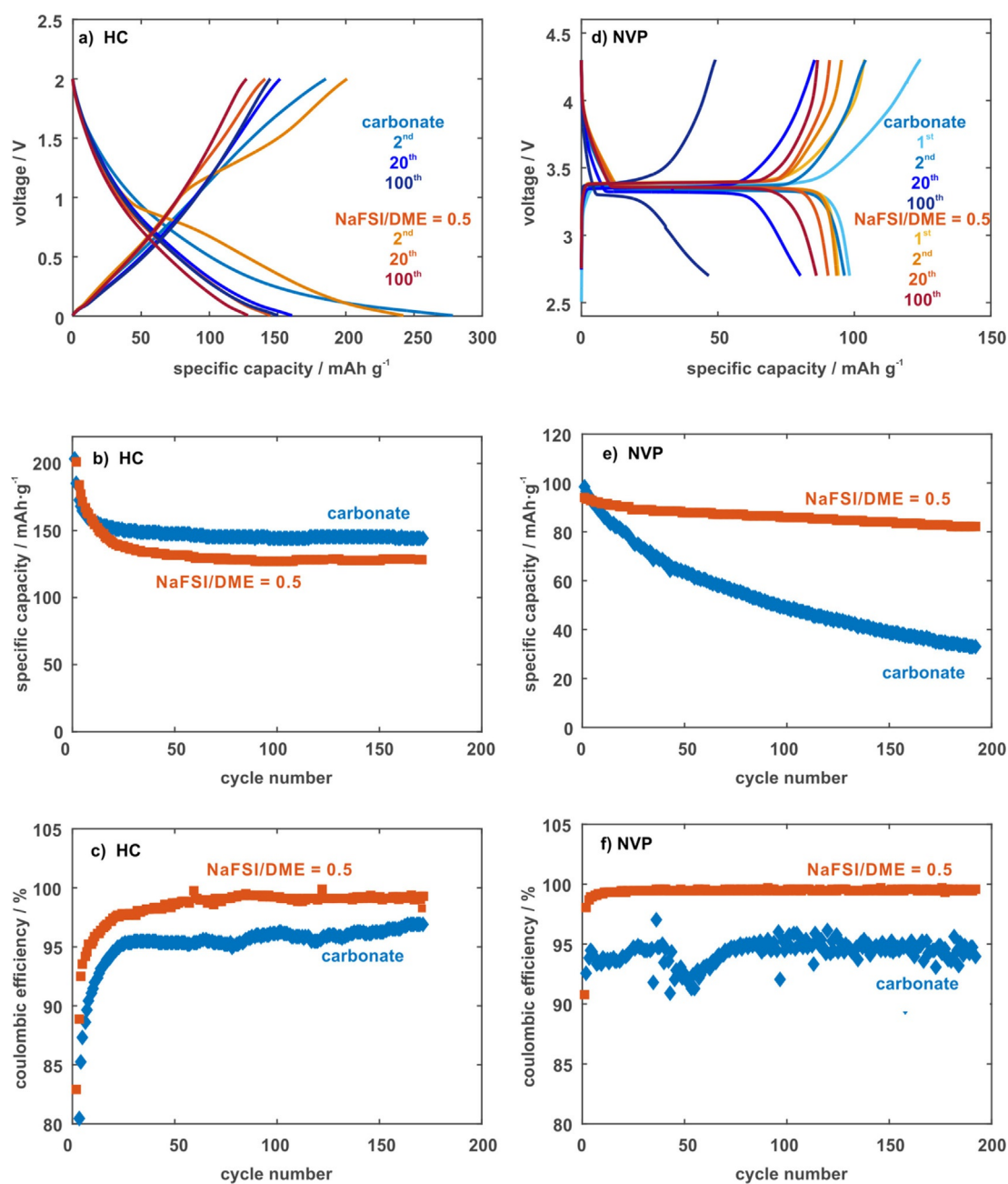


**Figure 4.** Galvanostatic cycling of half-cells with (a–c) HC anodes and (d–f) NVP cathodes at  $0.02 \text{ mA cm}^{-2}$  (roughly C/6). (a, d) Potential profiles of selected cycles, (b, e) specific capacities, and (c, f) coulombic efficiencies of carbonate and NaFSI/DME=0.5 electrolytes.



capacity is achieved after 20 cycles (Figure 4b). This capacity fade concurs with rising efficiencies as the SEI is formed. Excessive SEI formation, however, cannot explain the initial capacity fade, because the irreversible capacity is significantly lower in NaFSI/DME=0.5. Still, the SEI in NaFSI/DME=0.5 could be more resistive owing to its different composition. A higher resistance would, in turn, somewhat restrict accessing the full capacity of HC and, therefore, lower the capacity.<sup>[4c,e]</sup> Once the capacity stabilizes, efficiencies approach 95% for the carbonate electrolyte and 99% for NaFSI/DME=0.5. Overall, NaFSI/DME=0.5 exhibits a slightly stronger initial capacity fade than the carbonate electrolyte specifically tailored for this setup, but easily surpasses the carbonate electrolyte in terms of efficiency and long term cyclability.

Turning to NVP cathodes, they operate at a flat potential plateau of 3.4 V, limiting SEI formation to the Na-metal counter electrode. As NaFSI/DME=0.5 stabilizes Na metal efficiently, we expected it to stand out even more in this configuration. In fact, the NaFSI/DME=0.5 retains 91% of its initial capacity over the first 100 cycles, whereas in the carbonate electrolyte it is reduced to 47% of its initial capacity (Figure 4e). This severe capacity fade could be explained in two ways. First, electrolyte could be oxidized at the upper cutoff potential of 4.2 V, although fast oxidation only starts beyond 4.5 V on an inert electrode (Figure S4). To test this we lowered the upper cutoff to 3.9 V to minimize electrolyte oxidation. With the carbonate electrolyte the capacity fade is only slightly reduced (Figure S7) meaning that electrolyte oxidation cannot be the main reason for fading. Second, the electrolyte could be decomposed at the Na counter electrode; soluble products of these reactions could then cross to the cathode and deteriorate its performance. This crosstalk is spurred by the high solubility of sodium SEI components, such as Na<sub>2</sub>CO<sub>3</sub> and HCOONa,<sup>[8]</sup> and has been observed for carbonate-based electrolytes.<sup>[13,17]</sup> Indeed, we could nearly suppress capacity fade by replacing the Na counter electrode with a partially desodiated NVP electrode (Figure S7). This excludes electrolyte decomposition in the way it takes place on Na metal, including dissolution of decomposition products into the electrolyte. From the marked difference between Na/NVP and NVP/NVP cells in carbonate electrolyte, but nearly identical performance in the ether electrolyte, we infer that compounds formed at the Na metal in the carbonate electrolyte cause capacity fade at the NVP cathode owing to cross talk. Ethers show irrespective of Na or NVP counter electrode efficiencies of 99.5% after the first few cycles.

Clearly, the electrolyte dramatically influences the half-cell performance even if SEI formation does not occur on the working electrode. The influence is not limited to coulombic efficiencies, but also encompasses capacity fading. In developing novel electrode materials, the capacity fading might be mistakenly attributed to poor electrode performance when in fact an incompatible electrolyte is to blame. This further underlines that choosing a suitable electrolyte is crucial for developing new materials.

### The solid electrolyte interface on sodium metal and hard carbon

To further elucidate the contrasting performances of carbonate and NaFSI/DME=0.5 electrolytes with Na metal, HC, and NVP electrodes, we scrutinized the SEI formed therein. After cycling, the working electrodes were extracted from the half-cell and analyzed by FTIR, <sup>1</sup>H NMR, SEM, and energy dispersive X-ray spectroscopy (EDX). The results differ fundamentally for both electrolytes.

The SEI formed by the carbonate electrolyte contains a large fraction of semicarbonates, as suggested by the characteristic IR bands at 1645, 1300, and 820 cm<sup>-1</sup> (Figure 5a).<sup>[8]</sup> It is, however, difficult to unambiguously assign the IR spectra to specific Na organic compounds. To get direct evidence of the specific compounds, the anodes were washed with D<sub>2</sub>O, and the resulting solution was subjected to <sup>1</sup>H NMR spectroscopy. The spectra are shown in Figure 5c–d and are consistent with the presence of propylene glycol, ethylene glycol, and traces of formic acid and acetic acid, as well as residual EC and PC. The glycols are the expected products from the reaction of the Na ethyl and propyl dicarbonate and water according to the reaction R(OCO<sub>2</sub>Na)<sub>2</sub> + D<sub>2</sub>O → R(OD)<sub>2</sub> + Na<sub>2</sub>CO<sub>3</sub> + CO<sub>2</sub>. Analogously, formate and acetate arise from the reaction of Na formate and Na acetate with D<sub>2</sub>O. The <sup>1</sup>H NMR signals corresponding to the diols are the strongest observed in this study, reflecting the large amount of semicarbonates in the SEI formed from the carbonates (Figure 3). The traces of Na formate and acetate show signals at 8.45 and 1.9 ppm, respectively.<sup>[18]</sup> The singlet at 3.71 ppm could correspond to oligo- or polyether species, reflected by the broad FTIR band at 1100–1000 cm<sup>-1</sup>. These results suggest an SEI that is similar, at least qualitatively, to that on Li-ion negative electrodes, which is in accord with previous studies.<sup>[8]</sup>

The SEI in NaFSI/DME=0.5 differs for Na and HC surfaces; however, similarities can be discerned upon close investigation. The NaFSI salt clearly participates in SEI formation, as evidenced by three individual cues. First, several weak FTIR bands corresponding to NaFSI are present on both surfaces (Figure 5b, dashed lines; Table 2). Second, EDX analyses confirm a S content of 5 mol% and a fluorine content of 8 mol% that can only originate from the salt. Third, while the strong vibration at 985 cm<sup>-1</sup> cannot be linked directly to NaFSI, it has been observed in an EC/DMC/LiFSI electrolyte, but not in an EC/DMC/LiPF<sub>6</sub> mixture.<sup>[19]</sup> In fact, decomposition products originating from NaFSI can explain all major FTIR bands on HC. In contrast, the FTIR spectrum on Na also proves the presence of organic ethers, as shown by CH<sub>2</sub> stretching vibrations at 1490–1400 cm<sup>-1</sup> and C–O stretching vibrations at 1160 and 1040 cm<sup>-1</sup>.<sup>[20]</sup>

The <sup>1</sup>H NMR spectra somewhat contrast this tendency as HC yields higher concentrations of soluble organic components (Figure 5d). This discrepancy could be explained by the large surface area of HC, allowing a high absolute concentration of organic components, while their relative amount, as detected by FTIR, is low. A variety of organic ether moieties is found in the 3.95–3.65 ppm range. Additionally, formate and acetate

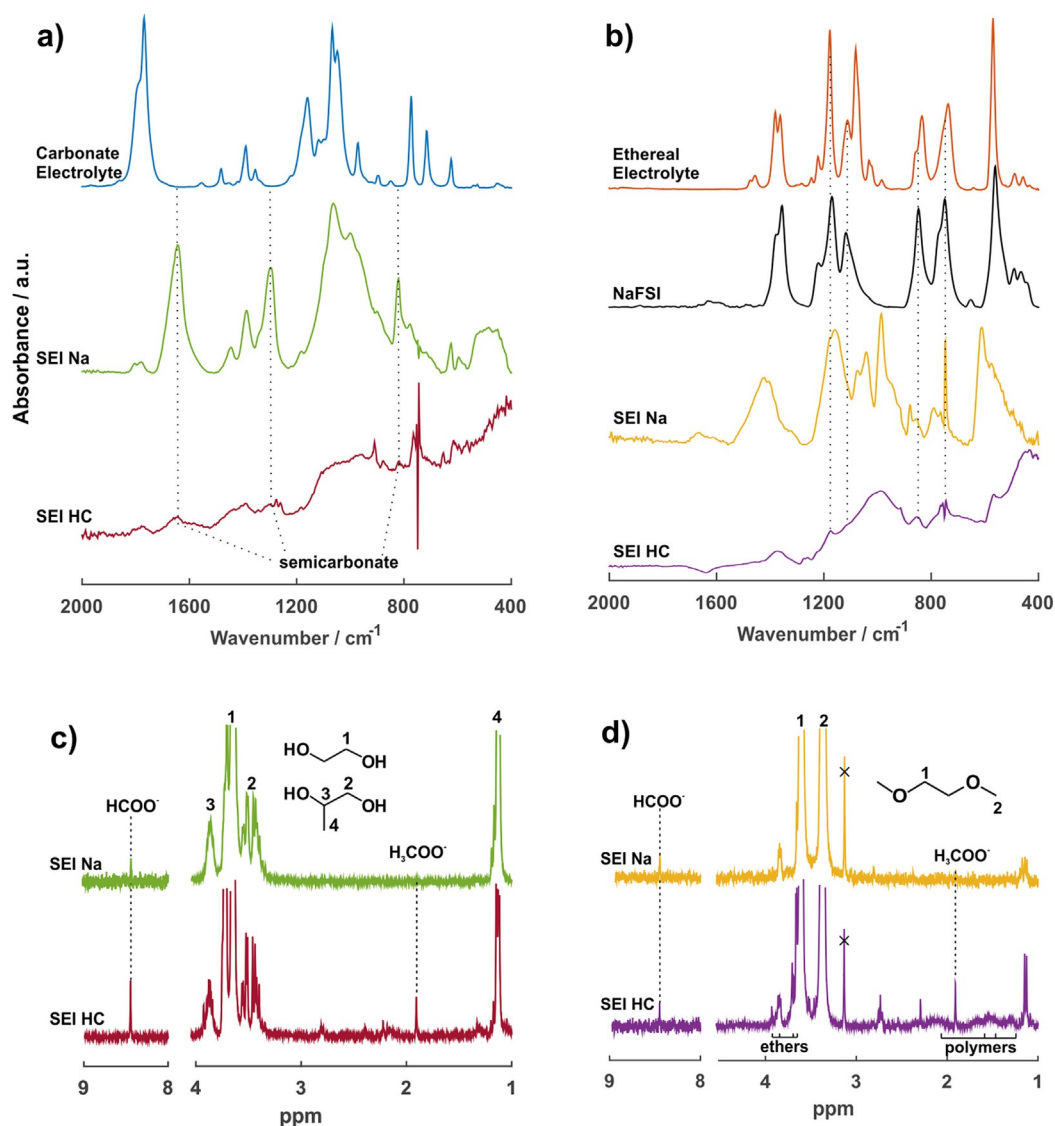


Figure 5. SEI analyses. (a–b) FTIR and (c–d) <sup>1</sup>H NMR spectra of the SEI formed on Na and HC in (a,c) carbonate and (b,d) NaFSI/DME = 0.5 electrolytes.

**Table 2.** Assignment of IR signals in the SEI formed by NaFSI/DME = 0.5 on Na and HC (Figure 5 b).

Signal [cm <sup>-1</sup> ]	Intensity <sup>[a]</sup>	Electrode	Functionality	Origin
1665	w	Na	C=O stretch	formate <sup>[12]</sup>
1424	s	Na	CH <sub>2</sub> bending	ether <sup>[13]</sup>
1361, 1372	w	Na, HC	SO <sub>2</sub> N stretch	NaFSI <sup>[12]</sup>
1177, 1175	m–s	Na, HC	S=O symm. stretch	NaFSI
1159	s	Na	C–O stretch	ethers <sup>[12]</sup>
1042	s	Na	C–O stretch	ethers <sup>[13]</sup>
985, 987	s	Na, HC	–	NaFSI <sup>[14]</sup>
853, 853	w	Na, HC	–	NaFSI
765, 765	w	Na, HC	–	formate <sup>[12]</sup>
747, 745	s, w	Na, HC	–	NaFSI

[a] w = weak, s = strong, m = medium.

were detected on both electrodes. On HC, four broad signals between 2.4 and 1.2 ppm are present. Signal broadening could be caused by hydrogen bonding at amine and alcohol func-

tionality. In D<sub>2</sub>O, however, such functionalities would exchange protons with the solvent. This would lead to a downfield shift towards the solvent residual peak at 4.79 ppm, which is not the case here. More likely, the broad signals indicate a polymeric, water-soluble species. With the largest signals at 2.2 and 1.5 ppm, the species could be poly(Na acrylate) or a similar polymer. Unfortunately, the FTIR spectra are ambiguous regarding this, thus further analyses are required to elucidate the structure of this polymer. To summarize, the SEI formed by NaFSI/DME = 0.5 comprises polymeric species, organic ethers and degradation products of the NaFSI salt. It is this SEI that enables highly reversible Na cycling and more reliable Na-ion half-cells.

## Conclusions

In conclusion, we report a liquid electrolyte, NaFSI in monoglyme at a mole ratio of 0.5, that permits reversible plating and stripping of Na metal with a coulombic efficiency reaching 97.7%. The high reversibility was found to arise from a combination of high cathodic stability of the electrolyte in combination with the formation of a thin and stable SEI that supports non-dendritic plating. The high reversibility may both enable Na metal batteries as well as more reliable assessment of Na storage materials in half-cells with Na metal as the counter electrode. We exemplify this by comparing the cyclability of SIB intercalation anode and cathode materials, hard carbon and sodium vanadium phosphate, in a carbonate electrolyte and the ethereal electrolyte. Apparent cyclability of these materials is found to be strongly aggravated by the influence of the Na metal electrode in an unsuitable electrolyte. Crosstalk between the electrodes is shown to arise from the solubility of typical carbonate borne Na-SEI compounds.

## Experimental Section

### Materials

NaClO<sub>4</sub> (Sigma–Aldrich) and NaFSI (Solvionic) salts were dissolved in EC (TCl), PC (Sigma–Aldrich), and DME (Sigma–Aldrich). All solvents had been dried over freshly activated molecular sieves resulting in a water content < 10 ppm, as determined by Karl–Fischer titration.

High surface HC electrodes were prepared by ball-milling a slurry of 80% HC, 10% Na carboxymethyl cellulose (NaCMC, Wolff Cellulosics), and 10% Super C65 carbon additive (Timcal) in Millipore water with three balls at 400 rpm for 45 min with a change of rotation direction every 15 min. The slurries were then cast on Cu foil with a 100 μm doctor blade, punched, and dried at 120 °C under vacuum. The average HC loading was around 0.8 mg cm<sup>-2</sup>. Low surface area HC was prepared according to a literature procedure<sup>[14e,21]</sup>. A slurry consisting of 80% HC, 10% polyvinylidene difluoride (PVdF, Arkema), and 10% Super P carbon additive (Timcal) in *N*-methylpyrrolidone (NMP, abcr) was stirred overnight, sonicated, and cast on an Al foil with a 150 μm doctor blade. The electrodes were then punched and dried at 120 °C under vacuum. The average HC loading was around 3 mg cm<sup>-2</sup>.

NVP electrodes were composed of 65% NVP, 10% PVdF, and 27% Super P in NMP. The mixture was homogenized in a ball mill at 400 rpm for 2 h with a change of rotation direction every 30 min, cast on Al foil with a wet thickness of 100 μm, punched, and dried at 120 °C under vacuum. The average NVP loading was 1.3 mg cm<sup>-2</sup>. All manipulations involving moisture sensitive or hygroscopic materials were performed in an Ar-filled glove box.

### Electrochemical Measurements

Galvanostatic cycling was performed on a MPG-2 potentiostat/galvanostat (BioLogic) in three-electrode Swagelok-type cells using a Whatman GF/F separator and Na metal (Sigma–Aldrich) as counter and reference electrode. Therefore, all reported potentials refer to the Na/Na<sup>+</sup> redox couple. Electrochemical impedance spectroscopy (EIS) for liquid electrolytes was measured using an in-house built impedance cell designed to allow measurements of samples down to 10<sup>-10</sup> S cm<sup>-1</sup>. The cell is placed in an in-house built tem-

perature control unit with temperature measurement at the sample position. Spectra for liquid electrolytes and Na/Na symmetric cells were recorded in a frequency range of 7 MHz to 100 MHz and an amplitude of 30 mV using a SP-300 (BioLogic) impedance analyzer that also controlled the temperature controller.

### Spectroscopic Characterization

After galvanostatic cycling, the cells were disassembled under N<sub>2</sub> atmosphere. Electrodes and separator were washed with CDCl<sub>3</sub> and dried at room temperature to remove remaining electrolyte. <sup>1</sup>H NMR spectra of the washing solutions were recorded to verify that no analyte was washed away. The electrode surface was then analyzed using an Alpha-P Fourier FTIR spectrometer (Bruker) with attenuated total reflection (ATR) unit inside an N<sub>2</sub>-filled glove box. Under ambient atmosphere, the electrodes and separators were washed with D<sub>2</sub>O. However, for the ethereal electrolyte, the analyte concentrations were so low that both samples had to be combined for an appreciable signal. Therefore, ethereal NMR spectra also contain remaining electrolyte from the separator. NMR spectra were collected on an Avance III 300 spectrometer (Bruker). SEM images and EDX spectra were taken on a VEGA II (Tescan) with an INCA x-act (Oxford instruments) EDX detector and an electron energy of 10 keV.

## Acknowledgements

The authors are indebted the Austrian Federal Ministry of Economy, Family and Youth, and the Austrian National Foundation for Research, Technology and Development, under the research program Research Studios Austria.

**Keywords:** battery · hard carbon · intercalation compounds · sodium · solid electrolyte interface

- [1] a) D. Kundu, E. Talaie, V. Duffort, L. F. Nazar, *Angew. Chem. Int. Ed.* **2015**, *54*, 3431–3448; *Angew. Chem.* **2015**, *127*, 3495–3513; b) N. Yabuuchi, K. Kubota, M. Dahbi, S. Komaba, *Chem. Rev.* **2014**, *114*, 11636–11682; c) P. Senguttuvan, G. Rousse, M. E. A. y. de Dompablo, H. Vezin, J. M. Tarascon, M. R. Palacin, *J. Am. Chem. Soc.* **2013**, *135*, 3897–3903; d) D. Wu, X. Li, B. Xu, N. Twu, L. Liu, G. Ceder, *Energy Environ. Sci.* **2015**, *8*, 195–202; e) R. J. Clément, P. G. Bruce, C. P. Grey, *J. Electrochem. Soc.* **2015**, *162*, A2589–A2604; f) P. Hartmann, C. L. Bender, M. Vračar, A. K. Dürr, A. Garsuch, J. Janek, P. Adelhelm, *Nat. Mater.* **2012**, *12*, 228–232; g) L. Otaegui, E. Goikolea, F. Aguesse, M. Armand, T. Rojo, G. Singh, *J. Power Sources* **2015**, *297*, 168–173.
- [2] U. S. G. Survey, U.S. Geological Survey, **2016**.
- [3] a) B. Dunn, H. Kamath, J.-M. Tarascon, *Science* **2011**, *334*, 928–935; b) V. Palomares, P. Serras, I. Villaluenga, K. B. Hueso, J. Carretero-Gonzalez, T. Rojo, *Energy Environ. Sci.* **2012**, *5*, 5884–5901; c) M. D. Slater, D. Kim, E. Lee, C. S. Johnson, *Adv. Funct. Mater.* **2013**, *23*, 947–958.
- [4] a) A. Ponrouch, E. Marchante, M. Courty, J. M. Tarascon, M. R. Palacin, *Energy Environ. Sci.* **2012**, *5*, 8572–8583; b) A. Ponrouch, R. Dedryvere, D. Monti, A. E. Demet, J. M. A. Mba, L. Croguennec, C. Masquelier, P. Johansson, M. R. Palacin, *Energy Environ. Sci.* **2013**, *6*, 2361–2369; c) A. Ponrouch, D. Monti, A. Boschini, B. Steen, P. Johansson, M. R. Palacin, *J. Mater. Chem. A* **2015**, *3*, 22–42; d) M. Sawicki, L. L. Shaw, *RSC Adv.* **2015**, *5*, 53129–53154; e) A. Ponrouch, M. R. Palacin, *Electrochem. Commun.* **2015**, *54*, 51–54.
- [5] a) K. Matsumoto, T. Hosokawa, T. Nohira, R. Hagiwara, A. Fukunaga, K. Numata, E. Itani, S. Sakai, K. Nitta, S. Inazawa, *J. Power Sources* **2014**, *265*, 36–39; b) C. S. Ding, T. Nohira, K. Kuroda, R. Hagiwara, A. Fukunaga, S. Sakai, K. Nitta, S. Inazawa, *J. Power Sources* **2013**, *238*, 296–300.

- [6] a) M. Dahbi, N. Yabuuchi, K. Kubota, K. Tokiwa, S. Komaba, *Phys. Chem. Chem. Phys.* **2014**, *16*, 15007–15028; b) D. A. Stevens, J. R. Dahn, *J. Electrochem. Soc.* **2000**, *147*, 1271–1273; c) P. Senguttuvan, G. Rousse, V. Seznec, J. M. Tarascon, M. R. Palacin, *Chem. Mater.* **2011**, *23*, 4109–4111; d) S. Komaba, W. Murata, T. Ishikawa, N. Yabuuchi, T. Ozeki, T. Nakayama, A. Ogata, K. Gotoh, K. Fujiwara, *Adv. Funct. Mater.* **2011**, *21*, 3859–3867; e) S. T. Myung, N. Takahashi, S. Komaba, C. S. Yoon, Y. K. Sun, K. Amine, H. Yashiro, *Adv. Funct. Mater.* **2011**, *21*, 3231–3241; f) J. W. Wang, X. H. Liu, S. X. Mao, J. Y. Huang, *Nano Lett.* **2012**, *12*, 5897–5902; g) Y. Kim, Y. Park, A. Choi, N. S. Choi, J. Kim, J. Lee, J. H. Ryu, S. M. Oh, K. T. Lee, *Adv. Mater.* **2013**, *25*, 3045–3049.
- [7] a) K. Kubota, N. Yabuuchi, H. Yoshida, M. Dahbi, S. Komaba, *MRS Bull.* **2014**, *39*, 416–422; b) P. Adelhelm, P. Hartmann, C. L. Bender, M. Busche, C. Eufinger, J. Janek, *Beilstein J. Nanotechnol.* **2015**, *6*, 1016–1055; c) S. Xin, Y. X. Yin, Y. G. Guo, L. J. Wan, *Adv. Mater.* **2014**, *26*, 1261–1265; d) X. W. Yu, A. Manthiram, *J. Phys. Chem. Lett.* **2014**, *5*, 1943–1947.
- [8] D. I. Iermakova, R. Dugas, M. R. Palacin, A. Ponrouch, *J. Electrochem. Soc.* **2015**, *162*, A7060–A7066.
- [9] C. Bommier, D. Leonard, Z. Jian, W. F. Stickle, P. A. Greaney, X. Ji, *Adv. Mater. Interfaces* **2016**, *3*, 1600449.
- [10] S. Komaba, T. Ishikawa, N. Yabuuchi, W. Murata, A. Ito, Y. Ohsawa, *ACS Appl. Mater. Interfaces* **2011**, *3*, 4165–4168.
- [11] a) J. F. Qian, X. Y. Wu, Y. L. Cao, X. P. Ai, H. X. Yang, *Angew. Chem. Int. Ed.* **2013**, *52*, 4633–4636; *Angew. Chem.* **2013**, *125*, 4731–4734; b) A. Darwiche, C. Marino, M. T. Sougrati, B. Fraise, L. Stievano, L. Monconduit, *J. Am. Chem. Soc.* **2012**, *134*, 20805–20811; c) Y. X. Wang, Y. G. Lim, M. S. Park, S. L. Chou, J. H. Kim, H. K. Liu, S. X. Dou, Y. J. Kim, *J. Mater. Chem. A* **2014**, *2*, 529–534.
- [12] A. Ponrouch, A. R. Goni, M. R. Palacin, *Electrochem. Commun.* **2013**, *27*, 85–88.
- [13] Y. Lee, J. Lee, H. Kim, K. Kang, N. S. Choi, *J. Power Sources* **2016**, *320*, 49–58.
- [14] R. Dugas, A. Ponrouch, G. Gachot, R. David, M. R. Palacin, J. M. Tarascon, *J. Electrochem. Soc.* **2016**, *163*, A2333–A2339.
- [15] a) Y. Yamada, K. Furukawa, K. Sodeyama, K. Kikuchi, M. Yaegashi, Y. Tateyama, A. Yamada, *J. Am. Chem. Soc.* **2014**, *136*, 5039–5046; b) R. Petibon, C. P. Aiken, L. Ma, D. Xiong, J. R. Dahn, *Electrochim. Acta* **2015**, *154*, 287–293; c) A. Orita, K. Kamijima, M. Yoshida, K. Dokko, M. Watanabe, *J. Power Sources* **2011**, *196*, 3874–3880; d) K. Yoshida, M. Nakamura, Y. Kazue, N. Tachikawa, S. Tsuzuki, S. Seki, K. Dokko, M. Watanabe, *J. Am. Chem. Soc.* **2011**, *133*, 13121–13129; e) L. M. Suo, Y. S. Hu, H. Li, M. Armand, L. Q. Chen, *Nat. Commun.* **2013**, *4*, 1481; f) J. F. Qian, W. A. Henderson, W. Xu, P. Bhattacharya, M. Engelhard, O. Borodin, J. G. Zhang, *Nat. Commun.* **2015**, *6*, 6362.
- [16] I. A. Shkrob, T. W. Marin, Y. Zhu, D. P. Abraham, *J. Phys. Chem. C* **2014**, *118*, 19661–19671.
- [17] T. D. Hatchard, M. N. Obrovac, *J. Electrochem. Soc.* **2014**, *161*, A1748–A1752.
- [18] S. A. Freunberger, Y. H. Chen, Z. Q. Peng, J. M. Griffin, L. J. Hardwick, F. Barde, P. Novak, P. G. Bruce, *J. Am. Chem. Soc.* **2011**, *133*, 8040–8047.
- [19] G. G. Eshetu, S. Grugeon, G. Gachot, D. Mathiron, M. Armand, S. Laruelle, *Electrochim. Acta* **2013**, *102*, 133–141.
- [20] a) D. Aurbach, Y. Gofer, *J. Electrochem. Soc.* **1991**, *138*, 3529–3536; b) D. Aurbach, Y. Gofer, J. Langzam, *J. Electrochem. Soc.* **1989**, *136*, 3198–3205.
- [21] W. Xing, J. S. Xue, J. R. Dahn, *J. Electrochem. Soc.* **1996**, *143*, 3046–3052.

Manuscript received: September 2, 2016

Revised: November 2, 2016

Accepted Article published: November 18, 2016

Final Article published: December 20, 2016

### 3.3 Optimizing concentration and cycling conditions

The central plating experiment in the previous contribution shows excellent efficiencies when Na is plated/stripped at  $0.2 \text{ mA cm}^{-2}$  to a capacity of  $0.5 \text{ mAh cm}^{-2}$  in a NaFSI/DME molar ratio of 0.5. These parameters are not coincidence, but the result of prior optimization steps that are not presented in the paper but shall be discussed here in more detail.

A report by Qian *et al.* provided the necessary starting point;<sup>139</sup> Li was plated onto a Cu foil at rates ranging from  $0.2$  to  $10 \text{ mA cm}^{-2}$  to a capacity of  $1 \text{ mAh cm}^{-2}$ . The electrolyte consisted of DME and  $4 \text{ M LiFSI}$ , which corresponds to a molar ratio of LiFSI/DME of 0.6. Generally, the solvent/salt ratio is critical in highly concentrated electrolyte. If it is too low, dendrite formation and premature cell death occur. If it is too high, conductivity and rate performance suffer. Therefore I prioritized the optimization of the solvent/salt ratio over the other two parameters\*.

#### 3.3.1 Solvent to salt ratio

Cyclic voltammetry results of various solvent/salt molar ratios are presented in Figure 3.2. The lowest salt/solvent ratio of 0.1 can be compared to state-of-the-art Li- or Na-ion electrolytes, while the highest ratio of 0.7 equals the concentration used by Qian *et al.* Finally, the ratio of 0.5 represents a compromise between these two extremes. Generally, the currents decrease upon increasing salt concentration, reflecting the fact that conductivity decreases due to ion pair formation and growing viscosity. However, the electrolyte with a ratio of 0.1 fails after only 6 cycles when the current starts to fluctuate and increases dramatically, most likely because of dendrite formation. In contrast, the electrolytes containing a NaFSI/DME ratio of 0.5 and 0.6 both sustain 20 cycles, although the peak shape changes during cycling. The reductive current increases, indicating a small change in surface area, while the overpotential during Na dissolution diminishes. The fluctuating current response in the last cycle reveals that the cells are starting to fail. Overall, a salt/solvent ratio of 0.5 seemed to ensure reversible cycling at decent currents.

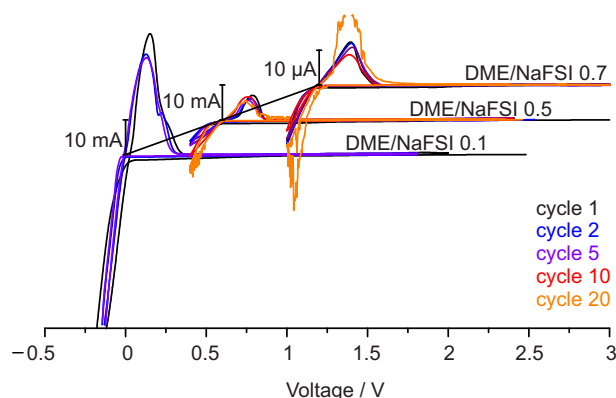


**Figure 3.2:** Cyclic voltammograms of Na plating at varying salt/solvent molar ratios with a rate of  $50 \text{ mV s}^{-1}$  to a negative cutoff limit of  $-0.2 \text{ V}$ . The substrate was a Cu foil with an area of  $0.785 \text{ cm}^2$ .

\*The solvent/salt ratio was finetuned once more in the contribution, once an approximate concentration and suitable cycling parameters had been found. The experiments presented here were conducted before that.



### 3.3.2 Cycling conditions

With the NaFSI/DME ratio fixed at 0.5, I proceeded to optimize current density and capacity in a series of galvanostatic experiments. Na was plated galvanostatically onto a Cu foil and subsequently stripped until the potential reached 1 V; current density and plating time, and thus capacity, were varied. To complicate matters, both parameters interdepend. While a current density of  $1 \text{ mA cm}^{-2}$  led to quick cell death even at low capacities, a current density of  $0.5 \text{ mA cm}^{-2}$  allowed capacities up to  $0.5 \text{ mAh cm}^{-2}$ , Figure 3.3a. The CE gradually increases with increasing capacity. At  $0.05 \text{ mAh cm}^{-2}$  the CE is only 84%, while it reaches 96% at  $0.5 \text{ mAh}$ . Clearly, losses to parasitic reactions are minimized in relative means and dendrites do not seem to form even at comparably high capacities.

Subsequently, the current density was varied at a constant capacity of  $0.5 \text{ mAh cm}^{-2}$ , Figure 3.3b. Increasing current densities slightly deteriorate CE, but more importantly they render the experiment less reproducible. While some cells sustained current densities of  $1 \text{ mA cm}^{-2}$ , others failed after a few cycles at  $0.5 \text{ mA cm}^{-2}$ . To ensure reproducibility, the current density was limited to  $0.2 \text{ mA cm}^{-2}$  for the following long term experiments.

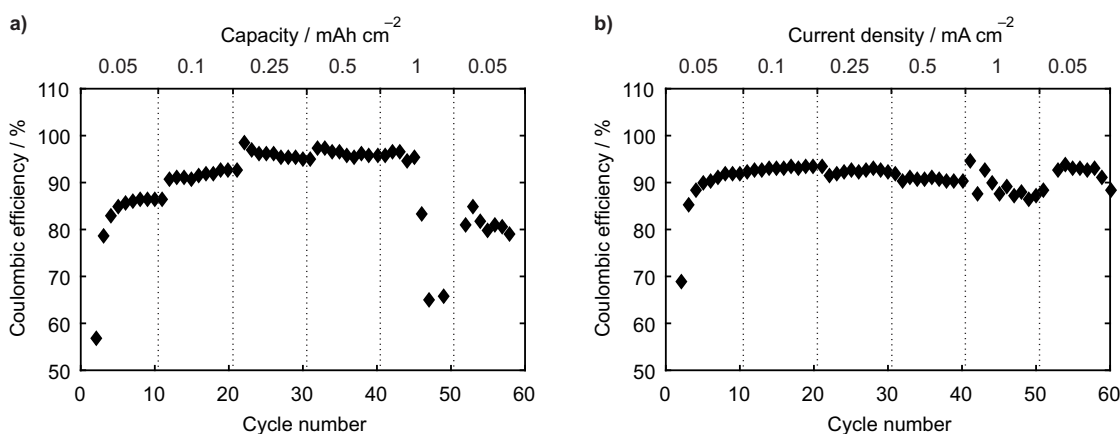


**Figure 3.3:** Optimization of capacity (a) at a constant current density of  $0.5 \text{ mA cm}^{-2}$  and current density (b) at a constant capacity of  $0.5 \text{ mAh cm}^{-2}$ . Na was plated galvanostatically onto a Cu foil and stripped until the potential reached  $1.0 \text{ V vs Na/Na}^+$ . The electrolyte was NaFSI/DME 0.5 (n/n).

## 4. Quantifying superoxide, peroxide and carbonaceous compounds

The SEI has been scrutinized with at least a dozen complimentary analysis methods, with the most prominent ones being Fourier transform infrared spectroscopy (FTIR) and X-ray-photoelectron spectroscopy (XPS). However, most of these methods allow only for semiquantitative analysis of very limited areas, whereas precise quantification over the entire electrode would be required to better assess the impact of parasitic reactions.

In this contribution we refine our previous analysis method<sup>165</sup> that separately determines the total amount of carbonates and organic carbon on the electrode. Additionally, the method covers the amount of alkaline peroxide or superoxides, the main discharge products in metal-O<sub>2</sub> batteries. This enables a facile and time-efficient analysis of the SEI in Li- and Na-ion batteries, as well as simultaneous analysis of main- and side products in Li-O<sub>2</sub> and Na-O<sub>2</sub> batteries (see Section 5.2), while pitfalls of previous methods are avoided.

### **Quantifying Total Superoxide, Peroxide and Carbonaceous Compounds in Metal-O<sub>2</sub> Batteries and the Solid Electrolyte Interface**

Bettina Schafzahl, Eléonore Mourad, Lukas Schafzahl, Yann K. Petit, Anjana R. Raju, Musthafa Ottakam Thotiyl, Martin Wilkening, Christian Slugovc, and Stefan A. Freunberger

*ACS Energy Lett.* 2018, 3, 170-176. Reprinted with permission, copyright 2017 American Chemical Society.

## 4.1 Side product and interphase analysis

The importance of understanding the SEI, as well as the difficulty in doing so, has been repeatedly stressed in the previous sections. This section will describe selected analysis methods, their capabilities and limitations.

It should be noted that dozens of methods have been used in interphase analysis including, but not limited to, acoustic emission (AE),<sup>166,167</sup> auger electron microscopy (AES),<sup>168,169</sup> AFM,<sup>114,128,129,170,171</sup> time of flight-secondary ion mass spectrometry (TOF-SIMS),<sup>172,173</sup> SEM,<sup>168,174</sup> transmission electron microscopy (TEM),<sup>175–177</sup> Raman spectroscopy,<sup>178–180</sup> X-ray absorption near edge structure (XANES),<sup>181</sup> EIS,<sup>116,124,176,182–185</sup> and NMR.<sup>103,176</sup> All of these methods have provided invaluable information; yet a discussion of them is beyond the scope of this work and I would like to kindly refer the interested reader to some excellent reviews on this topic.<sup>82,91,186</sup> Here, the focus will be on two of the most common methods: XPS and FTIR.

### 4.1.1 X-ray photoelectron spectroscopy

In XPS, X-rays with energies of 1.2-1.5 keV are directed at the sample and remove core electrons that are emitted as photoelectrons. The kinetic energies of these photoelectrons can be detected and depend on the orbitals the electrons were emitted from. This can be used to differentiate chemical environments such as C–C, C–N, C–O and C=O bonds and therefore reveals characteristic functional groups. XPS allows for analysis of all elements except H and He as long as they are close enough to the surface for the photoelectrons to escape (5 nm).<sup>187</sup> For profiling larger depths, XPS can be combined with ion sputtering.

However, sputtering and high-energy X-rays could induce further reactions of sensitive SEI components and falsify the results. Additionally, XPS operates under high-vacuum conditions, which usually require preliminary washing, drying and transport steps. During all these steps, samples are prone to contamination by moisture, oxygen, solvent vapor or other chemicals. Even if contaminations are avoided, soluble or volatile components will likely be removed in the process. Moreover, interpreting an XPS spectrum is not trivial, as the measured energies shift depending on microstructure and conductivity of the sample.<sup>91</sup> Precise evaluation of XPS data therefore requires good knowledge of the investigated system and reliable reference values.

### 4.1.2 Fourier transform infrared spectroscopy

FTIR detects functional groups based on their vibrational modes. Due to the low energies of IR irradiation (typically 4000 to 400  $\text{cm}^{-1}$  or 0.5 to 0.05 eV), FTIR is considered a nondestructive technique. Additionally, a FTIR spectrometer can operate under ambient pressure and argon atmosphere, thus eliminating the need for inert sample transport. Data interpretation is facilitated by vast databases and countless publications reporting the spectra of SEI components.<sup>91</sup>

Unfortunately, many SEI components have very similar functional groups such as carbonates, alkoxides and ethers and are difficult to distinguish.<sup>85</sup> Other components, like LiF, do not possess IR-active vibrational modes at all. Lastly, remaining electrolyte would strongly absorb IR radiation, which necessitates the same washing and drying steps as XPS.



### 4.1.3 Determining total amounts of SEI components

These complementary methods have established a rather detailed picture of the SEI composition and how it changes with electrode materials and electrolyte components. One drawback of both methods is, however, that they cannot determine the total amount of these components in the SEI. While in theory FTIR and XPS can both yield quantitative results, quantification is challenging on real electrodes with XPS and virtually impossible with FTIR. Moreover, this information is limited to a small area of the electrode. For determining the total amount of SEI components, a method is needed that is both quantitative and integral (*i.e.* covers the entire electrode).

One candidate is the electrochemical quartz crystal microbalance (EQCM), where the mass increase on the electrode is recorded *in-situ* and correlated to the charge passed in the electrode reaction. Ideally, this would result in distinct mass-per-electron ratios such as 6.9 for  $\text{Li}^+$  intercalation or 41 for  $\text{C}_1\text{Li}$  formation.<sup>82</sup> Unfortunately, several parasitic reactions proceed simultaneously in most cases, which results in convoluted mass-per-electron ratios that are hard to interpret.<sup>188,189</sup>

As a consequence, researchers have often resorted to SEI thickness to estimate the amount of side products. This simplification of course introduces errors as SEI thickness is not homogenous. This adds to systematic errors that arise from traditional measurement methods like XPS or AFM. In an XPS measurement, the depth is considered proportional to sputtering time,<sup>190</sup> neglecting that inorganic compounds will be sputtered much slower. In AFM measurements, the AFM tip itself is used to scrape off the SEI. However, the solid inner part of the SEI remains in place even after prolonged contact<sup>191</sup> suggesting that SEI-thicknesses measured with AFM tips should be reexamined.<sup>82</sup> As a result, total amounts of SEI components are hard to obtain.

Here we refine our previous method that sequentially and quantitatively transforms  $\text{M}_2\text{CO}_3$  and organic SEI components to  $\text{CO}_2$ , which is then detected by mass spectrometry (MS). Thus, total amounts of SEI components can be rapidly analyzed. Our modification further allows to simultaneously determine total amounts of  $\text{Li}_2\text{O}_2$  or  $\text{NaO}_2$ , the main discharge products of  $\text{Li-O}_2$  and  $\text{Na-O}_2$  batteries, respectively, rendering it a useful tool for investigating parasitic reactions in these systems.

# Quantifying Total Superoxide, Peroxide, and Carbonaceous Compounds in Metal–O<sub>2</sub> Batteries and the Solid Electrolyte Interphase

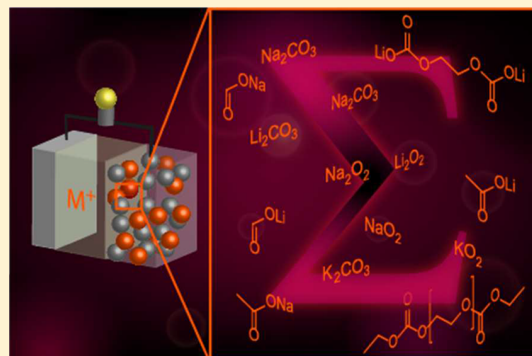
Bettina Schafzahl,<sup>†</sup> Eléonore Mourad,<sup>†</sup> Lukas Schafzahl,<sup>†</sup> Yann K. Petit,<sup>†</sup> Anjana R. Raju,<sup>†,‡</sup> Musthafa Ottakam Thotiyil,<sup>‡,§</sup> Martin Wilkening,<sup>†,§</sup> Christian Slugovc,<sup>†</sup> and Stefan A. Freunberger<sup>\*,†,§</sup>

<sup>†</sup>Institute for Chemistry and Technology of Materials, Graz University of Technology, Stremayrgasse 9, 8010 Graz, Austria

<sup>‡</sup>Department of Chemistry, Indian Institute of Science Education and Research (IISER) Pune, Dr. Homi Bhabha Road, Pashan, Pune 411008, India

## Supporting Information

**ABSTRACT:** Passivation layers on electrode materials are ubiquitous in nonaqueous battery chemistries and strongly govern performance and lifetime. They comprise breakdown products of the electrolyte including carbonate, alkyl carbonates, alkoxides, carboxylates, and polymers. Parasitic chemistry in metal–O<sub>2</sub> batteries forms similar products and is tied to the deviation of the O<sub>2</sub> balance from the ideal stoichiometry during formation/decomposition of alkaline peroxides or superoxides. Accurate and integral quantification of carbonaceous species and peroxides or superoxides in battery electrodes remains, however, elusive. We present a refined procedure to quantify them accurately and sensitively by pointing out and rectifying pitfalls of previous procedures. Carbonaceous compounds are differentiated into inorganic and organic ones. We combine mass and UV–vis spectrometry to quantify evolved O<sub>2</sub> and complexed peroxide and CO<sub>2</sub> evolved from carbonaceous compounds by acid treatment and Fenton's reaction. The capabilities of the method are exemplified by means of Li–O<sub>2</sub> and Na–O<sub>2</sub> cathodes, graphite anodes, and LiNi<sub>0.8</sub>Co<sub>0.15</sub>Al<sub>0.05</sub>O<sub>2</sub> cathodes.



Lithium-ion batteries based on aprotic organic electrolytes store the highest energies of all current technologies due to the high operating potential. Nevertheless, society demands further improvements with respect to energy storage, cost, lifetime, and materials sustainability.<sup>1,2</sup> Major routes to achieve these goals include advancing the currently used intercalation concept with higher-voltage cathodes<sup>3,4</sup> or replacing intercalation with higher-capacity conversion-type electrodes, such as the Si alloying anode<sup>5,6</sup> or the O<sub>2</sub> cathode,<sup>2,7</sup> and analogous routes with Na<sup>+</sup> as the mobile ion.<sup>8–13</sup> In all cases, the nature and quantity of parasitic chemistry with the electrolyte determine performance and lifetime.

Organic electrolytes decompose in contact with low-voltage anode materials such as graphite or Si to form the solid electrolyte interphase (SEI).<sup>14–22</sup> Cathode materials equally get covered by such a layer (termed the solid permeable interphase (SPI)), especially so for materials with reactive surfaces or high redox voltages above 4.2 V.<sup>23–25</sup> These layers comprise breakdown products of the electrolyte solvent and salt including carbonate, alkyl carbonates, alkoxides, carboxylates, and polymers (ethers and carbonates).<sup>15–21,23–26</sup> A

large body of work over the last decades has identified mechanisms and parasitic products that form.<sup>15–21,23–28</sup> Accurate and integral quantification of these species, however, remains elusive.<sup>29</sup> Methods to identify the SEI/SPI components have been summarized in excellent reviews and include FTIR, XPS, and NMR spectroscopy.<sup>14–16,29,30</sup> Li NMR and ICP-OES, for example, have been used to quantify Li at the interphase and total Li content.<sup>30–32</sup> However, Li content is not strictly tied to the overall interphase quantity as the compounds vary widely in Li-to-C ratio. Cell impedance is equally not directly linked to interphase quantity because the constituents contribute differently to impedance.<sup>33,34</sup> Total carbon content in the interphase would therefore be a key measure to assess.

Aprotic metal–O<sub>2</sub> cathodes store charge by forming/decomposing alkaline peroxides or superoxides.<sup>2,7</sup> Most typically, these are Li peroxide (Li<sub>2</sub>O<sub>2</sub>) or Na or K superoxide (NaO<sub>2</sub>, KO<sub>2</sub>), but also LiO<sub>2</sub>, Na<sub>2</sub>O<sub>2</sub>, or mixtures of peroxide

Received: November 10, 2017

Accepted: December 18, 2017

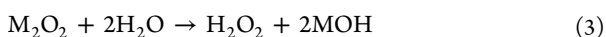
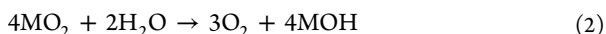
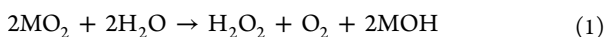
Published: December 18, 2017

and superoxide were reported.<sup>2,7,35–39</sup> Even though the reactions proceed at potentials within the electrochemical stability window of the electrolyte, reactive O<sub>2</sub> species decompose electrolyte and carbon and form parasitic products including carbonates and carboxylates.<sup>7,27,28,40–42</sup> These carbonaceous compounds trap mobile ions, raise cell impedance, and cause capacity loss and cell failure.<sup>2,7,14,15</sup> Parasitic chemistry in O<sub>2</sub> cathodes is tied to deviation of the O<sub>2</sub> balance from the ideal stoichiometry given by, e.g., O<sub>2</sub> + 2Li<sup>+</sup> + 2e<sup>-</sup> ↔ Li<sub>2</sub>O<sub>2</sub> and O<sub>2</sub> + Na<sup>+</sup> + e<sup>-</sup> ↔ NaO<sub>2</sub>, respectively. Concluding about the efficacy of measures to improve reversibility requires thus to relate the amount of peroxide or superoxide and the amount of parasitic products present to the charge passed.<sup>40,43</sup> However, known methods to measure these quantities feature significant inaccuracies.

Here we refine a previously reported method to more accurately quantify total superoxide/peroxide and carbonaceous compounds in battery electrodes. We show that widely used methods for these quantities reported in the context of metal–O<sub>2</sub> batteries have pitfalls, which are prone to significant systematic errors and which we here clear out with refinements. Carbonaceous compounds are differentiated into inorganic and organic ones. We combine mass spectrometry (MS) and UV–vis spectrometry to quantify evolved O<sub>2</sub> and complexed peroxide and CO<sub>2</sub> evolved from carbonaceous compounds by acid treatment and Fenton's reaction. The capabilities of this refined method are exemplified by means of Li–O<sub>2</sub> and Na–O<sub>2</sub> cathodes, graphite anodes, and Li–Ni<sub>0.8</sub>Co<sub>0.15</sub>Al<sub>0.05</sub>O<sub>2</sub> cathodes.

Spectroscopic and diffractive methods sensitive to alkaline (su)peroxides or carbonaceous compounds, such as XPS, FTIR, and XRD, cannot quantify the integral amount in the electrode. To quantify them, the compounds may be chemically extracted and, for consistency, ideally quantified with a single sensitive method. The strategy that we adopt here is to extract the compounds with aqueous solutions and to further digest them into O<sub>2</sub> and CO<sub>2</sub>, which can then be quantified by MS. We first examine the possibility to measure the entire O<sub>2</sub> and CO<sub>2</sub> by MS. Because evolving all of the O<sub>2</sub> from (su)peroxides turns out to be problematic, we combine MS and UV–vis to quantify (su)peroxides. We also revisit and optimize our previously reported procedure to measure inorganic and organic carbon to also work in conjunction with the (su)peroxides measurement and for the SEI/SPI: treating the sample with acid evolves CO<sub>2</sub> from inorganic carbonate and semicarbonates, and treating with Fenton's reagent evolves CO<sub>2</sub> from organics.

Alkaline superoxides and peroxides (M = Li, Na, K, Rb, Cs) dissolve according to<sup>44</sup>



Recently, Wang et al. have shown that NaO<sub>2</sub> and KO<sub>2</sub> hydrolyze according to eq 1, whereas LiO<sub>2</sub> follows eq 2, which they could rationalize based on the reaction free energies. LiO<sub>2</sub> can thus not be quantified via the H<sub>2</sub>O<sub>2</sub> formed.<sup>36</sup> We deal later on with the case that LiO<sub>2</sub> or mixtures of peroxide and superoxide are to be analyzed. Literature describes a range of methods to determine H<sub>2</sub>O<sub>2</sub>, including redox titration with I<sup>-</sup>, MnO<sub>4</sub><sup>-</sup>, and Ce<sup>4+</sup> or photometric

detection of Ti<sup>4+</sup> or Co<sup>2+</sup>–peroxo complexes.<sup>45</sup> A common pitfall is, however, that H<sub>2</sub>O<sub>2</sub> is prone to decompose into H<sub>2</sub>O and O<sub>2</sub>, which underestimates the content. The reaction is particularly favored by catalytic surfaces, which are often used in metal–O<sub>2</sub> cells.<sup>46</sup> In the context of metal–O<sub>2</sub> batteries, H<sub>2</sub>O<sub>2</sub> has been quantified by (1) iodometric titration after immersing the electrode in H<sub>2</sub>O and neutralizing with HCl<sup>40</sup> or (2) measuring the absorbance of the [Ti(O<sub>2</sub>)OH]<sup>+</sup> complex after immersing the electrode in acidic TiOSO<sub>4</sub> solution.<sup>38,44,47,48</sup>

To test whether and how much these methods could underestimate the H<sub>2</sub>O<sub>2</sub> by loss into the gas phase, we measured the evolved O<sub>2</sub> by MS during the immersion steps, Figure 1. The setup consisted of a hermetically sealed glass vial

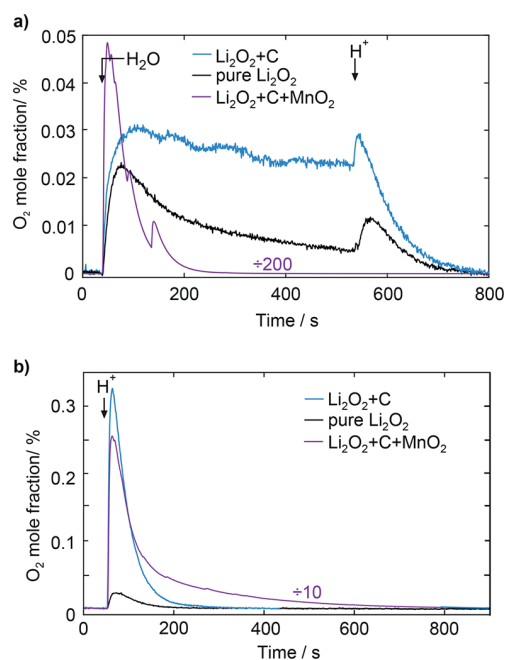


**Figure 1.** Oxygen loss into the gas phase upon sample preparation for peroxide/superoxide detection by titration (a) or photometry (b). The samples are pure Li<sub>2</sub>O<sub>2</sub> and mechanical mixtures of Li<sub>2</sub>O<sub>2</sub> with Super P carbon (1:1) and Li<sub>2</sub>O<sub>2</sub> with Super P carbon and  $\alpha$ -MnO<sub>2</sub> (1:0.6:0.4), which mimic discharged Li–O<sub>2</sub> cathodes without and with catalyst. Iodometric titration involves adding water followed by acid and is analyzed in (a). Photometry involves adding TiOSO<sub>4</sub> in 0.1 M H<sub>2</sub>SO<sub>4</sub> solution and is analyzed in (b).

equipped with a stirring bar and a lid with a septum and tubing for purge gas, Figure S1. The gas space was continuously purged into a MS for gas analysis. To resemble major electrode types, we tested pure Li<sub>2</sub>O<sub>2</sub> and mechanical mixtures of Li<sub>2</sub>O<sub>2</sub> with carbon black and a mixture with additional  $\alpha$ -MnO<sub>2</sub>.

Turning first to the preparation for titration, immersing pure Li<sub>2</sub>O<sub>2</sub> in H<sub>2</sub>O evolves O<sub>2</sub> at a somewhat fading rate after an initial peak, Figure 1a. Once acid is added, O<sub>2</sub> evolution rises again to fade thereafter quickly to the baseline. With the Li<sub>2</sub>O<sub>2</sub>/C mixture, O<sub>2</sub> evolves at a higher, nearly constant rate and also drops once acid is added. The O<sub>2</sub> amounts equate to ~3 and 8%, respectively, of the H<sub>2</sub>O<sub>2</sub>. With the Li<sub>2</sub>O<sub>2</sub>/C/MnO<sub>2</sub> mixture, O<sub>2</sub> evolves at initially ~400 times the previous rate to quantitatively evolve all O<sub>2</sub> within ~300 s. Turning to the preparation for Ti<sup>4+</sup> photometry, Figure 1b, immersing pure Li<sub>2</sub>O<sub>2</sub> or Li<sub>2</sub>O<sub>2</sub>/C or Li<sub>2</sub>O<sub>2</sub>/C/MnO<sub>2</sub> mixtures leads to

O<sub>2</sub> evolution in the same order as before. The O<sub>2</sub> amounts equate to 0.3, 7, and 55% of the total peroxide, respectively. Fast catalytic decomposition of H<sub>2</sub>O<sub>2</sub> by transition metal oxides is in accord with its use to probe catalytic activity<sup>46</sup> and renders measuring H<sub>2</sub>O<sub>2</sub> by titration or photometry alone impracticable for electrodes with catalysts. The results also show that significant amounts of H<sub>2</sub>O<sub>2</sub> can be lost with only marginally catalyzing C surfaces and even with pure Li<sub>2</sub>O<sub>2</sub>. Similarly, immersing NaO<sub>2</sub> or KO<sub>2</sub> in water or acid releases more O<sub>2</sub> than commensurate with eq 1, which indicates significant decomposition of the formed H<sub>2</sub>O<sub>2</sub>, Table 1.

**Table 1. Amount of Released O<sub>2</sub> with Respect to the NaO<sub>2</sub> or KO<sub>2</sub> Amount When Immersed in Water or Acid<sup>a</sup>**

	O <sub>2</sub> /NaO <sub>2</sub>	O <sub>2</sub> /KO <sub>2</sub>
ideal	0.5	0.5
immersed in H <sub>2</sub> O	0.554	0.523
immersed in 0.1 M H <sub>2</sub> SO <sub>4</sub>	0.520	0.528
immersed in 1 M H <sub>2</sub> SO <sub>4</sub>	0.525	0.557

<sup>a</sup>Note that for every mole of O<sub>2</sub>, two moles of H<sub>2</sub>O<sub>2</sub> are decomposed. For NaO<sub>2</sub>, Na–O<sub>2</sub> cathodes discharged in 0.5 M NaOTf in diglyme containing 40 ppm H<sub>2</sub>O were used. For KO<sub>2</sub>, commercial material was used. The total NaO<sub>2</sub> or KO<sub>2</sub> amount was determined by combining MS and UV–vis measurements.

Measuring O<sub>2</sub> from peroxide/superoxide by evolving it into the gas phase appears to be an attractive option given the described significant O<sub>2</sub> evolution. Prerequisite is to evolve O<sub>2</sub> quantitatively and to avoid reactive O<sub>2</sub> species, which could decompose organics into CO<sub>2</sub>. The latter would not allow one to distinguish CO<sub>2</sub> from organics and inorganics as intended and underestimate the peroxide/superoxide amount. Although effective in decomposing H<sub>2</sub>O<sub>2</sub>, transition metal oxides do form reactive species and prematurely decompose organics, Figure S2a. H<sub>2</sub>O<sub>2</sub> may, however, also catalytically be decomposed by Fe<sup>3+</sup>, for which either the Kremer–Stein mechanism<sup>44</sup> or other mechanisms involving HO<sub>2</sub>• or •OH were proposed.<sup>49</sup> Fe<sup>3+</sup> quantitatively decomposes all H<sub>2</sub>O<sub>2</sub>, Table S1 and Figure S3. When, however, Li acetate was added as a probe for reactive species, the sample evolved CO<sub>2</sub> (Figure S2b), indicating a pathway with reactive species.<sup>49</sup> Overall, quantifying superoxide and peroxide by evolving them as O<sub>2</sub> is problematic as reactive oxygen species form, which causes O<sub>2</sub> to be underestimated and organic carbon to be falsely assigned as inorganic.

Superoxide and peroxide may thus best be quantified by combining photometry of the [Ti(O<sub>2</sub>)OH]<sup>+</sup> complex and MS measurement of the O<sub>2</sub> evolved during sample preparation. In the case that electrodes containing only peroxides are measured, the O<sub>2</sub> comprises O<sub>2</sub> from H<sub>2</sub>O<sub>2</sub> decomposition. In the case of superoxides, the O<sub>2</sub> comprises the O<sub>2</sub> from quantitative disproportionation according to eq 1 and additional O<sub>2</sub> from H<sub>2</sub>O<sub>2</sub> decomposition (except for LiO<sub>2</sub>, which does not form H<sub>2</sub>O<sub>2</sub>). The total moles *n* of M<sub>2</sub>O<sub>2</sub> or MO<sub>2</sub> (M = Li, Na, K) are obtained via

$$n_{M_2O_2} = n_{H_2O_2} + 2n_{O_2} \quad M = \text{Li, Na, K} \quad (4)$$

$$n_{LiO_2} = \frac{3}{4}n_{O_2} \quad (5)$$

$$n_{MO_2} = \frac{4}{3}\left(n_{O_2} + \frac{1}{2}n_{H_2O_2}\right) \quad M = \text{Na, K} \quad (6)$$

These equations are derived in the Supporting Information discussion and Figure S4. In some cases, it was shown that Li–O<sub>2</sub> and Na–O<sub>2</sub> cells can yield mixtures of superoxide and peroxide as discharge products.<sup>35–39,48</sup> When mixtures are to be expected, determining the individual amounts additionally requires measurement of the moles *n* of Li<sup>+</sup> or Na<sup>+</sup>, as discussed in the Supporting Information discussion and Figure S5. The total moles *n* of M<sub>2</sub>O<sub>2</sub> and MO<sub>2</sub> are obtained via

$$n_{Li_2O_2} = \frac{6}{13}\left(\frac{4}{3}n_{Li^+} - \frac{1}{2}n_{H_2O_2} - n_{O_2}\right) \quad (7)$$

$$n_{LiO_2} = n_{Li^+} - 2n_{Li_2O_2} \quad (8)$$

for Li<sub>2</sub>O<sub>2</sub> and LiO<sub>2</sub> mixtures and

$$n_{Na_2O_2} = \frac{3}{4}n_{Na^+} - \frac{1}{2}n_{H_2O_2} - n_{O_2} \quad (9)$$

$$n_{NaO_2} = n_{Na^+} - 2n_{Na_2O_2} \quad (10)$$

for Na<sub>2</sub>O<sub>2</sub> and NaO<sub>2</sub> mixtures.

Calibrating UV–vis absorbance with H<sub>2</sub>O<sub>2</sub> is prone to yield a curve that does not pass through zero, that is, due to loss of H<sub>2</sub>O<sub>2</sub>.<sup>38</sup> To obtain the true H<sub>2</sub>O<sub>2</sub> concentration, we thus started from high-purity Li<sub>2</sub>O<sub>2</sub> and accounted for any H<sub>2</sub>O<sub>2</sub> loss by measuring evolved O<sub>2</sub>, Figure S6.

Fenton's reaction, which forms the highly reactive •OH radical via Fe<sup>2+</sup> + H<sub>2</sub>O<sub>2</sub> → Fe<sup>3+</sup> + OH<sup>−</sup> + •OH, is used to decompose organics into CO<sub>2</sub> and proceeds best at a pH of 3,<sup>50</sup> while peroxide/superoxide analysis is ideal at more acidic conditions (compare Figure 1b vs Figure 2d). To quantify peroxide/superoxide and carbonaceous compounds in combination, the optimized procedure for sample sizes of several mg, which are typically used in coin cells or Swagelok type cells, is shown in Figure 2. The procedure for metal–O<sub>2</sub> electrodes is summarized in Figure 2b, and the procedure for all other electrodes is in Figure 2c. The first involves as a first step acidifying the sample with 1 M H<sub>2</sub>SO<sub>4</sub>, upon which CO<sub>2</sub> evolves from M<sub>2</sub>CO<sub>3</sub>. The strongly acidic pH prevents excessive O<sub>2</sub> evolution from H<sub>2</sub>O<sub>2</sub>. To quantify the dissolved peroxide, after CO<sub>2</sub> and O<sub>2</sub> evolution have ceased, part of the solution is removed and mixed with TiOSO<sub>4</sub> solution and analyzed by UV–vis. The remaining solution in the MS setup is then diluted with H<sub>2</sub>O to reach the optimum pH of 3. Fenton's reaction is then initiated by adding FeSO<sub>4</sub> in 0.1 M H<sub>2</sub>SO<sub>4</sub> and then, over the course of several minutes, H<sub>2</sub>O<sub>2</sub> in 0.1 M H<sub>2</sub>SO<sub>4</sub> under vigorous stirring. For electrodes other than metal–O<sub>2</sub> cathodes, the first step is modified by adding a smaller amount of 1 M H<sub>2</sub>SO<sub>4</sub>, Figure 2c. Samples that contain alkylcarbonates (ROCO<sub>2</sub>M) such as in the SEI or the SPI evolve CO<sub>2</sub> according to ROCO<sub>2</sub>M + H<sub>2</sub>O → ROH + MOH + CO<sub>2</sub>. Successive treatment with acid and Fenton's reagent can quantitatively discriminate between CO<sub>2</sub> from M<sub>2</sub>CO<sub>3</sub> or the terminal –OCO<sub>2</sub>M groups of ROCO<sub>2</sub>M and CO<sub>2</sub> from organic moieties. Table 2 compares expected and evolved moles of CO<sub>2</sub> for a range of compounds including Li<sub>2</sub>CO<sub>3</sub>, Li acetate, and different Li alkylcarbonates. In all cases, the values match the expected values within 3% and confirm the reagents to expel the compounds selectively and quantitatively. Further on, we refer to inorganic CO<sub>2</sub> when evolving from acid and organic CO<sub>2</sub> when evolving from Fenton's reaction.

Figure 2d shows a typical concentration profile for O<sub>2</sub> and CO<sub>2</sub> during the analysis of a Li–O<sub>2</sub> cathode. For the particular cell, the presented method gives a Li<sub>2</sub>O<sub>2</sub> yield of 94% (based



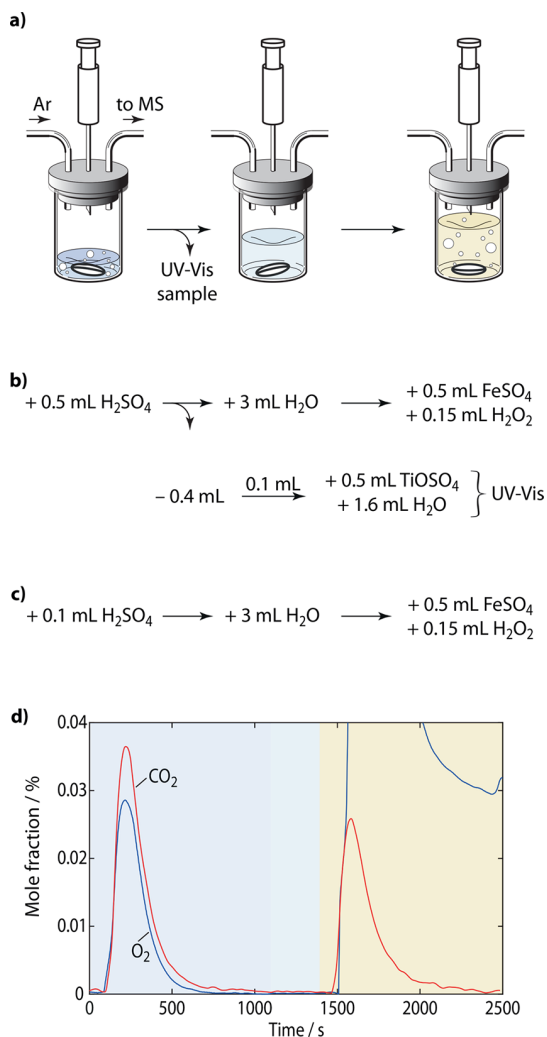


**Figure 2.** Analysis protocol to quantify total superoxide/peroxide and carbonaceous products in battery electrodes. (a) Schematic of the test setup and the sequence of solution addition and sample drawing. (b) Procedure for metal–O<sub>2</sub> cathodes. The concentrations in the added solutions are 1 M H<sub>2</sub>SO<sub>4</sub>, 0.5 M FeSO<sub>4</sub> in 0.1 M H<sub>2</sub>SO<sub>4</sub>, 10 wt % H<sub>2</sub>O<sub>2</sub> in 0.1 M H<sub>2</sub>SO<sub>4</sub>, and 2 wt % TiOSO<sub>4</sub> in 1 M H<sub>2</sub>SO<sub>4</sub>, respectively. Quantification of total superoxide/peroxide by combining O<sub>2</sub> detected by MS and H<sub>2</sub>O<sub>2</sub> by UV–vis photometry is detailed in the [Supporting Information discussion and Figures S4 and S5](#). (c) Procedure for electrodes other than metal–O<sub>2</sub>. (d) CO<sub>2</sub> and O<sub>2</sub> evolution during the course of a typical analysis. In the particular case, a discharged Li–O<sub>2</sub> cathode was measured. The color-coded background refers to the stages indicated in (a). CO<sub>2</sub> during the blue period stems from inorganic carbonates or terminal –OCO<sub>2</sub>Li groups in alkyl carbonates; CO<sub>2</sub> during the yellow shaded period evolves from organics being oxidized by Fenton’s reaction.

on the expected amount with respect to the charge passed), while UV–vis measurement alone after immersing the electrode in 2% TiOSO<sub>4</sub> in 0.1 M H<sub>2</sub>SO<sub>4</sub> gave a yield of only 85%. [Figure S8](#) shows a typical measurement of a Na–O<sub>2</sub> cathode. The optimized method gave a yield of 96%, whereas UV–vis alone gave a ~94% NaO<sub>2</sub> yield. [Figure 3](#) shows the values obtained with the optimized method over an entire discharge and charge cycle of a Li–O<sub>2</sub> and Na–O<sub>2</sub> cell.

[Figure 4](#) exemplifies the capabilities of the method to follow SEI/SPI evolution on graphite anodes and Li–

**Table 2.** Expected and Measured Moles of CO<sub>2</sub> Evolved Per Mole of Li<sub>2</sub>CO<sub>3</sub>, Li Acetate, and Li Alkylcarbonates<sup>a</sup>

compound	expected		found	
	inorganic	organic	inorganic	organic
Li <sub>2</sub> CO <sub>3</sub> <sup>b</sup>	1		1 ± 0.03	
CH <sub>3</sub> COOLi <sup>b</sup>		2		2 ± 0.01
CH <sub>3</sub> OCO <sub>2</sub> Li	1	1	1 ± 0.02	1 ± 0.02
CH <sub>3</sub> (CH <sub>2</sub> ) <sub>3</sub> OCO <sub>2</sub> Li	1	4	1 ± 0.02	4 ± 0.04

<sup>a</sup>Inorganic refers to CO<sub>2</sub> evolved from acid treatment and organic to CO<sub>2</sub> evolved from Fenton’s reagent. <sup>b</sup>A curve for the found vs the expected amount is given in [Figure S7](#).

Ni<sub>0.8</sub>Co<sub>0.15</sub>Al<sub>0.05</sub>O<sub>2</sub> cathodes. The electrodes were cycled vs Li-metal in LP30 electrolyte to various stages of charge, then stopped and analyzed. Electrodes were either washed with dimethyl carbonate or used unwashed to capture the difference that the washing introduces. It is a known problem for interphase analytics that washing is, on one hand, required for surface-sensitive methods such as XPS but, on the other hand, may alter the interphase composition. Unwashed electrodes were only analyzed for inorganic CO<sub>2</sub>, capturing M<sub>2</sub>CO<sub>3</sub> and terminal –OCO<sub>2</sub>M groups of alkylcarbonates, because Fenton’s reagent would decompose the electrolyte.

Considering first the initial lithiation of graphite, inorganic CO<sub>2</sub> in the unwashed electrodes continuously grows to full lithiation, [Figure 4a](#). Values for inorganic and organic CO<sub>2</sub> from the washed electrodes show, in contrast, a pronounced maximum at half lithiation and decrease to full lithiation. Multiple measurements at half lithiation confirm the values to be statistically significant. To interpret this behavior, it needs to be recalled what the values represent. Organic CO<sub>2</sub> captures all organic compounds not washed away by dimethyl carbonate. These may comprise not only Li-containing ones but also oligo carbonates, oligo ethylene oxides, carbonate-terminated ethylene oxides, and remaining electrolyte.<sup>19–21,26</sup> Declining amounts from half to full lithiation may be explained along the reaction schemes described by Gachot et al. by ongoing reactions triggered by CH<sub>3</sub>OLi, which breaks initially present oligo carbonates into the more soluble oligo ethylene oxides and CH<sub>3</sub>OCO<sub>2</sub>Li.<sup>19</sup> These reactions take place not only directly on the graphite surface but at a distance such as that in the separator. Conversion into more soluble or poorly attached species is also suggested by the trend of the inorganic CO<sub>2</sub> beyond the first lithiation in the unwashed electrodes, which captures Li<sub>2</sub>CO<sub>3</sub>, terminal –OCO<sub>2</sub>Li groups, and soluble compounds. Another feature seen in the washed electrodes is a tendency for higher/lower amounts in the lithiated/delithiated states, which is in accord with dynamic change in SEI thickness noted earlier by Edström et al.<sup>22</sup> A more detailed analysis of the underlying phenomena is, however, beyond the scope of this study, which is concerned with the method itself. As another example, we measured the SPI evolution on NCA cathodes, [Figure 4c](#). Inorganic CO<sub>2</sub> is slightly lower in the washed compared to unwashed electrodes and remains at nearly the same level without clear evolution. The main constituents in quantitative terms are organic compounds, which grow with cycle number and correlate well with the growing efficiency.

In conclusion, we present a refined method to accurately and sensitively quantify total superoxide or peroxide and carbonaceous compounds in battery electrodes. The method for peroxide and superoxide clears out pitfalls with uncontrolled

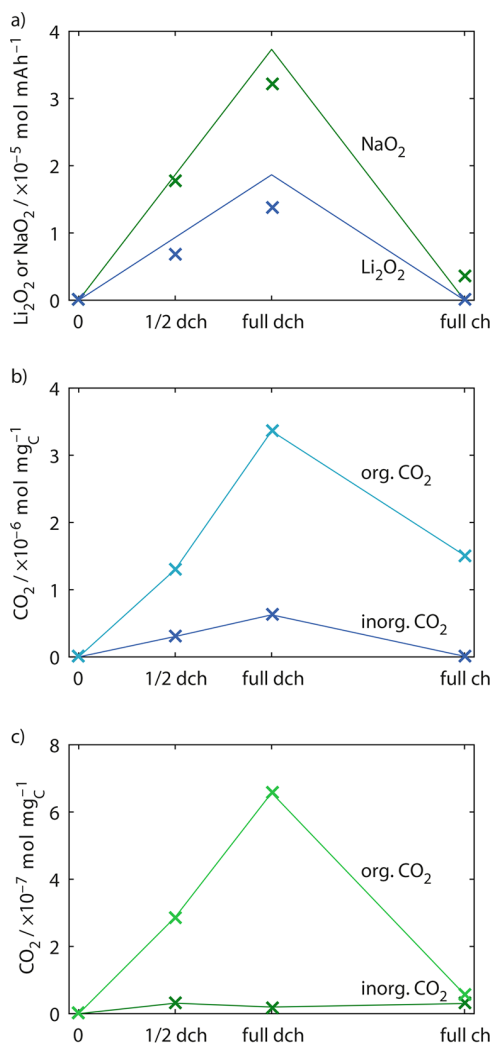


**Figure 3.** Product quantification over an entire discharge/charge cycle of a Li–O<sub>2</sub> and Na–O<sub>2</sub> cell determined at half and full discharge and full charge (labeled 1/2 dch, full dch, full ch, respectively). Li–O<sub>2</sub> cells comprised a Super P/PTFE working electrode, Li<sub>1-x</sub>FePO<sub>4</sub> reference and counter electrodes, and 0.1 M LiClO<sub>4</sub> in tetraglyme as the electrolyte and were run at 70 mA·g<sub>C</sub><sup>-1</sup> with full discharge corresponding to 1200 mAh·g<sub>C</sub><sup>-1</sup>. Na–O<sub>2</sub> cells comprised a carbon paper working electrode, Na metal reference and counter electrodes, and 0.1 M NaOTf in diglyme containing 40 ppm H<sub>2</sub>O as the electrolyte and were run at 90 μA·cm<sup>-2</sup> with full discharge corresponding to 1 mAh·cm<sup>-2</sup>. Markers represent the measured amounts of Li<sub>2</sub>O<sub>2</sub> and NaO<sub>2</sub>, respectively, and full lines represent the theoretical values. (b) Amounts of inorganic and organic CO<sub>2</sub> at the sampling points for the Li–O<sub>2</sub> cell. (c) Amounts of inorganic and organic CO<sub>2</sub> at the sampling points for the Na–O<sub>2</sub> cell. The first sampling point is in either case the electrode brought into contact with electrolyte overnight. Electrodes were washed with dimethoxyethane and dried under vacuum prior to analysis.

O<sub>2</sub> loss into the gas phase, which makes previously reported methods prone to underestimated values. Carbonaceous compounds are differentiated into inorganic and organic ones, and the measures can discriminate between soluble and insoluble compounds by comparing washed and unwashed electrodes.

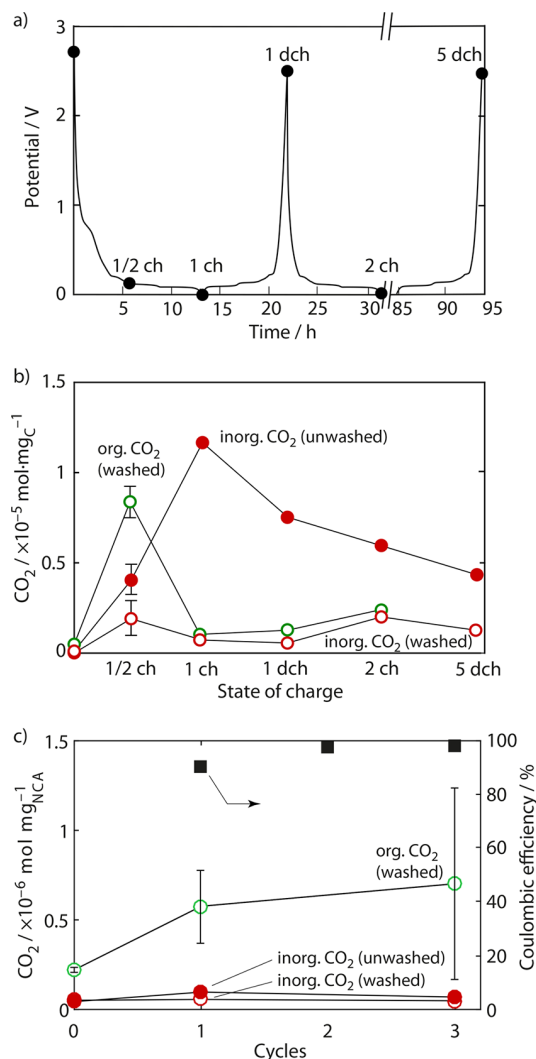


**Figure 4.** Evolution of total carbonaceous SEI and SPI components. The first sampling point is in either case the electrode brought in contact with electrolyte overnight. Electrodes were either washed with dimethyl carbonate prior to analysis or analyzed unwashed to capture soluble SEI components. Washed electrodes were analyzed with acid and Fenton's reaction for inorganic and organic CO<sub>2</sub>; unwashed electrodes were analyzed only with acid. (a) Voltage versus time during cycling of a graphite anode in LP30 electrolyte with the sampling points indicated by the black markers. (b) Amount of CO<sub>2</sub> found at the sampling points. (c) Evolution of Coulombic efficiency and total carbonaceous SPI components during cycling of a LiNi<sub>0.8</sub>Co<sub>0.15</sub>Al<sub>0.05</sub>O<sub>2</sub> cathode in LP30 electrolyte. The error bars are derived from at least three measurements.

## ■ ASSOCIATED CONTENT

### Supporting Information

The Supporting Information is available free of charge on the ACS Publications website at DOI: 10.1021/acsenerylett.7b01111.

Materials, experimental methods, supporting figures, and discussion (PDF)

## AUTHOR INFORMATION

## Corresponding Author

\*E-mail: freunberger@tugraz.at. Web: www.freunberger-lab.com.

## ORCID

Musthafa Ottakam Thotiyil: 0000-0002-2439-4708

Martin Wilkening: 0000-0001-9706-4892

Stefan A. Freunberger: 0000-0003-2902-5319

## Notes

The authors declare no competing financial interest.

## ACKNOWLEDGMENTS

S.A.F. is indebted to the European Research Council (ERC) under the European Union's Horizon 2020 research and innovation programme (Grant Agreement No. 636069) and the Austrian Federal Ministry of Science, Research and Economy and the Austrian Research Promotion Agency (Grant No. 845364).

## REFERENCES

- (1) Larcher, D.; Tarascon, J. M. Towards Greener and More Sustainable Batteries for Electrical Energy Storage. *Nat. Chem.* **2014**, *7*, 19–29.
- (2) Choi, J. W.; Aurbach, D. Promise and Reality of Post-Lithium-Ion Batteries with High Energy Densities. *Nat. Rev. Mater.* **2016**, *1*, 16013.
- (3) Brutti, S.; Greco, G.; Reale, P.; Panero, S. Insights About the Irreversible Capacity of  $\text{LiNi}_{0.5}\text{Mn}_{1.5}\text{O}_4$  Cathode Materials in Lithium Batteries. *Electrochim. Acta* **2013**, *106*, 483–493.
- (4) Xu, M.; Lu, D.; Garsuch, A.; Lucht, B. L. Improved Performance of  $\text{LiNi}_{0.5}\text{Mn}_{1.5}\text{O}_4$  Cathodes with Electrolytes Containing Dimethylmethylphosphonate (DMMP). *J. Electrochem. Soc.* **2012**, *159*, A2130–A2134.
- (5) Obrovac, M. N.; Chevrier, V. L. Alloy Negative Electrodes for Li-Ion Batteries. *Chem. Rev.* **2014**, *114*, 11444–11502.
- (6) Chevrier, V. L.; Ceder, G. Challenges for Na-Ion Negative Electrodes. *J. Electrochem. Soc.* **2011**, *158*, A1011–A1014.
- (7) Aurbach, D.; McCloskey, B. D.; Nazar, L. F.; Bruce, P. G. Advances in Understanding Mechanisms Underpinning Lithium–Air Batteries. *Nat. Energy* **2016**, *1*, 16128.
- (8) Kim, S.-W.; Seo, D.-H.; Ma, X.; Ceder, G.; Kang, K. Electrode Materials for Rechargeable Sodium-Ion Batteries: Potential Alternatives to Current Lithium-Ion Batteries. *Adv. Energy Mater.* **2012**, *2*, 710–721.
- (9) Slater, M. D.; Kim, D.; Lee, E.; Johnson, C. S. Sodium-Ion Batteries. *Adv. Funct. Mater.* **2013**, *23*, 947–958.
- (10) Ellis, B. L.; Nazar, L. F. Sodium and Sodium-Ion Energy Storage Batteries. *Curr. Opin. Solid State Mater. Sci.* **2012**, *16*, 168–177.
- (11) Ponrouch, A.; Marchante, E.; Courty, M.; Tarascon, J.-M.; Palacin, M. R. In Search of an Optimized Electrolyte for Na-Ion Batteries. *Energy Environ. Sci.* **2012**, *5*, 8572–8583.
- (12) Wu, D.; Li, X.; Xu, B.; Twu, N.; Liu, L.; Ceder, G.  $\text{NaTiO}_2$ : A Layered Anode Material for Sodium-Ion Batteries. *Energy Environ. Sci.* **2015**, *8*, 195–202.
- (13) Clément, R. J.; Bruce, P. G.; Grey, C. P. Manganese-Based P2-Type Transition Metal Oxides as Sodium-Ion Battery Cathode Materials. *J. Electrochem. Soc.* **2015**, *162*, A2589–A2604.
- (14) Xu, K. Nonaqueous Liquid Electrolytes for Lithium-Based Rechargeable Batteries. *Chem. Rev.* **2004**, *104*, 4303–4418.
- (15) Xu, K. Electrolytes and Interphases in Li-Ion Batteries and Beyond. *Chem. Rev.* **2014**, *114*, 11503–11618.
- (16) Verma, P.; Maire, P.; Novák, P. A Review of the Features and Analyses of the Solid Electrolyte Interphase in Li-Ion Batteries. *Electrochim. Acta* **2010**, *55*, 6332–6341.
- (17) Eshetu, G. G.; Grugeon, S.; Kim, H.; Jeong, S.; Wu, L.; Gachot, G.; Laruelle, S.; Armand, M.; Passerini, S. Comprehensive Insights into the Reactivity of Electrolytes Based on Sodium Ions. *ChemSusChem* **2016**, *9*, 462–471.
- (18) Kim, H.; Grugeon, S.; Gachot, G.; Armand, M.; Sannier, L.; Laruelle, S. Ethylene Bis-Carbonates as Telltales of SEI and Electrolyte Health, Role of Carbonate Type and New Additives. *Electrochim. Acta* **2014**, *136*, 157–165.
- (19) Gachot, G.; Grugeon, S.; Armand, M.; Pilard, S.; Guenot, P.; Tarascon, J.-M.; Laruelle, S. Deciphering the Multi-Step Degradation Mechanisms of Carbonate-Based Electrolyte in Li Batteries. *J. Power Sources* **2008**, *178*, 409–421.
- (20) Gireaud, L.; Grugeon, S.; Laruelle, S.; Pilard, S.; Tarascon, J.-M. Identification of Li Battery Electrolyte Degradation Products through Direct Synthesis and Characterization of Alkyl Carbonate Salts. *J. Electrochem. Soc.* **2005**, *152*, A850–A857.
- (21) Sasaki, T.; Abe, T.; Iriyama, Y.; Inaba, M.; Ogumi, Z. Formation Mechanism of Alkyl Dicarboxates in Li-Ion Cells. *J. Power Sources* **2005**, *150*, 208–215.
- (22) Bryngelsson, H.; Stjern Dahl, M.; Gustafsson, T.; Edström, K. How Dynamic Is the SEI? *J. Power Sources* **2007**, *174*, 970–975.
- (23) Philippe, B.; Hahlin, M.; Edström, K.; Gustafsson, T.; Siegbahn, H.; Rensmo, H. Photoelectron Spectroscopy for Lithium Battery Interface Studies. *J. Electrochem. Soc.* **2016**, *163*, A178–A191.
- (24) Younesi, R.; Christiansen, A. S.; Scipioni, R.; Ngo, D.-T.; Simonsen, S. B.; Edström, K.; Hjelm, J.; Norby, P. Analysis of the Interphase on Carbon Black Formed in High Voltage Batteries. *J. Electrochem. Soc.* **2015**, *162*, A1289–A1296.
- (25) Edström, K.; Gustafsson, T.; Thomas, J. O. The Cathode–Electrolyte Interface in the Li-Ion Battery. *Electrochim. Acta* **2004**, *50*, 397–403.
- (26) Gireaud, L.; Grugeon, S.; Pilard, S.; Guenot, P.; Tarascon, J.-M.; Laruelle, S. Mass Spectrometry Investigations on Electrolyte Degradation Products for the Development of Nanocomposite Electrodes in Lithium Ion Batteries. *Anal. Chem.* **2006**, *78*, 3688–3698.
- (27) McCloskey, B. D.; Bethune, D. S.; Shelby, R. M.; Girishkumar, G.; Luntz, A. C. Solvents' Critical Role in Nonaqueous Lithium–Oxygen Battery Electrochemistry. *J. Phys. Chem. Lett.* **2011**, *2*, 1161–1166.
- (28) Ottakam Thotiyil, M. M.; Freunberger, S. A.; Peng, Z.; Bruce, P. G. The Carbon Electrode in Nonaqueous  $\text{Li}-\text{O}_2$  Cells. *J. Am. Chem. Soc.* **2013**, *135*, 494–500.
- (29) Lu, J.; Wu, T.; Amine, K. State-of-the-Art Characterization Techniques for Advanced Lithium-Ion Batteries. *Nat. Energy* **2017**, *2*, 17011.
- (30) Dupré, N.; Cuisinier, M.; Guyomard, D. Electrode–Electrolyte Interface Studies in Lithium Batteries Using NMR. *Electrochem. Soc. Interface* **2011**, *20*, 61–67.
- (31) Schwieters, T.; Evertz, M.; Mense, M.; Winter, M.; Nowak, S. Lithium Loss in the Solid Electrolyte Interphase: Lithium Quantification of Aged Lithium Ion Battery Graphite Electrodes by Means of Laser Ablation Inductively Coupled Plasma Mass Spectrometry and Inductively Coupled Plasma Optical Emission Spectroscopy. *J. Power Sources* **2017**, *356*, 47–55.
- (32) Wan, C.; Xu, S.; Hu, M. Y.; Cao, R.; Qian, J.; Qin, Z.; Liu, J.; Mueller, K. T.; Zhang, J.-G.; Hu, J. Z. Multinuclear NMR Study of the Solid Electrolyte Interface Formed in Lithium Metal Batteries. *ACS Appl. Mater. Interfaces* **2017**, *9*, 14741–14748.
- (33) Zaban, A.; Aurbach, D. Impedance Spectroscopy of Lithium and Nickel Electrodes in Propylene Carbonate Solutions of Different Lithium Salts a Comparative Study. *J. Power Sources* **1995**, *54*, 289–295.
- (34) Lu, P.; Li, C.; Schneider, E. W.; Harris, S. J. Chemistry, Impedance, and Morphology Evolution in Solid Electrolyte Interphase Films During Formation in Lithium Ion Batteries. *J. Phys. Chem. C* **2014**, *118*, 896–903.

(35) Kang, J.-H.; Kwak, W.-J.; Aurbach, D.; Sun, Y.-K. Sodium Oxygen Batteries: One Step Further with Catalysis by Ruthenium Nanoparticles. *J. Mater. Chem. A* **2017**, *5*, 20678–20686.

(36) Wang, H.-H.; Lee, Y. J.; Assary, R. S.; Zhang, C.; Luo, X.; Redfern, P. C.; Lu, J.; Lee, Y. J.; Kim, D. H.; Kang, T.-G.; Indacochea, E.; Lau, K. C.; Amine, K.; Curtiss, L. A. Lithium Superoxide Hydrolysis and Relevance to Li–O<sub>2</sub> Batteries. *J. Phys. Chem. C* **2017**, *121*, 9657–9661.

(37) Zhai, D.; Wang, H.-H.; Yang, J.; Lau, K. C.; Li, K.; Curtiss, L. A.; Amine, K. Disproportionation in Li–O<sub>2</sub> Batteries Based on Large Surface Area Carbon Cathode. *J. Am. Chem. Soc.* **2013**, *135*, 15364–15372.

(38) Hartmann, P.; Bender, C. L.; Sann, J.; Durr, A. K.; Jansen, M.; Janek, J.; Adelhelm, P. A Comprehensive Study on the Cell Chemistry of the Sodium Superoxide (NaO<sub>2</sub>) Battery. *Phys. Chem. Chem. Phys.* **2013**, *15*, 11661–11672.

(39) Lu, J.; Jung Lee, Y.; Luo, X.; Chun Lau, K.; Asadi, M.; Wang, H.-H.; Brombosz, S.; Wen, J.; Zhai, D.; Chen, Z.; Miller, D. J.; Sub Jeong, Y.; Park, J.-B.; Zak Fang, Z.; Kumar, B.; Salehi-Khojin, A.; Sun, Y.-K.; Curtiss, L. A.; Amine, K. A Lithium–Oxygen Battery Based on Lithium Superoxide. *Nature* **2016**, *529*, 377–382.

(40) McCloskey, B. D.; Valery, A.; Luntz, A. C.; Gowda, S. R.; Wallraff, G. M.; Garcia, J. M.; Mori, T.; Krupp, L. E. Combining Accurate O<sub>2</sub> and Li<sub>2</sub>O<sub>2</sub> Assays to Separate Discharge and Charge Stability Limitations in Nonaqueous Li–O<sub>2</sub> Batteries. *J. Phys. Chem. Lett.* **2013**, *4*, 2989–2993.

(41) Mahne, N.; Schafzahl, B.; Leypold, C.; Leypold, M.; Grumm, S.; Leitgeb, A.; Strohmeier, G. A.; Wilkening, M.; Fontaine, O.; Kramer, D.; Slugovc, C.; Borisov, S. M.; Freunberger, S. A. Singlet Oxygen Generation as a Major Cause for Parasitic Reactions During Cycling of Aprotic Lithium–Oxygen Batteries. *Nat. Energy* **2017**, *2*, 17036.

(42) Schafzahl, L.; Mahne, N.; Schafzahl, B.; Wilkening, M.; Slugovc, C.; Borisov, S. M.; Freunberger, S. A. Singlet Oxygen During Cycling of the Aprotic Sodium–O<sub>2</sub> Battery. *Angew. Chem., Int. Ed.* **2017**, *56*, 15728–15732.

(43) Mahne, N.; Fontaine, O.; Thotiyil, M. O.; Wilkening, M.; Freunberger, S. A. Mechanism and Performance of Lithium–Oxygen Batteries – a Perspective. *Chem. Sci.* **2017**, *8*, 6716–6729.

(44) Wiberg, N.; Holleman, A. F.; Wiberg, E. *Inorganic Chemistry*; Academic Press: San Diego, CA, 2001.

(45) Kunze, U. R.; Schwedt, G. *Grundlagen der Quantitativen Analyse*; Wiley: Weinheim, Germany, 2009.

(46) Giordani, V.; Freunberger, S. A.; Bruce, P. G.; Tarascon, J.-M.; Larcher, D. H<sub>2</sub>O<sub>2</sub> Decomposition Reaction as Selecting Tool for Catalysts in Li–O<sub>2</sub> Cells. *Electrochem. Solid-State Lett.* **2010**, *13*, A180–A183.

(47) Meini, S.; Piana, M.; Tsiouvaras, N.; Garsuch, A.; Gasteiger, H. A. The Effect of Water on the Discharge Capacity of a Non-Catalyzed Carbon Cathode for Li–O<sub>2</sub> Batteries. *Electrochem. Solid-State Lett.* **2012**, *15*, A45–A48.

(48) Ren, X.; Lau, K. C.; Yu, M.; Bi, X.; Kreidler, E.; Curtiss, L. A.; Wu, Y. Understanding Side Reactions in K–O<sub>2</sub> Batteries for Improved Cycle Life. *ACS Appl. Mater. Interfaces* **2014**, *6*, 19299–19307.

(49) De Laat, J.; Gallard, H. Catalytic Decomposition of Hydrogen Peroxide by Fe(II) in Homogeneous Aqueous Solution: Mechanism and Kinetic Modeling. *Environ. Sci. Technol.* **1999**, *33*, 2726–2732.

(50) Duesterberg, C. K.; Mylon, S. E.; Waite, T. D. pH Effects on Iron-Catalyzed Oxidation Using Fenton's Reagent. *Environ. Sci. Technol.* **2008**, *42*, 8522–8527.



## 5. Singlet oxygen in the Na-O<sub>2</sub> battery

Na-O<sub>2</sub> batteries are a promising beyond Li-ion technology that could deliver high energy densities at low overpotentials. Unfortunately, their practical application is precluded by severe capacity fade leading to short lifetimes. The reasons for this remain unknown, which warrants further research.

We combined the method developed in Section 4.2 with other *in situ* and *ex situ* techniques to demonstrate that <sup>1</sup>O<sub>2</sub> forms during discharge, charge and rest, and is a major source of side-reactions in Na-O<sub>2</sub>-batteries. Together with previous investigations in our group,<sup>59</sup> this contribution completes the comprehensive picture of <sup>1</sup>O<sub>2</sub> formation in non-aqueous metal-O<sub>2</sub>-batteries.

The additional unpublished material contains attempts to mitigate these side-reactions using a <sup>1</sup>O<sub>2</sub> quencher. However, insufficient quencher stability under the given conditions resulted in slightly higher amounts of side-products.

### Singlet Oxygen during Cycling of the Aprotic Sodium-O<sub>2</sub> Battery

Lukas Schafzahl, Nika Mahne, Bettina Schafzahl, Martin Wilkening, Christian Slugovc, Sergey M. Borisov, and Stefan A. Freunberger

*Angew. Chem. Int. Ed.* 2017, 56, 15728-15732 (english)

*Angew. Chem.* 2017, 129, 15934-15938 (german)

open access - no permission required for reprinting

## 5.1 Singlet oxygen and its reactivity

With the fundamentals of Na-O<sub>2</sub> batteries explained in Section 1.2.3, this section is dedicated to <sup>1</sup>O<sub>2</sub> – a molecule with truly extraordinary features. Molecular oxygen can exist in three electronic states with the vast majority of it in its ground state (<sup>3</sup>Σ<sub>g</sub><sup>-</sup>). Ground state oxygen has two unpaired electrons of the same spin in its degenerate π\* orbitals, see Figure 5.1, and will be further referred to as triplet oxygen (<sup>3</sup>O<sub>2</sub>). In addition to the ground state, O<sub>2</sub> can assume two excited states. The first accommodates both electrons in one orbital and has the term symbol <sup>1</sup>Δ<sub>g</sub>. The second has again two unpaired electrons, but with opposite spin, and is termed <sup>1</sup>Σ<sub>g</sub><sup>+</sup>. The activation energies for the first and the second excited state are 0.97 and 1.63 eV, respectively.<sup>192,193</sup> Both excited states do not possess unpaired spins and are “singlet” oxygen, but the latter rapidly relaxes to the former and is normally disregarded.<sup>194</sup> The term singlet oxygen, or <sup>1</sup>O<sub>2</sub>, therefore refers to the <sup>1</sup>Δ<sub>g</sub> state.

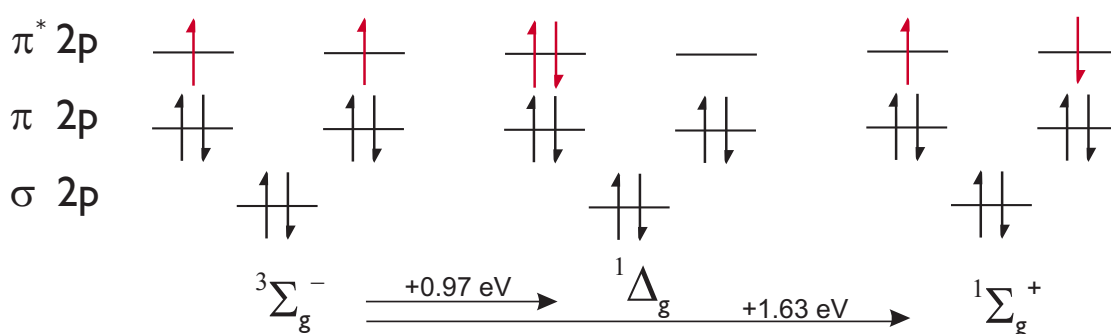


Figure 5.1: The electronic states of molecular oxygen.

The conversion from <sup>1</sup>O<sub>2</sub> to <sup>3</sup>O<sub>2</sub> is forbidden by spin, symmetry and parity selection rules, which theoretically imparts high lifetime on <sup>1</sup>O<sub>2</sub>. In practice, however, the lifetime of <sup>1</sup>O<sub>2</sub> strongly depends on its environment.<sup>195</sup> In collision free environments, such as the upper layers of our atmosphere, <sup>1</sup>O<sub>2</sub> may persist up to hours.<sup>196</sup> This changes drastically in solution, where its lifetime is reduced to microseconds.<sup>192,197,198</sup> When <sup>1</sup>O<sub>2</sub> is finally converted, it can relax via radiation-less pathways or upon emitting characteristic radiation at 1260 nm. This radiation can be used for direct observation of <sup>1</sup>O<sub>2</sub>, although its low intensity and overtones of C-H and O-H bonds severely limit the sensitivity.<sup>194</sup> Additionally, <sup>1</sup>O<sub>2</sub> can deactivate by chemically reacting with surrounding molecules like the solvent. Unlike direct relaxation, this reaction is not spin-forbidden rendering <sup>1</sup>O<sub>2</sub> an exceptionally reactive molecule.<sup>197</sup>

In nature, the reactivity of <sup>1</sup>O<sub>2</sub> is both a blessing and a curse. <sup>1</sup>O<sub>2</sub> can perturb cell operation and destroy an otherwise healthy cell, which is why nature provided us with beta-carotene and other antioxidants that quench <sup>1</sup>O<sub>2</sub>.<sup>199,200</sup> On the other hand, <sup>1</sup>O<sub>2</sub> plays a vital role as antibacterial or antimicrobial agent that wards off harmful intruders in plants and animals.<sup>200–203</sup> Humans have learned to exploit this role of <sup>1</sup>O<sub>2</sub> to fight cancer cells in the photodynamic therapy (DPT), where a photosensitizer is enriched in tumor cells and produces <sup>1</sup>O<sub>2</sub> upon irradiation with light.<sup>204</sup> In chemistry, <sup>1</sup>O<sub>2</sub> is synthesized using a photosensitizer that transfers its excitation energy to <sup>3</sup>O<sub>2</sub> and converts it to <sup>1</sup>O<sub>2</sub>.<sup>205</sup> Alternatively, <sup>1</sup>O<sub>2</sub> is obtained by treating M<sub>2</sub>O<sub>2</sub> (M=H<sup>+</sup>, Li<sup>+</sup>, Na<sup>+</sup>) with strong acids or Cl<sub>2</sub>.<sup>206</sup> <sup>1</sup>O<sub>2</sub> then acts as diene and readily undergoes cycloadditions or other organic reactions.<sup>207,208</sup>

In the context of batteries, <sup>1</sup>O<sub>2</sub> had long been overlooked. It was first speculated to

possibly form at high oxidation voltages by Hassoun *et al.* in 2011,<sup>209</sup> and McCloskey *et al.* cited it as a possible but unlikely reason for parasitic reactions in Li-O<sub>2</sub> batteries.<sup>57</sup> In 2016, Wandt *et al.* detected <sup>1</sup>O<sub>2</sub> when a Li-O<sub>2</sub> cell was charged to potentials >3.5 V.<sup>58</sup> Soon thereafter, a more comprehensive work by Mahne *et al.* demonstrated that <sup>1</sup>O<sub>2</sub> forms at all stages of cycling in a Li-O<sub>2</sub> cell and accounts for the majority of side-reactions.<sup>59</sup> This challenged the longstanding belief that side-reactions stem from the reactivity of Li<sub>2</sub>O<sub>2</sub> or LiO<sub>2</sub> with the electrolyte. Furthermore, it warranted similar research for Na-O<sub>2</sub> cells that, too, suffer from low cyclic stability for not fully elucidated reasons.

VIP **Batteries** Very Important Paper

International Edition: DOI: 10.1002/anie.201709351

German Edition: DOI: 10.1002/ange.201709351



# Singlet Oxygen during Cycling of the Aprotic Sodium–O<sub>2</sub> Battery

Lukas Schafzahl<sup>†</sup>, Nika Mahne<sup>†</sup>, Bettina Schafzahl, Martin Wilkening, Christian Slugovc, Sergey M. Borisov, and Stefan A. Freunberger\*

**Abstract:** Aprotic sodium–O<sub>2</sub> batteries require the reversible formation/dissolution of sodium superoxide (NaO<sub>2</sub>) on cycling. Poor cycle life has been associated with parasitic chemistry caused by the reactivity of electrolyte and electrode with NaO<sub>2</sub>, a strong nucleophile and base. Its reactivity can, however, not consistently explain the side reactions and irreversibility. Herein we show that singlet oxygen (<sup>1</sup>O<sub>2</sub>) forms at all stages of cycling and that it is a main driver for parasitic chemistry. It was detected in- and ex-situ via a <sup>1</sup>O<sub>2</sub> trap that selectively and rapidly forms a stable adduct with <sup>1</sup>O<sub>2</sub>. The <sup>1</sup>O<sub>2</sub> formation mechanism involves proton-mediated superoxide disproportionation on discharge, rest, and charge below ca. 3.3 V, and direct electrochemical <sup>1</sup>O<sub>2</sub> evolution above ca. 3.3 V. Trace water, which is needed for high capacities also drives parasitic chemistry. Controlling the highly reactive singlet oxygen is thus crucial for achieving highly reversible cell operation.

The need to advance batteries beyond the limits of current technology in terms of energy, sustainability, and cost has generated immense interest in rechargeable aprotic metal–O<sub>2</sub> batteries.<sup>[1]</sup> They store charge at the cathode by reversibly forming/decomposing Li<sub>2</sub>O<sub>2</sub> or NaO<sub>2</sub> in the Li–O<sub>2</sub> or Na–O<sub>2</sub> cell, respectively. Despite the lower theoretical specific capacity of 488 mAhg<sup>−1</sup> of NaO<sub>2</sub> and lower voltage of 2.27 V (vs. 1168 mAhg<sup>−1</sup> at 2.96 V for Li–O<sub>2</sub>), the Na–O<sub>2</sub> cell has been reported to have significant advantages over Li–O<sub>2</sub> with respect to rechargeability and energy efficiency.<sup>[2]</sup> Realizing the Na–O<sub>2</sub> cell, however, still faces many challenges in practice, including the Na-metal anode, lower than theoretical cathode capacity, and perhaps most importantly,

insufficient cycle life associated with parasitic chemistry (that is, side reactions) at the cathode.<sup>[2,3]</sup>

Since the very first papers published on Na–O<sub>2</sub> batteries, superoxide has been perceived responsible for parasitic chemistry with electrolyte and electrode.<sup>[1c,3,4]</sup> A key measure for parasitic chemistry is the ratio of e<sup>−</sup> passed to O<sub>2</sub> consumed/evolved. During discharge, this ratio is typically at the ideal value of one despite approximately 5% of the expected NaO<sub>2</sub> being missing and replaced by side products, such as Na<sub>2</sub>CO<sub>3</sub>, Na acetate, and Na formate. During subsequent resting and charge, more of these side products form and typically the e<sup>−</sup>/O<sub>2</sub> ratio deviates by several percent from one.<sup>[2a,3c,4b,5]</sup> Although less side products form than in the Li–O<sub>2</sub> cell, cyclability is similarly poor: restricted capacity can often be maintained for up to hundreds of cycles albeit at the expense of true energy, but at full discharge cells fail within some 10 cycles and capacity fading becomes significantly worse with rising charge cut-off voltage.<sup>[1c,2a,c,d,3a,d,6]</sup>

Superoxide's potential reactivity towards organic substrates stems from its nucleophilicity, basicity, and radical nature, which may cause nucleophilic substitutions, H<sup>+</sup> and H-atom abstraction.<sup>[7]</sup> Theoretical work, however, has revealed that all these reactions are unlikely with commonly used ether electrolytes owing to the high activation energies and strong endothermicity.<sup>[8]</sup> Also, the extent of parasitic chemistry at the various stages of cycling does not match the abundance of superoxide. Overall, the reactivity of superoxide cannot consistently explain the observed parasitic chemistry, which thus may only be inhibited with better knowledge about reactive species and their formation mechanism.

Herein we show that singlet oxygen (<sup>1</sup>Δ<sub>g</sub> or <sup>1</sup>O<sub>2</sub>), the first excited state of ground state triplet oxygen (<sup>3</sup>Σ<sub>g</sub><sup>−</sup> or <sup>3</sup>O<sub>2</sub>), is the reactive species, which drives parasitic reactions. It is generated at all stages of cycling in relative quantities resembling the occurrence of side reactions: relatively little during discharge, rest, and low charging voltages, and strongly increasing amounts at higher charging voltages.

Methods to sensitively detect <sup>1</sup>O<sub>2</sub> rely on chemical probes, which selectively react with <sup>1</sup>O<sub>2</sub>. Probes include spin traps and fluorophores, which become EPR active or fluorescing upon reaction with <sup>1</sup>O<sub>2</sub>.<sup>[9]</sup> However, these probes are not electrochemically inert in the relevant potential range between approximately 2 and 3.6 V versus Na/Na<sup>+</sup> and may react with superoxide. Previously, we have shown that 9,10-dimethylanthracene (DMA) fulfills all the requirements;<sup>[10]</sup> it is stable in contact with superoxide, reacts rapidly with <sup>1</sup>O<sub>2</sub> to its endoperoxide (DMA-O<sub>2</sub>), and has a sufficiently wide potential window (Figure S1 and Scheme S1 in the Supporting Information). <sup>1</sup>O<sub>2</sub> can either be monitored by DMA consumption via its absorbance or fluorescence between 300 and

[\*] L. Schafzahl,<sup>[†]</sup> N. Mahne,<sup>[†]</sup> B. Schafzahl, Prof. M. Wilkening, Prof. C. Slugovc, Dr. S. A. Freunberger  
Institute for Chemistry and Technology of Materials  
Graz University of Technology  
Stremayrgasse 9, 8010 Graz (Austria)  
E-mail: freunberger@tugraz.at

Prof. S. M. Borisov  
Institute for Analytical Chemistry and Food Chemistry  
Graz University of Technology  
Stremayrgasse 9, 8010 Graz (Austria)

[†] These authors contributed equally to this work.

Supporting information and the ORCID identification number(s) for the author(s) of this article can be found under:  
<https://doi.org/10.1002/anie.201709351>.

© 2017 The Authors. Published by Wiley-VCH Verlag GmbH & Co. KGaA. This is an open access article under the terms of the Creative Commons Attribution Non-Commercial License, which permits use, distribution and reproduction in any medium, provided the original work is properly cited, and is not used for commercial purposes.

500 nm (Figure S2), or by detecting DMA and DMA-O<sub>2</sub> via HPLC.

To probe whether <sup>1</sup>O<sub>2</sub> would form during discharge and charge we constructed Na–O<sub>2</sub> cells as detailed in the Methods Section of the Supporting Information with 0.5 M NaSO<sub>3</sub>CF<sub>3</sub> (NaOTf) in diglyme containing 40 ppm H<sub>2</sub>O and 30 mM DMA as the electrolyte. Water was used because it is required as a phase-transfer catalyst to allow large NaO<sub>2</sub> particles to grow.<sup>[2c]</sup> To specifically probe reactions at the cathode and to exclude unwanted reactions of electrolyte components with a Na-metal anode, we used the Na intercalation material Na<sub>3-x</sub>V<sub>2</sub>(PO<sub>4</sub>)<sub>3</sub> as the counter electrode. It operates at approximately 3.4 V versus Na/Na<sup>+</sup> and is thus well within the stability window of the electrolyte.<sup>[11]</sup> Cells were run at constant current to various states of discharge or charge, then stopped, and the electrolyte extracted and analyzed using HPLC (Figure 1).

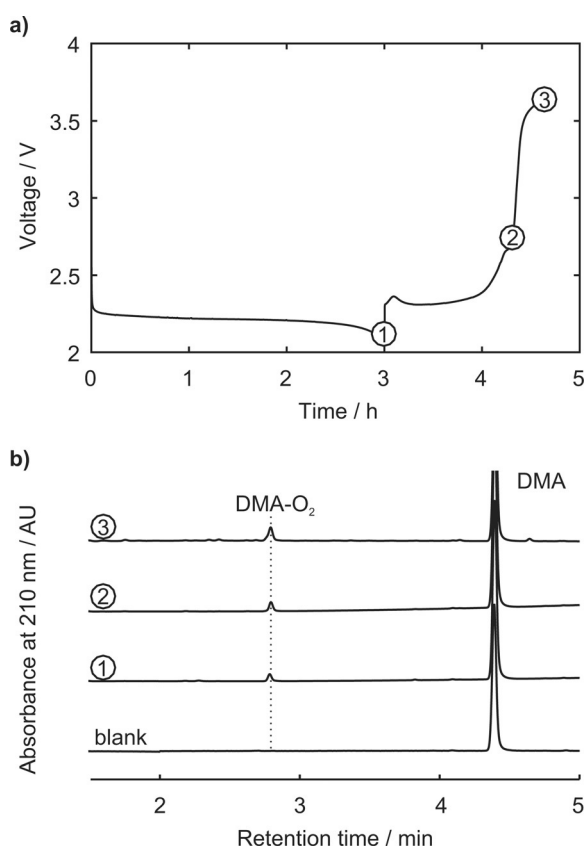


**Figure 1.** a) Load curve for galvanostatic cycling of a carbon-paper cathode at  $90 \mu\text{A cm}^{-2}$  in 0.5 M NaOTf in diglyme containing 40 ppm H<sub>2</sub>O and 30 mM DMA. b) HPLC runs of electrolyte samples taken at the points ①, ②, and ③ in (a), showing <sup>1</sup>O<sub>2</sub> to have formed as indicated by the conversion of DMA into DMA-O<sub>2</sub>. The blank sample was extracted from a cell that rested for 5 h.

The cycle curve shows flat discharge and charge plateaus at approximately 2.2 and 2.3 V, respectively, with a sharp rise in voltage when recharge approaches about 55% (Figure 1a). X-ray diffraction confirms that the cube-shaped discharge product is NaO<sub>2</sub> (Figure S3, S4) in accord with many previous

reports on similar cells.<sup>[1b,c,2a,b,3a]</sup> After discharge or recharge to 2.8 and 3.65 V, 4.1, 4.3, and 7.2%, respectively, of the DMA at the sample points ①, ②, and ③ was converted into DMA-O<sub>2</sub> (Figure 1b). The amounts of DMA-O<sub>2</sub> equate to 1.4, 1.3, and 2.1% of the O<sub>2</sub> involved based on the charge at these stages of cycling to have turned into <sup>1</sup>O<sub>2</sub>. <sup>1</sup>O<sub>2</sub> is thus generated both on discharge and charge, and charging to higher voltage yields significantly more <sup>1</sup>O<sub>2</sub>.

Operando spectroscopy is well suited to probe in detail onset potentials and reaction rates. An operando fluorescence set-up as detailed in the Supporting Information was constructed. Briefly, it consisted of a gas-tight quartz cuvette with a carbon paper working electrode and Na<sub>3-x</sub>V<sub>2</sub>(PO<sub>4</sub>)<sub>3</sub> as counter and reference electrode and an O<sub>2</sub> filled head space. The O<sub>2</sub>-saturated electrolyte was the same as before except for a lower DMA concentration ( $1.6 \times 10^{-5}$  M), which best suits fluorescence detection (see the Supporting Information). Excitation and emission wavelengths were chosen according to the maxima in the respective spectra (Figure S2).

While cells as in Figure 1 comprising a porous separator sandwiched between working and counter electrode typically yield NaO<sub>2</sub>, cycling the cathode in the operando setup yielded Na<sub>2</sub>O<sub>2</sub>·H<sub>2</sub>O as can be inferred from the high charging voltage (Figure S5). Rather similar thermodynamics of NaO<sub>2</sub> and Na<sub>2</sub>O<sub>2</sub> ( $E_{\text{O}_2/\text{NaO}_2}^0 = 2.27$  V,  $E_{\text{O}_2/\text{Na}_2\text{O}_2}^0 = 2.33$  V) were used to explain that the Na–O<sub>2</sub> cell could yield both as a discharge product.<sup>[1b,3b]</sup> Proton sources decisively influence the discharge product, yet the precise governing factors are unknown.<sup>[1b]</sup> The reason for peroxide rather than superoxide as a discharge product in the operando setup may be the large electrolyte-to-electrode volume ratio and the stirred electrolyte, both of which are essential for the method. The electrolyte after discharge in the operando setup also contains DMA-O<sub>2</sub>, revealing that discharge to Na<sub>2</sub>O<sub>2</sub> also forms <sup>1</sup>O<sub>2</sub> (Figure S6).

To investigate charging of NaO<sub>2</sub>, we first discharged a cathode in the standard cell and then placed it in the operando cell. Figure 2 shows the DMA concentration and consumption rate for stepwise potentiostatic charging up to 3.7 V. As soon as the cell was polarized to charging potentials, DMA was consumed at an initially moderate rate, which sharply increased beyond a voltage of about 3.3 V. Thermodynamically, <sup>1</sup>O<sub>2</sub> can be expected to form upon electrochemically oxidizing NaO<sub>2</sub> above  $E_{\text{O}_2/\text{NaO}_2}^0 + E({}^1\Delta_g \leftarrow {}^3\Sigma_g^-)$ . With 0.97 eV energy difference between <sup>1</sup>O<sub>2</sub> and <sup>3</sup>O<sub>2</sub> the thermodynamic threshold to evolve <sup>1</sup>O<sub>2</sub> can be estimated to be 3.24 V. <sup>1</sup>O<sub>2</sub> forming at high rate above approximately 3.3 V can thus be explained by the reaction  $\text{NaO}_2 \rightarrow \text{Na}^+ + \text{e}^- + {}^1\text{O}_2$  beyond the thermodynamic threshold of 3.24 V. Up to 3.3 V the <sup>1</sup>O<sub>2</sub> fraction is around 0.75 to 1.1% of the expected O<sub>2</sub> (Figure S7). Beyond 3.3 V this fraction increases steadily to around 4%.

Previously it was reported that most parasitic chemistry occurs during discharge and less on charge.<sup>[2a,3a]</sup> Charging above around 3.5 V caused the number of O<sub>2</sub> per e<sup>-</sup> evolved to deviate more significantly from one than at lower voltages. Correlating these findings with the results in Figure 1, Figure 2, and Figure S7 suggests that parasitic chemistry in the Na–O<sub>2</sub> cathode is closely related to <sup>1</sup>O<sub>2</sub> formation since

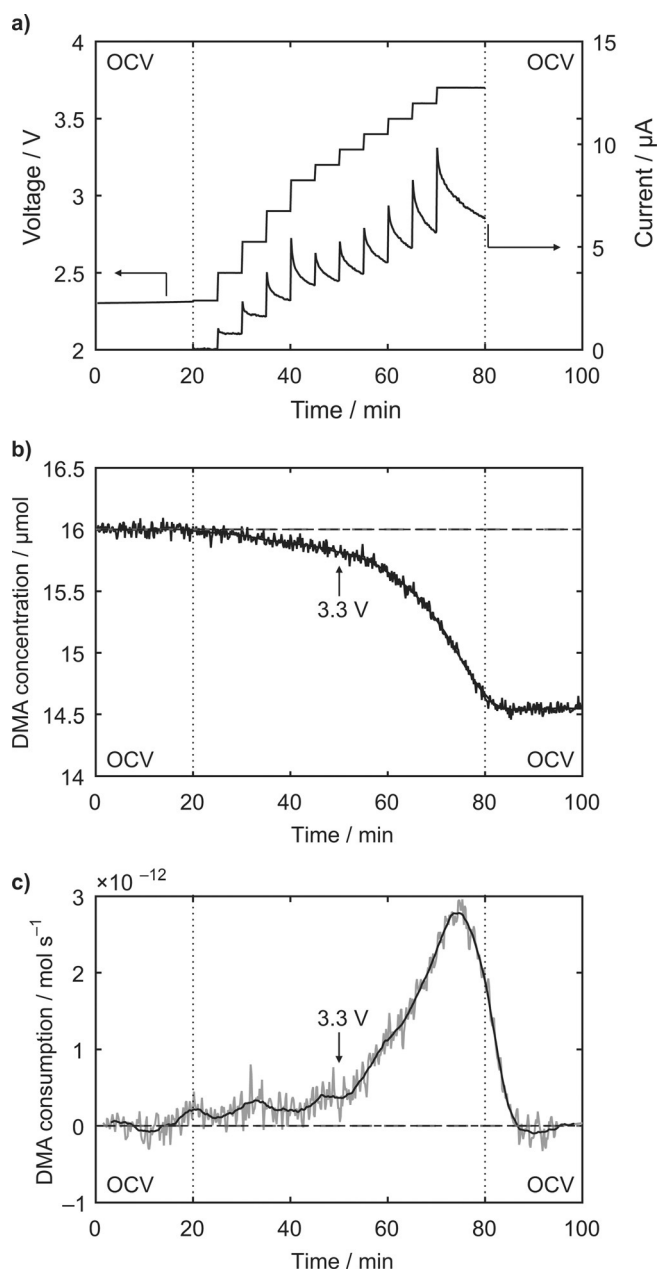
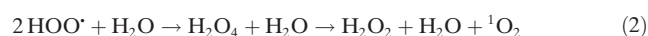
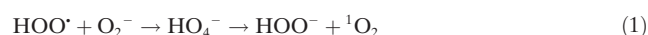


**Figure 2.** Operando fluorescence detection of  $^1\text{O}_2$  during potentiostatic charging of a Na- $\text{O}_2$  cathode. The carbon-paper cathode was first discharged in a Swagelok type cell to  $75 \text{ mAh cm}^{-2}$  in  $0.5 \text{ M NaOTf}$  in diglyme containing  $40 \text{ ppm H}_2\text{O}$  and then introduced into the operando setup containing the same electrolyte and additionally  $1.6 \times 10^{-5} \text{ M DMA}$ . a) Voltage and current profile. b) DMA concentration. c) DMA consumption rate.

the extent of side reactions follows the occurrence of  $^1\text{O}_2$ :  $^1\text{O}_2$  is formed at a higher rate during discharge than at charging below  $3.3 \text{ V}$  and at much higher rate above  $3.3 \text{ V}$ . In quantitative terms the  $1.4\%$   $^1\text{O}_2$  during discharge and an approximately  $95\%$  yield of  $\text{NaO}_2$  suggests a significant fraction of the side products stem from  $^1\text{O}_2$ . Measured  $^1\text{O}_2$  amounts represents a lower bound since at the low DMA concentration not necessarily all  $^1\text{O}_2$  will react with DMA and may undergo other decay routes, such as reactions with cell components.

While thermodynamics directly explains how  $^1\text{O}_2$  forms when  $\text{NaO}_2$  is oxidized above  $3.3 \text{ V}$ , its formation during discharge and recharge below  $3.3 \text{ V}$  is more surprising. With the Li- $\text{O}_2$  cell, disproportionation of the  $\text{LiO}_2$  intermediate to  $\text{Li}_2\text{O}_2$  was suggested as a major  $^1\text{O}_2$  source during discharge and low charging voltages.<sup>[10]</sup> This pathway is inactive in the Na- $\text{O}_2$  cell since discharge stops at  $\text{NaO}_2$ . When, however, water or other proton sources are present, oxygen reduction will lead to  $\text{HOO}^\cdot$ .<sup>[12]</sup> This soluble species enables proton-assisted phase-transfer catalysis, which allows the typical micron-sized  $\text{NaO}_2$  cubes to grow on discharge and to be oxidized on charge;  $\text{HOO}^\cdot$  is soluble and mobile in the electrolyte and precipitates  $\text{NaO}_2$  via the metathesis reaction  $\text{HOO}^\cdot + \text{Na}^+ \rightleftharpoons \text{NaO}_2 + \text{H}^+$ .<sup>[2c,13]</sup>  $\text{HOO}^\cdot$ , however, can be reduced by superoxide or disproportionate according to Equation (1) and (2),<sup>[12]</sup> which both have been shown to release  $^1\text{O}_2$ .<sup>[14]</sup>



That water is driving these reactions is supported by significantly less  $^1\text{O}_2$  being formed with dry electrolyte as compared to wet electrolyte (Figure S8).

These reactions may not only take place during discharge, where new superoxide is generated, but also at rest since the metathesis reaction is an equilibrium and allows  $\text{NaO}_2$  to redissolve into  $\text{HOO}^\cdot$ . A number of studies have shown instability of  $\text{NaO}_2$  upon prolonged rest.<sup>[3c,4,5]</sup> Although details vary, they generally report gradual conversion of  $\text{NaO}_2$  into  $\text{Na}_2\text{O}_2 \cdot \text{H}_2\text{O}$  accompanied by electrolyte degradation to form  $\text{NaOH}$ ,  $\text{Na}_2\text{CO}_3$ , and organic compounds including Na formate and acetate. Explanations included nucleophilic attack,  $\text{H}^+$  and H-atom abstraction by superoxide. To probe how  $^1\text{O}_2$  is involved in forming the parasitic products we first discharged electrodes in DMA-free electrolyte and then placed them for various times in electrolyte containing  $30 \text{ mM DMA}$ . X-ray diffraction after storage shows decreased  $\text{NaO}_2$  and side products to have formed in accord with previous studies (Figure S9). The electrolyte was then analyzed for DMA- $\text{O}_2$  and the electrodes were analyzed for  $\text{Na}_2\text{CO}_3$  content by immersing them in  $0.1 \text{ M H}_2\text{SO}_4$  and monitoring the  $\text{CO}_2$  evolved by mass spectrometry (Figure 3).  $^1\text{O}_2$  as indicated by the presence of DMA- $\text{O}_2$  continuously increases with resting time as does the  $\text{Na}_2\text{CO}_3$  content, which serves as an indication for the extent of parasitic products.

DMA- $\text{O}_2$  and  $\text{Na}_2\text{CO}_3$  roughly increase proportional to the square root of the resting time, which means that the formation rate decreases with time. The formed parasitic products thus partly passivate the  $\text{NaO}_2$  surface and slow down further decomposition. A larger amount of DMA- $\text{O}_2$  than additional  $\text{Na}_2\text{CO}_3$  formed, which can be explained by two phenomena. First,  $^1\text{O}_2$  trapped by DMA does not react with cell components and would thus have led to even more parasitic products without DMA. Second, other compounds than  $\text{Na}_2\text{CO}_3$  will form which are not expelled by acid. Overall, Figure 3 shows that the previously reported electro-



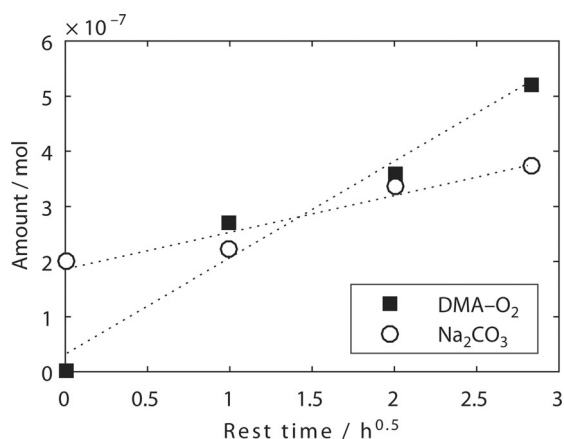
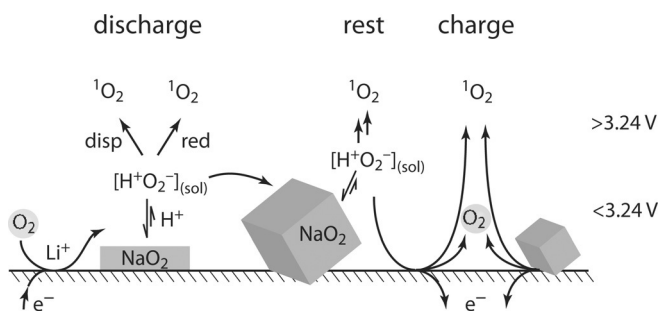


**Figure 3.**  $^1\text{O}_2$  generation and parasitic chemistry during prolonged contact of the discharge product  $\text{NaO}_2$  with the electrolyte. Cells were first discharged in DMA-free electrolyte (0.5 M NaOTf in diglyme containing 40 ppm  $\text{H}_2\text{O}$ ), then the cathodes washed and immersed in the same electrolyte containing additionally 30 mM DMA. After the times indicated the electrolyte was analyzed for DMA- $\text{O}_2$  and the electrodes for  $\text{Na}_2\text{CO}_3$ . The dotted lines are linear fits versus the square root of rest time.



**Scheme 1.** Pathways leading to  $^1\text{O}_2$  during discharge, rest, and charge. “Disp” = disproportionation and “red” = reduction.

lyte degradation upon resting is significantly driven by  $^1\text{O}_2$  formation.

Pathways to  $^1\text{O}_2$  during discharge, rest, and charge are summarized in Scheme 1. We suggest proton mediated superoxide disproportionation or reduction to interfere with the metathesis equilibrium  $\text{HOO}^\cdot + \text{Na}^+ \rightleftharpoons \text{NaO}_2 + \text{H}^+$  as a universal path to  $^1\text{O}_2$  during all stages of cycling. Upon charge at voltages exceeding the thermodynamic threshold of 3.24 V  $^1\text{O}_2$  evolves by direct electrochemical oxidation according to  $\text{NaO}_2 \rightarrow \text{Na}^+ + \text{e}^- + ^1\text{O}_2$ .

In conclusion we demonstrate that singlet oxygen forms at the cathode of the Na- $\text{O}_2$  cell during all stages of cycling and during rest, and accounts for a significant fraction of the side-products formed.  $^1\text{O}_2$  is thus a major hurdle in cycling the Na- $\text{O}_2$  cell via the reversible formation/decomposition of  $\text{NaO}_2$ . Water takes up an ambivalent role by being required for high capacity via solution-mediated growth and dissolution of large  $\text{NaO}_2$  deposits, and at the same time appearing to be the main driver for  $^1\text{O}_2$  formation during discharge and at low charging voltages. Future work should thus focus on finding ways to either prevent  $^1\text{O}_2$  formation or to efficiently eliminate it.

## Acknowledgements

S.A.F. is indebted to the European Research Council (ERC) under the European Union’s Horizon 2020 research and innovation programme (grant agreement No 636069) and the Austrian Federal Ministry of Science, Research and Economy and the Austrian Research Promotion Agency (grant No. 845364). We thank G. Strohmeier for help with the HPLC measurement, and J. Schlegl for manufacturing instrumentation for the methods used.

## Conflict of interest

The authors declare no conflict of interest.

**Keywords:** electrochemistry · Na- $\text{O}_2$  batteries · parasitic reactions · reaction mechanisms · singlet oxygen

**How to cite:** *Angew. Chem. Int. Ed.* **2017**, *56*, 15728–15732  
*Angew. Chem.* **2017**, *129*, 15934–15938

- [1] a) D. Aurbach, B. D. McCloskey, L. F. Nazar, P. G. Bruce, *Nat. Energy* **2016**, *1*, 16128; b) C. L. Bender, D. Schröder, R. Pinedo, P. Adelhelm, J. Janek, *Angew. Chem. Int. Ed.* **2016**, *55*, 4640–4649; *Angew. Chem.* **2016**, *128*, 4716–4726; c) P. Hartmann, C. L. Bender, M. Vračar, A. K. Dürr, A. Garsuch, J. Janek, P. Adelhelm, *Nat. Mater.* **2012**, *12*, 228–232.
- [2] a) B. D. McCloskey, J. M. Garcia, A. C. Luntz, *J. Phys. Chem. Lett.* **2014**, *5*, 1230–1235; b) R. Morasch, D. G. Kwabi, M. Tulodziecki, M. Risch, S. Zhang, Y. Shao-Horn, *ACS Appl. Mater. Interfaces* **2017**, *9*, 4374–4381; c) C. Xia, R. Black, R. Fernandes, B. Adams, L. F. Nazar, *Nat. Chem.* **2015**, *7*, 496–501; d) I. Landa-Medrano, C. Li, N. Ortiz-Vitoriano, I. Ruiz de Larramendi, J. Carrasco, T. Rojo, *J. Phys. Chem. Lett.* **2016**, *7*, 1161–1166.
- [3] a) P. Hartmann, C. L. Bender, J. Sann, A. K. Dürr, M. Jansen, J. Janek, P. Adelhelm, *Phys. Chem. Chem. Phys.* **2013**, *15*, 11661–11672; b) C. L. Bender, P. Hartmann, M. Vračar, P. Adelhelm, J. Janek, *Adv. Energy Mater.* **2014**, *4*, 1301863; c) S. Y. Sayed, K. P. C. Yao, D. G. Kwabi, T. P. Batcho, C. V. Amanchukwu, S. Feng, C. V. Thompson, Y. Shao-Horn, *Chem. Commun.* **2016**, *52*, 9691–9694; d) M. He, K. C. Lau, X. Ren, N. Xiao, W. D. McCulloch, L. A. Curtiss, Y. Wu, *Angew. Chem. Int. Ed.* **2016**, *55*, 15310–15314; *Angew. Chem.* **2016**, *128*, 15536–15540.
- [4] a) J. Kim, H. Park, B. Lee, W. M. Seong, H.-D. Lim, Y. Bae, H. Kim, W. K. Kim, K. H. Ryu, K. Kang, *Nat. Commun.* **2016**, *7*, 10670; b) T. Liu, G. Kim, M. T. L. Casford, C. P. Grey, *J. Phys. Chem. Lett.* **2016**, *7*, 4841–4846.
- [5] I. Landa-Medrano, R. Pinedo, X. Bi, I. Ruiz de Larramendi, L. Lezama, J. Janek, K. Amine, J. Lu, T. Rojo, *ACS Appl. Mater. Interfaces* **2016**, *8*, 20120–20127.
- [6] S. A. Freunberger, *Nat. Energy* **2017**, *2*, 17091.
- [7] a) D. T. Sawyer, J. S. Valentine, *Acc. Chem. Res.* **1981**, *14*, 393–400; b) D. Aurbach, M. L. Daroux, P. W. Faguy, E. Yeager, *J. Electrochem. Soc.* **1988**, *135*, 1863–1871.
- [8] a) V. S. Bryantsev, F. Faglioni, *J. Phys. Chem. A* **2012**, *116*, 7128–7138; b) V. S. Bryantsev, V. Giordani, W. Walker, M. Blanco, S. Zecevic, K. Sasaki, J. Uddin, D. Addison, G. V. Chase, *J. Phys. Chem. A* **2011**, *115*, 12399–12409; c) M. Carboni, A. G. Marrani, R. Spezia, S. Brutti, *Chem. Eur. J.* **2016**, *22*, 17188–17203; d) A. Khetan, H. Pitsch, V. Viswanathan, *J. Phys. Chem. Lett.* **2014**, *5*, 2419–2424; e) N. Mahne, O. Fontaine, M. O. Thotiyil, M. Wilkening, S. A. Freunberger, *Chem. Sci.* **2017**, *8*, 6716–6729.

- [9] a) P. R. Ogilby, *Chem. Soc. Rev.* **2010**, *39*, 3181–3209; b) J. Wandt, P. Jakes, J. Granwehr, H. A. Gasteiger, R.-A. Eichel, *Angew. Chem. Int. Ed.* **2016**, *55*, 6892–6895; *Angew. Chem.* **2016**, *128*, 7006–7009.
- [10] N. Mahne, B. Schafzahl, C. Leypold, M. Leypold, S. Grumm, A. Leitgeb, G. A. Strohmeier, M. Wilkening, O. Fontaine, D. Kramer, C. Slugovc, S. M. Borisov, S. A. Freunberger, *Nat. Energy* **2017**, *2*, 17036.
- [11] Y. Zhang, L. Ma, L. Zhang, Z. Peng, *J. Electrochem. Soc.* **2016**, *163*, A1270–A1274.
- [12] a) D. H. Chin, G. Chiericato, E. J. Nanni, D. T. Sawyer, *J. Am. Chem. Soc.* **1982**, *104*, 1296–1299; b) C. P. Andrieux, P. Hapiot, J. M. Saveant, *J. Am. Chem. Soc.* **1987**, *109*, 3768–3775; c) Y. Che, M. Tsushima, F. Matsumoto, T. Okajima, K. Tokuda, T. Ohsaka, *J. Phys. Chem.* **1996**, *100*, 20134–20137.
- [13] X. Gao, Z. P. Jovanov, Y. Chen, L. R. Johnson, P. G. Bruce, *Angew. Chem. Int. Ed.* **2017**, *56*, 6539–6543; *Angew. Chem.* **2017**, *129*, 6639–6643.
- [14] a) E. J. Corey, M. M. Mehrotra, A. U. Khan, *Biochem. Biophys. Res. Commun.* **1987**, *145*, 842–846; b) A. U. Khan, *J. Am. Chem. Soc.* **1981**, *103*, 6516–6517; c) W. H. Koppenol, *Nature* **1976**, *262*, 420–421; d) E. A. Mayeda, A. J. Bard, *J. Am. Chem. Soc.* **1974**, *96*, 4023–4024.

Manuscript received: September 10, 2017

Accepted manuscript online: October 11, 2017

Version of record online: November 2, 2017



VIP **Batterien** Very Important PaperDeutsche Ausgabe: DOI: 10.1002/ange.201709351  
Internationale Ausgabe: DOI: 10.1002/anie.201709351

## Singulett-Sauerstoff in der aprotischen Natrium-O<sub>2</sub>-Batterie

Lukas Schafzahl<sup>†</sup>, Nika Mahne<sup>†</sup>, Bettina Schafzahl, Martin Wilkening, Christian Slugovc, Sergey M. Borisov und Stefan A. Freunberger\*

**Abstract:** Aprotische Natrium-O<sub>2</sub>-Batterien basieren auf der reversiblen Bildung und Auflösung von Natrium-superoxid (NaO<sub>2</sub>) während des Zellbetriebs. Nebenreaktionen des Elektrolyten und der Elektrode mit dem stark nukleophilen und basischen NaO<sub>2</sub> führen zu mangelhafter Zyklenstabilität. Seine Reaktivität allein kann die Nebenreaktionen und schlechte Reversibilität jedoch nicht schlüssig erklären. Hier wird gezeigt, dass Singulett-Sauerstoff (<sup>1</sup>O<sub>2</sub>) in allen Phasen des Betriebs entsteht und eine Hauptursache für Nebenreaktionen ist. <sup>1</sup>O<sub>2</sub> wurde *in situ* und *ex situ* mit einem <sup>1</sup>O<sub>2</sub>-Fänger detektiert, der schnell und selektiv ein Addukt mit <sup>1</sup>O<sub>2</sub> bildet. Mechanistisch betrachtet entsteht <sup>1</sup>O<sub>2</sub> entweder durch protonenunterstützte Disproportionierung von Superoxid während des Entladens, Lagerns und Ladens unter ca. 3.3 V oder durch direkte elektrochemische <sup>1</sup>O<sub>2</sub>-Entwicklung über ca. 3.3 V. Spuren von Wasser ermöglichen hohe Kapazitäten, beschleunigen aber auch Nebenreaktionen. Daher muss das hochreaktive <sup>1</sup>O<sub>2</sub> unbedingt kontrolliert werden, um die Zelle reversibel zu betreiben.

Die Notwendigkeit, bei Batterien die Grenzen jetziger Technologien bezüglich Energie, Nachhaltigkeit und Kosten zu überwinden, hat enormes Interesse an wiederaufladbaren, aprotischen Metall-O<sub>2</sub>-Batterien hervorgerufen.<sup>[1]</sup> Li-O<sub>2</sub>- und Na-O<sub>2</sub>-Zellen speichern Ladung, indem sie in der Kathode reversibel Li<sub>2</sub>O<sub>2</sub> oder NaO<sub>2</sub> bilden und auflösen. Obwohl NaO<sub>2</sub> eine niedrigere spezifische Kapazität von 488 mAhg<sup>-1</sup> und eine Spannung von nur 2.27 V aufweist (gegenüber 1168 mAhg<sup>-1</sup> bei 2.96 V für Li<sub>2</sub>O<sub>2</sub>), wurde von bedeutenden Vorteilen der Na-O<sub>2</sub>-Zelle berichtet, vor allem in Bezug auf die Wiederaufladbarkeit und die Energieeffizienz.<sup>[2]</sup> Die

praktische Umsetzung der Na-O<sub>2</sub>-Zelle steht allerdings immer noch vor vielen Herausforderungen, darunter die Na-Metall-Anode, die gegenüber theoretischen Werten geringere Kapazität der Kathode und vor allem die schlechte Zyklenstabilität, die durch Nebenreaktionen an der Kathode verursacht wird.<sup>[2,3]</sup>

Seit den ersten veröffentlichten Arbeiten zu Na-O<sub>2</sub>-Batterien wurde Superoxid für die Nebenreaktionen mit dem Elektrolyten und der Elektrode verantwortlich gemacht.<sup>[1c,3,4]</sup> Eine wichtige Kenngröße für diese Nebenreaktionen ist das Verhältnis zwischen umgesetzten e<sup>-</sup> und verbrauchtem/freigesetztem O<sub>2</sub>. Während der Entladung entspricht diese Größe meist dem theoretischen Wert von eins, obwohl ca. 5 % des erwarteten NaO<sub>2</sub> fehlen und durch Nebenprodukte wie Na<sub>2</sub>CO<sub>3</sub>, Natriumacetat und Natriumformiat ersetzt sind. Während der darauffolgenden Lagerung und Ladung bilden sich mehr dieser Nebenprodukte, und das e<sup>-</sup>/O<sub>2</sub>-Verhältnis weicht typischerweise einige Prozent von eins ab.<sup>[2a,3c,4b,5]</sup> Auch wenn weniger Nebenprodukte gebildet werden als in einer Li-O<sub>2</sub>-Zelle, ist die Zyklenstabilität ähnlich schlecht: Beschränkte Kapazitäten können bis zu einigen hundert Zyklen aufrechterhalten werden, doch dies geht zulasten der wahren Energie. Bei voller Entladung fallen die Zellen hingegen schon bei ca. zehn Zyklen aus, und der Kapazitätsverlust verschlimmert sich noch durch höhere Spannungsgrenzen.<sup>[1c,2a,c,d,3a,d,6]</sup>

Die Reaktivität von Superoxid mit organischen Verbindungen entspringt seinen nukleophilen, basischen und radikalischen Eigenschaften, die zur Abstraktion von H<sup>+</sup> und H-Atomen führen können.<sup>[7]</sup> Theoretische Arbeiten haben allerdings gezeigt, dass all diese Reaktionen unwahrscheinlich sind, weil sie bei den häufig verwendeten Etherelektrolyten stark endotherm sind und hohe Aktivierungsenergien aufweisen.<sup>[8]</sup> Außerdem entspricht das Ausmaß der Nebenreaktionen nicht der Menge an Superoxid. Die Reaktivität von Superoxid kann daher die Nebenreaktionen nicht schlüssig erklären. Ein tieferes Verständnis reaktiver Spezies und ihrer Entstehung ist daher erforderlich, um Nebenreaktionen zu verhindern.

Hier identifizieren wir Singulett-Sauerstoff (<sup>1</sup>Δ<sub>g</sub> oder <sup>1</sup>O<sub>2</sub>), den ersten angeregten Zustand des Triplett-Sauerstoffs (<sup>3</sup>Σ<sub>g</sub><sup>-</sup> oder <sup>3</sup>O<sub>2</sub>), als die reaktive Spezies, die Nebenreaktionen verursacht. <sup>1</sup>O<sub>2</sub> wird in allen Phasen des Zellbetriebs gebildet. Die Menge an <sup>1</sup>O<sub>2</sub> gleicht jener der Nebenreaktionen: relativ wenig während Entladung, Lagerung und Ladung bei niedrigen Spannungen und wesentlich mehr bei der Ladung mit höheren Spannungen.

Empfindliche Detektion von <sup>1</sup>O<sub>2</sub> basiert auf chemischen Sonden, die selektiv mit <sup>1</sup>O<sub>2</sub> reagieren. Dazu gehören Radikalfänger und Fluorophore, die durch die Reaktion mit <sup>1</sup>O<sub>2</sub> EPR-aktiv werden oder fluoreszieren.<sup>[9]</sup> Diese Sonden sind

[\*] L. Schafzahl,<sup>[†]</sup> N. Mahne,<sup>[†]</sup> B. Schafzahl, Prof. M. Wilkening, Prof. C. Slugovc, Dr. S. A. Freunberger  
Institut für Chemische Technologie von Materialien  
Technische Universität Graz  
Stremayrgasse 9, 8010 Graz (Österreich)  
E-Mail: freunberger@tugraz.at

Prof. S. M. Borisov  
Institut für Analytische Chemie und Lebensmittelchemie  
Technische Universität Graz  
Stremayrgasse 9, 8010 Graz (Österreich)

[†] Diese Autoren trugen gleichermaßen zu dieser Arbeit bei.

Hintergrundinformationen und die Identifikationsnummern (ORCID) einiger Autoren sind unter: <https://doi.org/10.1002/ange.201709351> zu finden.

© 2017 Die Autoren. Veröffentlicht von Wiley-VCH Verlag GmbH & Co. KGaA. Dieser Open Access Beitrag steht unter den Bedingungen der Creative Commons Attribution Non-Commercial License, die eine Nutzung, Verbreitung und Vervielfältigung in allen Medien gestattet, sofern der ursprüngliche Beitrag ordnungsgemäß zitiert und nicht für kommerzielle Zwecke genutzt wird.

jedoch im Spannungsfenster zwischen ca. 2 und 3.6 V nicht elektrochemisch stabil und können mit Superoxid reagieren. Erst kürzlich haben wir gezeigt, dass 9,10-Dimethylantracen (DMA) alle Bedingungen erfüllt:<sup>[10]</sup> Es ist stabil gegen Superoxid, reagiert schnell mit  $^1\text{O}_2$  zum entsprechenden Endoperoxid (DMA- $\text{O}_2$ ) und hat ein ausreichend großes Stabilitätsfenster (Abbildung S1 und Schema S1 der Hintergrundinformationen).  $^1\text{O}_2$  wird dann entweder über den DMA-Verbrauch mittels Absorption oder Fluoreszenz bei  $\lambda = 300\text{--}500\text{ nm}$  (Abbildung S2) beobachtet oder durch die Bestimmung von DMA und DMA- $\text{O}_2$  mittels HPLC.

Um zu untersuchen, ob sich  $^1\text{O}_2$  während des Ladens und Entladens bildet, bauten wir Na- $\text{O}_2$ -Zellen mit einem Elektrolyten aus 0.5 M  $\text{NaSO}_3\text{CF}_3$  (NaOTf) in Diglyme, 40 ppm Wasser und 30 mM DMA (weitere Details siehe Hintergrundinformationen). Das Wasser wurde zugesetzt, da Wasser bekanntermaßen als Phasentransferkatalysator für das Wachstum von großen  $\text{NaO}_2$ -Partikeln benötigt wird.<sup>[2c]</sup> Außerdem verwendeten wir das Interkalationsmaterial  $\text{Na}_{3-x}\text{V}_2(\text{PO}_4)_3$  als Gegenelektrode, um ungewünschte Reaktionen des Elektrolyten mit einer Na-Metall-Anode zu vermeiden und unsere Untersuchung so auf die Kathode zu beschränken. Dieses Material arbeitet bei ca. 3.4 V gegen  $\text{Na}/\text{Na}^+$  und befindet sich damit deutlich im Stabilitätsfenster des

Elektrolyten.<sup>[11]</sup> Die Zellen wurden mit Konstantstrom bis zu verschiedenen Punkten entladen und geladen. Anschließend wurden die Entlade-/Ladevorgänge gestoppt, und der Elektrolyt wurde extrahiert und mittels HPLC analysiert (Abbildung 1).

Die Spannungskurve zeigt flache Entlade- und Ladeplateaus bei ca. 2.2 bzw. 2.3 V. Sobald die Ladung 55 % erreicht, steigt die Spannung steil an (Abbildung 1a). Das würfelförmige Entladeprodukt wurde mittels Röntgenbeugung (XRD) als  $\text{NaO}_2$  identifiziert (Abbildungen S3 und S4), was mit zahlreichen Berichten zu ähnlichen Zellen übereinstimmt.<sup>[1b,c,2a,b,3a]</sup> Nach dem Entladen oder Laden bis 2.8 und 3.65 V, wo die Elektrolytproben ①, ② und ③ gezogen wurden, waren 4.1, 4.3 bzw. 7.2 % des DMA zu DMA- $\text{O}_2$  umgesetzt (Abbildung 1b). Diese DMA- $\text{O}_2$ -Mengen bedeuten, dass 1.4, 1.3 bzw. 2.1 % des Sauerstoffs (basierend auf der Kapazität im jeweiligen Ladungszustand) in  $^1\text{O}_2$  umgewandelt wurden.  $^1\text{O}_2$ -Sauerstoff wird also während des Ladens und des Entladens generiert, und das Laden auf hohe Spannungen ergibt wesentlich mehr  $^1\text{O}_2$ .

Operando-Spektroskopie ermöglicht es, Startpotentiale und Reaktionsgeschwindigkeiten im Detail zu untersuchen. Dazu wurde eine operando-Fluoreszenzelle verwendet, wie im Methodenteil beschrieben. Die Zelle bestand aus Kohlenstoffpapier als Arbeitselektrode,  $\text{Na}_{3-x}\text{V}_2(\text{PO}_4)_3$  als Gegen- und Referenzelektrode und einem mit  $\text{O}_2$  gefüllten Gasraum. Der sauerstoffgesättigte Elektrolyt war derselbe wie zuvor, jedoch mit niedrigerer DMA-Konzentration ( $1.6 \times 10^{-5}\text{ M}$ ), um optimale Fluoreszenzdetektion zu ermöglichen (siehe Hintergrundinformationen). Anregungs- und Emissionswellenlängen wurden anhand der Maxima der jeweiligen Spektren gewählt (Abbildung S2).

In Zellen wie in Abbildung 1 mit einem porösen Separator zwischen Arbeits- und Gegenelektrode entsteht meist  $\text{NaO}_2$ . Im Unterschied dazu entstand in der operando-Zelle  $\text{Na}_2\text{O}_2 \cdot \text{H}_2\text{O}$ , was sich von der hohen Ladespannung ableiten lässt (Abbildung S5). Die ähnliche thermodynamische Stabilität von  $\text{NaO}_2$  und  $\text{Na}_2\text{O}_2$  ( $E_{\text{O}_2/\text{NaO}_2}^0 = 2.27\text{ V}$ ,  $E_{\text{O}_2/\text{Na}_2\text{O}_2}^0 = 2.33\text{ V}$ ) wurde als Erklärung herangezogen, warum Na- $\text{O}_2$ -Zellen beide Entladeprodukte bilden können.<sup>[1b,3b]</sup> Das Entladeprodukt wird entscheidend von Protonenquellen bestimmt, die genauen Einflussgrößen sind aber unbekannt.<sup>[1b]</sup> Die Ursachen für  $\text{Na}_2\text{O}_2$  statt  $\text{NaO}_2$  als Entladeprodukt in der operando-Zelle könnten das große Elektrolyt-zu-Elektrode-Volumenverhältnis und der gerührte Elektrolyt sein. Beide sind für die Methode unerlässlich. Nach der Entladung enthielt der Elektrolyt ebenfalls DMA- $\text{O}_2$ , was bedeutet, dass sich  $^1\text{O}_2$  auch beim Entladen zu  $\text{Na}_2\text{O}_2$  bildet (Abbildung S6).

Um das Laden von  $\text{NaO}_2$  zu untersuchen, entluden wir zuerst eine Kathode in einer gewöhnlichen Zelle und platzierten sie danach in der operando-Zelle. Abbildung 2 zeigt die DMA-Konzentration und die Geschwindigkeit des Verbrauchs für stufenweises potentiostatisches Laden bis 3.7 V. Sobald die Zelle auf Ladespannungen polarisiert wurde, wurde DMA langsam verbraucht. Über einer Spannung von ca. 3.3 V stieg der Verbrauch rapide an. Thermodynamisch ist die Bildung von  $^1\text{O}_2$  durch elektrochemische Oxidation von  $\text{NaO}_2$  oberhalb  $E_{\text{O}_2/\text{NaO}_2}^0 + E(^1\Delta_g \leftarrow ^3\Sigma_g^-)$  zu erwarten. Bei einer Energiedifferenz von 0.97 eV zwischen  $^1\text{O}_2$  und  $^3\text{O}_2$

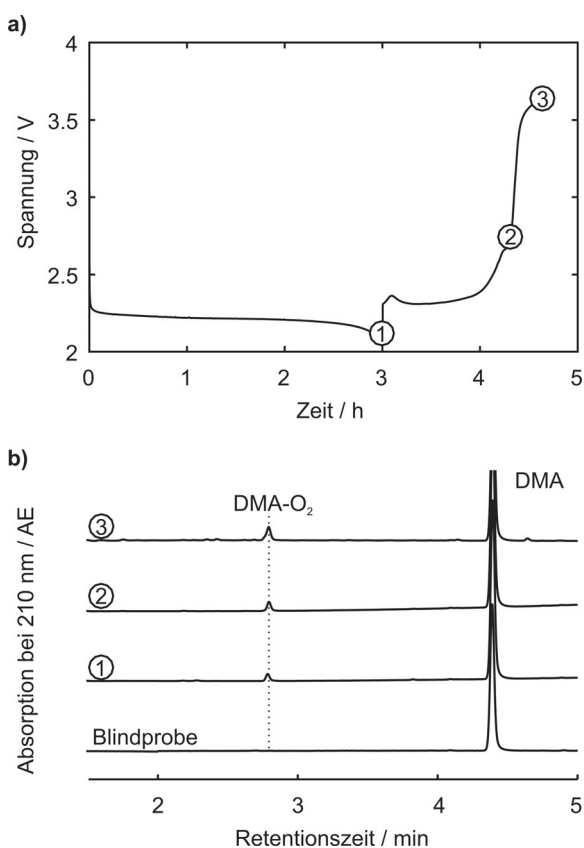


**Abbildung 1.** a) Ladekurve von galvanostatisch entladenen und geladenen Elektroden aus Kohlenstoffpapier bei  $90\ \mu\text{A cm}^{-2}$  in 0.5 M NaOTf in Diglyme mit 40 ppm  $\text{H}_2\text{O}$  und 30 mM DMA. b) HPLC-Analysen von Elektrolytproben zeigen die Bildung von  $^1\text{O}_2$  durch die Reaktion von DMA zu DMA- $\text{O}_2$ . Die Proben wurden an den Punkten ①, ② und ③ in (a) genommen, die Blindprobe wurde aus einer 5 h lang gelagerten Zelle extrahiert.

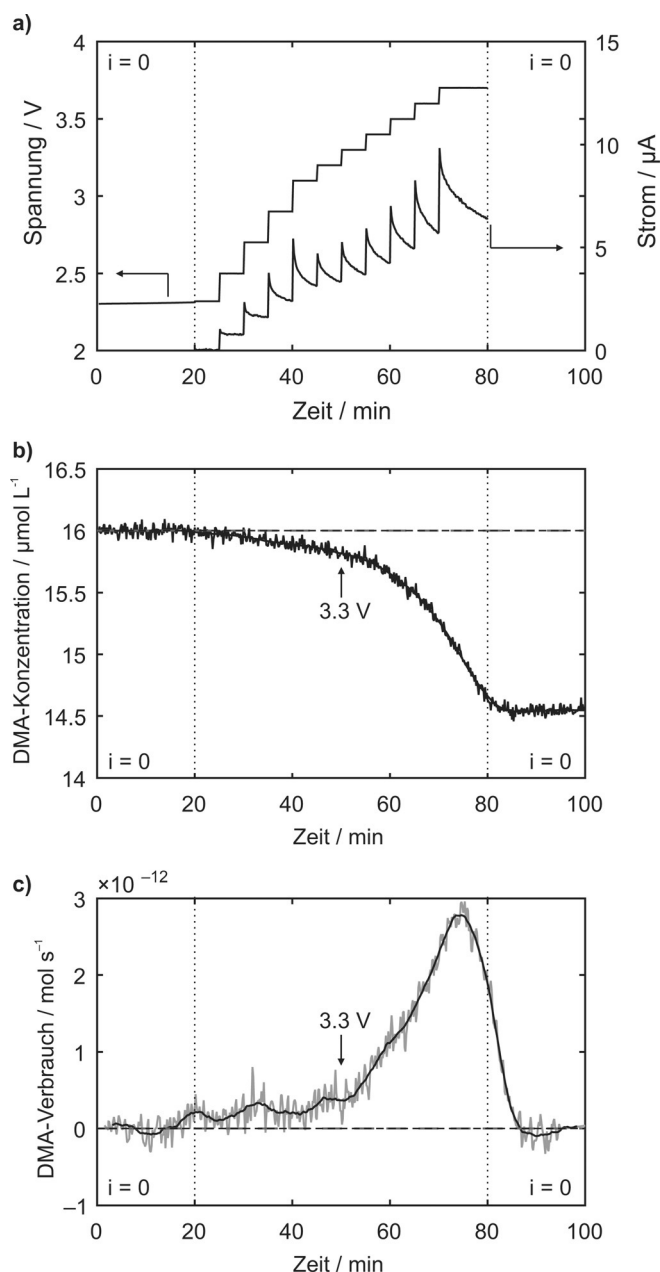


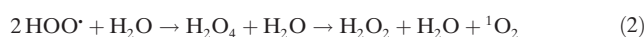
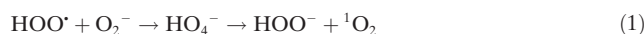
**Abbildung 2.** Operando-Fluoreszenzdetektion von  $^1\text{O}_2$  während potentiostatischen Ladens einer  $\text{Na-O}_2$ -Kathode. Die Kathode aus Kohlenstoffpapier wurde zuerst in einer Swagelokzelle bei  $75 \text{ mAh cm}^{-2}$  in  $0.5 \text{ M NaOTf}$  in Diglyme mit  $40 \text{ ppm}$  Wasser entladen und dann in einer operando-Zelle mit demselben Elektrolyten mit zusätzlich  $1.6 \times 10^{-5} \text{ M DMA}$  platziert. a) Spannungs- und Stromprofil. b) DMA-Konzentration. c) Geschwindigkeit des DMA-Verbrauchs.

kann eine thermodynamische Schwelle von  $3.24 \text{ V}$  abgeschätzt werden. Die hohe Geschwindigkeit, mit der  $^1\text{O}_2$  über ca.  $3.3 \text{ V}$  gebildet wird, erklärt sich also durch die Reaktion  $\text{NaO}_2 \rightarrow \text{Na}^+ + \text{e}^- + ^1\text{O}_2$  über der thermodynamischen Schwelle. Unter  $3.3 \text{ V}$  ist der Anteil von  $^1\text{O}_2$  etwa  $0.75\text{--}1.1\%$  des erwarteten  $\text{O}_2$  (Abbildung S7), darüber steigt dieser Anteil kontinuierlich auf ca.  $4\%$ .

Bisher wurde berichtet, dass Nebenreaktionen hauptsächlich während des Entladens auftreten und weniger während des Ladeplateaus.<sup>[2a,3a]</sup> Das Laden über ca.  $3.5 \text{ V}$  verur-

sacht eine größere Abweichung des  $\text{e}^-/\text{O}_2$ -Verhältnisses von eins als bei niedrigeren Spannungen. Die Kombination dieser Ergebnisse mit jenen aus Abbildung 1, 2 und S7 legt nahe, dass Nebenreaktionen in der  $\text{Na-O}_2$ -Kathode eng mit der  $^1\text{O}_2$ -Bildung zusammenhängen, denn das Ausmaß der Nebenreaktionen folgt genau dem Vorkommen von  $^1\text{O}_2$ : Während des Entladens wird mehr  $^1\text{O}_2$  gebildet als während des Ladens unter  $3.3 \text{ V}$ , und über  $3.3 \text{ V}$  nimmt die Bildung von  $^1\text{O}_2$  stark zu. In quantitativer Hinsicht weisen die  $1.4\%$   $^1\text{O}_2$  während des Entladens und ca.  $95\%$   $\text{NaO}_2$ -Ausbeute auf einen signifikanten Anteil an Nebenprodukten durch  $^1\text{O}_2$  hin. Dabei stellen die gemessenen  $^1\text{O}_2$ -Mengen eine untere Grenze dar, weil  $^1\text{O}_2$  durch die niedrige DMA-Konzentration möglicherweise nicht vollständig mit DMA reagiert und auf anderen Wegen deaktiviert werden könnte, beispielsweise durch die Reaktion mit Zellbestandteilen.

Während die Thermodynamik direkt erklärt, wie  $^1\text{O}_2$  durch die Oxidation von  $\text{NaO}_2$  über  $3.3 \text{ V}$  entsteht, ist die Bildung unter  $3.3 \text{ V}$  überraschender. In der  $\text{Li-O}_2$ -Zelle wurde die Disproportionierung der  $\text{LiO}_2$ -Zwischenstufe zu  $\text{Li}_2\text{O}_2$  als wesentliche  $^1\text{O}_2$ -Quelle während des Entladens und Ladens bei niedrigen Spannungen vorgeschlagen.<sup>[10]</sup> Dieser Reaktionsweg ist in  $\text{Na-O}_2$ -Zellen inaktiv, weil die Entladung bei  $\text{NaO}_2$  endet. Wenn aber Wasser oder andere Protonenquellen vorhanden sind, führt die Reduktion von Sauerstoff zu  $\text{HOO}^\cdot$ .<sup>[12]</sup> Diese lösliche Spezies ermöglicht protonenunterstützte Phasentransferkatalyse, die das Wachstum und die Oxidation der typischen, mikrometergroßen  $\text{NaO}_2$ -Würfels während des Ladens ermöglicht;  $\text{HOO}^\cdot$  ist löslich und mobil im Elektrolyten und fällt  $\text{NaO}_2$  mittels der Metathesereaktion  $\text{HOO}^\cdot + \text{Na}^+ \rightarrow \text{NaO}_2 + \text{H}^+$ .<sup>[2c,13]</sup>  $\text{HOO}^\cdot$  kann durch Superoxid reduziert werden oder über die Gleichungen (1) und (2) disproportionieren,<sup>[12]</sup> in denen erwiesenermaßen  $^1\text{O}_2$  entsteht.<sup>[14]</sup>



Dass Wasser diese Reaktionen antreibt, wird durch die geringere  $^1\text{O}_2$ -Bildung in trockenem als in feuchtem Elektrolyten untermauert (Abbildung S8).

Diese Reaktionen könnten nicht nur während des Entladens stattfinden, wo neues Superoxid entsteht, sondern auch während des Lagerns, denn die Metathesereaktion ist im Gleichgewicht und ermöglicht es dem  $\text{NaO}_2$ , sich wieder in  $\text{HOO}^\cdot$  aufzulösen. Mehrere Studien haben die Instabilität von  $\text{NaO}_2$  während längerer Lagerung gezeigt.<sup>[3c,4-5]</sup> Obwohl sich die Details unterscheiden, zeigen sie im Allgemeinen eine allmähliche Umwandlung von  $\text{NaO}_2$  zu  $\text{Na}_2\text{O}_2 \cdot \text{H}_2\text{O}$ . Gleichzeitig zersetzt sich der Elektrolyt, und es bilden sich  $\text{NaOH}$ ,  $\text{Na}_2\text{CO}_3$  und organische Verbindungen einschließlich Natriumformiat und -acetat. Die Erklärungen hierfür reichen von nukleophilen Angriffen bis zur Abstraktion von  $\text{H}^+$  oder  $\text{H}$ -Atomen durch Superoxid. Um zu überprüfen, wie  $^1\text{O}_2$  die Bildung von Nebenprodukten beeinflusst, entluden wir Elektroden in DMA-freiem Elektrolyten und lagerten sie danach über verschiedene Zeitspannen in Elektrolyten mit  $30 \text{ mM DMA}$ . Nach der Lagerung zeigten XRD-Analysen,



dass der  $\text{NaO}_2$ -Gehalt abnahm und sich Nebenprodukte bildeten, was mit bisherigen Studien übereinstimmt (Abbildung S9). Der Elektrolyt wurde danach auf DMA- $\text{O}_2$  hin untersucht, die Elektroden auf ihren  $\text{Na}_2\text{CO}_3$ -Gehalt. Dazu wurden sie mit 0.1M  $\text{H}_2\text{SO}_4$  versetzt, und das gebildete  $\text{CO}_2$  wurde mittels Massenspektrometrie gemessen (Abbildung 3).

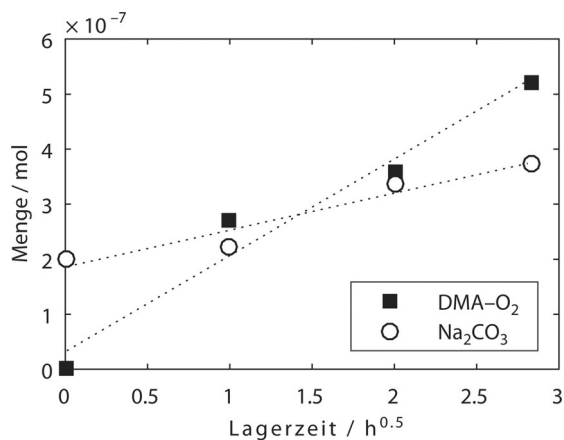


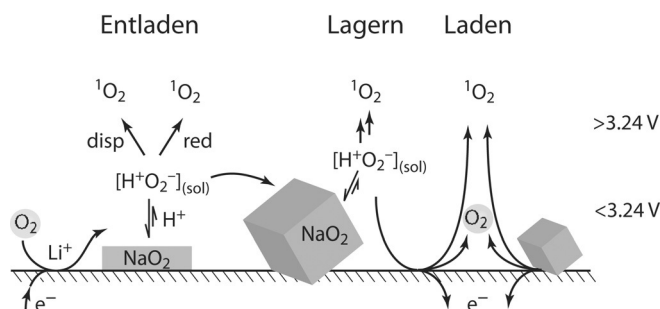
**Abbildung 3.**  $^1\text{O}_2$ -Bildung und Nebenreaktionen während der Lagerung des Entladeprodukts  $\text{NaO}_2$  im Elektrolyten. Die Zellen wurden zuerst in DMA-freiem Elektrolyten entladen (0.5M NaOTf in Diglyme mit 40 ppm  $\text{H}_2\text{O}$ ), danach wurden die Kathoden gewaschen und im selben Elektrolyten mit zusätzlich 30 mM DMA gelagert. Nach den angegebenen Zeiten wurden der Elektrolyt auf DMA- $\text{O}_2$  und die Elektroden auf  $\text{Na}_2\text{CO}_3$  analysiert. Die gepunkteten Linien sind lineare Regressionsgeraden gegen die Quadratwurzel der Lagerungszeit.

Die Menge an DMA- $\text{O}_2$  und damit auch an  $^1\text{O}_2$  nimmt kontinuierlich zu, genauso wie der  $\text{Na}_2\text{CO}_3$ -Gehalt als Indiz für die Menge an Nebenprodukten.

DMA- $\text{O}_2$  und  $\text{Na}_2\text{CO}_3$  nehmen ungefähr proportional zur Quadratwurzel der Lagerungszeit zu. Das bedeutet, die Bildungsgeschwindigkeit verringert sich mit der Zeit. Die gebildeten Nebenprodukte passivieren daher teilweise die  $\text{NaO}_2$ -Oberfläche und verlangsamen die weitere Zersetzung. Dass sich mehr DMA- $\text{O}_2$  als zusätzliches  $\text{Na}_2\text{CO}_3$  bildet, kann durch zwei Phänomene erklärt werden: Erstens reagiert das von DMA gefangene  $^1\text{O}_2$  nicht mehr mit Zellbestandteilen, weshalb es ohne DMA noch mehr Nebenprodukte gäbe. Zweitens werden sich auch andere Produkte als  $\text{Na}_2\text{CO}_3$  bilden, die nicht durch Säure abgebaut werden. Insgesamt zeigt Abbildung 3, dass die bereits beobachtete Elektrolytzersetzung während der Lagerung zu einem bedeutenden Teil von  $^1\text{O}_2$  verursacht wird.

Die Reaktionswege zu  $^1\text{O}_2$  während Entladung, Ladung und Lagerung sind in Schema 1 zusammengefasst. Wir schlagen vor, dass protonenunterstützte Disproportionierung oder Reduktion mit Superoxid in das Gleichgewicht der Metathesereaktion  $\text{HOO}^\bullet + \text{Na}^+ \rightleftharpoons \text{NaO}_2 + \text{H}^+$  eingreift und einen allgemeinen Weg zu  $^1\text{O}_2$  während aller Phasen des Zellbetriebs bildet. Während des Ladens bei Spannungen über der thermodynamischen Schwelle von 3.24 V wird  $^1\text{O}_2$  durch direkte elektrochemische Oxidation über die Reaktion  $\text{NaO}_2 \rightarrow \text{Na}^+ + \text{e}^- + ^1\text{O}_2$  freigesetzt.

Zusammenfassend zeigen wir, dass sich Singulett-Sauerstoff an der Kathode von  $\text{NaO}_2$ -Zellen während aller Phasen des Zellbetriebs und während der Lagerung bildet und für



**Schema 1.** Reaktionswege zu  $^1\text{O}_2$  während des Entladens, Lagerns und Ladens. „disp“ und „red“ bezeichnen Disproportionierungs- bzw. Reduktionsschritte.

einen bedeutenden Teil der gebildeten Nebenprodukte verantwortlich ist.  $^1\text{O}_2$  stellt daher eine bedeutende Hürde für die reversible Bildung und Auflösung von  $\text{NaO}_2$  und damit für den Betrieb von  $\text{NaO}_2$ -Zellen dar. Wasser nimmt dabei eine ambivalente Rolle ein, indem es durch lösungsunterstütztes Wachstum und Auflösung von  $\text{NaO}_2$ -Partikeln hohe Kapazitäten fördert, aber zugleich die Hauptursache für  $^1\text{O}_2$ -Bildung während der Entladung und Ladung bei niedrigen Spannungen ist. Zukünftige Arbeiten sollten den Fokus daher auf Möglichkeiten legen,  $^1\text{O}_2$ -Bildung zu verhindern oder effektiv zu unterdrücken.

## Danksagung

S.A.F. dankt dem Europäischen Forschungsrat unter dem Horizon 2020 Forschungs- und Innovationsprogramm (Projektnummer 636069) der Europäischen Union, dem Österreichischen Bundesministerium für Wissenschaft, Forschung und Wirtschaft und der Österreichischen Forschungsförderungsgesellschaft (Förderungsnummer 845364) für die Unterstützung. Wir danken G. Strohmeier für die Hilfe bei den HPLC-Messungen und J. Schlegl für die Anfertigung der für die Methoden notwendigen Apparaturen.

## Interessenkonflikt

Die Autoren erklären, dass keine Interessenkonflikte vorliegen.

**Stichwörter:** Elektrochemie ·  $\text{NaO}_2$ -Batterien · Nebenreaktionen · Reaktionsmechanismen · Singulett-Sauerstoff

**Zitierweise:** *Angew. Chem. Int. Ed.* **2017**, *56*, 15728–15732  
*Angew. Chem.* **2017**, *129*, 15934–15938

- [1] a) D. Aurbach, B. D. McCloskey, L. F. Nazar, P. G. Bruce, *Nat. Energy* **2016**, *1*, 16128; b) C. L. Bender, D. Schröder, R. Pinedo, P. Adelhelm, J. Janek, *Angew. Chem. Int. Ed.* **2016**, *55*, 4640–4649; *Angew. Chem.* **2016**, *128*, 4716–4726; c) P. Hartmann, C. L. Bender, M. Vračar, A. K. Dürr, A. Garsuch, J. Janek, P. Adelhelm, *Nat. Mater.* **2012**, *12*, 228–232.  
[2] a) B. D. McCloskey, J. M. Garcia, A. C. Luntz, *J. Phys. Chem. Lett.* **2014**, *5*, 1230–1235; b) R. Morasch, D. G. Kwabi, M. Tul-

- odziecki, M. Risch, S. Zhang, Y. Shao-Horn, *ACS Appl. Mater. Interfaces* **2017**, *9*, 4374–4381; c) C. Xia, R. Black, R. Fernandes, B. Adams, L. F. Nazar, *Nat. Chem.* **2015**, *7*, 496–501; d) I. Landa-Medrano, C. Li, N. Ortiz-Vitoriano, I. Ruiz de Larramendi, J. Carrasco, T. Rojo, *J. Phys. Chem. Lett.* **2016**, *7*, 1161–1166.
- [3] a) P. Hartmann, C. L. Bender, J. Sann, A. K. Durr, M. Jansen, J. Janek, P. Adelhelm, *Phys. Chem. Chem. Phys.* **2013**, *15*, 11661–11672; b) C. L. Bender, P. Hartmann, M. Vračar, P. Adelhelm, J. Janek, *Adv. Energy Mater.* **2014**, *4*, 1301863; c) S. Y. Sayed, K. P. C. Yao, D. G. Kwabi, T. P. Batcho, C. V. Amanchukwu, S. Feng, C. V. Thompson, Y. Shao-Horn, *Chem. Commun.* **2016**, *52*, 9691–9694; d) M. He, K. C. Lau, X. Ren, N. Xiao, W. D. McCulloch, L. A. Curtiss, Y. Wu, *Angew. Chem. Int. Ed.* **2016**, *55*, 15310–15314; *Angew. Chem.* **2016**, *128*, 15536–15540.
- [4] a) J. Kim, H. Park, B. Lee, W. M. Seong, H.-D. Lim, Y. Bae, H. Kim, W. K. Kim, K. H. Ryu, K. Kang, *Nat. Commun.* **2016**, *7*, 10670; b) T. Liu, G. Kim, M. T. L. Casford, C. P. Grey, *J. Phys. Chem. Lett.* **2016**, *7*, 4841–4846.
- [5] I. Landa-Medrano, R. Pinedo, X. Bi, I. Ruiz de Larramendi, L. Lezama, J. Janek, K. Amine, J. Lu, T. Rojo, *ACS Appl. Mater. Interfaces* **2016**, *8*, 20120–20127.
- [6] S. A. Freunberger, *Nat. Energy* **2017**, *2*, 17091.
- [7] a) D. T. Sawyer, J. S. Valentine, *Acc. Chem. Res.* **1981**, *14*, 393–400; b) D. Aurbach, M. L. Daroux, P. W. Faguy, E. Yeager, *J. Electrochem. Soc.* **1988**, *135*, 1863–1871.
- [8] a) V. S. Bryantsev, F. Faglioni, *J. Phys. Chem. A* **2012**, *116*, 7128–7138; b) V. S. Bryantsev, V. Giordani, W. Walker, M. Blanco, S. Zecevic, K. Sasaki, J. Uddin, D. Addison, G. V. Chase, *J. Phys. Chem. A* **2011**, *115*, 12399–12409; c) M. Carboni, A. G. Marrani, R. Spezia, S. Brutti, *Chem. Eur. J.* **2016**, *22*, 17188–17203; d) A. Khetan, H. Pitsch, V. Viswanathan, *J. Phys. Chem. Lett.* **2014**, *5*, 2419–2424; e) N. Mahne, O. Fontaine, M. O. Thotiyl, M. Wilkening, S. A. Freunberger, *Chem. Sci.* **2017**, *8*, 6716–6729.
- [9] a) P. R. Ogilby, *Chem. Soc. Rev.* **2010**, *39*, 3181–3209; b) J. Wandt, P. Jakes, J. Granwehr, H. A. Gasteiger, R.-A. Eichel, *Angew. Chem. Int. Ed.* **2016**, *55*, 6892–6895; *Angew. Chem.* **2016**, *128*, 7006–7009.
- [10] N. Mahne, B. Schafzahl, C. Leypold, M. Leypold, S. Grumm, A. Leitgeb, G. A. Strohmeier, M. Wilkening, O. Fontaine, D. Kramer, C. Slugovc, S. M. Borisov, S. A. Freunberger, *Nat. Energy* **2017**, *2*, 17036.
- [11] Y. Zhang, L. Ma, L. Zhang, Z. Peng, *J. Electrochem. Soc.* **2016**, *163*, A1270–A1274.
- [12] a) D. H. Chin, G. Chiericato, E. J. Nanni, D. T. Sawyer, *J. Am. Chem. Soc.* **1982**, *104*, 1296–1299; b) C. P. Andrieux, P. Hapiot, J. M. Saveant, *J. Am. Chem. Soc.* **1987**, *109*, 3768–3775; c) Y. Che, M. Tsushima, F. Matsumoto, T. Okajima, K. Tokuda, T. Ohsaka, *J. Phys. Chem.* **1996**, *100*, 20134–20137.
- [13] X. Gao, Z. P. Jovanov, Y. Chen, L. R. Johnson, P. G. Bruce, *Angew. Chem. Int. Ed.* **2017**, *56*, 6539–6543; *Angew. Chem.* **2017**, *129*, 6639–6643.
- [14] a) E. J. Corey, M. M. Mehrotra, A. U. Khan, *Biochem. Biophys. Res. Commun.* **1987**, *145*, 842–846; b) A. U. Khan, *J. Am. Chem. Soc.* **1981**, *103*, 6516–6517; c) W. H. Koppenol, *Nature* **1976**, *262*, 420–421; d) E. A. Mayeda, A. J. Bard, *J. Am. Chem. Soc.* **1974**, *96*, 4023–4024.

Manuskript erhalten: 10. September 2017

Akzeptierte Fassung online: 11. Oktober 2017

Endgültige Fassung online: 2. November 2017

## 5.4 An attempt to mitigate <sup>1</sup>O<sub>2</sub> induced parasitic reactions

In the paper we have demonstrated that <sup>1</sup>O<sub>2</sub> occurs in Na-O<sub>2</sub> batteries. The logical follow-up would be to negate or at least mitigate its detrimental effects, which can be achieved in two ways. First, the most fundamental solution would be to forestall <sup>1</sup>O<sub>2</sub> formation. Direct formation of <sup>1</sup>O<sub>2</sub> could be prevented by limiting the upper cutoff potential, but indirect formation involves only NaO<sub>2</sub> and H<sub>2</sub>O, both of which are vital for cell operation.<sup>70</sup> Second, <sup>1</sup>O<sub>2</sub> could be transformed to a less reactive species before it undergoes reactions with cell components. To that end, an additive could be added to the electrolyte that rapidly and selectively reacts with <sup>1</sup>O<sub>2</sub> thereby deactivating it. This would, of course, only mitigate the negative impact of <sup>1</sup>O<sub>2</sub> depending on the relative reaction kinetics of <sup>1</sup>O<sub>2</sub> with the additive and the cell components, but would be practically more feasible.

Possible additives for deactivating <sup>1</sup>O<sub>2</sub> are plentiful and include fluorescein and rhodamine.<sup>210</sup> However, the available options are drastically reduced by stringent requirements regarding their electrochemical and chemical stability.<sup>59</sup> One option would be DMA that was used in this study, but it reacts irreversibly with <sup>1</sup>O<sub>2</sub> and will therefore be depleted sooner or later. More preferable would be a quencher that deactivates <sup>1</sup>O<sub>2</sub> without being consumed, such as 1,4-diazabicyclo[2.2.2]octane (DABCO). DABCO has been shown to operate in non-aqueous systems and to be stable with superoxide,<sup>59,211</sup> but its electrochemical stability in Na based electrolytes had yet to be investigated.

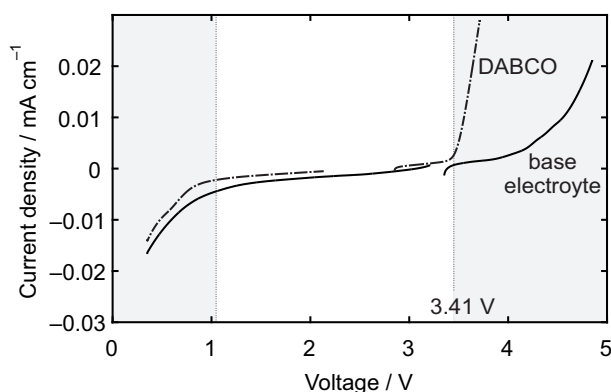


**Figure 5.2:** Electrochemical stability of 2 mM DABCO and the base electrolyte (0.1 M NaOTf in DME). Cyclic voltammetry was performed at a 3 mm glassy carbon disc electrode at a sweep rate of 50 mV s<sup>-1</sup> under Ar atmosphere.

The electrochemical stability of DABCO is presented in Figure 5.2. At reducing voltages, the current response of DABCO resembles the base electrolyte indicating that DABCO is even more stable than the other electrolyte components. At high voltages, in contrast, DABCO severely limits electrolyte stability and starts to decompose rapidly at 3.41 V. The stability window thus suffices for cell operation considering that the upper cutoff should be no higher than 3.24 V to avoid direct <sup>1</sup>O<sub>2</sub> formation.

What remains problematic, though, is the counter electrode. A NVP counter electrode operates at 3.4 V, which means that even minor overpotentials could lead to severe decomposition of DABCO. Indeed, decomposition was observed in cells containing 12 mM DABCO: After cycling, the separator was stained brownish. A Na counter electrode would also induce DABCO decomposition and would only work if the Na is passivated by a protective interface. Still, Na seemed the more promising option thus a Na counter electrode was used in further experiments.

To finally determine whether DABCO mitigates the detrimental effects of <sup>1</sup>O<sub>2</sub>, dupli-

cate cells with and without 12 mM DABCO were discharged to 1 mAh. Another set of cells was discharged to 1 mAh and charged to 3.3 V. The electrodes were then extracted and analyzed by mass spectrometry (see Section 4.2) with respect to  $\text{Na}_2\text{CO}_3$  formation and  $\text{NaO}_2$ -yield, Table 5.1. With DABCO,  $\text{NaO}_2$  yield after discharge decreases from 96.4 % to 84.2 %. This clearly demonstrates that DABCO cannot be considered an inert additive; instead it seems to interfere with the discharge mechanism. Strikingly, the CEs after one complete cycle are identical within margin of error. The apparent contrast between much lower  $\text{NaO}_2$  yield and identical CE can be reconciled if we assume that DABCO does not lead to  $\text{NaO}_2$  as the sole discharge product, but also forms  $\text{Na}_2\text{O}_2$ . Both products have almost equal free enthalpies of formation and the factors that govern selectivity are not yet fully understood.<sup>68,74</sup>  $\text{Na}_2\text{O}_2$ , however, evolves less  $\text{O}_2$  upon contact with acid which would lead to an underestimation of the yield during discharge and could explain this discrepancy. What is more serious, however, is that DABCO does not seem to reduce the amount of  $\text{Na}_2\text{CO}_3$ ; on the contrary, DABCO significantly increases the amount of side products formed. Overall, the negative impact of DABCO outweighs its possible benefits, at least in this cell setup where its stability cannot be guaranteed.

**Table 5.1:** Side product formation and  $\text{NaO}_2$ -yield with and without 12 mM DABCO.

	without DABCO	with DABCO
$\text{NaO}_2$ yield / %	96.4	84.2
$\text{Na}_2\text{CO}_3$ after disch. / mol	$2.0 * 10^{-7}$	$3.7 * 10^{-7}$
$\text{Na}_2\text{CO}_3$ after ch. / mol	$3.7 * 10^{-7}$	$4.2 * 10^{-7}$

In conclusion,  $^1\text{O}_2$  remains a major source of parasitic reactions in Na- $\text{O}_2$  batteries that needs to be addressed. Further research should focus on quenchers that reduce side product formation, as well as the factors governing  $^1\text{O}_2$  formation. While it might not be possible to forestall  $^1\text{O}_2$  formation completely, appropriate conditions could minimize it and thus help to make Na- $\text{O}_2$  batteries a reality.





## 6. Conclusion and outlook

In this thesis parasitic reactions and interphases in various Li-ion and beyond Li-ion chemistries were investigated. A comprehensive study of alkyl carbonates allows to better understand their role in the SEI, where they represent one of the less conductive, but more elastic components. Sodium alkyl carbonates become softer with increasing chain length and could thus contribute to a more flexible and resilient SEI. However, further studies have shown that long chained alkyl carbonates cannot be straightforwardly incorporated into the SEI, presumably due to their high solubility in the electrolyte. Yet, even exchanging dimethyl carbonate for diethyl carbonate in Na-ion batteries could yield a significantly more flexible SEI.

Parasitic reactions in Na-ion half cells could be effectively suppressed by employing a highly concentrated sodium bis(fluorosulfonyl)imide/dimethoxyethane electrolyte, which forms a stable SEI on Na and allows efficient Na cycling. Hopefully, such highly concentrated electrolytes will permit unhindered progress towards advanced intercalation materials for Na-ion batteries. The benefits of highly concentrated electrolytes, however, are not limited to Na-ion batteries and further applications can be envisioned: Their high oxidative and reductive stability could enable batteries with higher voltage, or they could mitigate parasitic reactions with the alkaline metal in Li-O<sub>2</sub> or Na-O<sub>2</sub> batteries.

Both Li-O<sub>2</sub> and Na-O<sub>2</sub> batteries are plagued by parasitic reactions due to singlet oxygen, which forms at all stages of cycling and generates a major part of side products. Inhibiting singlet oxygen in these beyond Li-ion chemistries will require suitable quenchers that are electrochemically and chemically stable in the cell environment. 1,4-diazabicyclo[2.2.2]octane reduced the amount of side products in Li-O<sub>2</sub> cells, but seemed to increase them in Na-O<sub>2</sub> cells. Further quenchers for singlet oxygen are currently investigated in our group, including quaternary ammonium salts and inorganic azides. On a wider scope, other sources of parasitic reactions should be uncovered, quantified and avoided or suppressed to enable metal oxygen batteries with far superior energy densities.



# A. Appendix

## A.1 Supplementary Material

This section contains supplementary material to all the contributions included in the thesis.

- **Long Chain Alkyl Carbonates as Solid Electrolyte Interface Components: Structure, Ion Transport and Mechanical Properties**, see p. 14.
- **An Electrolyte for Reversible Cycling of Sodium Metal and Intercalation Compounds**, see p. 35.  
The original article and supplementary information can be found under: <https://dx.doi.org/10.1002/cssc.201601222>. Reprinted with permission.
- **Quantifying Total Superoxide, Peroxide and Carbonaceous Compounds in Metal-O<sub>2</sub> Batteries and the Solid Electrolyte Interface**, see p. 48.  
The original article and supplementary information can be found under: <https://doi.org/10.1021/acseenergylett.7b01111>. Open access.
- **Singlet Oxygen during Cycling of the Aprotic Sodium-O<sub>2</sub> Battery**, see p. 58.  
The original article and supplementary information can be found under: <https://doi.org/10.1002/anie.201709351> (english) or <https://doi.org/10.1002/ange.201709351> (german). Open access.

## Supporting Information for

# Long Chain Li and Na Alkyl Carbonates as Solid Electrolyte Interface Components: Structure, Ion Transport and Mechanical Properties

Lukas Schafzahl<sup>1</sup>, Heike M. A. Ehmman<sup>1</sup>, Manfred Kriechbaum<sup>2</sup>, Jürgen Sattelkow<sup>3,4</sup>, Thomas Ganner<sup>3</sup>, Harald Plank<sup>3,4</sup>, Martin Wilkening<sup>1,5</sup>, Stefan A. Freunberger<sup>1\*</sup>

<sup>1</sup>Institute for Chemistry and Technology of Materials, Graz University of Technology, Stremayrgasse 9, 8010 Graz, Austria

<sup>2</sup>Institute of Inorganic Chemistry, Graz University of Technology, Stremayrgasse 9, 8010 Graz, Austria

<sup>3</sup>Institute of Electron Microscopy and Nanoanalysis (FELMI), Graz University of Technology, Steyrergasse 17, 8010 Graz, Austria

<sup>4</sup>Graz Centre for Electron Microscopy (ZFE), Steyrergasse 17, 8010 Graz, Austria

<sup>5</sup>Christian Doppler Laboratory for Lithium Batteries, and Institute for Chemistry and Technology of Materials, Graz University of Technology, Stremayrgasse 9, 8010 Graz, Austria

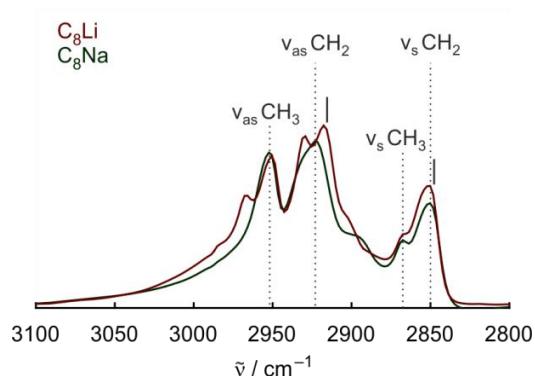


Figure S1. Magnified FTIR spectra of long-chained C<sub>8</sub>Li and C<sub>8</sub>Na showing C-H stretching ( $\nu$ ) vibrations. The relative proximity of the methylene stretch vibrations  $\nu_s CH_2$  and  $\nu_{as} CH_2$  to their position in a crystalline material (black bars) indicate a large part of all-*trans* conformation, while the small distance shows a certain remaining disorder in the system. The intensity ratio  $I_{2850}/I_{2922}$  of these bands is also proportional to the order in the system; it is around 0.65 for both samples. Note that the methyl vibration  $\nu_{as} CH_3$  is split for C<sub>8</sub>Li reveals a low symmetry around the terminal methyl group.

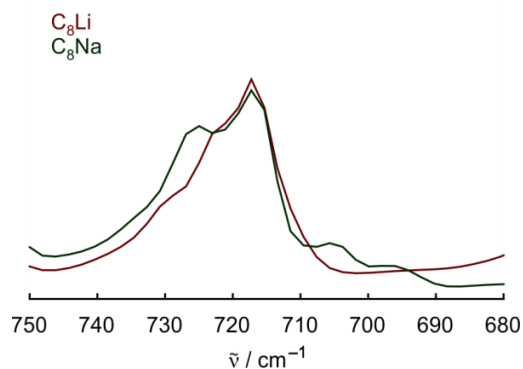


Figure S2. Magnified FTIR spectra of long long-chained  $C_8Li$  and  $C_8Na$  showing C-H rocking ( $\delta$ ) vibrations. The band for  $C_8Na$  is split due to interaction with adjacent alkyl chains. In contrast, the degenerate band of  $C_8Li$  indicates weak inter-chain interaction.

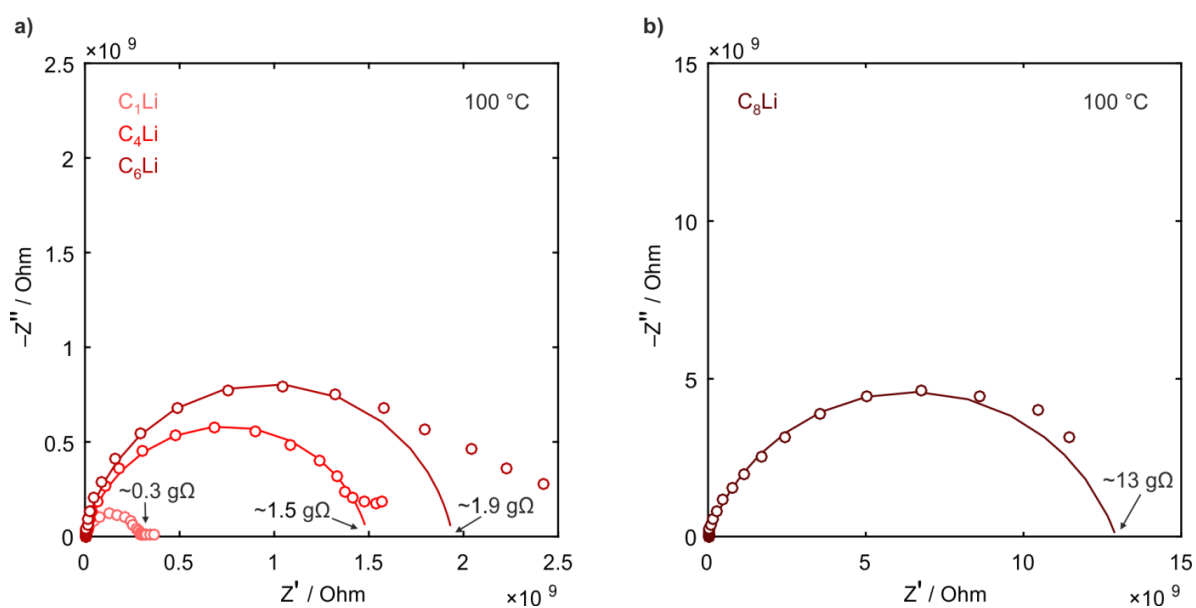


Figure S3: Complex plane plot of  $C_1Li$ ,  $C_4Li$  and  $C_6Li$  (a) and  $C_8Li$  (b) at 100 °C. The solid lines are fits that use an equivalent circuit with a resistor and a constant phase element connected in parallel ( $R_1CPE_1$ ), see Table S1. The capacitances are in the range of 150-300 pF indicating ionic movements along the grain boundaries.

Table S1: Fitting results from Figure S3.

	$R_1 / \Omega$	$\sigma / \text{S cm}^{-1}$	$C_1 / \text{F}$	$n_1$
$\text{C}_1\text{Li}$	$2.9 \times 10^8$	$5.7 \times 10^{-10}$	$1.6 \times 10^{-10}$	0.88
$\text{C}_4\text{Li}$	$1.5 \times 10^9$	$6.8 \times 10^{-11}$	$2.9 \times 10^{-10}$	0.84
$\text{C}_6\text{Li}$	$1.9 \times 10^9$	$4.4 \times 10^{-11}$	$1.8 \times 10^{-10}$	0.88
$\text{C}_8\text{Li}$	$1.3 \times 10^{10}$	$1.2 \times 10^{-11}$	$2.4 \times 10^{-10}$	0.79

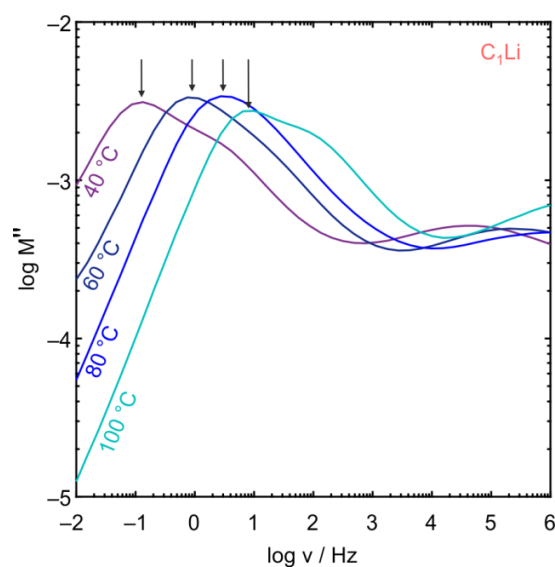


Figure S4. The frequency of the maximum of the electric Modulus  $M''$  depends on temperature, as shown exemplary for  $\text{C}_1\text{Li}$ . This temperature dependence follows an Arrhenius behavior shown in Fig 4c and allows to determine the activation energies using Arrhenius equation  $k = A \times e^{-\frac{E_a}{k_b \times t}}$  where  $k_b$  is the Boltzmann constant. For  $\text{C}_1\text{Li}$ , data extracted from conductivity spectra are plotted versus the right axis for comparison.



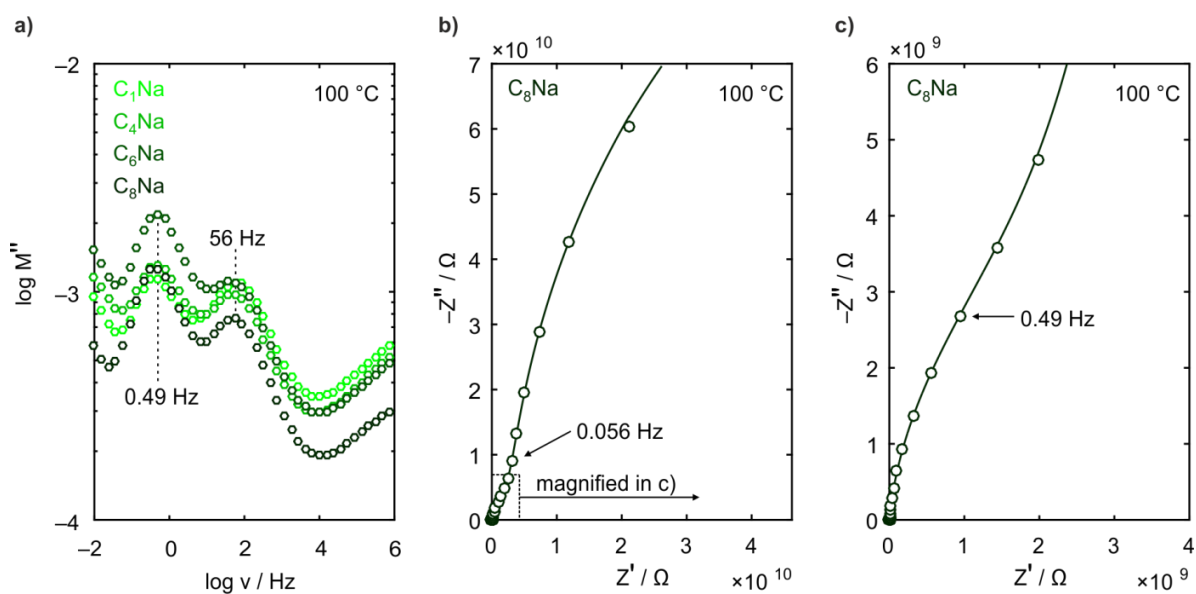


Figure S5: The plot of the electric modulus  $M''$  against the frequency clarifies the position of the two plateaus at  $0.49$  and  $56\text{ Hz}$  (a). The onset of the third plateau  $< 0.05\text{ Hz}$  is visible in the exemplary complex plane plot of  $C_8Na$  (b) that is magnified in (c). The solid lines are fits that use an equivalent circuit with two resistors and constant phase elements that are connected in parallel for each cycle  $(R_1CPE_1)(R_2CPE_2)$ , see Table S2.

Table S2: Fitting results from Figure S4 b and c.

	$R_1 / \Omega$	$C_1 / \text{F}$	$n_1$	$R_2 / \Omega$	$C_2 / \text{F}$	$n_2$
$C_8Na$	$2 * 10^9$	$2 * 10^{-10}$	0.96	$3 * 10^{11}$	$2 * 10^{-10}$	0.96

## Supplementary information

# An Electrolyte for Reversible Cycling of Na Metal and Na Intercalation Compounds

Lukas Schafzahl, Ilie Hanzu, Martin Wilkening, and Stefan A. Freunberger\*

Institute for Chemistry and Technology of Materials, Graz University of Technology, Stremayrgasse 9, 8010 Graz, Austria

\* to whom correspondence should be addressed: [freunberger@tugraz.at](mailto:freunberger@tugraz.at)

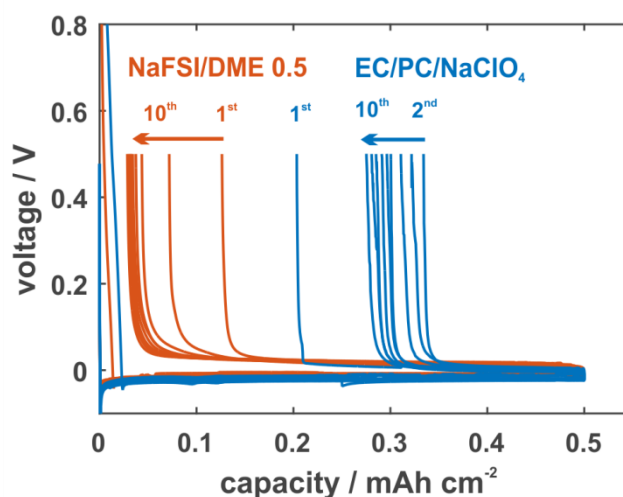


**Figure S1 | Plating and stripping of Na metal on Cu.** Potential evolution during the first 10 cycles of sodium plating at  $0.2 \text{ mA cm}^{-2}$  in  $1 \text{ M NaClO}_4$  in EC/PC (1/1 m/m) and NaFSI/DME (0.5 n/n).

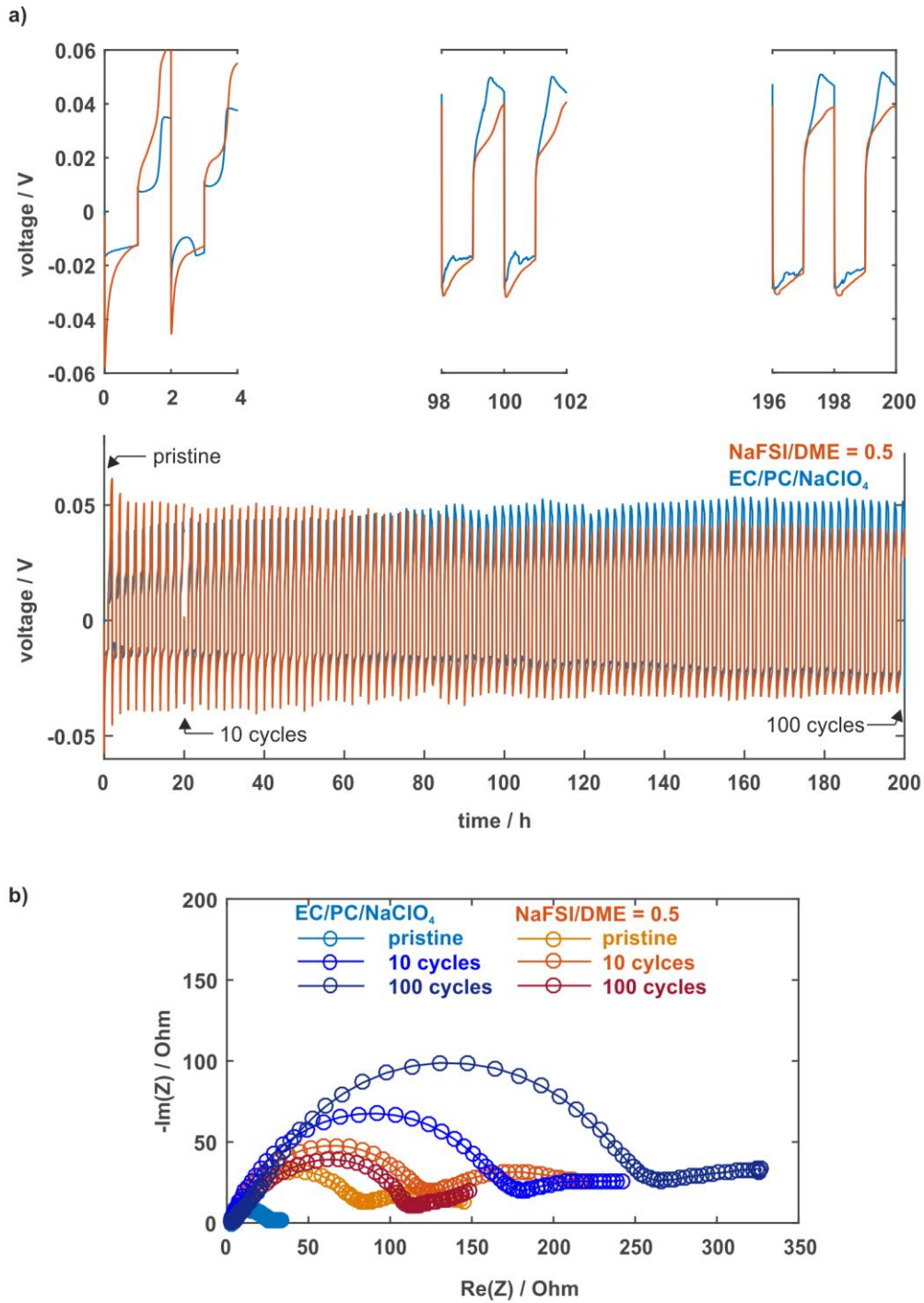


**Figure S2 | Galvanostatic cycling in symmetric Na/Na cells.** Potential profiles (a) and impedance spectra (b) of symmetric Na/Na cells cycled at  $0.02 \text{ mAh cm}^{-2}$  in  $1 \text{ M NaClO}_4$  in EC/PC (1/1 m/m) and NaFSI/DME (0.5 n/n). The top plots in (a) are expanded views from the bottom plot.

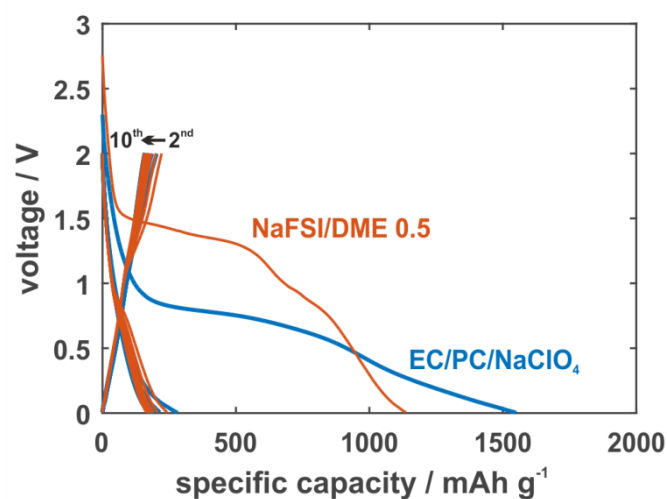


**Figure S3 | Initial cycles of high surface area HC electrodes vs Na counter electrodes.** Galvanostatic cycling of HC electrodes at  $0.02 \text{ mA cm}^{-2}$  (roughly C/6) in 1 M  $\text{NaClO}_4$  in EC/PC (1/1 m/m) and NaFSI/DME (0.5 n/n).

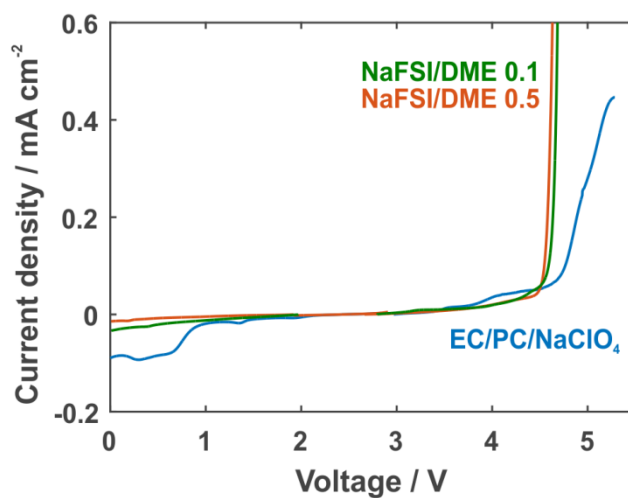


**Figure S4 | Electrochemical stability of the electrolytes.** Cyclic voltammograms of a glassy carbon electrode at  $10 \text{ mV} \cdot \text{s}^{-1}$  in 1 M  $\text{NaClO}_4$  in EC/PC (1/1 m/m) and DME electrolytes with a NaFSI/DME ratio of 0.1 and 0.5.

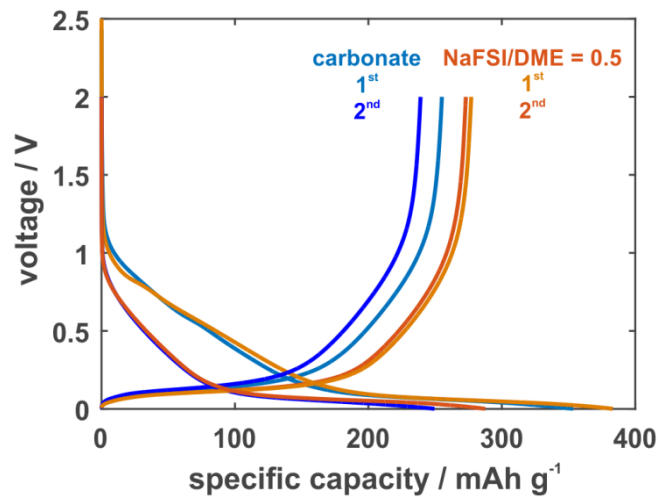


**Figure S5 | Initial cycles of low surface area HC vs Na counter electrodes.** Galvanostatic cycling of low surface area HC at C/10 in 1 M NaClO<sub>4</sub> in EC/PC (1/1 m/m) and NaFSI/DME (0.5 n/n).

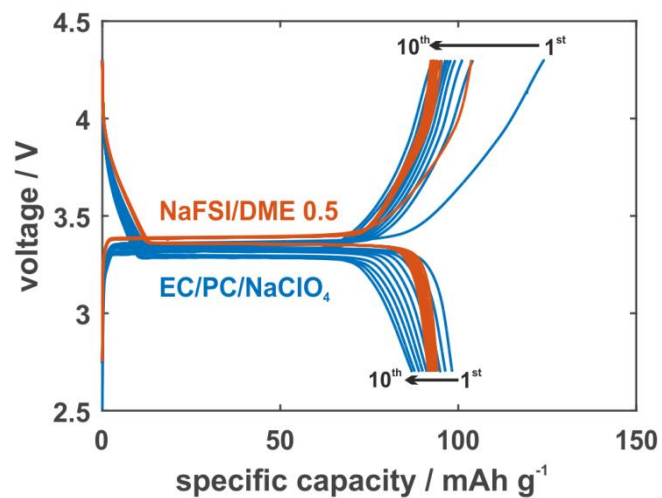


**Figure S6 | Initial cycles of NVP electrodes vs Na metal electrodes.** Galvanostatic cycling of NVP electrodes at 0.02 mA cm<sup>2</sup> (roughly C/6) in 1 M NaClO<sub>4</sub> in EC/PC (1/1 m/m) and NaFSI/DME (0.5 n/n).

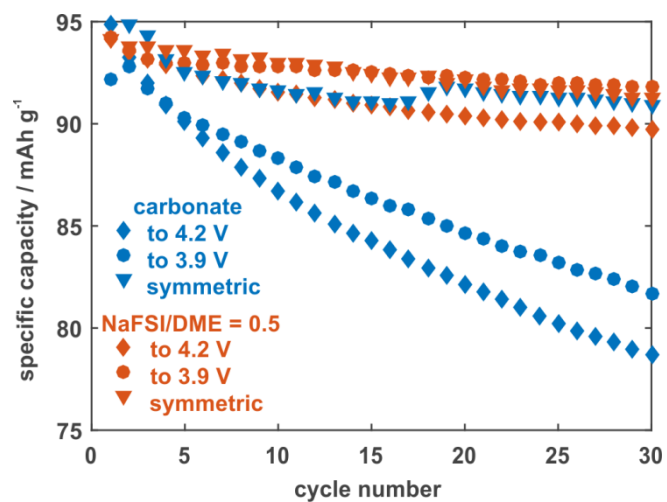


**Figure S7 | Galvanostatic cycling of NVP half cells and NVP/NVP symmetric cells.** Galvanostatic cycling of NVP electrodes at 0.02 mA cm<sup>2</sup> (roughly C/6) in 1 M NaClO<sub>4</sub> in EC/PC (1/1 m/m) and NaFSI/DME (0.5 n/n). NVP half cells with an upper cutoff potential of 4.2 V (diamonds) and 3.9 V (circles) and NVP/NVP symmetric cells with an upper cutoff potential of 3.9 V (triangles).

## Supplementary information

# Quantifying Total Superoxide, Peroxide and Carbonaceous Compounds in Metal-O<sub>2</sub> Batteries and the Solid Electrolyte Interphase

Bettina Schafzahl,<sup>†</sup> Eléonore Mourad,<sup>†</sup> Lukas Schafzahl,<sup>†</sup> Yann K. Petit,<sup>†</sup> Anjana R. Raju,<sup>†,‡</sup> Musthafa Ottakam Thotiyil,<sup>‡</sup> Martin Wilkening,<sup>†</sup> Christian Slugovc,<sup>†</sup> Stefan A. Freunberger<sup>\*,†</sup>

<sup>†</sup>Institute for Chemistry and Technology of Materials, Graz University of Technology, Stremayrgasse 9, 8010 Graz, Austria

<sup>‡</sup>Department of Chemistry, Indian Institute of Science Education and Research (IISER) Pune, Dr. Homi Bhabha Road, Pashan, Pune, 411008, India

\* Corresponding Author: [freunberger@tugraz.at](mailto:freunberger@tugraz.at)

## Materials and Methods:

### Chemicals

Ethylene glycol dimethyl ether (DME, >99.0%), diethylene glycol dimethyl ether (DEGDME, >99 %) and sodium trifluoromethanesulfonate (NaOTf, >98 %), were purchased from TCI EUROPE. Tetraethylene glycol dimethyl ether (tetraglyme, TEGDME, ≥99%) and LiClO<sub>4</sub> (battery grade, dry, 99.99%) were purchased from Sigma-Aldrich. Formic acid (puriss. ~98%) was bought from Fluka Analytical. Acetonitrile (HiPerSolv CHROMANORM Prolabo) was purchased from VWR Chemicals. Graphite and conductive carbon (SuperC65) were purchased from Timcal. Polyvinylidene difluoride (PvdF) was purchased from Arkema. N-methylpyrrolidone (NMP) was purchased from abcr. LiNi<sub>0.8</sub>Co<sub>0.15</sub>Al<sub>0.05</sub>O<sub>2</sub> (NCA) was purchased from Ecopro. High purity oxygen (O<sub>2</sub> 3.5, >99.95 vol %), high purity Ar (Ar 5.0, >99.999 vol %) and a mixture of Ar 6.0 and O<sub>2</sub> 5.5 (Ar 5.01 vol%) were purchased from Messer Austria GmbH. Moisture determination of solvents and electrolytes according to Karl Fischer titration was performed on a TitroLine KF trace (Schott Instruments). Solvents were purified by distillation and further dried over activated molecular sieves. LiClO<sub>4</sub> was dried under vacuum for 24 h at 160 °C. All other chemicals were used without further purification. Li<sub>2</sub>O<sub>2</sub> was synthesized



according to a previously reported procedure<sup>1</sup>. Li alkylcarbonates and  $\alpha$ -MnO<sub>2</sub> nanowires were synthesized as reported previously.<sup>2</sup> Water was obtained from a Millipore purification unit.

## Mass Spectrometry

The MS setup was built in-house and is similar to the one described previously.<sup>3</sup> It consisted of a commercial quadrupole mass spectrometer (Balzers) with a turbomolecular pump (Pfeiffer), which is backed by a membrane pump and leak inlet, which samples from the purge gas stream. The setup was calibrated for different gases (Ar, O<sub>2</sub>, CO<sub>2</sub>, H<sub>2</sub>, N<sub>2</sub> and H<sub>2</sub>O) using calibration mixtures in steps over the anticipated concentration ranges to capture nonlinearity and cross-sensitivity. All calibrations and quantifications were performed using in-house software written in MATLAB. The purge gas system consisted of a digital mass flow controller (Bronkhorst) and stainless steel tubing.

The sample setup consists of a glass vial with a volume of 7 mL equipped with a small stirring bar. A PEEK plug with glued in PEEK tubes and an exchangeable septum is sealed against the glass vial with a flat silicone rubber seal, which are all pressed by an Al clamp. During the measurement, the solutions are added through a septum using a syringe and the gas flow is regulated using a four way valve. The gas flow is fixed to 5 mL per minute. Before the measurement is started, all solutions were degassed with N<sub>2</sub> for at least 15 minutes to remove dissolved CO<sub>2</sub> and O<sub>2</sub>.

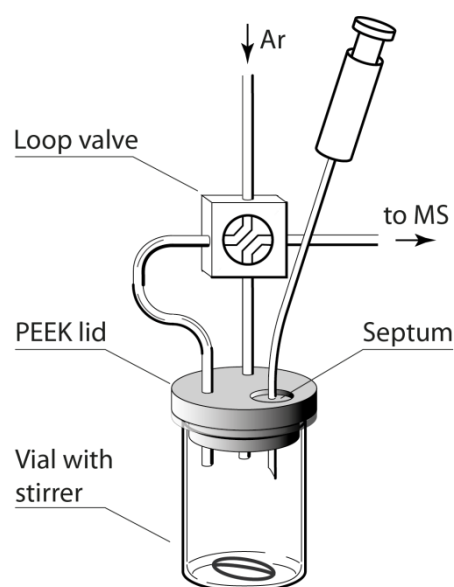


**Figure S1.** Schematic of the sample setup consisting of vial with stirrer, PEEK lid with septum, purge tubing with a loop valve and a syringe.

## Electrode Fabrication and Cell Design

Li-O<sub>2</sub> cathodes were made from a slurry of Super P carbon black (TIMCAL) with PTFE (60% dispersion in H<sub>2</sub>O, Aldrich) binder in the ratio 9:1 (m/m) using isopropanol. The slurry was then coated onto a stainless steel mesh current collector. The electrodes were vacuum dried at 120 °C for 24 h and then transferred to an Ar filled glove box without exposure to air. For the Na-air cells, carbon paper cathodes (Freudenberg H2315) were heated to 900 °C under Ar/H<sub>2</sub> (95/5 vol/vol) atmosphere. The glass fiber separators (Whatman) were washed with ethanol and dried overnight at 170 °C under vacuum prior to use. The LiFePO<sub>4</sub> counter electrodes were made by mixing partially delithiated active material with Super P and PTFE in the ratio 8:1:1(m/m/m). The electrodes were vacuum dried at 120 °C for 24 h. The counter electrode had three-fold the expected capacity of the positive electrode. The electrochemical cells used to investigate cycling were based on a Swagelok design. Typical Li-O<sub>2</sub> working electrodes had a carbon mass loading of 1 mg and the cells were assembled with 100 μL electrolyte. Li-O<sub>2</sub> cells comprised a Super P/PTFE working electrode, Li<sub>1-x</sub>FePO<sub>4</sub> reference and counter electrodes and 0.1M LiClO<sub>4</sub> in tetraglyme as the electrolyte and were run at 70 mA·g<sub>c</sub><sup>-1</sup>. Na-O<sub>2</sub> cells comprised a carbon paper working electrode, Na metal reference and counter electrodes and 0.1M NaOTf in diglyme containing 40 ppm H<sub>2</sub>O as the electrolyte and were run at 90 μA·cm<sup>-2</sup>.

For Li-ion cells, graphite anodes were prepared from a slurry of 83% graphite, 8.5% conductive carbon and 8.5% polyvinylidene difluoride in NMP. NCA cathodes were prepared from a slurry of 84% NCA, 8% PvdF and 8% conductive carbon. Both slurries were stirred overnight, sonicated and cast on a Cu and Al foil, respectively. Subsequently, electrodes were punched and dried at 120 °C under vacuum. The average loading was roughly 1 mg cm<sup>-2</sup> for graphite anodes and roughly 3 mg cm<sup>-2</sup> for NCA cathodes.

Electrochemical tests were run on either a SP-300 (BioLogic SA, France) or BT-2000 (Arbin Instruments) potentiostat/galvanostat. For the analysis of the electrodes, batteries were, after cycling, disassembled in an argon filled glovebox without exposure to air. If not noted otherwise, all electrodes were washed and dried before measuring. DMC (metal-ion batteries) or DME (metal-air cells) were used for that purpose and the solvent was subsequently removed under reduce pressure. The washing/drying step was done within one hour after the cells were finished.

## Spectroscopic Methods

### UV-vis Spectroscopy

Absorption spectra were recorded on a UV-vis spectrophotometer (Varian Cary 50). 2 wt% solution of Ti(IV)-oxysulfate solution in 1 M H<sub>2</sub>SO<sub>4</sub> was used for the detection of peroxides except for data in Fig.

1 where 2 % Ti(IV)-oxysulfate solution in 0.1 M H<sub>2</sub>SO<sub>4</sub> was used as reported earlier.<sup>4,5</sup> The absorbance at the maximum at 405 nm was chosen for all measurements.

Calibrating UV-vis absorbance with H<sub>2</sub>O<sub>2</sub> is prone to yield a curve that does not pass through zero, i.e. due to loss of H<sub>2</sub>O<sub>2</sub>.<sup>4</sup> To obtain the true H<sub>2</sub>O<sub>2</sub> concentration, we thus started from high purity Li<sub>2</sub>O<sub>2</sub> and accounted for any H<sub>2</sub>O<sub>2</sub> loss by measuring evolved O<sub>2</sub> with the MS, Fig. S6.

## Supplementary Discussion and Figures:

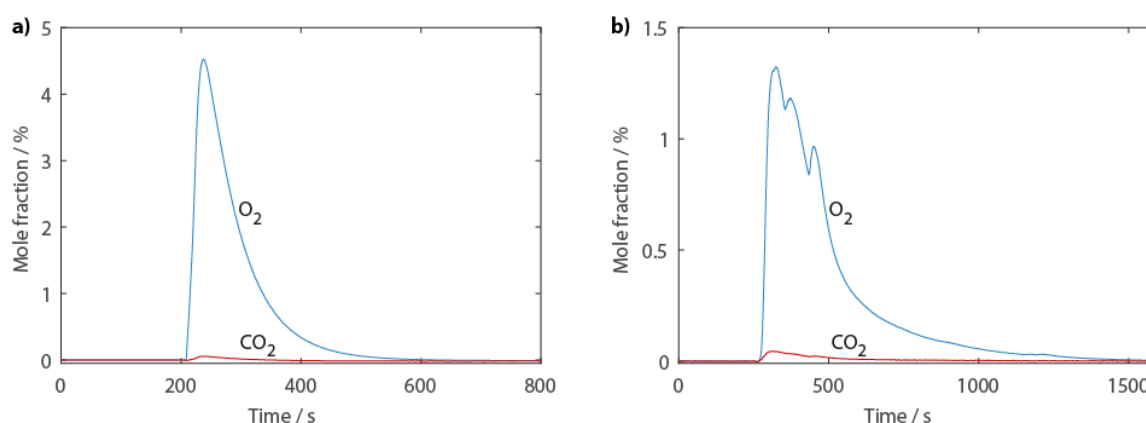
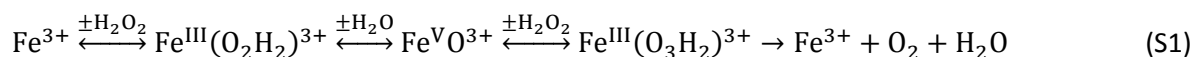


**Figure S2.** CO<sub>2</sub> evolution indicates reactive species upon expelling O<sub>2</sub> from H<sub>2</sub>O<sub>2</sub>. In either case the H<sub>2</sub>O<sub>2</sub> source was Li<sub>2</sub>O<sub>2</sub> and Li acetate was used as organic probe molecule. (a) A mixture of Li<sub>2</sub>O<sub>2</sub>/CH<sub>3</sub>COOLi (90/10 wt.%) was mixed with an equal amount of α-MnO<sub>2</sub> nanowires and immersed in 1 M H<sub>2</sub>SO<sub>4</sub> solution. The CO<sub>2</sub> amount corresponds to ~10% of the CH<sub>3</sub>COOLi to be decomposed. (b) The Li<sub>2</sub>O<sub>2</sub>/CH<sub>3</sub>COOLi mixture was immersed in 0.5 M FeCl<sub>3</sub> solution. The CO<sub>2</sub> amount corresponds to ~12% of the CH<sub>3</sub>COOLi to be decomposed.

## Quantifying total peroxide/superoxide by total O<sub>2</sub> evolution

Fe<sup>3+</sup> decomposes H<sub>2</sub>O<sub>2</sub> catalytically for which either the Kremer-Stein-Mechanism



or other mechanisms involving HO<sub>2</sub><sup>•</sup> or <sup>•</sup>OH were proposed.<sup>6,7</sup> Fe<sup>3+</sup> decomposes H<sub>2</sub>O<sub>2</sub> quantitatively as shown in Table S1 for various Fe<sup>3+</sup>-to-Li<sub>2</sub>O<sub>2</sub> ratios and in Fig. S3 for different amounts of Li<sub>2</sub>O<sub>2</sub>.

**Table S1.** Oxygen yield for various Fe<sup>3+</sup>-to-Li<sub>2</sub>O<sub>2</sub> ratios.

Fe <sup>3+</sup> concentration (M)	Fe <sup>3+</sup> -to-Li <sub>2</sub> O <sub>2</sub> ratio	O <sub>2</sub> yield (%)
0.05	0.2/1	96
0.1	0.6/1	100
0.5	2.5/1	99
1	4/1	101

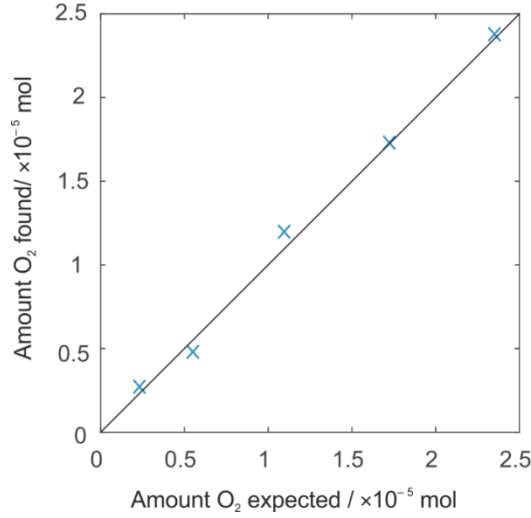
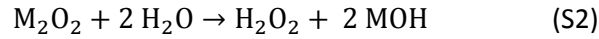


**Figure S3.** Comparison of the amount of Li<sub>2</sub>O<sub>2</sub> used and O<sub>2</sub> evolved using 0.1 M FeCl<sub>3</sub>. Linear regression gives  $n_{\text{O}_2, \text{found}} = 1.015 \cdot n_{\text{O}_2, \text{expected}}$  with  $R^2 = 0.9948$ .

### Quantifying total peroxide/superoxide by combining MS and UV-vis

Superoxide and peroxide are quantified by combining photometry of the [Ti(O<sub>2</sub>)OH]<sup>+</sup> complex<sup>7</sup> and MS measurement of the O<sub>2</sub> evolved during sample preparation as shown in Fig. 2a-c. We first consider the case that the discharge product is either Li<sub>2</sub>O<sub>2</sub>, Na<sub>2</sub>O<sub>2</sub>, NaO<sub>2</sub>, or KO<sub>2</sub>, but no mixtures thereof. When M<sub>2</sub>O<sub>2</sub> is measured, acidifying the sample will convert the Li<sub>2</sub>O<sub>2</sub> according to



while part of the H<sub>2</sub>O<sub>2</sub> will decompose into H<sub>2</sub>O and O<sub>2</sub> according to



Thus any one mole O<sub>2</sub> evolved corresponds to 2 moles M<sub>2</sub>O<sub>2</sub>, which are not any more present as H<sub>2</sub>O<sub>2</sub> and therefore not captured by UV-Vis. One mole of H<sub>2</sub>O<sub>2</sub> detected as [Ti(O<sub>2</sub>)OH]<sup>+</sup> by UV-vis correspond to one mole of M<sub>2</sub>O<sub>2</sub>. The moles of H<sub>2</sub>O<sub>2</sub> and O<sub>2</sub> per mol of M<sub>2</sub>O<sub>2</sub> as a function of the H<sub>2</sub>O<sub>2</sub> loss into the gas phase are plotted in Fig. S4a.

With  $x$  being the fraction of H<sub>2</sub>O<sub>2</sub> lost, the moles  $n$  of H<sub>2</sub>O<sub>2</sub> and O<sub>2</sub> are

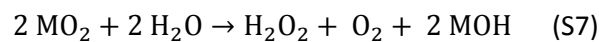
$$n_{\text{H}_2\text{O}_2} = n_{\text{M}_2\text{O}_2} - x \cdot n_{\text{M}_2\text{O}_2} \quad (\text{S4})$$

$$n_{\text{O}_2} = 0.5x \cdot n_{\text{M}_2\text{O}_2} \quad (\text{S5})$$

Thus moles of Li<sub>2</sub>O<sub>2</sub> are

$$n_{\text{M}_2\text{O}_2} = n_{\text{H}_2\text{O}_2} + 2 \cdot n_{\text{O}_2} \quad (\text{S6})$$

When NaO<sub>2</sub> or KO<sub>2</sub> is measured, acidifying the sample will convert the MO<sub>2</sub> according to



while again part of the H<sub>2</sub>O<sub>2</sub> will decompose into H<sub>2</sub>O and O<sub>2</sub> according to Eq. S3. With  $x$  being the fraction of H<sub>2</sub>O<sub>2</sub> lost, the moles of H<sub>2</sub>O<sub>2</sub> and O<sub>2</sub> are

$$n_{\text{H}_2\text{O}_2} = 0.5 \cdot n_{\text{MO}_2} - 0.5x \cdot n_{\text{MO}_2} \quad (\text{S8})$$

$$n_{\text{O}_2} = 0.5 \cdot n_{\text{MO}_2} + 0.25x \cdot n_{\text{MO}_2} \quad (\text{S9})$$

Thus the moles of  $\text{MO}_2$  are

$$n_{\text{MO}_2} = \frac{4}{3} \left( n_{\text{O}_2} + \frac{1}{2} \cdot n_{\text{H}_2\text{O}_2} \right) \quad (\text{S10})$$

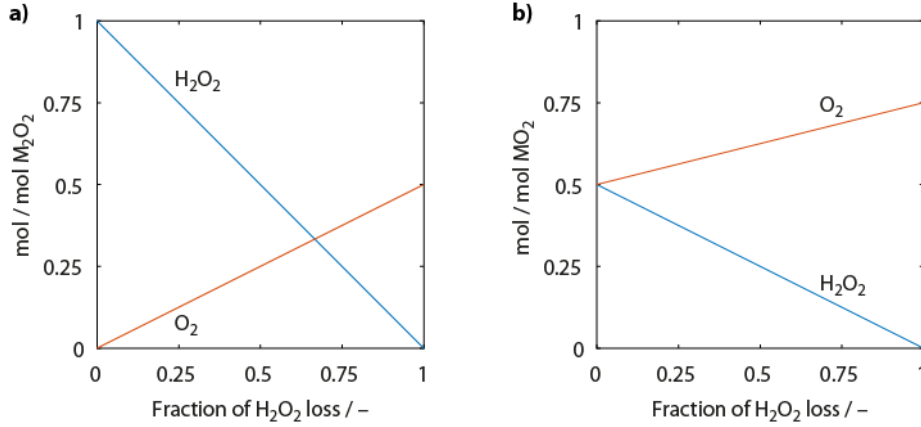
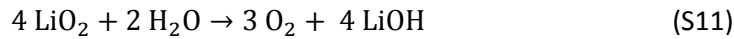


**Figure S4.** Amount of  $\text{O}_2$  in the gas phase and  $\text{H}_2\text{O}_2$  in the solution as a function of the fraction of theoretical amount of  $\text{H}_2\text{O}_2$  lost into the gas phase for (a)  $\text{M}_2\text{O}_2$  as given in Eq. S4 and S5, and (b)  $\text{NaO}_2$  or  $\text{KO}_2$  as given in Eq. S8 and S9.

When mixtures of  $\text{MO}_2$  and  $\text{M}_2\text{O}_2$  ( $\text{M} = \text{Li}$  or  $\text{Na}$ ) are expected, two cases need to be distinguished.

- l)  $\text{LiO}_2$  decomposes according to



without forming  $\text{H}_2\text{O}_2$  while  $\text{Li}_2\text{O}_2$  forms  $\text{H}_2\text{O}_2$  via Eq. S2.<sup>8</sup> Since both the fraction  $x$  of  $\text{H}_2\text{O}_2$  being lost and the  $\text{Li}_2\text{O}_2$ -to- $\text{LiO}_2$  ratio are unknowns,  $n_{\text{Li}^+}$  needs to be obtained as a third measure next to  $n_{\text{H}_2\text{O}_2}$  and  $n_{\text{O}_2}$ . According to Equations S2, S3, and S11 these measures are connected to  $n_{\text{Li}_2\text{O}_2}$  and  $n_{\text{LiO}_2}$  via

$$n_{\text{H}_2\text{O}_2} = n_{\text{Li}_2\text{O}_2} - x \cdot n_{\text{Li}_2\text{O}_2} \quad (\text{S12})$$

$$n_{\text{O}_2} = 0.5x \cdot n_{\text{Li}_2\text{O}_2} + \frac{4}{3} \cdot n_{\text{LiO}_2} \quad (\text{S13})$$

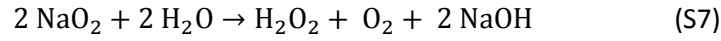
$$n_{\text{Li}^+} = 2 n_{\text{Li}_2\text{O}_2} + n_{\text{LiO}_2} \quad (\text{S14})$$

These quantities are plotted as a function of  $\text{LiO}_2$  mole fraction in Fig. S7a for various values of  $\text{H}_2\text{O}_2$  loss  $x$ . The moles of  $\text{Li}_2\text{O}_2$  and  $\text{LiO}_2$  are then obtained via

$$n_{\text{Li}_2\text{O}_2} = \frac{6}{13} \left( \frac{4}{3} n_{\text{Li}^+} - \frac{1}{2} n_{\text{H}_2\text{O}_2} - n_{\text{O}_2} \right) \quad (\text{S15})$$

$$n_{\text{LiO}_2} = n_{\text{Li}^+} - 2 n_{\text{Li}_2\text{O}_2} \quad (\text{S16})$$

II)  $\text{NaO}_2$  decomposes according to



thus forming  $\text{H}_2\text{O}_2$ .<sup>8</sup>  $\text{Na}_2\text{O}_2$  forms  $\text{H}_2\text{O}_2$  via Eq. S2. Since both the fraction  $x$  of  $\text{H}_2\text{O}_2$  being lost and the  $\text{Na}_2\text{O}_2$ -to- $\text{NaO}_2$  ratio are unknowns,  $n_{\text{Na}^+}$  needs to be obtained as a third measure next to  $n_{\text{H}_2\text{O}_2}$  and  $n_{\text{O}_2}$ . According to Equations S2, S3, and S7 these measures are connected to  $n_{\text{Na}_2\text{O}_2}$  and  $n_{\text{NaO}_2}$  via

$$n_{\text{H}_2\text{O}_2} = n_{\text{Na}_2\text{O}_2} + \frac{1}{2} \cdot n_{\text{NaO}_2} - x \cdot n_{\text{Na}_2\text{O}_2} + \frac{x}{2} \cdot n_{\text{NaO}_2} \quad (\text{S17})$$

$$n_{\text{O}_2} = \frac{x}{2} \cdot n_{\text{Na}_2\text{O}_2} + \frac{1}{2} \cdot n_{\text{NaO}_2} + \frac{x}{4} \cdot n_{\text{NaO}_2} \quad (\text{S18})$$

$$n_{\text{Na}^+} = 2 n_{\text{Na}_2\text{O}_2} + n_{\text{NaO}_2} \quad (\text{S19})$$

These quantities are plotted as a function of  $\text{LiO}_2$  mole fraction in Fig. S7b for various values of  $\text{H}_2\text{O}_2$  loss  $x$ . The moles of  $\text{Na}_2\text{O}_2$  and  $\text{NaO}_2$  are then obtained via

$$n_{\text{Na}_2\text{O}_2} = \frac{3}{4} n_{\text{Na}^+} - \frac{1}{2} n_{\text{H}_2\text{O}_2} - n_{\text{O}_2} \quad (\text{S20})$$

$$n_{\text{NaO}_2} = n_{\text{Na}^+} - 2n_{\text{Na}_2\text{O}_2} \quad (\text{S21})$$

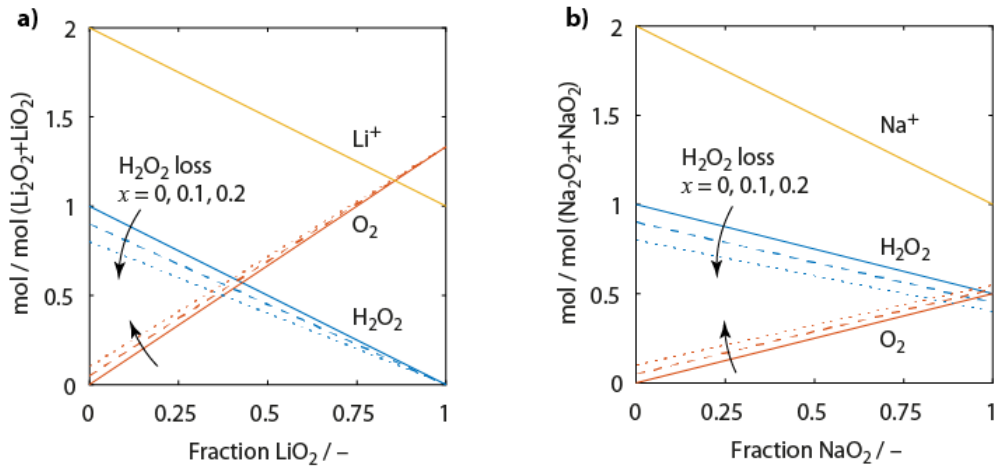


**Figure S5.** Analysis of mixtures of  $\text{MO}_2$  and  $\text{M}_2\text{O}_2$  ( $\text{M} = \text{Li}$  or  $\text{Na}$ ). Amount of  $\text{O}_2$  in the gas phase and  $\text{H}_2\text{O}_2$  and  $\text{M}^+$  in the solution as a function of the mole fraction of superoxide in the mixture. In either case the effect of a  $\text{H}_2\text{O}_2$  loss of 0, 10, 20% (*i.e.*,  $x = 0, 0.1, 0.2$ ) into the gas phase is examined. (a) Analysis of  $\text{LiO}_2/\text{Li}_2\text{O}_2$  mixtures as given in Eq. S12, S13 and S14. (b) Analysis of  $\text{NaO}_2/\text{Na}_2\text{O}_2$  mixtures as given in Eq. S17, S18 and S19.

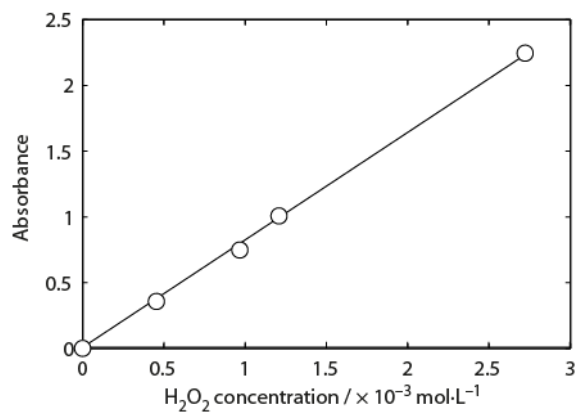


**Figure S6.** Calibration curve for UV-vis absorbance vs true  $\text{H}_2\text{O}_2$  concentration. Linear regression gives  $A = 819.84 \cdot c_{\text{H}_2\text{O}_2}$  with  $R^2 = 0.9992$ .

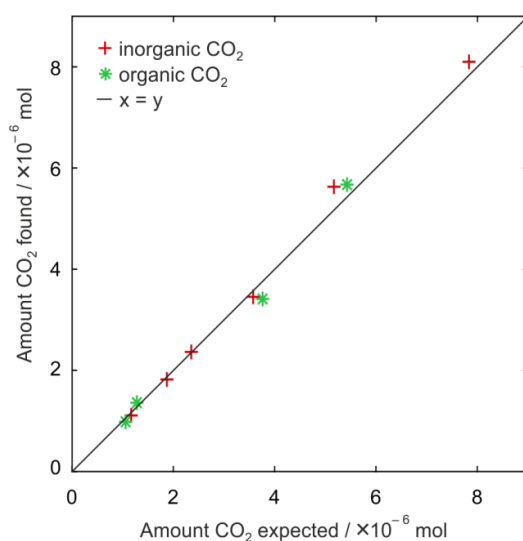


**Figure S7.** Detection accuracy for inorganic and organic carbonaceous compounds. Mechanical mixtures of  $\text{Li}_2\text{CO}_3$  and Li acetate were analyzed using the protocol shown in Fig. 2. Linear regression gives for the inorganic  $\text{CO}_2$   $n_{\text{CO}_2,\text{found}} = 1.033 \cdot n_{\text{CO}_2,\text{expected}}$  with  $R^2 = 0.9954$  and for the organic  $\text{CO}_2$   $n_{\text{CO}_2,\text{found}} = 0.999 \cdot n_{\text{CO}_2,\text{expected}}$  with  $R^2 = 0.986$ .

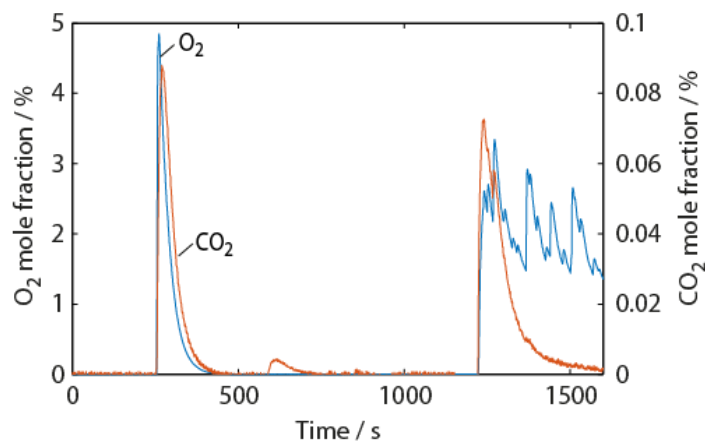


**Figure S8.** Exemplary MS data for measuring a discharged  $\text{Na-O}_2$  cathode.



## Supplementary References

- (1) Ottakam Thotiyl, M. M.; Freunberger, S. A.; Peng, Z.; Bruce, P. G. The Carbon Electrode in Nonaqueous Li–O<sub>2</sub> Cells. *J. Am. Chem. Soc.* **2013**, *135*, 494-500.
- (2) Freunberger, S. A.; Chen, Y.; Peng, Z.; Griffin, J. M.; Hardwick, L. J.; Bardé, F.; Novák, P.; Bruce, P. G. Reactions in the Rechargeable Lithium–O<sub>2</sub> Battery with Alkyl Carbonate Electrolytes. *J. Am. Chem. Soc.* **2011**, *133*, 8040-8047.
- (3) Chen, Y.; Freunberger, S. A.; Peng, Z.; Bardé, F.; Bruce, P. G. Li–O<sub>2</sub> Battery with a Dimethylformamide Electrolyte. *J. Am. Chem. Soc.* **2012**, *134*, 7952-7957.
- (4) Hartmann, P.; Bender, C. L.; Sann, J.; Durr, A. K.; Jansen, M.; Janek, J.; Adelhalm, P. A Comprehensive Study on the Cell Chemistry of the Sodium Superoxide (NaO<sub>2</sub>) Battery. *Phys. Chem. Chem. Phys.* **2013**, *15*, 11661-11672.
- (5) Meini, S.; Piana, M.; Tsiouvaras, N.; Garsuch, A.; Gasteiger, H. A. The Effect of Water on the Discharge Capacity of a Non-Catalyzed Carbon Cathode for Li–O<sub>2</sub> Batteries. *Electrochem. Solid State Lett.* **2012**, *15*, A45-A48.
- (6) De Laat, J.; Gallard, H. Catalytic Decomposition of Hydrogen Peroxide by Fe(III) in Homogeneous Aqueous Solution: Mechanism and Kinetic Modeling. *Environ. Sci. Technol.* **1999**, *33*, 2726-2732.
- (7) Wiberg, N.; Holleman, A. F.; Wiberg, E. *Inorganic Chemistry*; Academic Press: San Diego, USA; 2001.
- (8) Wang, H.-H.; Lee, Y. J.; Assary, R. S.; Zhang, C.; Luo, X.; Redfern, P. C.; Lu, J.; Lee, Y. J.; Kim, D. H.; Kang, T.-G.; Indacochea, E.; Lau, K. C.; Amine, K.; Curtiss, L. A. Lithium Superoxide Hydrolysis and Relevance to Li–O<sub>2</sub> Batteries. *J. Phys. Chem. C* **2017**, *121*, 9657-9661.

## Supporting Information

### **Singlet Oxygen during Cycling of the Aprotic Sodium–O<sub>2</sub> Battery**

*Lukas Schafzahl<sup>+</sup>, Nika Mahne<sup>+</sup>, Bettina Schafzahl, Martin Wilkening, Christian Slugovc, Sergey M. Borisov, and Stefan A. Freunberger\**

anie\_201709351\_sm\_miscellaneous\_information.pdf

## **Author Contributions**

L.S. Data curation: Equal; Software: Supporting; Visualization: Supporting

N.M. Data curation: Equal; Methodology: Lead; Visualization: Supporting

B.S. Data curation: Supporting; Methodology: Supporting

M.W. Funding acquisition: Supporting; Resources: Supporting; Writing – review & editing: Supporting

C.S. Conceptualization: Supporting; Funding acquisition: Supporting; Project administration: Supporting; Resources: Supporting; Supervision: Supporting; Writing – review & editing: Supporting

S.B. Methodology: Equal; Resources: Supporting; Supervision: Supporting; Writing – review & editing: Supporting.

## Supplementary information

### Materials and Methods:

#### Chemicals

Diethylene glycol dimethyl ether (DEGDME, >99.0%), 9,10-dimethylantracene (DMA, >98.0 %) and sodium trifluoromethanesulfonate (NaOTf, >98%) were purchased from TCI EUROPE. Tetraethylene glycol dimethyl ether (TEGDME, ≥99%), and H<sub>2</sub>O (CHROMASOLV for HPLC) were purchased from Sigma-Aldrich®. Acetonitrile (HiPerSolv CHROMANORM Prolabo) was purchased from VWR Chemicals. High purity oxygen (O<sub>2</sub> 3.5, >99.95% vol) was purchased from Messer Austria GmbH. Moisture determination of all used solvents and electrolytes according to Karl Fischer titration was performed on a TitroLine KF trace (Schott Instruments). Solvents were purified by distillation and further dried over activated molecular sieves. The other chemicals were used without further purification. The sensitizer palladium(II) *meso*-tetra(4-fluorophenyl)tetrabenzoporphyrin was synthesized according to a previously reported procedure<sup>[1]</sup>.

#### Electrode Fabrication and Cell Design

Binder-free carbon fiber gas diffusion layer (GDL) cathodes (Freudenberg 2315, Quintech) were heated at 900 °C under H<sub>2</sub>/Ar (5/95 vol/vol) atmosphere. Na<sub>3</sub>V<sub>2</sub>(PO<sub>4</sub>)<sub>3</sub> (NVP) was synthesized according to a previously published procedure<sup>[2]</sup> and coated with a conductive poly(3,4-ethylenedioxythiophene) layer.<sup>[3]</sup> Self-standing NVP counter electrodes were prepared by mixing active material with Super P (TIMCAL) and PTFE in the ratio 8:1:1 (m/m/m). The electrodes were subsequently dried overnight under vacuum at 120 °C and then transferred to an Ar filled glove box without exposure to air. Their capacity was at least 0.750 mAh and thus exceeded the cathode ~3-fold. The glass fibre separators (Whatman GF-F) were washed with ethanol and dried overnight under vacuum at 200 °C. The electrochemical cells used to investigate cycling were based on a Swagelok design and the cells were assembled with 140 µL electrolyte.

#### Electrochemical Methods

Electrochemical tests were run on either a SP-300 (BioLogic SA, France) or BT-2000 (Arbin Instruments) potentiostat/galvanostat. Cyclic voltammograms were recorded in a three-electrode arrangement with glassy carbon disc working electrode (BAS Inc.), a Pt wire counter electrode and

partially desodiated NVP as reference electrode inside a glass cell with PTFE lid. The cells were run inside an Ar filled glovebox and purged with high-purity Ar.

### UV-Vis Spectroscopy

Absorption spectra were recorded on a UV-Vis spectrophotometer (Varian Cary 50). The molar absorption coefficient of DMA was determined as an average of three independent measurements.

### Operando Fluorescence Measurements

Excitation and emission spectra were recorded on a Fluorolog 3 fluorescence spectrometer (Horiba) equipped with a NIR-sensitive photomultiplier R2658 (300 -1050 nm) from Hamamatsu. The in-situ fluorescence measurements were performed in front face mode. The measurements were performed in kinetic acquisition modus with 0.1 s excitation every 10 s to minimize photobleaching of the DMA. The fluorophore concentration was adjusted to attain an absorbance of 0.2 to avoid inner filter effects and to achieve better correlation between the observed fluorescence intensity (proportional to the amount of the absorbed light) and absorption (proportional to the concentration) of the  $^1\text{O}_2$  trap. DMA was excited at 378 nm and the emission was detected at 425 nm.

The cell for *operando* fluorescence was a 1 cm absorption high precision quartz cell (Hellma Analytics) with a purpose made gas-tight PTFE-lid. The working electrode was a carbon fibre GDL (see above) mounted on a stainless steel wire that had been pre-discharged to 1 mAh in a swagelok cell. The reference and counter electrodes were partially desodiated NVP on an stainless steel or Al-foil current collector, respectively. The assembling was performed in an Ar filled glovebox. The cell contained a magnetic stirrer bar, was filled with electrolyte, streamed with  $\text{O}_2$ , further connected with a pure  $\text{O}_2$  reservoir and hermetically sealed before being placed it in the spectrometer. During the measurement the electrolyte was stirred to ensure  $\text{O}_2$  saturation and uniform DMA concentration.

The DMA concentration of  $1.6 \times 10^{-5}$  M for the operando fluorescence was chosen to optimize the sensitivity of the method. At an absorbance of  $A = 0.2$  (measurement conditions), 37% of the excitation light is absorbed by the chromophore ( $= 1 - 10^{-A}$ ). In a hypothetical example, reaction of 10% of DMA with  $^1\text{O}_2$  will decrease absorbance by 10%, i.e. from 0.2 to 0.18. Thus, after the reaction 34% of the excitation light will be absorbed by the chromophore. Since the fluorescence intensity is proportional to the amount of the absorbed light, the decrease of fluorescence intensity will be  $(37 - 34)/37 * 100 = 8\%$ . Analogous calculation with 10 times the DMA concentration ( $A = 2$ ) results in 99% of excitation light absorbed before bleaching and 98.4% of the excitation light absorbed after bleaching. Thus, the decrease of fluorescence intensity would be  $(99 - 98.4)/99 * 100 = 0.6\%$  which is

much lower than for the comparably low concentration of the trap. Therefore, a relatively low concentration of DMA is essential for the best sensitivity of operando fluorescence.

### **Carbonate/Carboxylate and NaO<sub>2</sub> Quantification**

The procedure was performed as described earlier<sup>[4]</sup>. The purge gas flow was typically 5 mL/min. The NaO<sub>2</sub> content was measured using TiOSO<sub>4</sub> according to a previously described procedure.<sup>[5]</sup>

### **Photo-chemical Generation of <sup>1</sup>O<sub>2</sub>**

To perform experiments with a known generation of <sup>1</sup>O<sub>2</sub> we used in situ photogeneration with the sensitizer palladium(II) *meso*-tetra(4-fluorophenyl)tetrabenzoporphyrin<sup>[1]</sup>. The sensitizer was irradiated with a red LED light source (643 nm, 7 W).

### **HPLC-MS Measurements**

HPLC-MS (high-performance liquid chromatography coupled with mass spectrometry) was used for determining the degree of conversion from DMA to DMA-O<sub>2</sub>. The sample handling was performed inside an Ar filled glovebox. The electrolyte was extracted from the cell using DME that was then removed by evaporation at room temperature. 10 μL of the residue were diluted with 90 μL of TEGDME and a volume of 1 μL was injected into the HPLC. The HPLC instrument was an Agilent Technologies 1200 Series (Agilent Technology, USA) with a multiple wavelength UV-Vis detector (Agilent Technology G1365C MWD SL). The samples were separated by a reversed-phase Poroshell column (120 EC-C8, 3.0 mm × 100 mm, Ø 2.7 μm, Agilent Technology, USA) using a gradient system of acetonitrile (solvent B) and water containing 0.01% formic acid (solvent A). A pre-column (UHPLC 3PK, Poroshell 120 EC-C8 3.0 × 5 mm 2.7 μm, Agilent Technology, USA) was connected before the reversed phase column. The elution started with isocratic solvent B of 50% over the course of 1 min and was then increased to 100% of B within 5 min at a flow rate of 0.7 mL/min. The column was held at 20 °C throughout the measurements. The eluent was monitored via an UV-Vis detector at the wavelengths of 210 nm and 254 nm.

The extent of the transformation of 9,10-dimethylanthracene (DMA) to 9,10-dimethylanthracene-endoperoxide (DMA-O<sub>2</sub>) was determined from the absorbance at 210 nm and the molar absorption coefficients  $\epsilon_{DMA,210\text{ nm}}$  and  $\epsilon_{DMA-O_2,210\text{ nm}}$ . The latter was determined from DMA-O<sub>2</sub>, which was obtained by conversion of DMA with photogenerated <sup>1</sup>O<sub>2</sub>.

## Supplementary Figures:

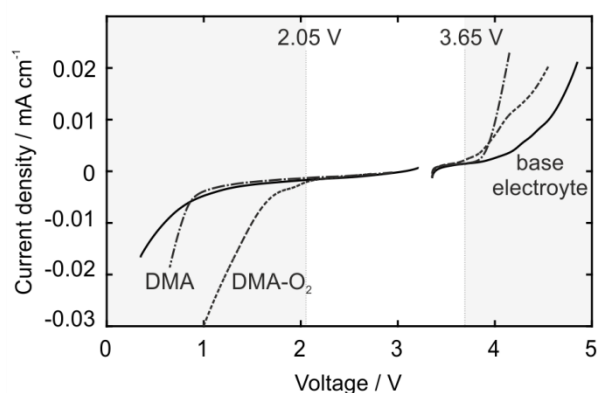
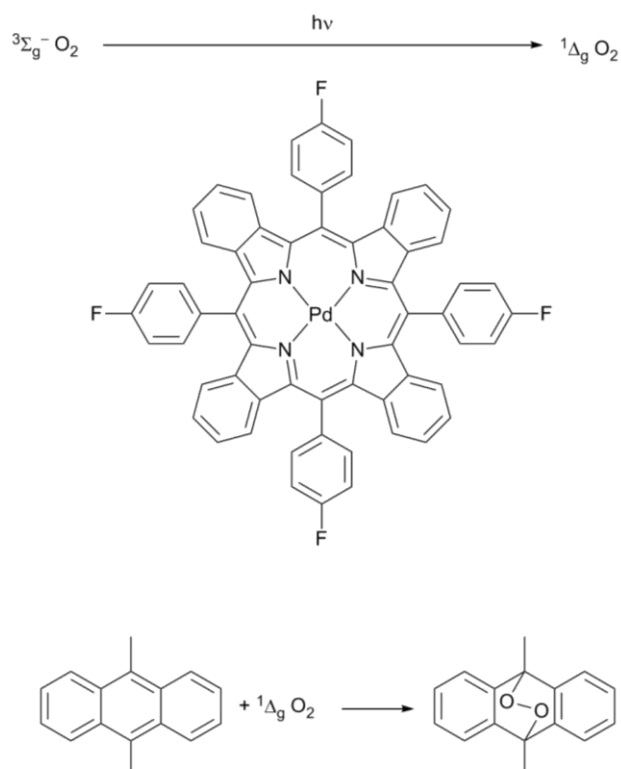


**Figure S1.** Electrochemical stability of 9,10-dimethylantracene (DMA) and 9,10-dimethylantracene-endoperoxide (DMA-O<sub>2</sub>). Cyclic voltammetry was performed at a 3 mm glassy carbon disc electrode at a sweep rate of 50 mV·s<sup>-1</sup>. First 2 mM DMA and 0.1 M NaOTf in diglyme were measured under Ar-atmosphere. <sup>1</sup>O<sub>2</sub> was then generated photochemically with the sensitizer palladium(II) *meso*-tetra(4-fluorophenyl)tetrabenzoporphyrin under O<sub>2</sub>-atmosphere and then the formed DMA-O<sub>2</sub> was measured under Ar-atmosphere.



**Scheme S1.** Photogeneration of <sup>1</sup>O<sub>2</sub> from <sup>3</sup>O<sub>2</sub> using the sensitizer palladium(II) *meso*-tetra(4-fluorophenyl)tetrabenzoporphyrin (top). Reaction of 9,10-dimethylantracene with singlet oxygen to 9,10-dimethylantracene-endoperoxide (bottom).



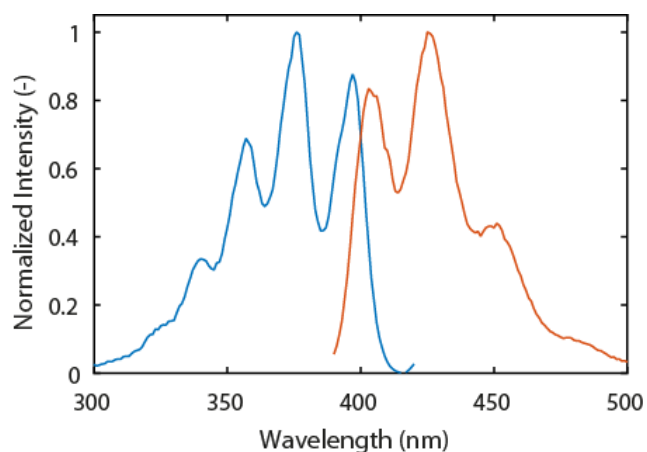


**Figure S2.** Excitation spectrum (blue trace,  $\lambda_{em}=425\text{nm}$ ) and the emission spectrum (orange trace,  $\lambda_{ex}=378\text{nm}$ ) of dimethylantracene.<sup>[6]</sup> The excitation was recorded from 300nm – 420nm with  $\lambda_{em}=425\text{nm}$ . The emission was recorded from 380nm-500nm with  $\lambda_{ex}=378\text{nm}$ .

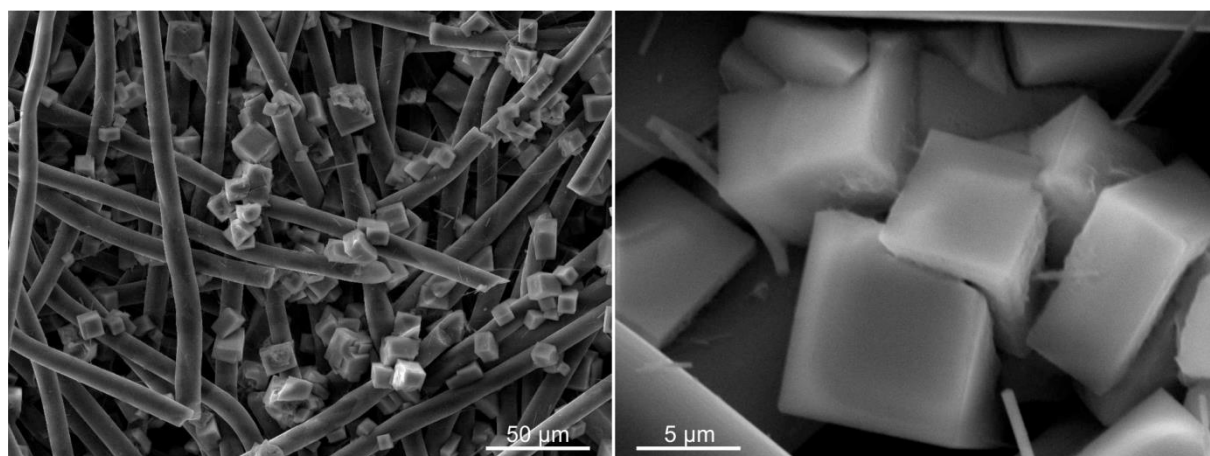


**Figure S3.** SEM images of a discharged Na-O<sub>2</sub> cathode corresponding to Figure 1a.

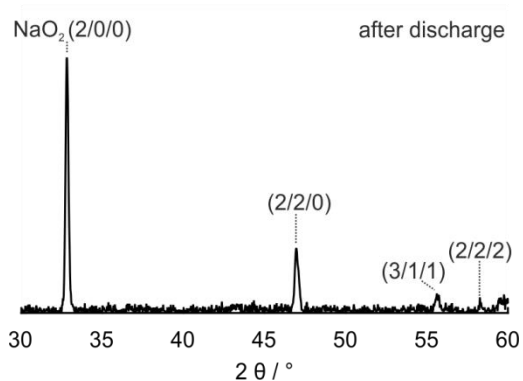


**Figure S4.** Powder XRD pattern of a discharged Na-O<sub>2</sub> cathode corresponding to Figure 1a.

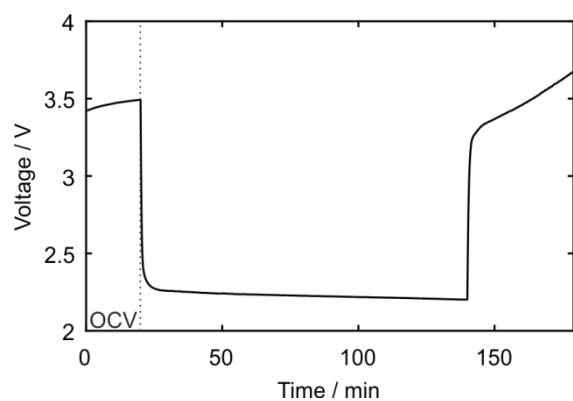


**Figure S5.** Load curve for galvanostatic cycling of a carbon paper cathode in the operando fluorescence setup in 0.5M NaOTf in diglyme containing 40 ppm H<sub>2</sub>O and 1.6×10<sup>-5</sup> M DMA. The high charging voltage suggests Na<sub>2</sub>O<sub>2</sub>·H<sub>2</sub>O as the discharge product in accord with previous reports.<sup>[7]</sup> Due to the small capacity achieved in the operando setup the formed phase could not be determined by XRD.

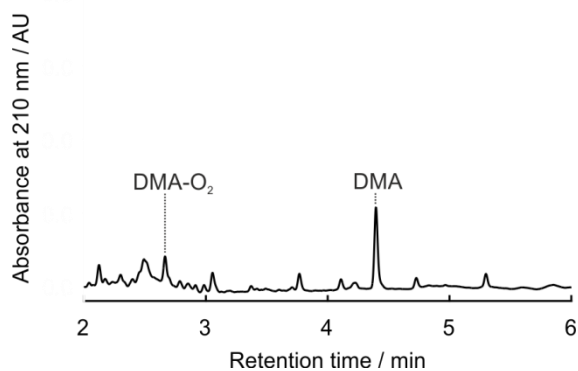


**Figure S6.** HPLC run of the electrolyte taken from the operando fluorescence setup after a single galvanostatic discharge showing <sup>1</sup>O<sub>2</sub> to form as indicated by the conversion of DMA to DMA-O<sub>2</sub>. The electrolyte was in 0.5 M NaOTf in diglyme containing 40 ppm H<sub>2</sub>O and 1.6 × 10<sup>-5</sup> M DMA.

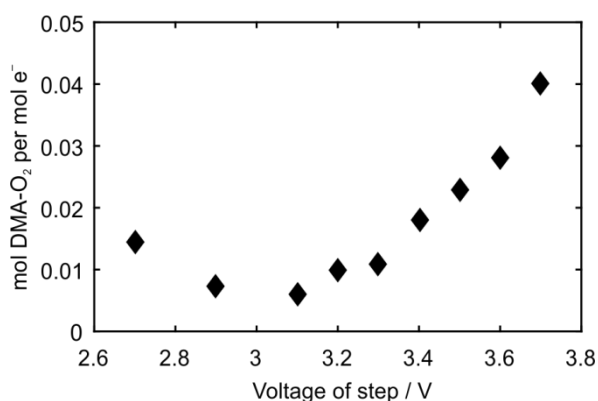


**Figure S7.** Fraction of the oxidized NaO<sub>2</sub> (based on charge) liberating <sup>1</sup>O<sub>2</sub> as determined by operando fluorescence (Fig. 2).

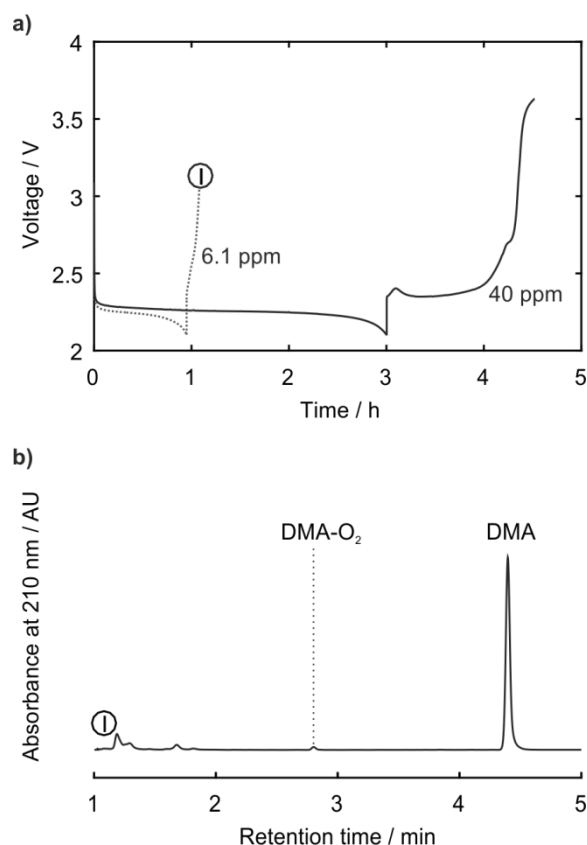


**Figure S8.** a) Load curve for galvanostatic cycling of a carbon paper electrode at  $90 \mu\text{A cm}^{-2}$  in 0.5 M NaOTf in diglyme containing 40 ppm of water or no additional water (6 ppm). b) HPLC data after discharge in nominally dry electrolyte and electrolyte containing 40 ppm water.

Figure S8 compares the voltage profiles with nominally dry electrolyte (6 ppm H<sub>2</sub>O) and electrolyte containing 40 ppm H<sub>2</sub>O. With the dry electrolyte, discharge capacity is reduced to a third and recharge voltage climbs immediately above 3 V in accord with Nazar et al. (*Nat. Chem.* **2015**, *7*, 496-501), who explained this behaviour by proton-induced phase transfer catalysis. HPLC analysis of the electrolyte shows ~10% as much DMA-O<sub>2</sub> to have formed as with the wet electrolyte. The amount of <sup>1</sup>O<sub>2</sub> per unit of charge was therefore significantly lower in the dry electrolyte as compared to the wet electrolyte, which supports the conclusion that proton sources drive <sup>1</sup>O<sub>2</sub> formation.

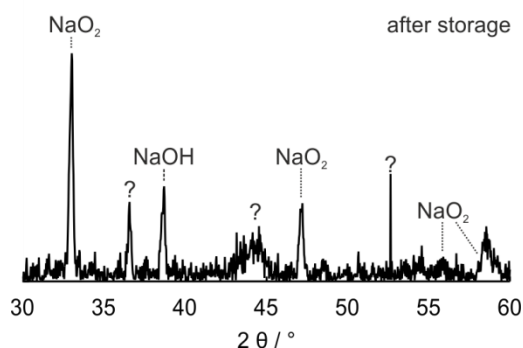


**Figure S9.** Powder XRD pattern of discharged Na-O<sub>2</sub> cathode after prolonged contact with the electrolyte. The cathode was first discharged in DMA-free electrolyte (0.5 M NaOTf in diglyme containing 40 ppm H<sub>2</sub>O), then washed and immersed in the same electrolyte additionally containing 30 mM DMA.

## Supplementary References

- [1] S. M. Borisov, G. Nuss, W. Haas, R. Saf, M. Schmuck, I. Klimant, *J. Photochem. Photobiol. A* **2009**, *201*, 128-135.
- [2] Y. Zhang, L. Ma, L. Zhang, Z. Peng, *J. Electrochem. Soc.* **2016**, *163*, A1270-A1274.
- [3] D. Lepage, C. Michot, G. Liang, M. Gauthier, S. B. Schougaard, *Angew. Chem. Int. Ed.* **2011**, *50*, 6884-6887.
- [4] M. M. Ottakam Thotiyl, S. A. Freunberger, Z. Peng, P. G. Bruce, *J. Am. Chem. Soc.* **2013**, *135*, 494-500.
- [5] P. Hartmann, C. L. Bender, J. Sann, A. K. Durr, M. Jansen, J. Janek, P. Adelhelm, *Phys. Chem. Chem. Phys.* **2013**, *15*, 11661-11672.
- [6] N. Mahne, B. Schafzahl, C. Leypold, M. Leypold, S. Grumm, A. Leitgeb, G. A. Strohmeier, M. Wilkening, O. Fontaine, D. Kramer, C. Slugovc, S. M. Borisov, S. A. Freunberger, *Nat. Energy* **2017**, *2*, 17036.
- [7] C. L. Bender, D. Schröder, R. Pinedo, P. Adelhelm, J. Janek, *Angew. Chem. Int. Ed.* **2016**, 4640–4649.

## A.2 Abbreviations

Abbreviation	Meaning
$^1\text{O}_2$	singlet oxygen in $^1\Delta_g$ state
$^3\text{O}_2$	triplet oxygen
$\epsilon$	relative permittivity
$\eta$	viscosity
$\nu$	frequency
$\sigma$	ionic conductivity
ACN	acetonitrile
AE	acoustic emission
AES	auger electron spectroscopy
AFM	atomic force microscopy
ATR	attenuated total reflection
CE	coulombic efficiency
CMC	carboxymethyl cellulose
$\text{C}_x\text{Li}$	lithium alkyl carbonate w. x carbon atoms in alkyl chain
$\text{C}_x\text{Li}_2$	lithium alkyl dicarbonate w. x carbon atoms in alkyl chain
$\text{C}_x\text{Na}$	sodium alkyl carbonate w. x carbon atoms in alkyl chain
$\text{C}_x\text{Na}_2$	sodium alkyl dicarbonate w. x carbon atoms in alkyl chain
d	interlayer spacing of lamellae
DABCO	1,4-diazabicyclo[2.2.2]octane
DBC	dibutyl carbonate
DC	dodecylene carbonate
DCM	dichloromethane
DEC	diethyl carbonate
DMA	9,10-dimethyl anthracene
DMA-O <sub>2</sub>	9,10-dimethyl anthracene endoperoxide
DMC	dimethyl carbonate
DME	dimethoxyethane
DMSO	dimethyl sulfoxide
DOC	dioctyl carbonate
DPT	photodynamic therapy
E	energy density
$E_a$	activation energy
EC	ethylene carbonate
EDX	dispersive X-ray spectroscopy
EIS	electrochemical impedance spectroscopy
EMC	ethyl methyl carbonate
EPR	electron paramagnetic resonance
EQCM	electrochemical quartz microbalance
FEC	fluoroethylene carbonate

Abbreviation	Meaning
FSI <sup>-</sup>	bis(fluorosulfonyl)imide anion
FTIR	Fourier transform infrared spectroscopy
HC	hard carbon
HC	hexylene carbonate
HOMO	highest unoccupied molecular orbital
HPLC	high performance liquid chromatography
ICP-OES	inductively coupled plasma optical emission spectrometry
LAC	lithium alkyl carbonate
LADC	lithium alkyl dicarbonate
LCO	LiCoO <sub>2</sub>
LEDC	lithium ethylene dicarbonate
LFP	LiFePO <sub>4</sub>
LMO	Li <sub>2</sub> Mn <sub>2</sub> O <sub>4</sub>
LUMO	lowest unoccupied molecular orbital
MS	mass spectrometry
NCA	LiNi <sub>0.80</sub> Co <sub>0.15</sub> Al <sub>0.05</sub> O <sub>2</sub>
NMC	LiNi <sub>0.33</sub> Mn <sub>0.33</sub> Co <sub>0.33</sub> O <sub>2</sub>
NMP	<i>N</i> -methylpyrrolidone
NMR	nuclear magnetic resonance
NVP	Na <sub>3</sub> V <sub>2</sub> (PO <sub>4</sub> ) <sub>3</sub>
OCV	open circuit voltage
OTf <sup>-</sup>	trifluoromethanesulfonate anion
PC	propylene carbonate
PXRD	powder X-ray diffraction
Q	capacity
SAC	sodium alkyl carbonate
SAXS	small angle X-ray scattering
SEI	solid electrolyte interphase
SEM	scanning electron microscopy
SPI	solid permeable membrane
TEM	transmission electron microscopy
TFSI <sup>-</sup>	bis(trifluoromethane)sulfonamide anion
TOF-SIMS	time of flight-secondary ion mass spectrometry
UV-vis	ultraviolet visible spectroscopy
V	voltage
VC	vinylene carbonate
VTF equation	Vogel-Tamann-Fulcher equation
XANES	X-ray absorption near edge structure
XPS	X-ray photoelectron spectroscopy
XRD	X-ray diffraction





## B. Bibliography

- [1] Mizushima, K., Jones, P. C., Wiseman, P. J. & Goodenough, J. B.  $\text{Li}_x\text{CoO}_2$  - a New Cathode Material for Batteries of High-Energy Density. *Materials Research Bulletin* **15**, 783–789 (1980).
- [2] Hunter, J. C. Preparation of a New Crystal Form of Manganese-Dioxide -  $\lambda\text{-MnO}_2$ . *Journal of Solid State Chemistry* **39**, 142–147 (1981).
- [3] Pillot, C. The Rechargeable Battery Market and Main Trends 2014-2025 (2015).
- [4] Blomgren, G. E. The Development and Future of Lithium Ion Batteries. *Journal of the Electrochemical Society* **164**, A5019–A5025 (2017).
- [5] Selim, R. & Bro, P. Some Observations on Rechargeable Lithium Electrodes in a Propylene Carbonate Electrolyte. *Journal of the Electrochemical Society* **121**, 1457–1459 (1974).
- [6] Rauh, R. D. & Brummer, S. B. Effect of Additives on Lithium Cycling in Propylene Carbonate. *Electrochimica Acta* **22**, 75–83 (1977).
- [7] Koch, V. R. & Young, J. H. Stability of Secondary Lithium Electrode in Tetrahydrofuran-Based Electrolytes. *Journal of the Electrochemical Society* **125**, 1371–1377 (1978).
- [8] Yoshimatsu, I., Hirai, T. & Yamaki, J. Lithium Electrode Morphology during Cycling in Lithium Cells. *Journal of the Electrochemical Society* **135**, 2422–2427 (1988).
- [9] Nishi, Y. The development of lithium ion secondary batteries. *Chemical Record* **1**, 406–413 (2001).
- [10] Dey, A. N. & Sullivan, B. P. Electrochemical Decomposition of Propylene Carbonate on Graphite. *Journal of the Electrochemical Society* **117**, 222–226 (1970).
- [11] Besenhard, J. O. & Fritz, H. P. The Electrochemistry of Black Carbons. *Angewandte Chemie-International Edition in English* **22**, 950–975 (1983).
- [12] Fong, R., Vonsacken, U. & Dahn, J. R. Studies of Lithium Intercalation into Carbons Using Nonaqueous Electrochemical-Cells. *Journal of the Electrochemical Society* **137**, 2009–2013 (1990).
- [13] Kasnatscheew, J. *et al.* The truth about the 1st cycle Coulombic efficiency of  $\text{LiNi}_{1/3}\text{Co}_{1/3}\text{Mn}_{1/3}\text{O}_2$  (NCM) cathodes. *Physical Chemistry Chemical Physics* **18**, 3956–3965 (2016).
- [14] He, P., Yu, H. J., Li, D. & Zhou, H. S. Layered lithium transition metal oxide cathodes towards high energy lithium-ion batteries. *Journal of Materials Chemistry* **22**, 3680–3695 (2012).
- [15] Belharouak, I., Sun, Y. K., Liu, J. & Amine, K.  $\text{Li}(\text{Ni}_{1/3}\text{Co}_{1/3}\text{Mn}_{1/3})\text{O}_2$  as a suitable cathode for high power applications. *Journal of Power Sources* **123**, 247–252 (2003).
- [16] Zhuang, G. V. *et al.*  $\text{Li}_2\text{CO}_3$  in  $\text{LiNi}_{0.8}\text{Co}_{0.15}\text{Al}_{0.05}\text{O}_2$  cathodes and its effects on capacity and power. *Journal of Power Sources* **134**, 293–297 (2004).

- [17] Chung, S. Y., Bloking, J. T. & Chiang, Y. M. Electronically conductive phospho-olivines as lithium storage electrodes. *Nature Materials* **1**, 123–128 (2002).
- [18] Padhi, A. K., Nanjundaswamy, K. S. & Goodenough, J. B. Phospho-olivines as positive-electrode materials for rechargeable lithium batteries. *Journal of the Electrochemical Society* **144**, 1188–1194 (1997).
- [19] Obrovac, M. N. & Chevrier, V. L. Alloy Negative Electrodes for Li-Ion Batteries. *Chemical Reviews* **114**, 11444–11502 (2014).
- [20] Cui, L. F., Hu, L. B., Choi, J. W. & Cui, Y. Light-Weight Free-Standing Carbon Nanotube-Silicon Films for Anodes of Lithium Ion Batteries. *ACS Nano* **4**, 3671–3678 (2010).
- [21] Hwang, T. H., Lee, Y. M., Kong, B. S., Seo, J. S. & Choi, J. W. Electrospun Core-Shell Fibers for Robust Silicon Nanoparticle-Based Lithium Ion Battery Anodes. *Nano Letters* **12**, 802–807 (2012).
- [22] Lee, K. T. & Cho, J. Roles of nanosize in lithium reactive nanomaterials for lithium ion batteries. *Nano Today* **6**, 28–41 (2011).
- [23] Zhong, Q. M., Bonakdarpour, A., Zhang, M. J., Gao, Y. & Dahn, J. R. Synthesis and electrochemistry of  $\text{LiNi}_x\text{Mn}_{2-x}\text{O}_4$ . *Journal of the Electrochemical Society* **144**, 205–213 (1997).
- [24] Patoux, S. *et al.* High voltage spinel oxides for Li-ion batteries: From the material research to the application. *Journal of Power Sources* **189**, 344–352 (2009).
- [25] You, Y. & Manthiram, A. Progress in High-Voltage Cathode Materials for Rechargeable Sodium-Ion Batteries. *Advanced Energy Materials* **8**, 1701785 (2018).
- [26] Kim, J. H., Pieczonka, N. P. W. & Yang, L. Challenges and Approaches for High-Voltage Spinel Lithium-Ion Batteries. *Chemphyschem* **15**, 1940–1954 (2014).
- [27] Manthiram, A., Chung, S. H. & Zu, C. X. Lithium-Sulfur Batteries: Progress and Prospects. *Advanced Materials* **27**, 1980–2006 (2015).
- [28] Muldoon, J., Bucur, C. B. & Gregory, T. Quest for Nonaqueous Multivalent Secondary Batteries: Magnesium and Beyond. *Chemical Reviews* **114**, 11683–11720 (2014).
- [29] Larcher, D. & Tarascon, J. M. Towards greener and more sustainable batteries for electrical energy storage. *Nature Chemistry* **7**, 19–29 (2015).
- [30] Kimball, S. M. U.S. Geological Survey: Mineral commodity summaries 2016 (2016).
- [31] Ponrouch, A. *et al.* Non-aqueous electrolytes for sodium-ion batteries. *Journal of Materials Chemistry A* **3**, 22–42 (2015).
- [32] Steen, B. A Systematic Approach to Environmental Priority Strategies in In Product Development (EPS), version 2000 Models and Data. Report, Chalmers University of Technology (1999).
- [33] Ponrouch, A. *et al.* Towards high energy density sodium ion batteries through electrolyte optimization. *Energy & Environmental Science* **6**, 2361–2369 (2013).
- [34] Irisarri, E., Ponrouch, A. & Palacin, M. R. Review-Hard Carbon Negative Electrode Materials for Sodium-Ion Batteries. *Journal of the Electrochemical Society* **162**, A2476–A2482 (2015).
- [35] Sawicki, M. & Shaw, L. L. Advances and challenges of sodium ion batteries as post lithium ion batteries. *Rsc Advances* **5**, 53129–53154 (2015).

- [36] Ponrouch, A. & Palacin, M. R. On the high and low temperature performances of Na-ion battery materials: Hard carbon as a case study. *Electrochemistry Communications* **54**, 51–54 (2015).
- [37] Abraham, K. M. & Jiang, Z. A polymer electrolyte-based rechargeable lithium/oxygen battery. *Journal of the Electrochemical Society* **143**, 1–5 (1996).
- [38] Aurbach, D., McCloskey, B. D., Nazar, L. & Bruce, P. G. Advances in understanding mechanisms underpinning lithium-air batteries. *Nature Energy* **1**, 16128 (2016).
- [39] Laoire, C. O., Mukerjee, S., Abraham, K. M., Plichta, E. J. & Hendrickson, M. A. Influence of Nonaqueous Solvents on the Electrochemistry of Oxygen in the Rechargeable Lithium-Air Battery. *Journal of Physical Chemistry C* **114**, 9178–9186 (2010).
- [40] Johnson, L. *et al.* The role of LiO<sub>2</sub> solubility in O<sub>2</sub> reduction in aprotic solvents and its consequences for Li-O<sub>2</sub> batteries. *Nature Chemistry* **6**, 1091–1099 (2014).
- [41] Viswanathan, V. *et al.* Electrical conductivity in Li<sub>2</sub>O<sub>2</sub> and its role in determining capacity limitations in non-aqueous Li-O<sub>2</sub> batteries. *Journal of Chemical Physics* **135**, 214704 (2011).
- [42] Mahne, N., Fontaine, O., Thotiyl, M. O., Wilkening, M. & Freunberger, S. A. Mechanism and performance of lithium-oxygen batteries - a perspective. *Chemical Science* **8**, 6716–6729 (2017).
- [43] Adams, B. D. *et al.* Current density dependence of peroxide formation in the Li-O<sub>2</sub> battery and its effect on charge. *Energy & Environmental Science* **6**, 1772–1778 (2013).
- [44] Kwabi, D. G. *et al.* The effect of water on discharge product growth and chemistry in Li-O<sub>2</sub> batteries. *Physical Chemistry Chemical Physics* **18**, 24944–24953 (2016).
- [45] Bruce, P. G., Freunberger, S. A., Hardwick, L. J. & Tarascon, J. M. Li-O<sub>2</sub> and Li-S batteries with high energy storage. *Nature Materials* **11**, 19–29 (2012).
- [46] Girishkumar, G., McCloskey, B., Luntz, A. C., Swanson, S. & Wilcke, W. Lithium - Air Battery: Promise and Challenges. *Journal of Physical Chemistry Letters* **1**, 2193–2203 (2010).
- [47] Radin, M. D. & Siegel, D. J. Charge transport in lithium peroxide: relevance for rechargeable metal-air batteries. *Energy & Environmental Science* **6**, 2370–2379 (2013).
- [48] Tian, F., Radin, M. D. & Siegel, D. J. Enhanced Charge Transport in Amorphous Li<sub>2</sub>O<sub>2</sub>. *Chemistry of Materials* **26**, 2952–2959 (2014).
- [49] Chen, Y., Freunberger, S. A., Peng, Z., Fontaine, O. & Bruce, P. G. Charging a LiO<sub>2</sub> battery using a redox mediator. *Nature Chemistry* **5**, 489–494 (2013).
- [50] Kwak, W. J. *et al.* Understanding the behavior of Li-oxygen cells containing LiI. *Journal of Materials Chemistry A* **3**, 8855–8864 (2015).
- [51] Bergner, B. J., Schurmann, A., Peppler, K., Garsuch, A. & Janek, J. TEMPO: A Mobile Catalyst for Rechargeable Li-O<sub>2</sub> Batteries. *Journal of the American Chemical Society* **136**, 15054–15064 (2014).
- [52] Feng, N. N., He, P. & Zhou, H. S. Enabling Catalytic Oxidation of Li<sub>2</sub>O<sub>2</sub> at the Liquid-Solid Interface: The Evolution of an Aprotic Li-O<sub>2</sub> Battery. *ChemSusChem* **8**, 600–602 (2015).
- [53] Kundu, D., Black, R., Adams, B. & Nazar, L. F. A Highly Active Low Voltage Redox Mediator for Enhanced Rechargeability of Lithium-Oxygen Batteries. *Acs Central Science* **1**, 510–515 (2015).

- [54] Cheng, F. Y. & Chen, J. Metal-air batteries: from oxygen reduction electrochemistry to cathode catalysts. *Chemical Society Reviews* **41**, 2172–2192 (2012).
- [55] Luntz, A. C. & McCloskey, B. D. Nonaqueous Li-Air Batteries: A Status Report. *Chemical Reviews* **114**, 11721–11750 (2014).
- [56] Freunberger, S. A. *et al.* Reactions in the Rechargeable Lithium-O<sub>2</sub> Battery with Alkyl Carbonate Electrolytes. *Journal of the American Chemical Society* **133**, 8040–8047 (2011).
- [57] McCloskey, B. D. *et al.* Limitations in Rechargeability of Li-O<sub>2</sub> Batteries and Possible Origins. *Journal of Physical Chemistry Letters* **3**, 3043–3047 (2012).
- [58] Wandt, J., Jakes, P., Granwehr, J., Gasteiger, H. A. & Eichel, R. A. Singlet Oxygen Formation during the Charging Process of an Aprotic Lithium-Oxygen Battery. *Angewandte Chemie-International Edition* **55**, 6892–6895 (2016).
- [59] Mahne, N. *et al.* Singlet oxygen generation as a major cause for parasitic reactions during cycling of aprotic lithium-oxygen batteries. *Nature Energy* **2**, 17036 (2017).
- [60] Liu, L. *et al.* Stabilization of Li Metal Anode in DMSO-Based Electrolytes via Optimization of Salt-Solvent Coordination for Li-O<sub>2</sub> Batteries. *Advanced Energy Materials* **7**, 1602605 (2017).
- [61] Giordani, V. *et al.* Synergistic Effect of Oxygen and LiNO<sub>3</sub> on the Interfacial Stability of Lithium Metal in a Li/O<sub>2</sub> Battery. *Journal of the Electrochemical Society* **160**, A1544–A1550 (2013).
- [62] Hartmann, P. *et al.* A rechargeable room-temperature sodium superoxide (NaO<sub>2</sub>) battery. *Nature Materials* **12**, 228–232 (2013).
- [63] Li, Y. L. *et al.* Superior catalytic activity of nitrogen-doped graphene cathodes for high energy capacity sodium-air batteries. *Chemical Communications* **49**, 11731–11733 (2013).
- [64] Liu, W., Sun, Q., Yang, Y., Xie, J. Y. & Fu, Z. W. An enhanced electrochemical performance of a sodium-air battery with graphene nanosheets as air electrode catalysts. *Chemical Communications* **49**, 1951–1953 (2013).
- [65] Liu, W. M., Yin, W. W., Ding, F., Sang, L. & Fu, Z. W. NiCo<sub>2</sub>O<sub>4</sub> nanosheets supported on Ni foam for rechargeable nonaqueous sodium-air batteries. *Electrochemistry Communications* **45**, 87–90 (2014).
- [66] Jian, Z. L. *et al.* High capacity Na-O<sub>2</sub> batteries with carbon nanotube paper as binder-free air cathode. *Journal of Power Sources* **251**, 466–469 (2014).
- [67] Kim, J., Lim, H. D., Gwon, H. & Kang, K. Sodium-oxygen batteries with alkyl-carbonate and ether based electrolytes. *Physical Chemistry Chemical Physics* **15**, 3623–3629 (2013).
- [68] Bender, C. L., Schroder, D., Pinedo, R., Adelhelm, P. & Janek, J. One- or Two-Electron Transfer? The Ambiguous Nature of the Discharge Products in Sodium-Oxygen Batteries. *Angewandte Chemie-International Edition* **55**, 4640–4649 (2016).
- [69] Ortiz-Vitoriano, N. *et al.* Rate-Dependent Nucleation and Growth of NaO<sub>2</sub> in Na-O<sub>2</sub> Batteries. *Journal of Physical Chemistry Letters* **6**, 2636–2643 (2015).
- [70] Xia, C., Black, R., Fernandes, R., Adams, B. & Nazar, L. F. The critical role of phase-transfer catalysis in aprotic sodium oxygen batteries. *Nature Chemistry* **7**, 496–501 (2015).
- [71] McCloskey, B. D., Garcia, J. M. & Luntz, A. C. Chemical and Electrochemical Differences in Nonaqueous Li-O<sub>2</sub> and Na-O<sub>2</sub> Batteries. *Journal of Physical Chemistry Letters* **5**, 1230–1235 (2014).

- [72] Hartmann, P. *et al.* A comprehensive study on the cell chemistry of the sodium superoxide (NaO<sub>2</sub>) battery. *Physical Chemistry Chemical Physics* **15**, 11661–11672 (2013).
- [73] Bi, X. X. *et al.* Investigating dendrites and side reactions in sodium-oxygen batteries for improved cycle lives. *Chemical Communications* **51**, 7665–7668 (2015).
- [74] Bender, C. L., Hartmann, P., Vracar, M., Adelhelm, P. & Janek, J. On the Thermodynamics, the Role of the Carbon Cathode, and the Cycle Life of the Sodium Superoxide (NaO<sub>2</sub>) Battery. *Advanced Energy Materials* **4**, 1301863 (2014).
- [75] Das, S. K., Lau, S. & Archer, L. A. Sodium-oxygen batteries: a new class of metal-air batteries. *Journal of Materials Chemistry A* **2**, 12623–12629 (2014).
- [76] Landa-Medrano, I. *et al.* Sodium-Oxygen Battery: Steps Toward Reality. *Journal of Physical Chemistry Letters* **7**, 1161–1166 (2016).
- [77] Black, R. *et al.* The Nature and Impact of Side Reactions in Glyme-based Sodium-Oxygen Batteries. *Chemsuschem* **9**, 1795–1803 (2016).
- [78] Zhuang, G. V., Yang, H., Ross, P. N., Xu, K. & Jow, T. R. Lithium methyl carbonate as a reaction product of metallic lithium and dimethyl carbonate. *Electrochemical and Solid State Letters* **9**, A64–A68 (2006).
- [79] Gireaud, L., Grugeon, S., Laruelle, S., Pilard, S. & Tarascon, J. M. Identification of Li battery electrolyte degradation products through direct synthesis and characterization of alkyl carbonate salts. *Journal of the Electrochemical Society* **152**, A850–A857 (2005).
- [80] Xu, K. *et al.* Syntheses and characterization of lithium alkyl mono- and dicarbonates as components of surface films in Li-ion batteries. *Journal of Physical Chemistry B* **110**, 7708–7719 (2006).
- [81] Ponrouch, A., Marchante, E., Courty, M., Tarascon, J. M. & Palacin, M. R. In search of an optimized electrolyte for Na-ion batteries. *Energy & Environmental Science* **5**, 8572–8583 (2012).
- [82] Xu, K. Electrolytes and Interphases in Li-Ion Batteries and Beyond. *Chemical Reviews* **114**, 11503–11618 (2014).
- [83] Fry, A. J. *Synthetic Organic Electrochemistry* (Wiley, 1989).
- [84] Naejus, R., Lemordant, D., Coudert, R. & Willmann, P. Excess thermodynamic properties of binary mixtures containing linear or cyclic carbonates as solvents at the temperatures 298.15 K and 315.15 K. *Journal of Chemical Thermodynamics* **29**, 1503–1515 (1997).
- [85] Xu, K. Nonaqueous liquid electrolytes for lithium-based rechargeable batteries. *Chemical Reviews* **104**, 4303–4417 (2004).
- [86] Smart, M. C., Ratnakumar, B. V. & Surampudi, S. Electrolytes for low-temperature lithium batteries based on ternary mixtures of aliphatic carbonates. *Journal of the Electrochemical Society* **146**, 486–492 (1999).
- [87] Ding, M. S., Xu, K., Zhang, S. S. & Jow, T. R. Liquid/solid phase diagrams of binary carbonates for lithium batteries part II. *Journal of the Electrochemical Society* **148**, A299–A304 (2001).
- [88] Winter, M. The Solid Electrolyte Interphase - The Most Important and the Least Understood Solid Electrolyte in Rechargeable Li Batteries. *Zeitschrift Fur Physikalische Chemie-International Journal of Research in Physical Chemistry & Chemical Physics* **223**, 1395–1406 (2009).
- [89] Xu, K. & von Cresce, A. Interfacing electrolytes with electrodes in Li ion batteries. *Journal of Materials Chemistry* **21**, 9849–9864 (2011).

- [90] Xu, K. & Cresce, A. V. Li<sup>+</sup>-solvation/desolvation dictates interphasial processes on graphitic anode in Li ion cells. *Journal of Materials Research* **27**, 2327–2341 (2012).
- [91] Verma, P., Maire, P. & Novak, P. A review of the features and analyses of the solid electrolyte interphase in Li-ion batteries. *Electrochimica Acta* **55**, 6332–6341 (2010).
- [92] Tsubouchi, S. *et al.* Spectroscopic Characterization of Surface Films Formed on Edge Plane Graphite in Ethylene Carbonate-Based Electrolytes Containing Film-Forming Additives. *Journal of the Electrochemical Society* **159**, A1786–A1790 (2012).
- [93] Nie, M. Y. *et al.* Lithium Ion Battery Graphite Solid Electrolyte Interphase Revealed by Microscopy and Spectroscopy. *Journal of Physical Chemistry C* **117**, 1257–1267 (2013).
- [94] Nie, M. Y., Abraham, D. P., Chen, Y. J., Bose, A. & Lucht, B. L. Silicon Solid Electrolyte Interphase (SEI) of Lithium Ion Battery Characterized by Microscopy and Spectroscopy. *Journal of Physical Chemistry C* **117**, 13403–13412 (2013).
- [95] Shu, J. Study of the Interface Between Li<sub>4</sub>Ti<sub>5</sub>O<sub>12</sub> Electrodes and Standard Electrolyte Solutions in 0.0–0.5 V. *Electrochemical and Solid State Letters* **11**, A238–A240 (2008).
- [96] Dedryvere, R. *et al.* XPS valence characterization of lithium salts as a tool to study electrode/electrolyte interfaces of Li-ion batteries. *Journal of Physical Chemistry B* **110**, 12986–12992 (2006).
- [97] Marom, R., Haik, O., Aurbach, D. & Halalay, I. C. Revisiting LiClO<sub>4</sub> as an Electrolyte for Rechargeable Lithium-Ion Batteries. *Journal of the Electrochemical Society* **157**, A972–A983 (2010).
- [98] Aurbach, D., Daroux, M. L., Faguy, P. W. & Yeager, E. Identification of Surface-Films Formed on Lithium in Propylene Carbonate Solutions. *Journal of the Electrochemical Society* **134**, 1611–1620 (1987).
- [99] Shkrob, I. A., Zhu, Y., Marin, T. W. & Abraham, D. Reduction of Carbonate Electrolytes and the Formation of Solid-Electrolyte Interface (SEI) in Lithium-Ion Batteries. 1. Spectroscopic Observations of Radical Intermediates Generated in One-Electron Reduction of Carbonates. *Journal of Physical Chemistry C* **117**, 19255–19269 (2013).
- [100] Zhuang, G. R. V., Xu, K., Yang, H., Jow, T. R. & Ross, P. N. Lithium ethylene dicarbonate identified as the primary product of chemical and electrochemical reduction of EC in 1.2 m LiPF<sub>6</sub>/EC : EMC electrolyte. *Journal of Physical Chemistry B* **109**, 17567–17573 (2005).
- [101] Xu, K., Lam, Y. F., Zhang, S. S., Jow, T. R. & Curtis, T. B. Solvation sheath of Li<sup>+</sup> in nonaqueous electrolytes and its implication of graphite/electrolyte interface chemistry. *Journal of Physical Chemistry C* **111**, 7411–7421 (2007).
- [102] Dedryvere, R. *et al.* Characterization of lithium alkyl carbonates by X-ray photoelectron spectroscopy: experimental and theoretical study. *J Phys Chem B* **109**, 15868–75 (2005).
- [103] Leifer, N. *et al.* C-13 Solid State NMR Suggests Unusual Breakdown Products in SEI Formation on Lithium Ion Electrodes. *Journal of the Electrochemical Society* **158**, A471–A480 (2011).
- [104] Augustsson, A. *et al.* Solid electrolyte interphase on graphite Li-ion battery anodes studied by soft X-ray spectroscopy. *Physical Chemistry Chemical Physics* **6**, 4185–4189 (2004).
- [105] Xiao, A., Yang, L., Lucht, B. L., Kang, S. H. & Abraham, D. P. Examining the Solid Electrolyte Interphase on Binder-Free Graphite Electrodes. *Journal of the Electrochemical Society* **156**, A318–A327 (2009).

- [106] Ota, H., Sakata, Y., Inoue, A. & Yamaguchi, S. Analysis of vinylene carbonate derived SEI layers on graphite anode. *Journal of the Electrochemical Society* **151**, A1659–A1669 (2004).
- [107] Shkrob, I. A., Zhu, Y., Marin, T. W. & Abraham, D. Reduction of Carbonate Electrolytes and the Formation of Solid-Electrolyte Interface (SEI) in Lithium-Ion Batteries. 2. Radiolytically Induced Polymerization of Ethylene Carbonate. *Journal of Physical Chemistry C* **117**, 19270–19279 (2013).
- [108] Kanamura, K., Tomura, H., Shiraishi, S. & Takehara, Z. I. Xps Analysis of Lithium Surfaces Following Immersion in Various Solvents Containing LiPF<sub>4</sub>. *Journal of the Electrochemical Society* **142**, 340–347 (1995).
- [109] Kanamura, K., Shiraishi, S. & Takehara, Z. Electrochemical deposition of very smooth lithium using nonaqueous electrolytes containing HF. *Journal of the Electrochemical Society* **143**, 2187–2197 (1996).
- [110] Harilal, S. S., Allain, J. P., Hassanein, A., Hendricks, M. R. & Nieto-Perez, M. Reactivity of lithium exposed graphite surface. *Applied Surface Science* **255**, 8539–8543 (2009).
- [111] Xiao, A., Yang, L. & Lucht, B. L. Thermal reactions of LiPF<sub>6</sub> with added LiBOB - Electrolyte stabilization and generation of LiF<sub>4</sub>OP. *Electrochemical and Solid State Letters* **10**, A241–A244 (2007).
- [112] Xu, M. Q., Xiao, A., Li, W. S. & Lucht, B. L. Investigation of Lithium Tetrafluoro-oxalatophosphate as a Lithium-Ion Battery Electrolyte. *Electrochemical and Solid State Letters* **12**, A155–A158 (2009).
- [113] Xu, M. Q., Xiao, A., Li, W. S. & Lucht, B. L. Investigation of Lithium Tetrafluoro-oxalatophosphate [LiPF<sub>4</sub>(C<sub>2</sub>O<sub>4</sub>)] as a Lithium-Ion Battery Electrolyte for Elevated Temperature Performance. *Journal of the Electrochemical Society* **157**, A115–A120 (2010).
- [114] Zhang, J. *et al.* Direct Observation of Inhomogeneous Solid Electrolyte Interphase on MnO Anode with Atomic Force Microscopy and Spectroscopy. *Nano Letters* **12**, 2153–2157 (2012).
- [115] Aurbach, D. *et al.* The Study of Electrolyte-Solutions Based on Ethylene and Diethyl Carbonates for Rechargeable Li Batteries .1. Li Metal Anodes. *Journal of the Electrochemical Society* **142**, 2873–2882 (1995).
- [116] Lu, P., Li, C., Schneider, E. W. & Harris, S. J. Chemistry, Impedance, and Morphology Evolution in Solid Electrolyte Interphase Films during Formation in Lithium Ion Batteries. *Journal of Physical Chemistry C* **118**, 896–903 (2014).
- [117] Aurbach, D., Einely, Y. & Zaban, A. The Surface-Chemistry of Lithium Electrodes in Alkyl Carbonate Solutions. *Journal of the Electrochemical Society* **141**, L1–L3 (1994).
- [118] Abouimrane, A. *et al.* Sodium insertion in carboxylate based materials and their application in 3.6 V full sodium cells. *Energy & Environmental Science* **5**, 9632–9638 (2012).
- [119] Philippe, B., Valvo, M., Lindgren, F., Rensmo, H. & Edstrom, K. Investigation of the Electrode/Electrolyte Interface of Fe<sub>2</sub>O<sub>3</sub> Composite Electrodes: Li vs Na Batteries. *Chemistry of Materials* **26**, 5028–5041 (2014).
- [120] Shi, S. Q. *et al.* Direct Calculation of Li-Ion Transport in the Solid Electrolyte Interphase. *Journal of the American Chemical Society* **134**, 15476–15487 (2012).
- [121] Shi, S. Q., Qi, Y., Li, H. & Hector, L. G. Defect Thermodynamics and Diffusion Mechanisms in Li<sub>2</sub>CO<sub>3</sub> and Implications for the Solid Electrolyte Interphase in Li-Ion Batteries. *Journal of Physical Chemistry C* **117**, 8579–8593 (2013).

- [122] Borodin, O., Zhuang, G. R. V., Ross, P. N. & Xu, K. Molecular Dynamics Simulations and Experimental Study of Lithium Ion Transport in Dilithium Ethylene Dicarboxate (vol 117, pg 7433, 2013). *Journal of Physical Chemistry C* **117**, 16749–16749 (2013).
- [123] Bedrov, D., Borodin, O. & Hooper, J. B. Li<sup>+</sup> Transport and Mechanical Properties of Model Solid Electrolyte Interphases (SEI): Insight from Atomistic Molecular Dynamics Simulations. *Journal of Physical Chemistry C* **121**, 16098–16109 (2017).
- [124] Iermakova, D. I., Dugas, R., Palacin, M. R. & Ponrouch, A. On the Comparative Stability of Li and Na Metal Anode Interfaces in Conventional Alkyl Carbonate Electrolytes. *Journal of The Electrochemical Society* **162**, A7060–A7066 (2015).
- [125] McDowell, M. T., Lee, S. W., Nix, W. D. & Cui, Y. 25th Anniversary Article: Understanding the Lithiation of Silicon and Other Alloying Anodes for Lithium-Ion Batteries. *Advanced Materials* **25**, 4966–4984 (2013).
- [126] Zheng, J. Y. *et al.* 3D visualization of inhomogeneous multi-layered structure and Young's modulus of the solid electrolyte interphase (SEI) on silicon anodes for lithium ion batteries. *Physical Chemistry Chemical Physics* **16**, 13229–13238 (2014).
- [127] Shin, H., Park, J., Han, S., Sastry, A. M. & Lu, W. Component-/structure-dependent elasticity of solid electrolyte interphase layer in Li-ion batteries: Experimental and computational studies. *Journal of Power Sources* **277**, 169–179 (2015).
- [128] Wang, L. X., Deng, D., Lev, L. C. & Ng, S. In-situ investigation of solid-electrolyte interphase formation on the anode of Li-ion batteries with Atomic Force Microscopy. *Journal of Power Sources* **265**, 140–148 (2014).
- [129] Tokranov, A., Sheldon, B. W., Li, C. Z., Minne, S. & Xiao, X. C. In Situ Atomic Force Microscopy Study of Initial Solid Electrolyte Interphase Formation on Silicon Electrodes for Li-Ion Batteries. *Acs Applied Materials & Interfaces* **6**, 6672–6686 (2014).
- [130] Weadock, N. *et al.* Determination of mechanical properties of the SEI in sodium ion batteries via colloidal probe microscopy. *Nano Energy* **2**, 713–719 (2013).
- [131] Schafzahl, L. *Characterization of Lithium- and Sodium Alkyl carbonates as SEI components for the design of novel electrolytes*. Thesis (2015).
- [132] Kenar, J. A., Knothe, G. & Copes, A. L. Synthesis and characterization of dialkyl carbonates prepared from mid-, long-chain, and Guerbet alcohols. *Journal of the American Oil Chemists Society* **81**, 285–291 (2004).
- [133] Aoyagi, N., Furusho, Y. & Endo, T. Effective synthesis of cyclic carbonates from carbon dioxide and epoxides by phosphonium iodides as catalysts in alcoholic solvents. *Tetrahedron Letters* **54**, 7031–7034 (2013).
- [134] Choi, N. S., Han, J. G., Ha, S. Y., Park, I. & Back, C. K. Recent advances in the electrolytes for interfacial stability of high-voltage cathodes in lithium-ion batteries. *Rsc Advances* **5**, 2732–2748 (2015).
- [135] Ma, L., Xia, J. & Dahn, J. R. Improving the High Voltage Cycling of Li[Ni<sub>0.42</sub>Mn<sub>0.42</sub>Co<sub>0.16</sub>]O<sub>2</sub> (NMC442)/Graphite Pouch Cells Using Electrolyte Additives. *Journal of the Electrochemical Society* **161**, A2250–A2254 (2014).
- [136] Tarnopolskiy, V. *et al.* Beneficial influence of succinic anhydride as electrolyte additive on the self-discharge of 5 V LiNi<sub>0.4</sub>Mn<sub>1.6</sub>O<sub>4</sub> cathodes. *Journal of Power Sources* **236**, 39–46 (2013).
- [137] Wang, D. Y. *et al.* A Systematic Study of Electrolyte Additives in Li[Ni<sub>1/3</sub>Mn<sub>1/3</sub>Co<sub>1/3</sub>]O<sub>2</sub> (NMC)/Graphite Pouch Cells. *Journal of the Electrochemical Society* **161**, A1818–A1827 (2014).



- 
- [138] Yu, L. *et al.* Preferential Adsorption of Solvents on the Cathode Surface of Lithium Ion Batteries. *Angewandte Chemie-International Edition* **52**, 5753–5756 (2013).
- [139] Qian, J. F. *et al.* High rate and stable cycling of lithium metal anode. *Nature Communications* **6**, 6362 (2015).
- [140] Shkrob, I. A., Marin, T. W., Zhu, Y. & Abraham, D. P. Why Bis(fluorosulfonyl)imide Is a "Magic Anion" for Electrochemistry. *Journal of Physical Chemistry C* **118**, 19661–19671 (2014).
- [141] Lee, J. *et al.* Ultraconcentrated Sodium Bis(fluorosulfonyl)imide-Based Electrolytes for High-Performance Sodium Metal Batteries. *Acs Applied Materials & Interfaces* **9**, 3723–3732 (2017).
- [142] Takada, K. *et al.* Unusual Passivation Ability of Superconcentrated Electrolytes toward Hard Carbon Negative Electrodes in Sodium-Ion Batteries. *Acs Applied Materials & Interfaces* **9**, 33802–33809 (2017).
- [143] Kim, H. *et al.* Recent Progress in Electrode Materials for Sodium-Ion Batteries. *Advanced Energy Materials* **6**, 1600943 (2016).
- [144] Komaba, S. *et al.* Electrochemical Na Insertion and Solid Electrolyte Interphase for Hard-Carbon Electrodes and Application to Na-Ion Batteries. *Advanced Functional Materials* **21**, 3859–3867 (2011).
- [145] Vidal-Abarca, C. *et al.* Improving the cyclability of sodium-ion cathodes by selection of electrolyte solvent. *Journal of Power Sources* **197**, 314–318 (2012).
- [146] Jian, Z. L. *et al.* Superior Electrochemical Performance and Storage Mechanism of Na<sub>3</sub>V<sub>2</sub>(PO<sub>4</sub>)<sub>3</sub> Cathode for Room-Temperature Sodium-Ion Batteries. *Advanced Energy Materials* **3**, 156–160 (2013).
- [147] Hatchard, T. D. & Obrovac, M. N. Evaluation of Electrolyte Salts and Solvents for Na-Ion Batteries in Symmetric Cells. *Journal of the Electrochemical Society* **161**, A1748–A1752 (2014).
- [148] Rudola, A., Aurbach, D. & Balaya, P. A new phenomenon in sodium batteries: Voltage step due to solvent interaction. *Electrochemistry Communications* **46**, 56–59 (2014).
- [149] Bommier, C. *et al.* New Paradigms on the Nature of Solid Electrolyte Interphase Formation and Capacity Fading of Hard Carbon Anodes in Na-Ion Batteries. *Advanced Materials Interfaces* **3**, 1600449 (2016).
- [150] Komaba, S. *et al.* Fluorinated Ethylene Carbonate as Electrolyte Additive for Rechargeable Na Batteries. *Acs Applied Materials & Interfaces* **3**, 4165–4168 (2011).
- [151] Ponrouch, A., Goni, A. R. & Palacin, M. R. High capacity hard carbon anodes for sodium ion batteries in additive free electrolyte. *Electrochemistry Communications* **27**, 85–88 (2013).
- [152] Lee, Y., Lee, J., Kim, H., Kang, K. & Choi, N. S. Highly stable linear carbonate-containing electrolytes with fluoroethylene carbonate for high-performance cathodes in sodium-ion batteries. *Journal of Power Sources* **320**, 49–58 (2016).
- [153] Dugas, R. *et al.* Na Reactivity toward Carbonate-Based Electrolytes: The Effect of FEC as Additive. *Journal of The Electrochemical Society* **163**, A2333–A2339 (2016).
- [154] Jeong, S. K., Inaba, M., Iriyama, Y., Abe, T. & Ogumi, Z. Electrochemical intercalation of lithium ion within graphite from propylene carbonate solutions. *Electrochemical and Solid State Letters* **6**, A13–A15 (2003).

- [155] Yamada, Y. *et al.* Unusual Stability of Acetonitrile-Based Superconcentrated Electrolytes for Fast-Charging Lithium-Ion Batteries. *Journal of the American Chemical Society* **136**, 5039–5046 (2014).
- [156] Yamada, Y., Takazawa, Y., Miyazaki, K. & Abe, T. Electrochemical Lithium Intercalation into Graphite in Dimethyl Sulfoxide-Based Electrolytes: Effect of Solvation Structure of Lithium Ion. *Journal of Physical Chemistry C* **114**, 11680–11685 (2010).
- [157] Yamada, Y. *et al.* General Observation of Lithium Intercalation into Graphite in Ethylene-Carbonate-Free Superconcentrated Electrolytes. *Acs Applied Materials & Interfaces* **6**, 10892–10899 (2014).
- [158] Yamada, Y., Yaegashi, M., Abe, T. & Yamada, A. A superconcentrated ether electrolyte for fast-charging Li-ion batteries. *Chemical Communications* **49**, 11194–11196 (2013).
- [159] Ueno, K. *et al.* Glyme-Lithium Salt Equimolar Molten Mixtures: Concentrated Solutions or Solvate Ionic Liquids? *Journal of Physical Chemistry B* **116**, 11323–11331 (2012).
- [160] Yoshida, K. *et al.* Oxidative-Stability Enhancement and Charge Transport Mechanism in Glyme-Lithium Salt Equimolar Complexes. *Journal of the American Chemical Society* **133**, 13121–13129 (2011).
- [161] Petibon, R., Aiken, C. P., Ma, L., Xiong, D. & Dahn, J. R. The use of ethyl acetate as a sole solvent in highly concentrated electrolyte for Li-ion batteries. *Electrochimica Acta* **154**, 287–293 (2015).
- [162] Suo, L. M., Hu, Y. S., Li, H., Armand, M. & Chen, L. Q. A new class of Solvent-in-Salt electrolyte for high-energy rechargeable metallic lithium batteries. *Nature Communications* **4**, 1481 (2013).
- [163] Suo, L. M. *et al.* "Water-in-salt" electrolyte enables high-voltage aqueous lithium-ion chemistries. *Science* **350**, 938–943 (2015).
- [164] Terada, S. *et al.* Physicochemical properties of pentaglyme-sodium bis(trifluoromethanesulfonyl)amide solvate ionic liquid. *Physical Chemistry Chemical Physics* **16**, 11737–11746 (2014).
- [165] Thotiyil, M. M. O., Freunberger, S. A., Peng, Z. Q. & Bruce, P. G. The Carbon Electrode in Nonaqueous Li-O<sub>2</sub> Cells. *Journal of the American Chemical Society* **135**, 494–500 (2013).
- [166] Ohzuku, T., Tomura, H. & Sawai, K. Monitoring of particle fracture by acoustic emission during charge and discharge of Li/MnO<sub>2</sub> cells. *Journal of the Electrochemical Society* **144**, 3496–3500 (1997).
- [167] Kircheva, N., Genies, S., Brun-Buisson, D. & Thivel, P. X. Study of Solid Electrolyte Interface Formation and Lithium Intercalation in Li-Ion Batteries by Acoustic Emission. *Journal of the Electrochemical Society* **159**, A18–A25 (2012).
- [168] Kominato, A. *et al.* Analysis of surface films on lithium in various organic electrolytes. *Journal of Power Sources* **68**, 471–475 (1997).
- [169] Morigaki, K. & Ohta, A. Analysis of the surface of lithium in organic electrolyte by atomic force microscopy, Fourier transform infrared spectroscopy and scanning auger electron microscopy. *Journal of Power Sources* **76**, 159–166 (1998).
- [170] Campana, F. P., Buqa, H., Novak, P., Kotz, R. & Siegenthaler, H. In situ atomic force microscopy study of exfoliation phenomena on graphite basal planes. *Electrochemistry Communications* **10**, 1590–1593 (2008).
- [171] Mogi, R., Inaba, M., Iriyama, Y., Abe, T. & Ogumi, Z. In situ atomic force microscopy study on lithium deposition on nickel substrates at elevated temperatures. *Journal of the Electrochemical Society* **149**, A385–A390 (2002).

- [172] Gachot, G. *et al.* Deciphering the multi-step degradation mechanisms of carbonate-based electrolyte in Li batteries. *Journal of Power Sources* **178**, 409–421 (2008).
- [173] Peled, E. *et al.* Composition, depth profiles and lateral distribution of materials in the SEI built on HOPG-TOF SIMS and XPS studies. *Journal of Power Sources* **97-8**, 52–57 (2001).
- [174] Schafzahl, L., Hanzu, I., Wilkening, M. & Freunberger, S. A. An Electrolyte for Reversible Cycling of Sodium Metal and Intercalation Compounds. *Chemsuschem* **10**, 401–408 (2017).
- [175] Dolle, M., Grugeon, S., Beaudoin, B., Dupont, L. & Tarascon, J. M. In situ TEM study of the interface carbon/electrolyte. *Journal of Power Sources* **97-8**, 104–106 (2001).
- [176] Smart, M. C. *et al.* Irreversible capacities of graphite in low-temperature electrolytes for lithium-ion batteries. *Journal of the Electrochemical Society* **146**, 3963–3969 (1999).
- [177] Liu, X. H. *et al.* Anisotropic Swelling and Fracture of Silicon Nanowires during Lithiation. *Nano Letters* **11**, 3312–3318 (2011).
- [178] Zhang, S. S., Xu, K. & Jow, T. R. Electrochemical impedance study on the low temperature of Li-ion batteries. *Electrochimica Acta* **49**, 1057–1061 (2004).
- [179] McCloskey, B. D., Bethune, D. S., Shelby, R. M., Girishkumar, G. & Luntz, A. C. Solvents' Critical Role in Nonaqueous Lithium-Oxygen Battery Electrochemistry. *Journal of Physical Chemistry Letters* **2**, 1161–1166 (2011).
- [180] Baddour-Hadjean, R., Navone, C. & Pereira-Ramos, J. P. In situ Raman microspectrometry investigation of electrochemical lithium intercalation into sputtered crystalline V<sub>2</sub>O<sub>5</sub> thin films. *Electrochimica Acta* **54**, 6674–6679 (2009).
- [181] Akai, T., Ota, H., Namita, H., Yamaguchi, S. & Nomura, M. XANES study on solid electrolyte interface of Li ion battery. *Physica Scripta* **T115**, 408–411 (2005).
- [182] Itagaki, M. *et al.* In situ electrochemical impedance spectroscopy to investigate negative electrode of lithium-ion rechargeable batteries. *Journal of Power Sources* **135**, 255–261 (2004).
- [183] Chen, Z. H., Liu, J. & Amine, K. Lithium difluoro(oxalato)borate as salt for lithium-ion batteries. *Electrochemical and Solid State Letters* **10**, A45–A47 (2007).
- [184] Krueger, S. *et al.* How Do Reactions at the Anode/Electrolyte Interface Determine the Cathode Performance in Lithium-Ion Batteries? *Journal of the Electrochemical Society* **160**, A542–A548 (2013).
- [185] Dedryvere, R. *et al.* Electrode/Electrolyte Interface Reactivity in High-Voltage Spinel LiMn<sub>1.6</sub>Ni<sub>0.4</sub>O<sub>4</sub>/Li<sub>4</sub>Ti<sub>5</sub>O<sub>12</sub> Lithium-Ion Battery. *Journal of Physical Chemistry C* **114**, 10999–11008 (2010).
- [186] Lu, J., Wu, T. P. & Amine, K. State-of-the-art characterization techniques for advanced lithium-ion batteries. *Nature Energy* **2**, 17011 (2017).
- [187] Bryngelsson, H., Stjerndahl, M., Gustafsson, T. & Edstrom, K. How dynamic is the SEI? *Journal of Power Sources* **174**, 970–975 (2007).
- [188] Kwon, K., Kong, F. P., McLarnon, F. & Evans, J. W. Characterization of the SEI on a carbon film electrode by combined EQCM and spectroscopic ellipsometry. *Journal of the Electrochemical Society* **150**, A229–A233 (2003).
- [189] Kwon, K. & Evans, J. W. Comparison between cyclic voltammetry and chronoamperometry when coupled with EQCM for the study of the SEI on a carbon film electrode. *Electrochimica Acta* **49**, 867–872 (2004).

- [190] Xiong, S. Z., Xie, K., Diao, Y. & Hong, X. B. Characterization of the solid electrolyte interphase on lithium anode for preventing the shuttle mechanism in lithium-sulfur batteries. *Journal of Power Sources* **246**, 840–845 (2014).
- [191] von Cresce, A., Russell, S. M., Baker, D. R. & Gaskell, K., K. J. and Xu. In Situ and Quantitative Characterization of Solid Electrolyte Interphases. *Nano Letters* **14**, 1405–1412 (2014).
- [192] Adam, W., Kazakov, D. V. & Kazakov, V. P. Singlet-oxygen chemiluminescence in peroxide reactions. *Chemical Reviews* **105**, 3371–3387 (2005).
- [193] Ogilby, P. R. Singlet oxygen: there is indeed something new under the sun. *Chemical Society Reviews* **39**, 3181–3209 (2010).
- [194] Schweitzer, C. & Schmidt, R. Physical mechanisms of generation and deactivation of singlet oxygen. *Chemical Reviews* **103**, 1685–1757 (2003).
- [195] Ogilby, P. R. & Foote, C. S. Chemistry of Singlet Oxygen .42. Effect of Solvent, Solvent Isotopic-Substitution, and Temperature on the Lifetime of Singlet Molecular-Oxygen (1-Delta-G). *Journal of the American Chemical Society* **105**, 3423–3430 (1983).
- [196] Badger, R. M., Wright, A. C. & Whitlock, R. F. Absolute Intensities of Discrete and Continuous Absorption Bands of Oxygen Gas at 1.26 and 1.065  $\mu$  and Radiative Lifetime of 11andag State of Oxygen. *Journal of Chemical Physics* **43**, 4345 (1965).
- [197] Mckeown, E. & Waters, W. A. Oxidation of Organic Compounds by Singlet Oxygen. *Journal of the Chemical Society B: Physical Organic* **0**, 1040–1046 (1966).
- [198] Ogilby, P. R. & Foote, C. S. Chemistry of Singlet Oxygen .34. Unexpected Solvent Deuterium-Isotope Effects on the Lifetime of Singlet Molecular-Oxygen (1-Delta-G). *Journal of the American Chemical Society* **103**, 1219–1221 (1981).
- [199] Krieger-Liszkay, A. & Trebst, A. Tocopherol is the scavenger of singlet oxygen produced by the triplet states of chlorophyll in the PSII reaction centre. *Journal of Experimental Botany* **57**, 1677–1684 (2006).
- [200] Flors, C. & Nonell, S. Light and singlet oxygen in plant defense against pathogens: Phototoxic phenalenone phytoalexins. *Accounts of Chemical Research* **39**, 293–300 (2006).
- [201] Reddi, E. *et al.* Photophysical properties and antibacterial activity of meso-substituted cationic porphyrins. *Photochemistry and Photobiology* **75**, 462–470 (2002).
- [202] Mosinger, J., Jirsak, O., Kubat, P., Lang, K. & Mosinger, B. Bactericidal nanofabrics based on photoproduction of singlet oxygen. *Journal of Materials Chemistry* **17**, 164–166 (2007).
- [203] Maisch, T. *et al.* The role of singlet oxygen and oxygen concentration in photodynamic inactivation of bacteria. *Proceedings of the National Academy of Sciences of the United States of America* **104**, 7223–7228 (2007).
- [204] Bonnett, R. *Chemical Aspects of Photodynamic Therapy*. Advanced Chemistry Texts (Gorden and Breach Science Publishers, 2000).
- [205] Zhao, Z. *et al.* Effect of defects on photocatalytic activity of rutile TiO<sub>2</sub> nanorods. *Nano Research* **8**, 4061–4071 (2015).
- [206] Li, Q. *et al.* A spectroscopic study on singlet oxygen production from different reaction paths using solid inorganic peroxides as starting materials. *Bulletin of the Korean Chemical Society* **28**, 1656–1660 (2007).

- 
- [207] Montagnon, T., Tofi, M. & Vassilikogiannakis, G. Using singlet oxygen to synthesize polyoxygenated natural products from Furans. *Accounts of Chemical Research* **41**, 1001–1011 (2008).
- [208] Margaros, L., Montagnon, T., Tofi, M., Pavlakos, E. & Vassilikogiannakis, G. The power of singlet oxygen chemistry in biomimetic syntheses. *Tetrahedron* **62**, 5308–5317 (2006).
- [209] Hassoun, J., Croce, F., Armand, M. & Scrosati, B. Investigation of the O<sub>2</sub> Electrochemistry in a Polymer Electrolyte Solid-State Cell. *Angewandte Chemie International Edition* **50**, 2999–3002 (2011).
- [210] Ogilby, P. R. Singlet oxygen: there is still something new under the sun, and it is better than ever. *Photochemical & Photobiological Sciences* **9**, 1543–1560 (2010).
- [211] Enko, B. *et al.* Singlet Oxygen-Induced Photodegradation of the Polymers and Dyes in Optical Sensing Materials and the Effect of Stabilizers on These Processes. *Journal of Physical Chemistry A* **117**, 8873–8882 (2013).